Final Report

Ultra-Efficient Hybrid Aircraft

AE3200: Design Synthesis

Group 3

Delft University of Technology

TU Delft

This page is intentionally left blank.

Final Report

Ultra-Efficient Hybrid Aircraft

by

Group 3

Student Name	Student Number
Giorgio Balbo	4682440
Lisa Blom	4996747
Jelle Kok	4664949
Constança Miranda de Andrade Veiga	4786327
Christoph Pabsch	5064015
Igor Pszczolkowski	5091934
Luke Shu	5031281
Annemijn Stokman	4848896
Jennifer Thornton	4855876
Guillermo Van	4780000

Version History

Version	Comment
1.0	Draft Version, submitted on 15/06/2022
1.1	Updated Draft Version, submitted on 16/06/2022
2.0	Final Version, submitted on 21/06/2022

Tutor:	J. van Campen
Coaches:	J. Maruhashi and R. Pasolari
Teaching Assistant:	L. Dijkstra
Project Duration:	April, 2022 - June, 2022
Faculty:	Faculty of Aerospace Engineering, Delft

TU Delft

Executive Overview

Reducing the emissions of ultra-fine particles in the vicinity of airports to minimise detrimental health effects for near-airport residents and airport personnel has been the main objective of the project. This report details the realisation of this goal which was done by designing a hybrid aircraft with notable improvements in the efficiency and emission characteristics. The aircraft in question is named the 'Low Emission Alternative Fuel' aircraft, or 'LEAF'. Design of essential components and systems is presented along with evaluation of aspects needed for LEAF aircraft to enter the market by 2035.

Market Analysis

To determine if there is a market opportunity for an ultra-efficient hybrid aircraft a thorough market analysis on several topics was conducted. First, the current aviation market and its growth potential was analysed. The 2022 current market size is $180.43 billion and has an expected compound annual growth rate of 13.8% [1]. In addition, single-aisle aircraft occupy the majority of the market and the need for short-to-medium aircraft is expected to grow. By analysing same-class aircraft, it was identified that currently there are no aircraft that produce as minimal emissions in terms of CO_2 and NO_x as the LEAF aircraft. Hence, the project will take advantage of this market gap.

An analysis of the future market was also conducted to evaluate possible future aircraft competitors. Airbus has published that they are working on three low-emission projects, the ZEROe, BLADE, and E-Fan X. The ZEROe is expected to be LEAF's biggest competitor given that it is a low-emission aircraft likely to enter the market in 2035.

The mission of this project is to improve the air quality and, hence, the health of airport workers and surrounding communities. Three main harmful pollutants are identified: ultra-fine air particles, CO_2 and NOx emissions. To determine the extent to which the aircraft should reduce emissions, it is of paramount importance to analyse the health effects of these pollutants. After extensive research, it is concluded that ultra-fine particles are ultra-toxic and cause both cardiovascular and respiratory illnesses. Exposure to these particles, while also inhaling CO_2 and NOx in the air from aircraft emissions, causes approximately 8000 premature deaths per year [2].

Performance Analysis

The first step in designing an aircraft is to perform a flight performance analysis to obtain preliminary parameters. First, a Class I Weight estimation is performed followed by constructing a payload-range diagram, a V-n diagram (load factor versus speed), and thrust & wing loading diagram. These diagrams are found respectively in Figure 1a, Figure 1b, and Figure 2.

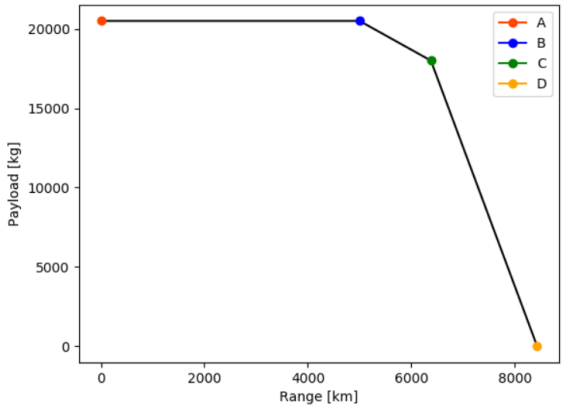

(a) Payload Range Diagram: indicating the initial point (A), and the range at maximum payload (B), design payload (C) and zero payload (D)

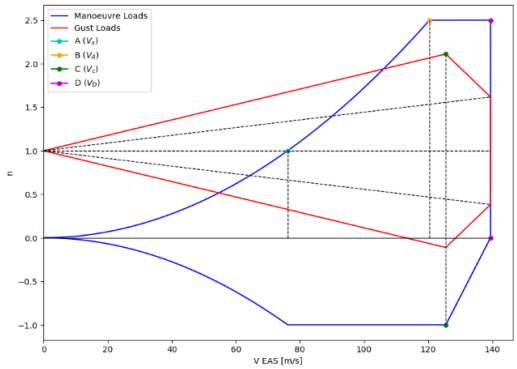

(b) Manoeuvre and Gust Load Diagram

Figure 1: Flight Performance Plots

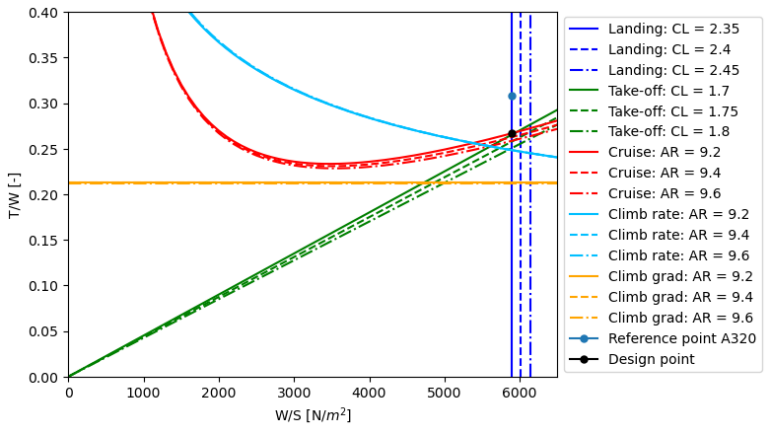

Figure 2: Thrust & Wing Loading Diagram

Aerodynamics

Wing Planform Design

For the wing planform, a design consisting of two trapezoids is preferred over a design consisting of a single trapezoid. A reason for this is that more space for storing the main landing gear can be created. Another reason is that the root chord can be enlarged by using two trapezoids. This is beneficial for the wing structure, since more load paths can be created and bending stresses can be reduced. Finally, the lift reduction at the root due to fuselage interference can be limited by enlarging the wing area at the root locally, allowing for a local increase in lift. Furthermore, the leading edge sweep was kept constant, and with the taper ratio, surface area and aspect ratio, the planform could be constructed.

Wing Airfoil Selection

After an extensive trade-off on airfoil selection, the supercritical NLF(1)-0215F airfoil was selected to be the most optimal airfoil given the LEAF's aircraft characteristics.

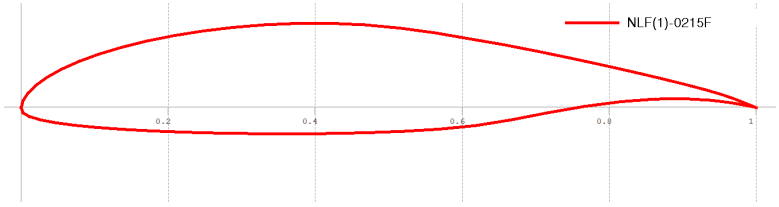

Figure 3: NLF(1)-0215F

Lift and Drag Estimation

After selecting the airfoil and determining the wing planform parameters, a lift and drag estimation is conducted. This analysis yielded the two following plots:

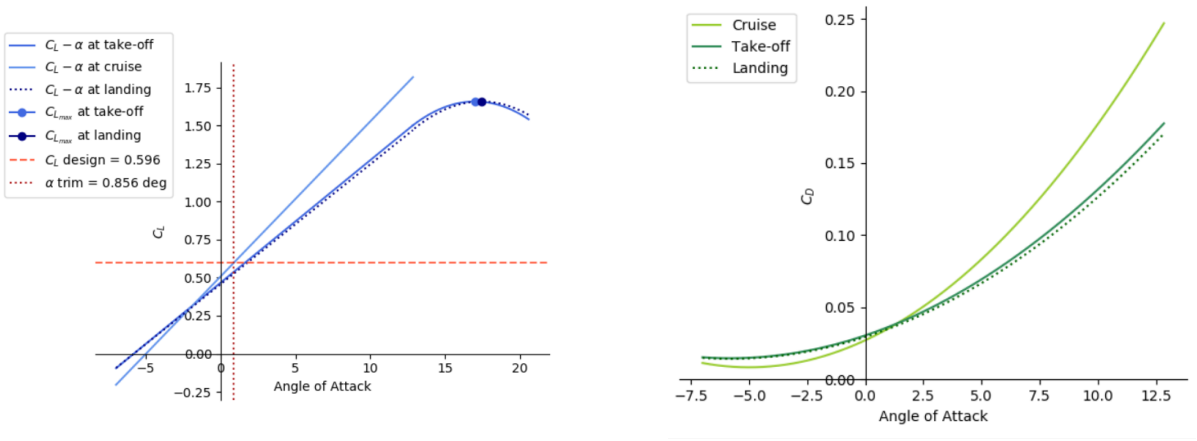

(a) Lift Coefficient versus Angle of Attack

(b) Drag Coefficient versus Angle of Attack

Figure 4: Lift and Drag Estimation

High-Lift Devices and Control Surfaces

First, to design the control surfaces for the wing the aileron design is conducted. In order to obtain the complete aileron design, an iterative process was set up where the spanwise position was altered until the roll rate requirement was met, thereby omitting the possibility of over-designed ailerons. Secondly, high-lift devices were sized. After a trade-off comparing design complexity, efficiency, occupied wingspan and maintenance is completed, a single slotted Fowler flap and a Krueger flap were selected to be the best combination. The wing planform layout including mobile wing surfaces is shown in the figure below:

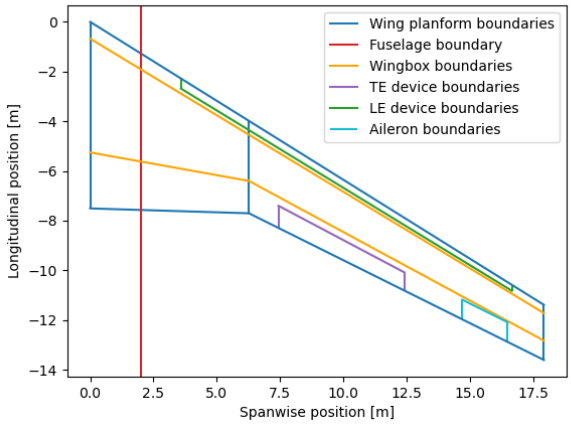

Figure 5: Wing Planform Design

Internal Configuration

The internal configuration of the LEAF-aircraft was based on that of an A320 in order to ensure that the passenger experience on this aircraft is comparable to that on an A320. Figure 6 shows the cross-section of the fuselage of the LEAF aircraft. In longitudinal direction the LEAF aircraft is $7.2\,\mathrm{m}$ longer than an A320. This is due to the fact that there is one large liquid hydrogen tank in the rear end of the aircraft. This tank has been placed there with a relative high offset from the lower skin of the fuselage to ensure safety during a possible belly landing.

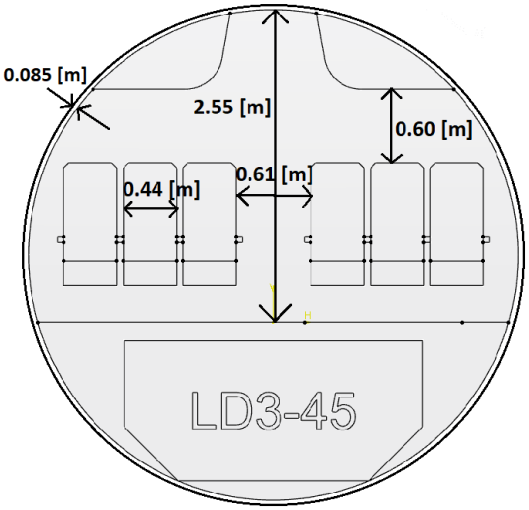

Figure 6: Cabin and cargo hold cross-section with dimensions in metres

Energy Storage

There are three layers in the hydrogen tank: the inner pressure wall, the insulation foam and protective fairing. The materials chosen for these are Al7068-T6511, reticulated vitreous carbon foam and aluminium honeycomb respectively. The tank shape will be cylindrical with hemispheres on each side, as a fully spherical tank would not fit in the fuselage and such design will maximise pressure and volume performance for the same weight. As a result, the hydrogen inner tank parameters chosen are 56 kg/m^3 for mixture density, 2.67 MPa for maximum allowed pressure and 3.5 for the length to radius ratio of the inner tank. The total volume of the assembly is 50.81 m^3, the total mass is 2644 83kg, the outer diameter is 3.15 m and the total length is 7.55 m. The inner tank wall thickness and mass are 10.4 mm and 1605.95 kg respectively. For the foam layer, the thickness is 29.3 mm and the mass is 941.41 kg. For the fairing, the thickness is chosen to be 15.7 mm and its mass is 97.47 kg. At this stage, the geometry is optimised for fitting inside the tail cone and will result in minimum extra fuselage length.

Power and Propulsion

The concept for engine architecture has been selected. The chosen architecture is a twin spool geared turbofan with a combustion chamber in which both kerosene and hydrogen can be combusted. This design has proven to be the most efficient in terms of both weight and performance. Its main characteristics are summarised in Table 1. The engine, which is shown in Figure 7, was developed with certain constraints in mind, including the maximum temperature or the overall pressure ratio. The values were constrained with values which take into account development of the engines until the predicted market entry in 2035.

Table 1: Engine dimensions and specification. (*: gear, **: combustion chamber.)

Fan diameter [m]	Bypass Ratio [-]	Π_{fan} [-]	Π_{LPC} [-]	Π_{HPC} [-]	F_{bypass} [N]	F_{core} [N]	stage layout
2.35	11.5	1.663	2.02	8.316	83187	6814	1-G*-2-6-CC**-1-2

The emission characteristics of the aircraft have been analysed using a flight profile simulation, where an average flight profile of the LEAF aircraft was estimated based on flight data of similar class aircraft. Based on that analysis and an estimation of combustion products obtained from Chemical Equilibrium and Applications software [3], the emission composition based on altitude has been investigated. The overview of most important emitted compounds, H_2O, CO_2 and NOx is presented in Figure 8.

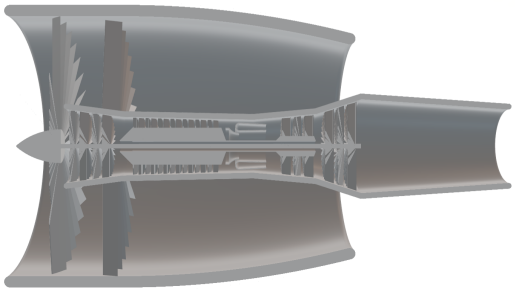

Figure 7: Side view of the engine

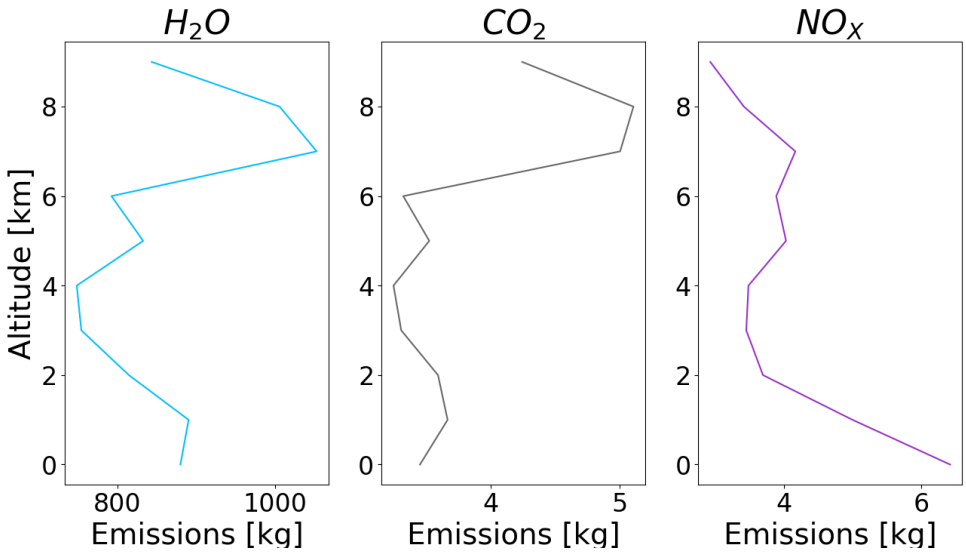

Figure 8: Emissions for climb and descent phases using hydrogen

Furthermore, options of pre-mixing the hydrogen and kerosene were evaluated in order to further reduce emissions by achieving a leaner burn. It has been determined that the most optimal strategy is to first burn pure hydrogen and, once it has been depleted, switch to kerosene.

State-of-the-art aircraft use polluting and loud jet engines to propel themselves during ground operations. That is why it has been decided to place electric motors in the main landing gear wheels. Since four main landing gear wheels have been chosen instead of eight, there will also be four electric motors. Each electric motor must be able to provide a maximum driving torque of about 7500 Nm and a maximum braking torque of $12\,500$ Nm. Braking is done regenerative, from which 64% of total needed electrical energy for ground operations can be obtained. This energy is stored at 684 kW in the ultracapacitors on board. The rest of the energy needed for ground operations will come from the hydrogen fuel cell APU. To ensure a safe braking system even when the electric motors do not work for some reason, a pneumatic braking system with ferromagnetic braking discs, cast iron,is put into place to not interfere with the magnetic field of the electric motors.

Structures and Materials

The structures part of the aircraft has been split in 3 different structural divisions: the fuselage structure, the wingbox and the empennage structure. The wingbox structure is mainly defined by the wing skin, the stringers, the spar webs and the ribs. For the empennage, the same structural components are used in the wingboxes of the horizontal and vertical tail. In order to achieve the most efficient and light design possible, the numbers and spacing of stringers and spacing of ribs was optimised and is varying over the wingspan (or the span of the horizontal and vertical tail respectively.

In the fuselage structure, the fuselage thickness, the frames and the stringers were the main structural components designed. Additionally, the bulkhead at the end of the passenger cabin was sized and the support structure of the hydrogen tank was determined. In order to optimise the fuselage structure, it was split into 5 different sections (4 in front and 1 behind the bulkhead) with a different skin thickness. Furthermore, a different

frame spacing and size was chosen for the part behind the bulkhead.

Regarding the materials, the requirement of recyclability was driving the choice of materials. Therefore, and also because of their lower footprint, metals were preferred over composite materials. Because of their relatively low density and sufficient material properties, different aluminium alloys were chosen from the metals. For the fuselage, Al 7075 T6 was chosen due to its high yield strength. Differently, for the wingbox Al 7149 was chosen, as it has a higher corrosion resistance, which is required for the wingbox in contact with fuel. The same material has been chosen for the empennage.

In conclusion, the final mass distribution of the structural design can be observed in Figure 9. As can be seen, the biggest part from the structural mass arises from the wingbox, with more than 50% of the total structural mass. The fuselage makes up for slightly less than 40% of the total structural mass. Finally, the overall empennage structure represents less than 10% of the total aircraft structural mass.

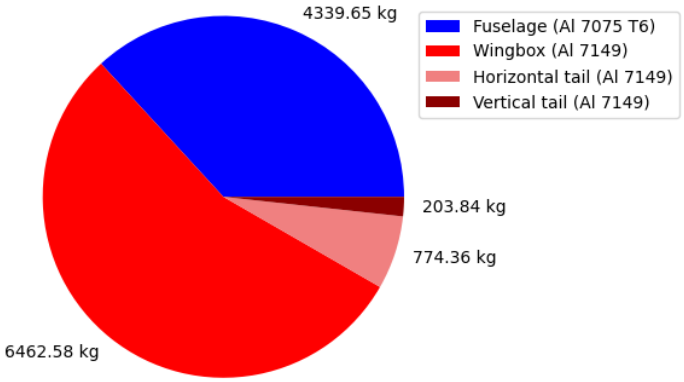

Figure 9: Mass distribution for the aircraft structures

Stability, Control and Balance

In order to obtain the optimal solution for wing and landing gear positions, leading to the smallest possible horizontal tail surface area, the wing position is varied along the fuselage. The forward and aft aircraft center of gravity (CG) positions are calculated, and the corresponding initial landing gear positions are established. Then, it is checked whether the landing gear positions comply with the given landing gear constraints. The wing positions that lead to a possible landing gear design are documented along with their corresponding cg and landing gear positions. From these options, the solution that requires the smallest horizontal tail surface area is selected. After this, the lateral position of the main landing gear is determined. The possible options that comply with all constraints are documented, and the option requiring the smallest landing gear length is selected. This length is then compared to the minimum length required for the longitudinal positioning. The highest value of these is limiting. For the LEAF aircraft, it turned out that the longitudinal positioning is limiting. This length is adopted and it is checked whether the lateral positioning requirements are still met. With this, the landing gear positions are determined. A schematic front view of the aircraft with the indicated landing gear lengths, is shown below:

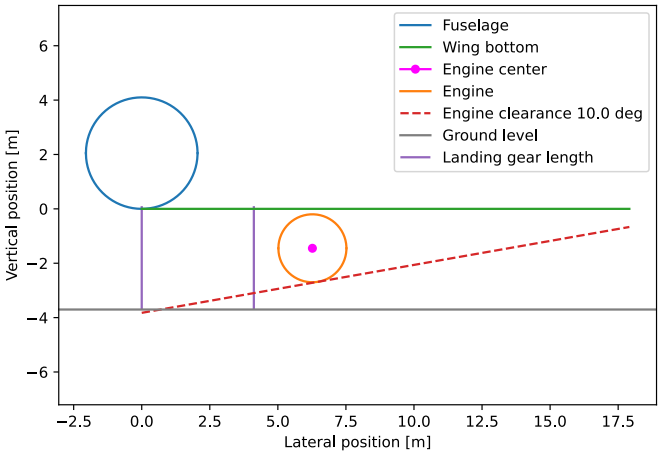

Figure 10: Schematic front view of the lateral landing gear positions

Aircraft Systems

Design for systems essential for aircraft operation have been determined. These systems include the electrical, hydraulic, pneumatic and fuel systems. Design of these systems is based on standards adopted by the modern airliners, with the biggest differences being the inclusion of a second fuel system for hydrogen distribution. Furthermore, the electrical system accommodates regenerative braking for better energy efficiency. Apart from those systems, hardware and software block diagrams have been constructed as well as the communication flow diagram to better illustrate the aircraft components during operation and their interactions.

Operations & Logistics

Airport operations and logistics comprises of refueling hydrogen and kerosene, passenger and cargo loading and unloading and maintenance. Hydrogen refueling is performed as follows; hydrogen is produced from a green-source off-site, liquefied, transported to a storage facility, and then brought to the aircraft using refueling trucks. Kerosene is easily refueled using underground fuel hydrants. Figure 11 depicts the ground handling arrangement at the airport in-between flights. Lastly, the airline must perform maintenance checks in compliance with airworthiness authorities to ensure the safety of the aircraft and its passengers.

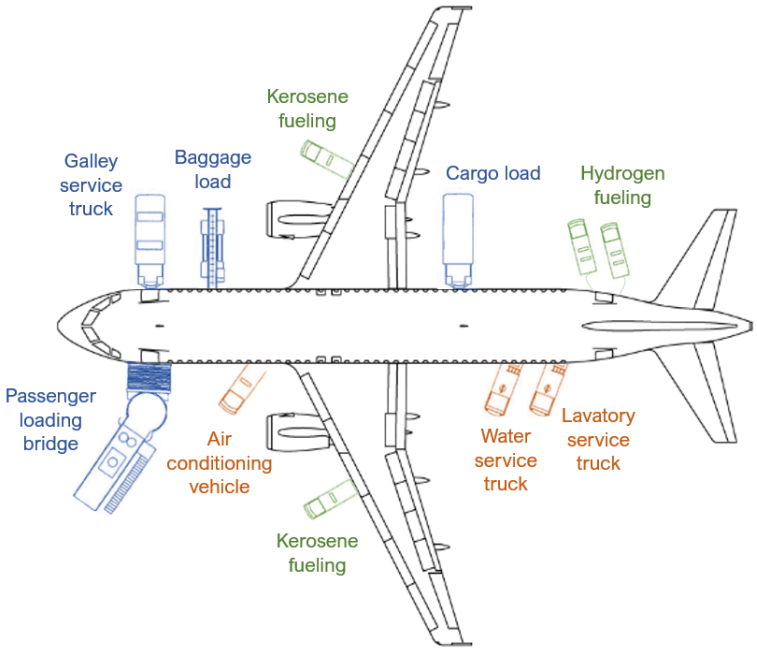

Figure 11: Ground handling arrangement [4] [5] [6]

Financial Analysis

To check if the LEAF aircraft is economically sustainable a financial analysis of the aircraft has been performed. This analysis is subdivided into the acquisition cost, return on investment and direct operational costs. The acquisition cost is estimated by using statistical estimation formulas from T. Zhao [7] and Raymer [8]. These formulas calculate the manufacturing acquisition cost by taking the sum of the engine, airframe and avionics costs. By also taking into account a profit of 10%, which is a widely used percentage in the passenger jet industry, a total acquisition cost of €117.73 million is obtained. The development cost of the LEAF aircraft is estimated to be 150% of that of an A320, which would result in €2775 million. Plotting the total cumulative profit of the LEAF aircraft against the number of aircraft units sold the graph in Figure 12 is obtained.

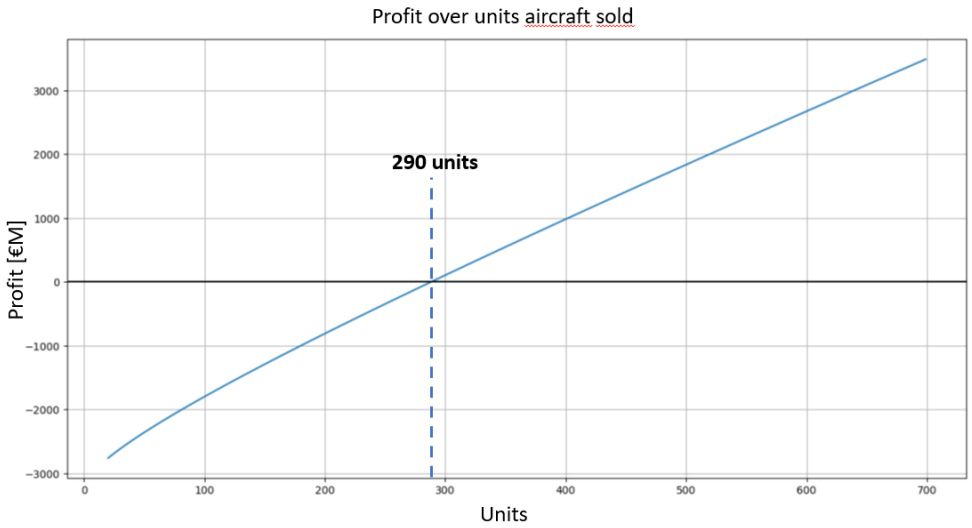

Figure 12: Profit of the LEAF aircraft over the amount of units sold. Note that the line is not fully linear. This is because the costs of labour becomes lower when more units are sold, thus the acquisition cost will be lower as well while the profit stays at 10%.

From this graph it can be derived that the amount of aircraft that need to be sold in order to break even and start making a positive profit is about 290. Comparing this amount to the amount of A320s that were sold by Airbus over the years it can be estimated that it will take about five years for the LEAF aircraft to be profitable.

The direct operational cost of an aircraft is a combination of the financial cost, crew cost, charges and fees, maintenance cost and fuel cost. A total cost breakdown of this has been made and can be seen in Figure 13. From this a total direct operational cost for the airline is estimated at €16870 per flight on average.

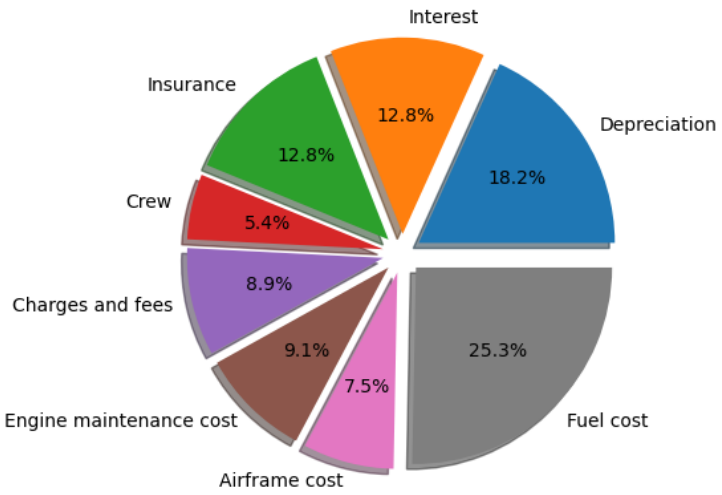

Figure 13: Cost breakdown DOC: sub-category division

Nomenclature

Abbreviations

Abbreviation	Definition	Abbreviation	Definition
ACARS	Aircraft communications addressing and reporting system	IP	intermediate pressure
ADC	Air data computer	LC	load case
ADS-B	Automatic dependent surveillance - broadcast	L/D	lift-to-drag
AHRS	Altitude and heading reference system	LE	leading edge
AL	Airline	LEAF	Low Emission Alternative Fuel
AP	Airport	LFL	Lower Flammability Limit
APU	Auxiliary Power Unit	LHV	lower heating value
ATAG	Air Transport Action Group	LNG	Liquefied natural gas
BPR	bypass ratio	MA	Manufacturer
CAGR	compound annual growth rate	MAC	Mean Aerodynamic Chord
CBS	cost breakdown structure	MNS	Mission Need Statement
CEA	Chemical Equilibrium and Applications	MTOW	Maximum take-off weight
CFD	computational fluid dynamics	OEW	Operational empty weight
CG	Center of Gravity	PAH	polycyclic aromatic hydrocarbons
CVR	cockpit voice recorder	PAX	Passengers
DH	Data Handling	PM	particulate matter
DI	deliver interval	POS	Project Objective Statement
DOC	direct operational cost	PPE	personal protective equipment
EAS	Equivalent airspeed	PTU	Power Transfer Unit
EMM	engine material maintenance	RAMS	Reliability, Availability, Maintainability and Safety
ENV	Environmental organisations	RAT	ram air turbine
EOL	end-of-life	RE	Near-airport residents and airport personnel
FBS	Functional Breakdown Structure	RefProp	Reference Fluid Thermodynamic and Transport Properties
FF	Form factor	RF	radiative forcing
FFD	Functional Flow Diagram	RMP	Radio management panel
FIS	flight information services - broadcast	RVC	reticulated vitreous carbon
FQIS	Fuel quality indication system	SAF	Sustainable Aviation Fuel
GI	gravimetric index	SAR	Specific air range
GNSS	Global navigation satellite system	S/W	Software
GPU	Ground Power Unit	TACS	Traffic alert collision avoidance system
GPWS	Ground proximity warning system	TAS	True airspeed
HF	High frequency	TAT	Turn around time
HLD	High-lift device	TAWS	Terrain awareness warning system
HP	high pressure	TE	Trailing edge
HSR	high-speed train	TIS-B	Traffic information service - broadcast
H/W	Hardware	TRL	Technology Readiness Level
ICe	electric intercity train	UFP	Ultra-Fine Particles
IF	Interference factor	VHF	Very high frequency
IFE	in-flight entertainment	WAAS	Wide area augmentation system

Symbols

Symbol	Definition	Unit
AR	Aspect ratio	[-]
$b_{1/2}$	Half wing span	[m]
b_{in}	Inwards trapezoid wing span	[m]
b_{out}	Outwards trapezoid wing span	[m]
$\bar{c}$	Chord	[m]
c_r	Root chord	[m]
c_{kink}	Kink chord length	[m]
c_t	Tip chord	[m]
(t/c)	Thickness ratio	[-]
C_M	Moment coefficient	[-]
C_D	Drag coefficient	[-]
C_L	Lift coefficient	[-]
$C_{L_{TO}}$	Lift coefficient at Take-off	[-]
$C_{L_{A-h}}$	Lift coefficient derivative w.r.t α at tail	[-]
$C_{L_{alpha_{A-h}}}$	Lift coefficient at ...	[-]
e	Oswald Efficiency factor	[-]
L/D	Lift-to-drag ratio	[-]
W/S	Wing loading	[-]
T/W	Thrust loading	[-]
T	Thrust	[kN]
S	Wing surface area	[m^2]
$S_{1/2}$	Half wing surface area	[m^2]
n	Load factor	[-]
TOP	Take-off-parameter	[-]
M_{dd}	Drag divergence Mach number	[-]
$M^{\dagger}$	Supercritical technology factor	[-]
V	Velocity	[m/s]
$V_{S_{land}}$	Stall speed at landing	[m/s]
g	gravitational force	[m/s^2]
$x_{cg_{fwd}}$	forward center of gravity	[m]
$x_{cg_{aft}}$	aft center of gravity	[m]
x_{LEMAC}	longitudinal position of MAC	[m]
x_{nw}	longitudinal nose wheel position	[m]
x_{mw}	longitudinal main wheel position	[m]
y_{mlg}	lateral main landing gear position	[m]
l_{lg}	landing gear length	[m]
S_h	Horizontal tail surface area	[m^2]
V_h	Horizontal tail flow speed	[m/s]
l_h	Horizontal tail arm length	[m]
W_{TO}	Maximum take-off weight	[kg]
W_E	Empty weight	[kg]
W_F	Fuel weight	[kg]
W_{Fused}	Used fuel weight	[kg]
W_{Fres}	Reserve fuel weight	[kg]
W_{tfo}	Weight of trapped fuel and oil used	[kg]
W_{PLtot}	Total payload weight	[kg]
M_{FF}	Mission fuel-fraction	[-]
E	Energy stored	[MJ]
m	Mass	[kg]
t	Thickness	[m]
r	Radius	[m]
T	Temperature	[° C]
p	Pressure	[Pa]
$\dot{m}$	Mass flow	[kg/s]
c_p	Specific heat capacity	[J/kgK]
$\dot{Q}$	Heat transfer rate	[J/s]

Symbol	Definition	Unit
R	Specific gas constant	[J/Kmol]
$K_{(}Ic)$	Fracture Toughness	[MPa]
α	Angle of attack	[°]
α_h	Angle of attack of the tail	[°]
ρ	Density	[kg/m^3]
σ	Density ratio	[m]
σ_{yield}	Yield strength	[Pa]
λ	Taper ratio	[-]
$\Lambda_{0.25c}$	Quarter-chord sweep angle	[°]
Λ_{LE}	Leading edge sweep angle	[°]
$\Lambda_{TE_{in}}$	Trailing edge sweep angle for inward trapezoid	[°]
$\Lambda_{TE_{out}}$	Trailing edge sweep angle for outward trapezoid	[°]
$\varkappa$	Specific heat ratio	[J/kgK]
$(1 - d\varepsilon/d\alpha)$	Downwash gradient	[-]
μ	Efficiency	[-]
ψ	Equivalence ratio	[-]

Contents

1

Introduction

Annemijn

Over the years the emission of carbon dioxide (CO_2) and ultra-fine particles (UFPs) by aircraft has become an increasing problem. Especially in the neighbourhood of airports where health effects are visible and black dust consisting of ultra-fine particles (UFPs) is found on windowsills regularly. This is one of the driving factors in research that is ongoing globally to find ways to reduce emissions in the aviation industry and that of the LEAF aircraft as well. This project therefore aims to find a way to still make use of air-transportation but reduce the amount of emissions by using a hybrid power system. By using an alternative, green energy source in the vicinity of airports, the emissions of ultra-fine particles, carbon dioxide and nitrogen oxides (NO_x) will be limited. During the design, improving the living conditions to the populations living close to airports and the global environment as well is kept in mind constantly. This report contains the research, analysis and design steps performed to achieve this objective and will be the base for further development and production of the LEAF aircraft in 2035.

This report begins with Chapter 2 where a revised plan for the organisation of the project and important baseline decisions can be found. The strategy to construct an aircraft as sustainable as possible that is used throughout the whole design process is explained in Chapter 3. In Chapter 4 the health effects of emissions and competition on the market will be researched. Next, the design of all different aspects of the LEAF aircraft and their respective challenges are discussed in Chapter 6 to Chapter 12. An iteration on the design is then done in Chapter 13 and in Chapter 18 the extent to which the requirements were fulfilled is considered. For post-DSE design, a production plan is written in Chapter 15 and the further organisation is visualised in Chapter 16. Finally an analysis about financial aspects of the design is in Chapter 17.

Project Objectives

It is of paramount importance to define the project objectives at the beginning to ensure that each individual team member effort is directed towards the common goal of the project.

Project Objective Statement

Design an aircraft that minimises the emission of ultra-fine particles at the airport, the energy consumption, and the overall impact on the environment.

The project ideals can be further broken down into the following bullet points:

- The aircraft must achieve a 100% reduction of CO_2 and non-CO_2 emissions with respect to the current state of the art during ground operations at the airport.
- The aircraft must achieve a 30% reduction of CO_2 and an 80% reduction of non-CO_2 emissions with respect to the current state of the art.
- Aircraft is able to reach same cruise speed, altitude, and range (at same payload) as an A320-200.
- Most parts of the plane need to be made from recycled material.
- The aircraft should enter service in 2035.

Mission Need Statement

Aircraft pollution in the form of CO_2 and ultra-fine air particles emitted by aircraft must be reduced by at least 30% and 80% respectively, as well as a 100% reduction of each during ground operations in and around airports, in order to improve the air quality and therefore the health of airport workers and communities living around airports.

2
Project Baseline

The project starts with identifying the stakeholder requirements. These are given in Section 2.1. After they are specified, a functional analysis can be performed. This is covered in Section 2.2. When the functions are identified, several aircraft concepts are proposed that can perform the functions. After a trade-off of the concepts, one concept is chosen and developed further. A summary of the trade-off results is provided in Section 2.3.

2.1. Stakeholder Requirements

Guillermo, Igor

The high-level requirements, which are derived from the mission statement as well as demands of the customer, are stakeholder requirements. To derive stakeholder requirements, first the stakeholders need to be identified. After conducting an analysis, all the stakeholders were defined as shown below:

- **RE:** Near-airport residents and airport personnel
- **ENV:** Environmental organisations
- **AL:** Airline
- **AP:** Airport
- **MA:** Manufacturer
- **PAX:** Passengers

In order to better identify the requirements a further division based on the origin of the requirement has been included in the identifier. The categories include: PERF - performance, SAF - safety, SUS - sustainability and FIN - finance. The stakeholder requirements are presented in Tables 2.1 - 2.6.

Table 2.1: Stakeholder requirements for airline

Identifier	Requirement
RAP-AL-PERF-01	The flight performance of the aircraft shall be comparable to that of an A320-200
RAP-AL-PERF-02	The aircraft shall operate with a 10% reduced overall final energy consumption compared to the A320-200.
RAP-AL-PERF-03	The aircraft shall be able to carry an amount of passengers or amount of cargo that is competitive with the A320-200
RAP-AL-PERF-04	The total turn around time for the aircraft shall be the same as for an A320-200.
RAP-AL-SAF-01	The aircraft shall be able to safely land using either energy source.
RAP-AL-SUS-01	The aircraft shall include an hybrid energy system which is able to be upgraded with more efficient components as the technology evolves.
RAP-AL-SUS-02	The aircraft shall have a nominal lifetime of 30 years.
RAP-AL-FIN-01	The acquisition cost shall be maximum 25% above the cost of an A320-200.
RAP-AL-FIN-02	The operating cost shall not exceed the cost of an A320-200 by more than 25%.
RAP-AL-FIN-03	The amount of training required for A320-200 pilots to operate the aircraft shall be minimised.

Table 2.2: Stakeholder requirements for airport

Identifier	Requirement
RAP-AP-PERF-01	The aircraft shall be able to operate at the same airports as the A320-200.
RAP-AP-PERF-02	The refuelling system shall be possible to be integrated with existing airport infrastructure.

Table 2.3: Stakeholder requirements for residents

Identifier	Requirement
RAP-RE-SUS-01	The aircraft shall achieve a 90% reduction of harmful non-CO_2 emissions during ground operations. [1]
RAP-RE-SUS-02	The aircraft shall not produce more noise pollution than an A320-200.

Table 2.4: Stakeholder requirements for passengers

Identifier	Requirement
RAP-PAX-PERF-01	The general passenger experience shall be comparable to that of an A320-200.

Table 2.5: Stakeholder requirements for manufacturer

Identifier	Requirement
RAP-MA-PERF-01	All parts of the aircraft shall be manufacturable with existing manufacturing techniques.
RAP-MA-PERF-02	The aircraft shall maintain structural integrity at all times.
RAP-MA-SAF-01	All manufacturing processes will comply with industry safety standards and regulations.
RAP-MA-SAF-02	The aircraft shall comply with EASA's JAR25.
RAP-MA-FIN-01	The aircraft shall enter service in 2035.

Table 2.6: Stakeholder requirements for airport personnel and environmental organisations

Identifier	Requirement
RAP-ENV-SUS-01	The aircraft shall achieve an 80% overall reduction of harmful non-CO_2 emissions with respect to the current state of the art.
RAP-ENV-SUS-02	The aircraft shall achieve a 30% overall reduction of CO_2 emissions with respect to the current state of the art.
RAP-ENV-SUS-03	The aircraft shall achieve a 100% reduction of CO_2 emissions during ground operations.
RAP-ENV-SUS-04	At least 90% of the aircraft parts shall be recyclable at end-of-life. [1]
RAP-ENV-SUS-05	At least 5% of the aircraft parts shall be reusable at end-of-life. [1]

Harmful emissions are defined by the UN Environment Programme as emissions that harm both humans and the ecosystem after repeated exposure. These include PM2.5 (fine particles that are 2.5 microns or less in diameter) and nitrogen oxides (NOx) [2].

2.2. Functional Analysis

Christoph, Lisa

In order to obtain the FFD and FBS, the Mission Need Statement was analysed and five main phases of the aircraft life were set up. These phases serve as Function Level 1. The phases were then broken down into main functions within a certain phase, resulting in Function Level 2. Breaking down functions is repeated until the desired level of detail is achieved. For the FFD, a progression until Function Level 3 was developed and for the FBS, Function Level 4 was the objective (one Function Level 5 is achieved for one fourth level function). From each function, requirements can be derived.

The five main phases covering Function Level 1 are the production of the aircraft, ground operations, flight operations, maintenance and end-of-life operations. The phase 'ground operations' defines all functions carried out at the airport before entering the runway and after exiting the runway. 'Flight operations' defines all functions carried out between and including take-off and landing.

[1] Negotiated with customer [9]

[2] URL `https://www.unep.org/news-and-stories/story/5-dangerous-pollutants-youre-breathing-every-day` [cited 06 June 2022]

2.2.1. Functional Flow Diagram

An FFD chronologically visualises the order in which the functions must be performed. Both functions carried out in sequence and functions carried out in parallel are displayed. The distinction is indicated in both of the diagrams. Figure 2.1 describes the flow of the five main phases (Function Level 1) with their sub-functions (Function Level 2). Figures 2.2 to 2.6 all describe the flow of the second level functions with their sub functions (Function Level 3), for the main phases respectively. Therefore, every figure corresponds to one main phase. The legend shown in Figure 2.1 applies to all figures up to and including Figure 2.6.

2.2.2. Functional Breakdown Structure

The FBS displays how functions are broken down into sub-functions, to achieve a higher level of detail. All functions up until Function Level 3 are shown in both the FFD and FBS. However, the FBS goes into detail by one more level. Therefore, the FBS complements the FFD as it displays more specific functions that are derived from the functions shown in the FFD. The FBS is displayed in Figure 2.7.

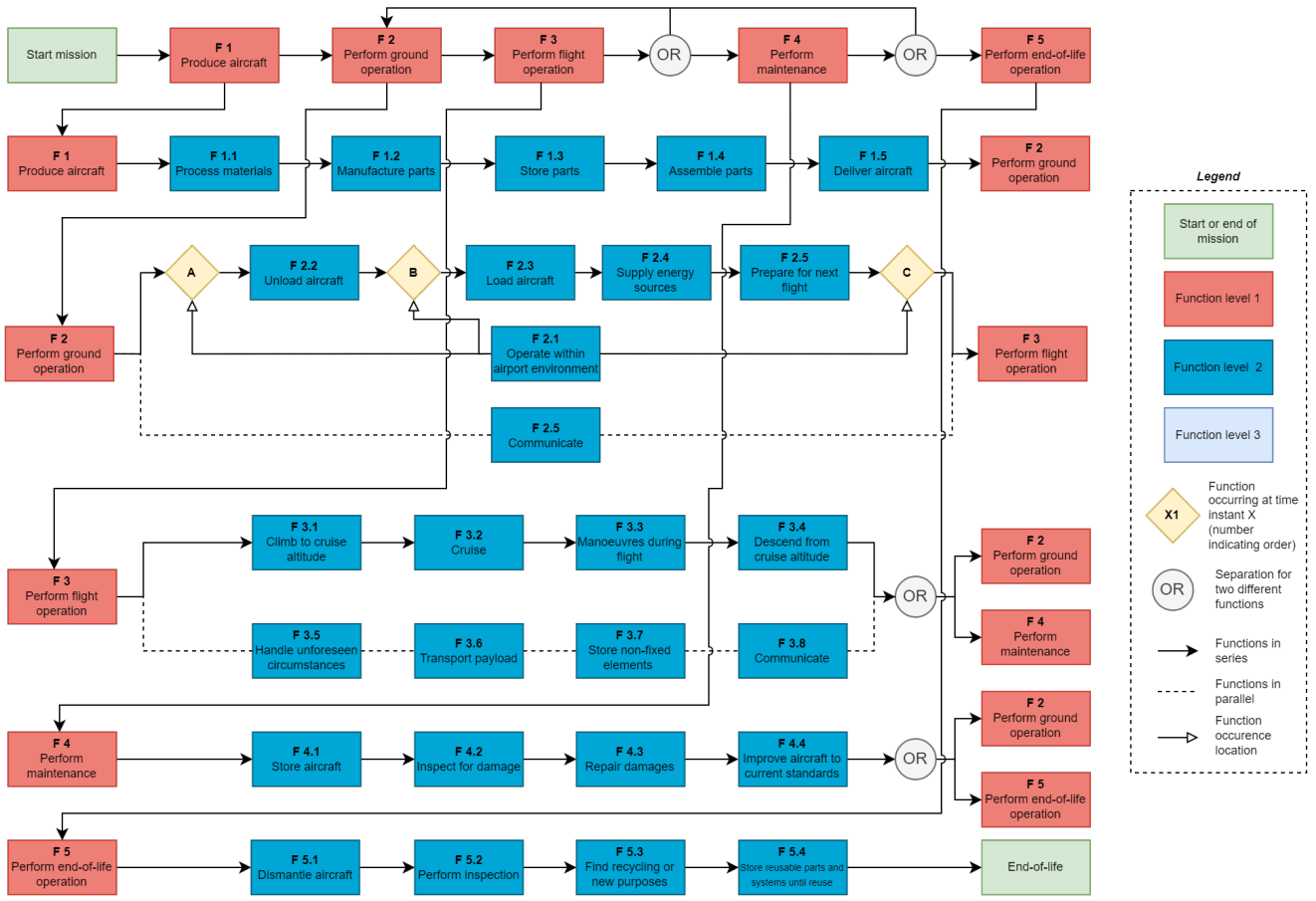

Figure 2.1: Functional Flow Diagram: main overview

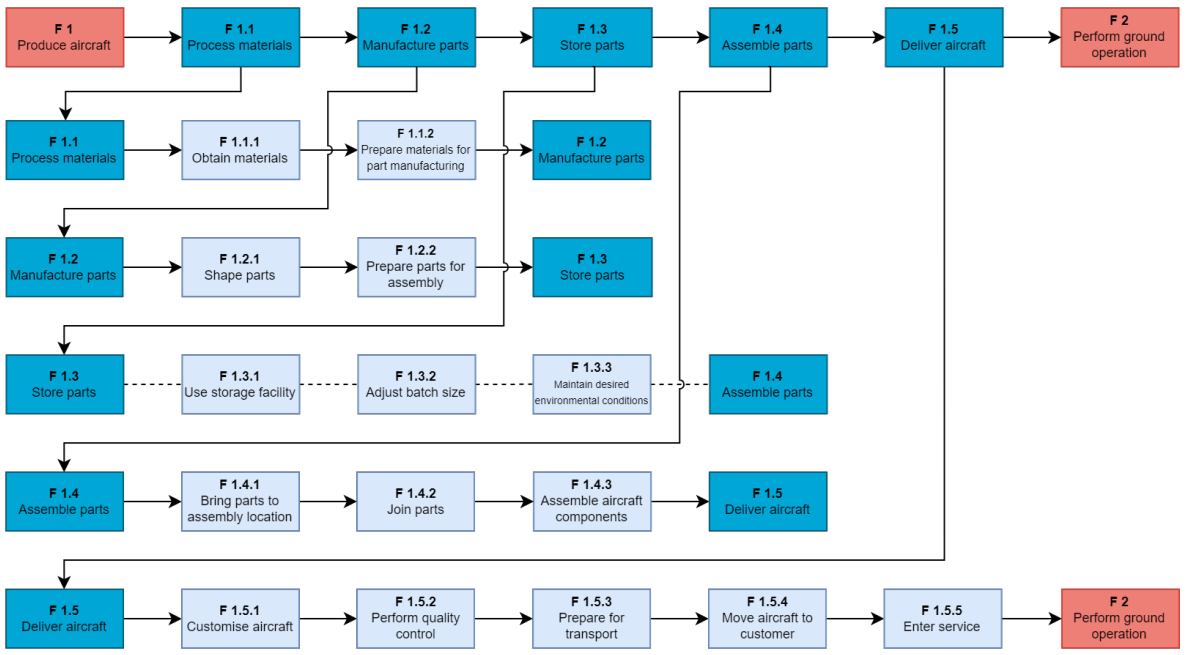

Figure 2.2: Functional Flow Diagram: production phase

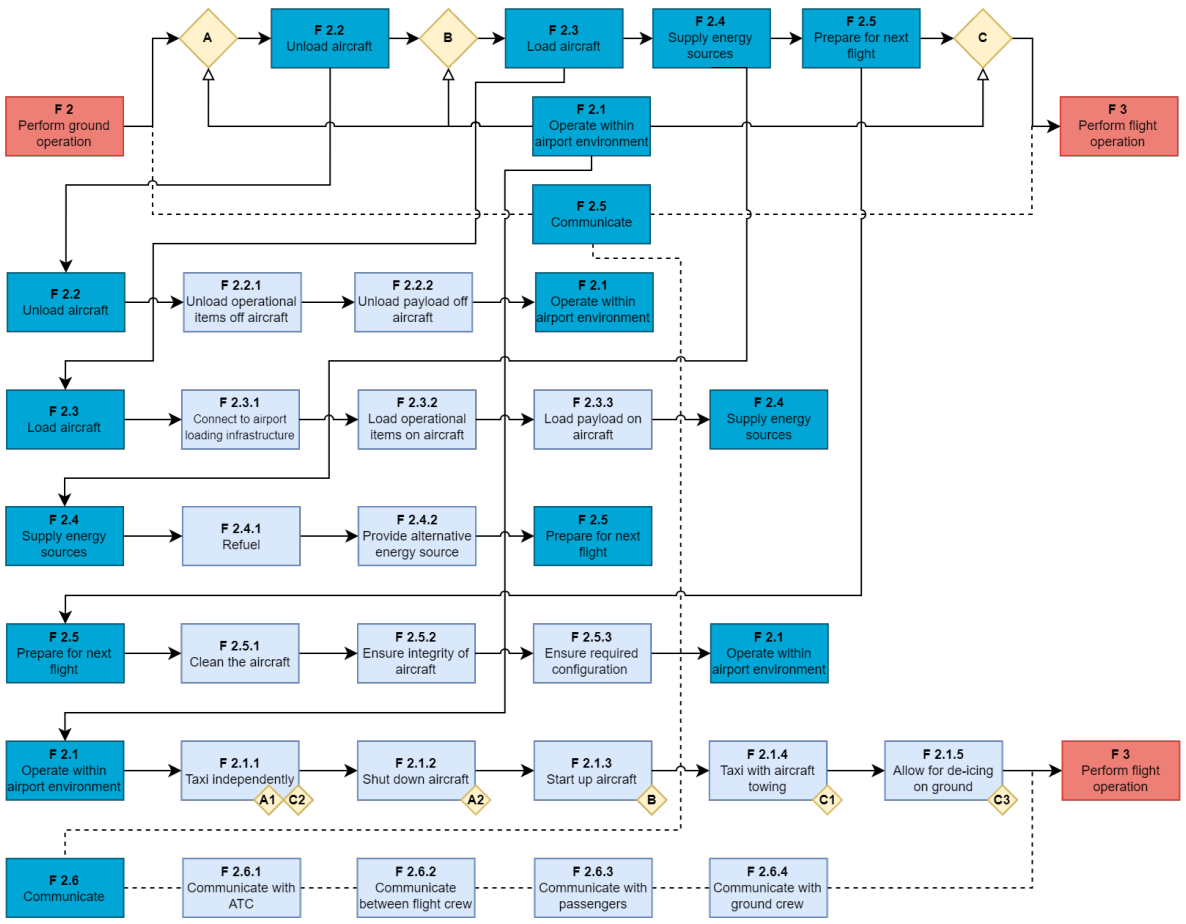

Figure 2.3: Functional Flow Diagram: ground operation phase

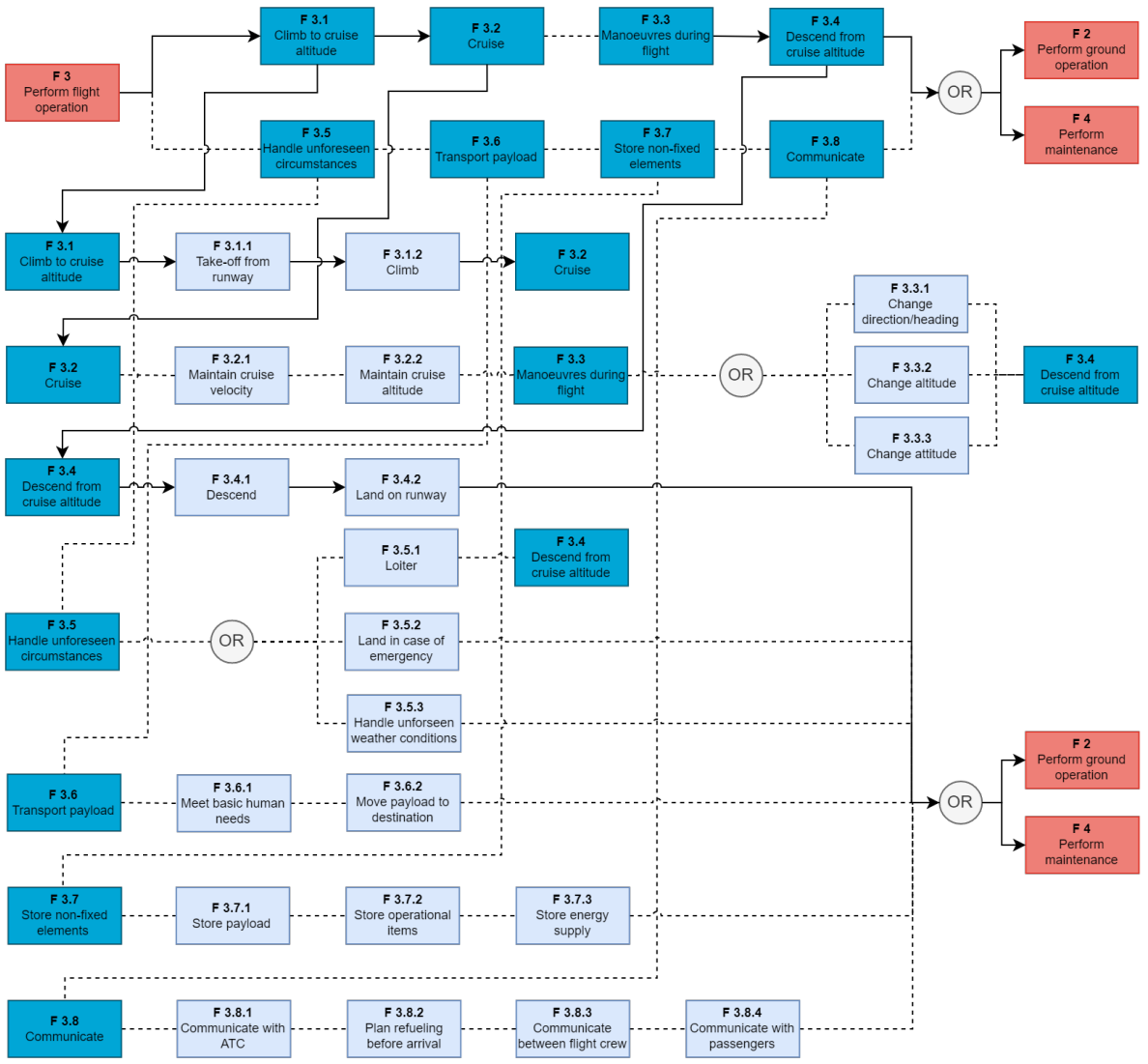

Figure 2.4: Functional Flow Diagram: flight operation phase

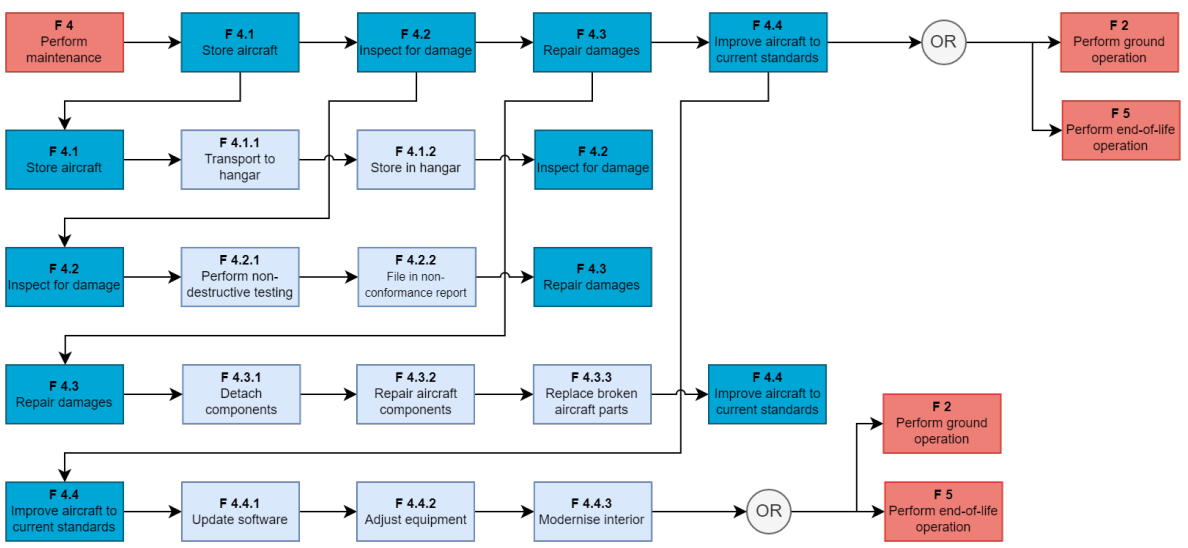

Figure 2.5: Functional Flow Diagram: maintenance phase

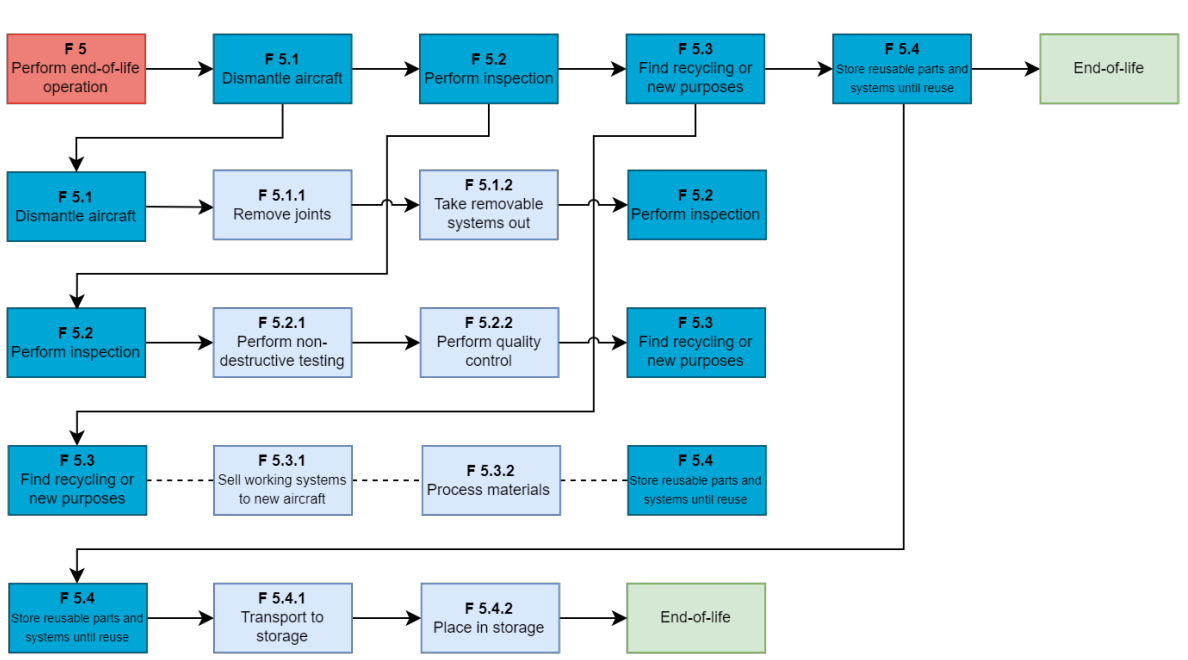

Figure 2.6: Functional Flow Diagram: end-of-life operation phase

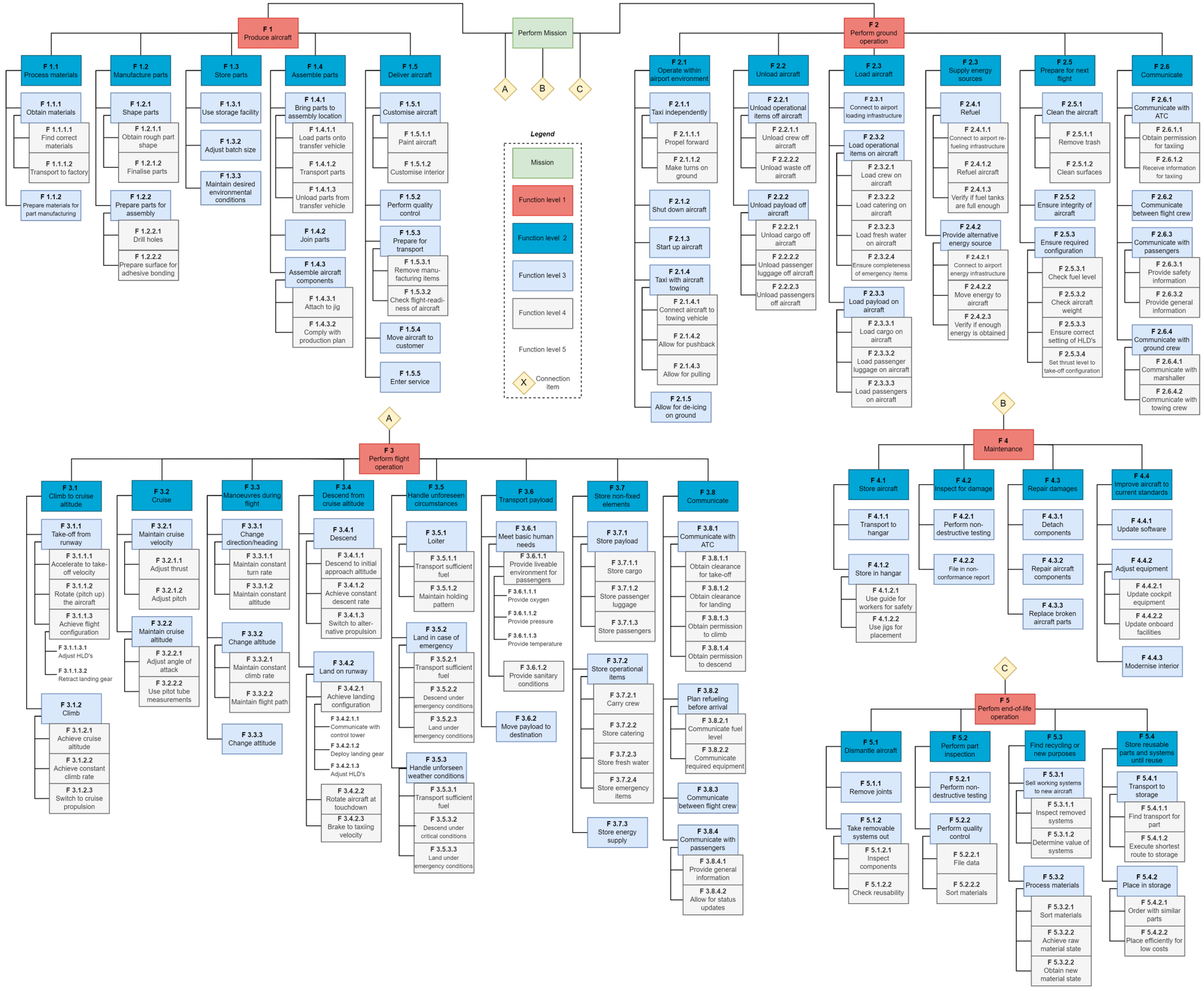

Figure 2.7: Functional Breakdown Structure

2.3. Summary of Trade-Off Results *Guillermo*

Before designing the LEAF aircraft in detail it was necessary to do three general trade-offs that will drive the design and influence the feasibility of the goal heavily. These trade-offs are about the energy source, propulsion system and configuration of the aircraft.

2.3.1. Energy Source Trade-Off

For the storage of energy on board the LEAF aircraft the four different design options listed below were considered:

- Liquid hydrogen (H_2), stored under -252.9 °C
- Liquid ammonia (NH_3), stored under -33 °C
- Battery, where the data projected for 2030 is used
- Methanol (CH_3OH)

The criteria that were looked at in order to make a proper trade-off were the weight, volume, cost, emissions, flammability and technology readiness level, or TRL. The highest selection criteria weights were given to the weight and TRL, because these two would influence the compliance with the stakeholder requirements the most. From this trade-off it has been decided to use liquid hydrogen as the energy source for the LEAF aircraft. The only shortcoming of liquid hydrogen is its high flammability and low specific volume. These shortcomings are dealt with later on in the design phase.

Another trade-off that was made regarding the energy source was the refueling method, because this would influence the design of the energy storage system heavily. Two refueling options were considered: refueling one big liquid hydrogen tank or swapping several smaller tanks on the tarmac. For this trade-off the volume efficiency, refuelling time and logistical complexity were the most important selection criteria to be looked at. This resulted in a higher score for refueling one big liquid hydrogen tank. This tank was chosen to be placed in the back of the aircraft with some offset from the lower skin of the fuselage to ensure safety during a possible belly landing.

2.3.2. Propulsion System Trade-Off

Now that it is known that liquid hydrogen will be the energy source of the LEAF aircraft it is possible to make a trade-off for the propulsion system. The design options listed below were considered in this trade-off:

- Separate jet fuel powered and electrically powered turboprop engines
- Hybrid jet fuel and electrically powered turboprop engines
- Separate jet fuel powered and hydrogen powered turboprop engines
- Hybrid jet fuel and hydrogen powered turboprop engines
- Hybrid jet fuel and hydrogen powered turbofan engines
- Separate jet fuel powered and hydrogen powered turbofan engines
- Hybrid jet fuel powered turbofan engines with electrically powered fans
- Separate jet fuel powered turbofan engines and electrically powered fan engines

The selection criteria that were looked at are the acquisition cost, development risk, mass, energy efficiency, emissions and thrust. The energy efficiency, mass and thrust were the most important selection criteria due to its large influence on complying with some of the stakeholder requirements. From this trade-off the top three propulsion systems were chosen for further analysis. These propulsion systems are hybrid jet fuel and hydrogen powered turbofan engines, hybrid jet fuel powered turbofan engines with electrically powered fans and Separate jet fuel powered turbofan engines and electrically powered fan engines. These were chosen as the possible propulsion systems of the aircraft in part due to their high mass performance and thrust. Also, these propulsion systems were the only ones that did not have an unacceptable score for any of the selection criteria.

2.3.3. Configuration Trade-Off

The configuration of the aircraft regards the vertical wing positioning together with the empennage configuration. Because some configurations are better for different propulsion systems a trade-off was made for different combinations of the configuration and propulsion system. All these design options considered all listed in Table 2.7.

Table 2.7: Design options with respective number and name

Name
A320 type aircraft
Fokker 70 type aircraft
Hydroplane type aircraft
V-tail aircraft
Modified hydroplane type aircraft
H-tail aircraft
AVRO type aircraft

The selection criteria that were looked at for this trade-off were the stability & control of the configuration, development risk, mass performance, L/D ratio, operations and noise emissions. L/D ratio and mass performance were the most important selection criteria looked at for this trade-off. In this trade-off the A320 type aircraft with two hybrid kerosene and hydrogen powered turbofan engines mounted under the wing have the highest scored the highest. Therefore, for a further detailed analysis and design of the LEAF aircraft this configuration and propulsion system is also chosen.

3

Sustainable Development Strategy

Sustainability can be broken down into three main categories: environmental, social and economic. These represent sustainability with respect to the planet, people, and management respectively. Section 3.1 details how the project is environmentally sustainable by reducing both air pollution and wasteful practices. Section 3.2 presents the social sustainability measures with respect to employees, customers and local communities. Section 3.3 specifies how production costs, operational and maintenance costs are minimised.

The United Nations has developed 17 goals in order to achieve a better and more sustainable future for all. The LEAF aircraft contributes to 3 out of the 17 sustainable development goals directly. These can be seen in Figure 3.1 [1]. With respect to goal seven, achieve affordable and clean energy, the LEAF aircraft contributes to the share of renewable energy and energy efficiency improvement. With respect to goal 12, target 12.5, "By 2030, substantially reduce waste generation through prevention, reduction, recycling and reuse.", is directly achieved by LEAF. Lastly, goal 13, climate action, is accomplished due to LEAF's reduced emissions.

Figure 3.1: UN's Sustainable Development Goals

3.1. Environmental Sustainability

Constança

Environmental sustainability is of paramount importance in order to preserve the planet. The goal is to conserve Earth's natural resources while also protecting its ecosystem. To achieve this, RAP must emit the lowest possible amount of harmful particles and noise emissions. The health effects of these emissions can be found in detail in the Baseline report. Likewise, it is crucial that the end-of-life of the aircraft components are also environmentally friendly.

Emissions

Aircraft engines are one of the main global pollutants [2]. Its emissions are dependent on the fuel consumption, engine technology and fuel constituents. One of the main objectives of LEAF is to reduce emissions that harm the health of humans and contribute to global warming, in particular during ground-operations, take-off and landing. The following key measures will be implemented to make the aircraft environmentally friendly.

- **Maximise efficiency.**
  - By maximising the efficiency of the aircraft, it is possible to decrease the fuel consumption. Hence, less emissions released per flight.
  - Reduces CO_2 and NOx emissions, in particular during cruise.
  - Can be achieved by reducing drag by using riblets.
- **Use secondary zero emissions propulsion system for ground-operations, take-off and landing.**
  - By eliminating the emissions of CO_2, NOx and ultra-fine particles it is possible to not harm the health of the airport personnel and airport surrounding communities.
  - This is directly related to the requirement RAP-SYS-SUS-02 to -07.
- **Produce minimum noise emissions.**

[1] URL sdgs.un.org/goals [cited 20 June 2022]
[2] URL `https://www.icao.int/environmental-protection/pages/aircraft-engine-emissions.aspx` [cited 04 May 2022]

  - Exposure to loud noises has several health effects on humans such as high blood pressure, sleep disruptions and stress. At the same time, noise pollution has a big impact on the well-being of wildlife.
  - Predominantly created by the fan and jet noise of turbofan engines.
  - Increasing engine bypass ratios, increasing engine performance and lowering the fan tip speed are ways to reduce noise pollution.
  - This is related to requirements RAP-SYS-SUS-08 to -10.

Material

To create the most environmentally sustainable aircraft, it is important to consider its sustainable impact throughout its entire lifetime. Therefore, the end-of-life of each aircraft component needs to be environmentally friendly. With this in mind, the following measures are taken:

- **Use recyclable materials.**
  - By maximising the use of recyclable materials for each aircraft component, waste and thus pollution can be reduced.
  - Reduces carbon footprint and reduces the need for harvesting raw materials, which consumes more energy than recycling energy.
  - Related to requirement RAP-SYS-SUS-11.
- **Maximise use of bio-degradable materials.**
  - Bio-materials breakdown naturally and do not harm the environment.
  - Possible bio-degradable materials are cork (used for insulation), mycelium (bonding agent), and bamboo (aircraft interior)

3.2. Social Sustainability *Constança*

Social sustainability is vital for a healthy relationship between workers (employees), stakeholders (e.g. customers) and local communities. This is achieved by creating and implementing proactive measures to foster internal morale, relationship, respect and loyalty and employee engagement. Table 3.1 details the infrastructure used to ensure social sustainability.

Table 3.1: Social sustainability measures across the project

Employees	**Customers**	**Local communities**	**Workers in value chain**
- Ensure fair labour and wages - Promote well-being in the workplace - Provide safe working conditions - Employ social equality - Provide training when needed	- Keep airlines informed - Maximise transparency - Keep airlines inclusive in the design process	- Promote open-source information - Create a safe and healthy environment	- Not use harmful substances in production - Keep them informed and engaged

Advantages of adopting social sustainability measures:

- Helps retain and attract business partners
- Improves risk management
- Happy workers - work better
- Increases reputation among community
- Reliable and open source of innovation

The complete life cycle of the aircraft will contribute to social sustainability as well.project will create many new jobs, where the employees will be able to connect with each other. These employees will also have a salary which will help boost the local economy. Both consequences may improve the living conditions of these workers and thus improve social sustainability.

3.3. Economic Sustainability *Constança*

Economic sustainability aims to optimise financial growth while also ensuring environmental and social sustainability. Hence, measures with respect to production, operations and maintenance are implemented to reduce costs. Figure 3.2 presents the Five Steps Approach used for optimisation of systems, thus reducing waste.

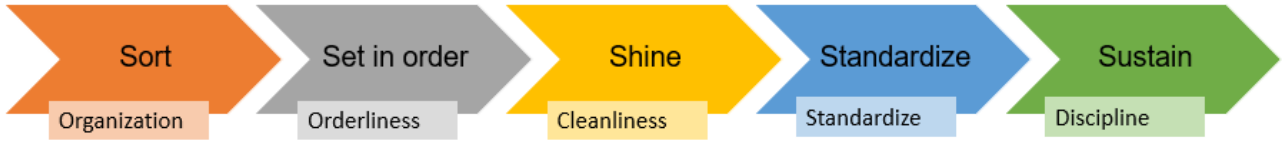

Figure 3.2: 5 Steps Approach

First, there is the Sort stage; all items or services have been examined and segregated. The crucial and unnecessary items have to be separated and then the redundant items removed. Second, in the Simplify stage the remaining items are identified and organised. Third, in the Shine stage the workplace is cleaned and key items are identified for visual control. Fourth, the Standardise stage ensures that the previous steps are performed regularly and correctly. Lastly, Sustain stage promotes the use of the 5S principle.

Production Costs

Production of aircraft involves a lot of costly processes due to the scale and complexity of the product. For this reason, it is crucial to manufacture and assemble the aircraft with as little waste as possible, i.e., implement lean manufacturing. The following list details the steps taken to minimise waste, thus reducing costs.

- **Optimise production line.** To reduce costs, it is of paramount importance that the manufacturing line is as efficient as possible. This can be done by:
  - Reducing waiting times between stations.
  - Inspecting possible bottlenecks in the material flow.
  - Evaluating the most optimal layout to improve the throughput and utilisation rate.
  - Implementing training to reduce learning curve.
- **Use low-cost materials.** To achieve highest cost efficiency, it is important to choose the best material with the highest performance to cost ratio while also ensuring recyclability requirements.
- **Strengthen supply base.** Ensure that the raw material providers supply the necessary materials on time, and without fault. Secure a second provider in case the main primary provider fails to meet the requests.
- **Design for high allowable tolerances.** By reducing the allowable tolerances in part manufacturing, cheaper and universal machinery can be used.
- **Implement cellular manufacturing.** Lowers transport and possible delays by arranging both equipment and workstations in a way that provides smooth and optimal flow of materials and components through the process. Furthermore, it improves efficiency by grouping similar processes together.
- **Standardise work.** Its benefits are detailed as follows:
  - Reduces variations in the output.
  - Increases worker efficiency by helping them structure their work and makes training easier.
  - Aids/promotes continuous improvement in part manufacturing.

Operational and Maintenance Costs

Optimising operational and maintenance costs is a key priority for airlines as they incur these costs throughout the operational lifetime of the aircraft. Thus, it is crucial that LEAF is most attractive to airlines financially. The following parameters can be made to reduce these costs:

- Aircraft designer
  - **Minimise fuel consumption and cost.** Fuel cost is the highest operational cost for airlines. Optimising it attracts customers and improves sustainability.
  - **Design long-lasting subsystems.** Subsystems that are highly reliable, signify low maintenance necessity over its operational lifetime.
  - **Design for easy maintenance access points.** This reduces complexity, consequently reducing costs in terms of labour and machinery.
- Airlines
  - **Focus on preventive maintenance.** Regular maintenance checks increases reliability thus preventing breakdowns, reduces significant cost and improves safety.
  - **Invest in training.** By having a highly skilled workforce, efficiency is improved.
  - **Automate maintenance checks.** Reduces human error, and can be performed continuously. In other words, the same machine can work 24/7 while a group of workers cannot.

4

Market Analysis

For the project to have a successful entry in the market in 2035, it is of vital importance to conduct a thorough market analysis on the aviation market and its potential growth. First, an analysis of the current aviation market and its size is followed by a future market investigation. This is followed by a study on the health and environmental effects of both ultra-fine particles and gas-phase emissions (CO_2 and NOx). Section 4.3 details LEAF's target customers, with respect to expect market growth. Section 4.4 details the different possible alternative clean energy sources for aviation. Lastly, the effects of hydrogen combustion by-products is investigated.

4.1. Aviation Market and Competition

Constança

Current Market

Before designing the next hybrid generation of an A320 type aircraft, it is of paramount importance to analyse the current market for this aircraft category. This category consists of single-aisle, short-to-medium range characteristics. Figure 4.1 shows that single-aisle aircraft occupy most of the market[1]. The single-aisle market is further broken down into the top aircraft manufacturers; where Airbus and Boeing lead the market almost equally[2]. The current market size in 2022 for commercial aircraft is $180.43 billion [1]. Additionally, it is expected to grow at a compound annual growth rate of 13.8% [1]. In other words, the market is expected to reach $968.63 billion in 2035.

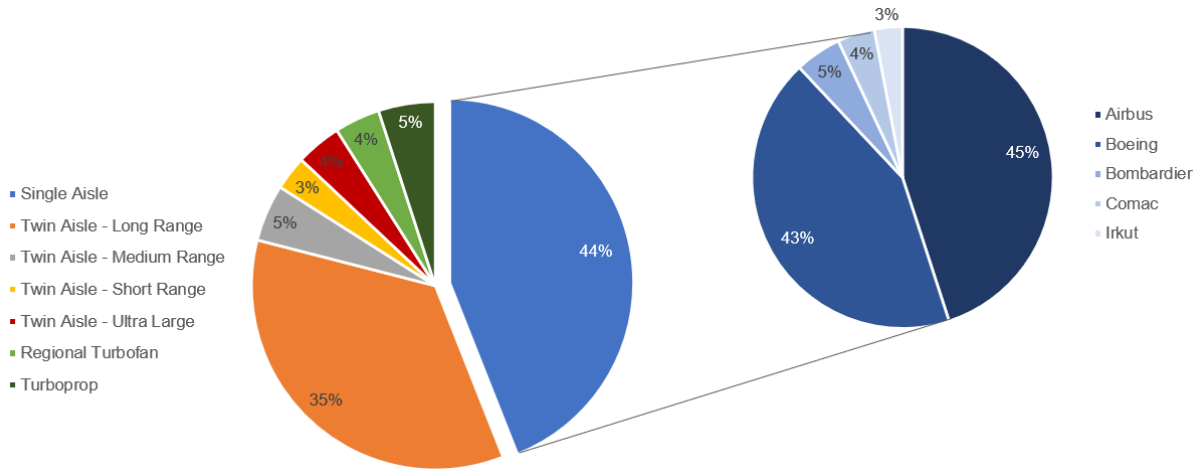

Figure 4.1: Aviation market share between 2016 and 2035

Between the years 1990 and 2019, CO_2 emissions have decreased by 53%, corresponding to a compound annual growth rate (CAGR) of -2.6% [10]. Currently, the two main aircraft that are comparable to LEAF are the Airbus A320NEO and the Boeing 737 Max. With the A320NEO producing 50% less NOx emissions and the B737MAX8 operating with a reduction in both CO_2 and NOx by 20% and 50% respectively, in comparison to the LEAF aircraft. The A320NEO offers 15% less fuel burn than today's A320s. The B737MAX8 aircraft will be up to 12% more fuel efficient per seat than B737s in operation today.

To analyse the possible market gap for the LEAF aircraft, several similar aircraft in terms of maximum passenger capacity and range were studied. Table 4.1 shows the following trends. Overall, LEAF does substantially

[1] URL `https://www.flightglobal.com/insight-from-flightglobal-flight-fleet-forecasts-single-aisle-outlook-2016-2035/121497.article` [cited 25 April 2022]

[2] URL `https://aviationweek.com/mro/mro-market-share-aircraft-categorization-2029` [cited 25 April 2022]

better with regards to both CO_2 and NOx emissions. Comparing to the B737MAX8, which is currently the most sustainable aircraft in this category, LEAF emits 28.4% less CO_2 and 78% less NOx emissions. In terms of acquisition cost, LEAF is more expensive, however, only by 14% relative to the A320NEO and by 4% compared to the B737MAX8. It must be noted that the LEAF price is a preliminary estimation derived from the requirement RAP-AL-FIN-03. With respect to noise emissions, the National Institute on Deafness and Other Communication Disorders stated that, "Long or repeated exposure to sound at or above 85dB can cause hearing loss" [11]. For this reason, an ultimate threshold of 84 dB during approach and take-off is designed for.

Table 4.1: Aircraft Characteristics [12][13][14]

Type	**Max Pax**	**Range** [km]	**Acquisition Cost** [$ million]	**CO_2** [g/RPK]	**NOx** [kg]	**Approach Noise** [EPNdB]
A320-200	180	6,150	101.0	87	11.28	96.1
A321	236	5,930	114.9	75	8	96.7
A319	156	6,900	92.3	105	7.46	94.6
A320NEO	194	6,300	110.6	63	5.64	-
B737-800	162	5,765	106.1	80	10.3	96.9
B737-700	149	6,370	89.1	100	10.3	96.0
B737-900	189	4,587	112.6	77	10.3	96.6
B737MAX8	210	6,570	121.6	61.6	5.15	-
RAP	180	6,150	126.3	44.1	1.128	84

Future Market

The LEAF aircraft is estimated to enter the market in 2035. In order to determine the feasibility of its success it is important to analyse possible future competitors and market gaps. The biggest future competitor will be Airbus ZEROe aircraft, which is a zero-emission commercial aircraft with hybrid hydrogen propulsion. Information about said aircraft is scarce online, hence its characteristics are not known and an analysis on the competition cannot be conducted. Sean Newsum, Boeing's sustainability strategy director, has stated that Boeing's commercial aircraft will operate using 100% biofuel by 2030. Both companies have the target of halving emissions by 2050.

Given that LEAF will be a short-to-medium range aircraft, it is also important to consider trains, especially high-speed trains as a competitor. In particular, Europe and Asia have plans to expand their train line network and to increase the number of 'bullet trains'. For example, China aims to reach 50.000 km in high-speed train lines by 2025 [3]. At the same time, Japan is expanding their maglev train network to connect its cities. With respect to sustainability, countries are commited to reduce their diesel powered trains by 2050 [4].

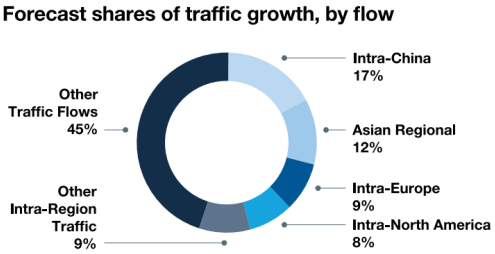

Figure 4.2: Boeing Forecast for Air Traffic Growth [15]

Furthermore, both Airbus and Boeing have a thorough market analysis of the aviation industry until 2040. From Figure 4.2, it can be seen that the Asian market will grow considerably. Airbus estimates that in the next 20 years the fleet in the Asia-Pacific area will increase by a 2.5 factor, while China will require triple its current fleet [10]. Overall, China will have the largest traffic flow and the highest growth will be within all of Asia. Section 4.3 will dive into the potential customers for the LEAF aircraft based on the foreseen market opportunity.

The transportation sector is one of the largest contributors of greenhouse gas emissions. These emissions come primarily from burning fossil fuel for cars, ships, trains, and planes [5]. The main pollutants emitted by aircraft engines in operations are carbon dioxide (CO_2), nitrogen oxides (NO_X), sulphur oxides (SO_X), unburnt hydrocarbons, carbon monoxide (CO), particulate matter (PM) and soot.

[3] URL https://edition.cnn.com/travel/article/future-rail-travel-cmd/index.html [cited 08 June 2022]
[4] URL https://www.un.org/en/climatechange/net-zero-coalition [cited 08 June 2022]
[5] URL https://www.epa.gov/ghgemissions/sources-greenhouse-gas-emissions [cited 02 June 2022]

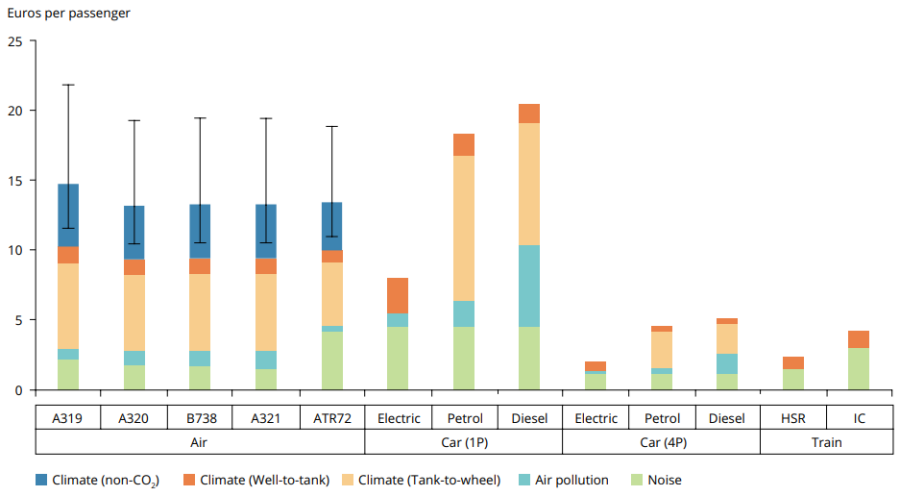

Figure 4.3: Emission costs of different transport modes (500 km) [16]

The transport modes included are the five most frequently used types of aircraft, an electric intercity train (ICe), a high-speed train (HSR) and three types of cars with an occupancy rate of one person and four people for each type.

4.2. Health and Environmental Analysis *Constança*

Emissions not only cause damage to Earth's environment but also its population health. For this reason, their effects should be analysed to determine the extent to which their emission should be reduced. Emissions can be categorised in two groups: ultra-fine particles and gas-phase emissions (CO_2 & NOx).

4.2.1. Ultra-Fine Particles

Studies have shown that human exposure to ultra-fine particulate matter (UFP) is linked to several health effects on both the cardiovascular and respiratory systems [17]. Ultra-fine particles are formed in combustion processes, and they can be composed of carbon, metallic or be volatile/semi-volatile. By definition they are nanoscale sized particles (less than 0.1 µm or 100 nm in diameter). Given their extremely small size, UFPs can easily inhabit the lungs and diffuse into vital organs [18]. Due to their high toxicity and large concentration in and around airports, a number of research studies have been conducted in recent years. Ultra-fine particles have diverse health effects, and they will be detailed in the following section to highlight the importance of reducing them in aviation.

Due to their size and high diffusivity, UFP rapidly enter the lungs and deposit in the alveolar region. The alveolar region comprises tiny air sacs (alveoli) that exchange carbon dioxide and oxygen between the lungs and blood. UFP can easily penetrate the blood vessels, which may cause oxidative stress and inflammation [20]. Oxidative stress induces not only cardiovascular diseases but also carcinogenicity, genotoxicity, neurotoxicity, and teratogenicity [6] [18]. In other words, possibly causing asthma, bronchitis, and damage to cells, proteins and DNA. In addition, UFPs have the ability to retain in the lungs for long periods of time causing further damage. It is important to note that, unlike other particles, UFPs are comparatively more toxic as they can carry metals and polycyclic aromatic hydrocarbons (PAHs) [21], which may cause impaired lung function in the human body [22]. Figure 4.4 summarises the health effects of UFPs.

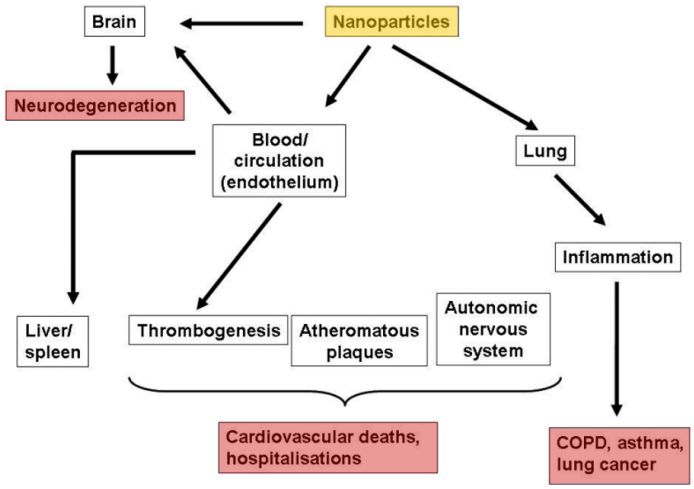

Figure 4.4: Health Effects of UFP Exposure [19]

[6] Carcinogenicity is the tendency to produce cancer. Genotoxicity is damage to DNA causing gene mutations. Neurotoxicity refers to damage to the brain or peripheral nervous system. Teratogenicity is the ability to cause defects in a developing fetus.

Emissions are populated by a broad range of harmful particles. It is important to note that PM2.5 fine particles and PM0.1 ultra-fine particles are the most toxic given the health damage that they cause [18]. Furthermore, research shows that there is a strong correlation between the following diseases and the exposure of particles smaller than $2.5\,\mu m$.

- Asthma
- Chronic obstructive pulmonary disease (COPD)
- Pulmonary fibrosis
- Neurodegenerative diseases
- Cancer
- Type II Diabetes

Throughout the last years, health organisations and airports have identified several health anomalies in airport personnel and communities living in the vicinity of airports. Three workers at Copenhagen Airport contracted bladder cancer, and their continuous exposure to ultra-fine particles was identified as the primary cause [23]. It must be noted that UFPs are also present in other environments, such as traffic congestions and even kitchens. However, the concentration of UFPs is much larger in airports compared to the normal environment of humans. Furthermore, a study showed that children living within an 8-km radius of the Boston Logan International Airport were more prone to develop asthma and experience respiratory symptoms [22]. Children are the most vulnerable group with respect to the possible health effects of UFP pollution given that their exposure began in the womb and continued through their early years of life, weakening their immune system [24].

In order to comprehend the full health effects of ultra-fine particles not only in the short-term but also long term, it is important to conduct more thorough research, in particular with regards to airport personnel and the population living around airports. Moreover, research has showed that about 90% of the measured particles were ultra-fine particles in airports [20]. Hence, it is important for the aviation industry to work towards emitting zero emissions not only for the environment but also for the health of susceptible populations.

4.2.2. CO_2 and NOx Emissions

Health effects

The combustion of kerosene in aircraft engines causes emissions that not only impact the environment but also deteriorates Earth's air quality. Consequently, the health of humans has simultaneously been worsening with emission increases. Research estimates that approximately 8000 premature mortalities per year are caused by aircraft emissions, with 88% related to cardiopulmonary diseases [2]. The health effects of emissions can further be categorised per emitter. SOx emissions depend on the propellant sulphur level and fuel consumption [25]. In high concentration regions, these molecules are a respiratory irritant, that induce airflow constraints [26]. NOx emissions not only depend on fuel consumption but also on the combustor and engine technology [25]. This emitter has been associated with both respiratory infections and is a catalyst for inhaled allergen side-effects [26]. Overall, exposure to air pollution can be divided into two health effects: physical and mental. These effects are detailed as follows [27]:

- Slow lung development in fetuses.
- Central nervous system. More specifically, increased concentrations of NO_2 are associated with dementia and NOx with Parkinson's disease.
- Increase in infant mortality [28].
- More prone to respiratory illnesses, such as chronic obstructive pulmonary disease.
- Increase in cardiovascular diseases, such as hypertensive heart disease and minor heart-strokes.

Environmental effects

According to the Air Transport Action Group (ATAG), the global aviation industry is responsible for producing 2.1% of all human induced CO_2 emissions and 12% of travel related CO_2 emissions [7]. Approximately 5% of total global warming is caused by the aviation industry [8]. Emissions from flight are more damaging to the environment than the same emissions produced at ground level, as emissions at altitude can trigger many chemical and physical processes that affect climate change [29]. To state what the most polluting way of transport is, depends on how many passengers are in a vehicle. All road transport together are responsible for 74% of all CO_2 emissions [7]. If the term road transport is then subdivided in smaller terms like petrol medium car, bus

[7] URL `https://www.atag.org/facts-figures.html` [cited 28 April 2022]

[8] URL `https://www.bbc.com/future/article/20200218-climate-change-how-to-cut-your-carbon-emissions-when-flying` [cited 28 April 2022]

and national train, it turns out that domestic flight is in fact the way of transport with highest amount of CO_2 per passenger kilometer. [9].

Greenhouse gas emissions from aviation changes atmospheric concentration, consequently changing the energy balance of the atmosphere. This phenomenon is known as radiative forcing. Climate change is predominantly caused by radiative forcing, however the atmosphere is a complex system and therefore radiative forcing has non-linear effects on the environment. The different chemical compounds released from aircraft emissions contribute differently to the amount of radiative forcing that is observed. The largest contributors to environmental damage are CO_2 and O_3, carbon dioxide and ozone, where methane (CH_4) has a negative effect.

4.3. Customers

Constança

One of the main stakeholders and the sole customer of the LEAF aircraft are airlines. In order for the aircraft to operate, whether by transporting passengers or carrying freight cargo, an airline must organise, perform maintenance and operate the logistics of the aircraft. Although, theoretically, all airlines are potential customers, an analysis was conducted to see which airlines should be targeted to purchase the LEAF aircraft. To determine these airlines two main parameters were used: sustainability goals of the airline and population growth.

Trends in population growth, global aging and middle class growth in Africa and Asia-Pacific are expected to have a large impact on the airline industry, influencing not only where people live but how they live. More travelers are expected from non-traditional markets where middle classes are growing. Airline traffic growth in the Asia-Pacific region is 5%, Africa 5.4%, while the world average is expected to be 4% [15]. Boeing expects Chinese airlines will need 8,700 new aircraft [10]. Airbus expects demand for 2,210 planes in India over the next 20 years [11]. From this analysis, both China and India are the two key markets desired to enter, followed by Africa due to its incredibly high population growth rate. Lastly, airlines with a strong desire to be as sustainable as possible were investigated. Air France-KLM is strongly committed to reduce its environmental impact to achieve the climate objective of reaching net zero CO_2 emissions by 2050. Hence, the promote and use sustainable aviation fuels, optimise operational efficiency and perform carbon offsetting [12].

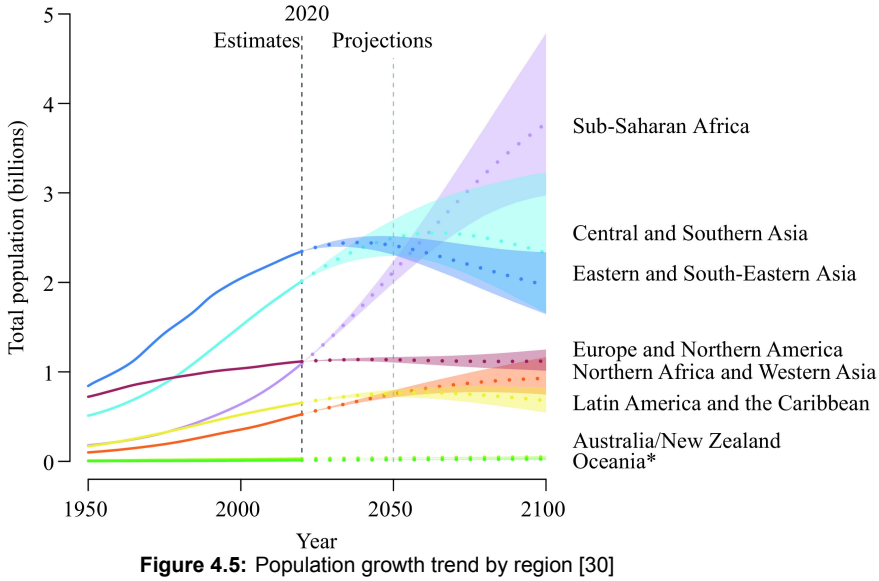

Figure 4.5: Population growth trend by region [30]

Main airlines to target are:

- Indigo: main airline in India with a fleet size of 277, of which 68% are short-to-medium range aircraft
- Air China: fleet of 475 aircraft
- China Eastern airlines: 600 aircraft, 66% are A320-class aircraft
- China Southern airlines: 642 aircraft
- Ethiopian airlines: biggest airline in Africa
- Air France-KLM: highly committed to be sustainable

4.4. Alternative Clean Energy Sources

Constança

RED II requires EU member states to achieve a minimum share of renewable energy within their transportation sector of 14% by 2030 (among other things) [EU 2018, Art. 25] [31]. The aviation transport sector requires

[9] URL https://www.statista.com/statistics/1185559/carbon-footprint-of-travel-per-kilometer-by-mode-of-transport/ [cited 09 May 2022]

[10] URL https://www.bloomberg.com/news/articles/2021-09-23/boeing-sees-chinese-airlines-buying-8%2D700-new-aircraft-by-2040 [cited 06 June 2022]

[11] URL https://www.reuters.com/business/aerospace-defense/airbus-expects-india-orders-make-up-6-its%2Dtotal-over-next-20-years-2022-03-24/ [cited 06 June 2022]

[12] URL https://sustainabilityreport2020.airfranceklm.com/ [cited 08 June 2022]

fuels with high energy density. specific energy, high flash-point (less flammable).

- SAF: Sustainable Aviation Fuel
  - Sustainable aviation fuels (SAF) are renewable or waste-derived aviation fuels.
  - As SAF uses renewable feedstocks, it recycles carbon rather than adding carbon to the atmosphere. This reduces carbon emissions by 70%, particular matter by 90% and sulfur emissions by 100% [13]. Hence, significantly reducing the aviation industry's emission footprint and fossil fuel dependency.
  - A considerable disadvantage is its high production costs compared to conventional aviation fuels. However, as the demand for SAF increases due to sustainability goals completely overcompensate the assumed SAF production cost reductions and leads to overall additional fuel costs [31].
- Aviation biofuel
  - Aviation biofuel is made primarily from biomass resources using thermochemical or biochemical methods.
  - Non-edible oil crops are mainly used for the production of biologial aviation fuels, thus making the fuel renewable [32]. Feedstock can be found worldwide, hence production is not location limited.
  - Contains low temperature performance, low flash point, and good thermal stability.
  - Main two disadvantages are specified as follows. May cause afforestation, further affecting biodiversity and increasing atmospheric carbon dioxide [33]. Supply process is challenging due to the complexity of achieving the right fuel quality and suitable blending for its effective functioning.
- Hydrogen (liquid or gas)
  - Hydrogen is not only readily available but also has good specific energy properties and is environmentally friendly. Hydrogen has the highest energy per unit mass compared to any other chemical fuel [34].
  - For hydrogen propulsion to be feasible, its density per unit volume must be increased.
  - Two main by-products of hydrogen combustion are water vapour and nitrogen oxides [35]. However, these NO_X emissions are extremely low compared to those released when burning kerosene [36].
  - Hydrogen fuel cells can be used on-board of aircraft to power different systems that are currently powered by batteries.
  - There are five main disadvantages: high technology cost, hydrogen production and storage, refuelling infrastructures, and engine design.
    - Hydrogen can be captured from several sources; feedstocks such as coal and natural gas, and renewable sources, such as water and biomass [37].
    - Hydrogen can be stored as a liquid in cryogenic tanks or it can be stored as a pressurised gas. Storing hydrogen as a gas is advantageous in terms of fast filling-releasing rate [36].
    - Burning hydrogen for aviation purposes as a jet fuel requires a substantial modification of the traditional combustion chamber.
- Batteries - electric
  - Performance is constrained by the battery's energy density and discharge rate.
  - Main disadvantages is its significant mass increase.
  - Currently, lithium batteries are the most feasible option as they offer the highest available specific energy out of all battery technologies [38].
- Liquefied natural gas (LNG) (also known as methane)
  - Liquefied natural gas has higher energy content per unit mass than conventional jet fuel, but requires two to four times as much volume to hold the same amount of energy as jet fuel [39].
  - Approximately, fossil methane can reduce 25% of carbon dioxide, -80 % of nitrogen oxides, -100 % of the direct soot effect and -50 % of the contrail effect [40]. If the effects of water and sulphur are neglected, the methane engine could reduce 49% of climate change effects based on emissions [40].

[13] URL `https://skynrg.com/sustainable-aviation-fuel/` [cited 07 June 2022]

4.5. Evaluation of Effects of Hydrogen Combustion Byproducts *Jenny*

The cruise altitude for general passenger aircraft and that decided for the LEAF aircraft is approximately 11 000 km, which is primarily inside the stratosphere. Therefore for commercial flights, a large proportion of the flight will occur in this level of the atmosphere. Troposphere is the name given to the lower band of the atmosphere, which is where effects on the ground are considered. When different energy sources are combusted, their emissions will affect different parts of the atmosphere in different ways. The effects of hydrogen combustion on the health of the population surrounding the airport and the global environment are evaluated at both atmospheric levels in the following section.

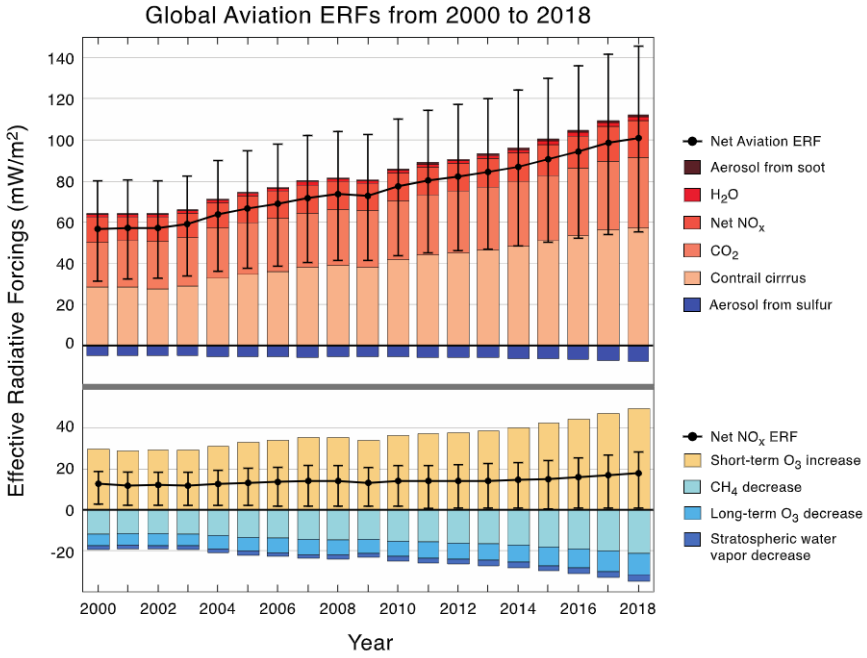

Figure 4.6: Effective radiative forcing of aviation emissions [41]

4.5.1. Water Vapour

Water vapour can have different effects depending on its location in the atmosphere: effects in the troposphere can vary compared to those in the stratosphere. While there are no significant implications on health, water vapour does contribute slightly to radiative forcing as can be seen in Figure 4.6. However, its biggest climate impact comes from the contribution to contrail formation rather than direct effects of H_2O.

4.5.2. Contrail Formation

Aviation causes an increase in global cloudiness with contrail formation. This occurs when the ambient atmosphere is super-saturated with respect to ice [41]. The temperature threshold condition should also be met, more specifically water droplets must freeze in order for a temperature drop of approximately -40°Celsius to be achieved [14]. Formed contrails can have both a warming and cooling effect, where at night warming is predominant. Uncertainty in contrail modelling is in part due to ice crystal formation which can be accelerated through emission of water vapour. Furthermore, contrail soot ice-crystals decrease the albedo at solar wavelengths, leading to an increase in top of atmosphere radiative forcing caused by contrails. The effect of contrails is in large part due to aviation traffic and distribution. The effect of contrails could potentially be reduced through the use of hydrogen combustion as the byproduct of soot would not be present. Furthermore, flight re-routing can be considered to minimise contrail formation and its RF in the long term (100 years) but this will result in an energy penalty, meaning that more fuel may need to be carried onboard resulting in a larger tank size.

In conclusion, it can be deduced that combustion of hydrogen is recommended at lower altitudes as it will have negligible adverse effects on the health of the population in and around airports. Use of hydrogen combustion should be limited in the upper atmosphere as there is evidence that it contributes a substantial amount to RF that is effective in the short term. Atmospheric conditions should be considered for flight routing as it can impact the contrail formation.

[14] URL nature.com/articles/s41467-018-04068-0 [cited 21 June 2022]

5
Risk Analysis

A detailed risk analysis is crucial in order to identify, already at early stages of the design phases, possible causes for development delay of the aircraft or malfunctioning during its use. The following Section 5.1 therefore summarises all identified risks and shows their likelihood and consequence in a risk map. Subsequently, Section 5.2 and Section 5.3 explain the risk mitigation strategies and show an updated risk map after risk mitigation.

5.1. Risk Identification and Mapping

Christoph, Lisa, Annemijn

In a first step, possible risks were identified. They were sorted within six different risk categories, which will be presented in this section. The first category is related to scheduling of the mission (SCD), which implies the danger of not meeting delivery of the first aircraft in 2035. The second category is related to the costs of the mission (CST). The risks are therefore related to the competitiveness of the design and the requirements specifying the cost range this aircraft should meet. The third category is related to difficulties that might occur during the development of the aircraft (DEV). They arise from technological challenges and most importantly from the propulsion system. Most risks detected are related to the fourth category, the technical functioning of the aircraft (TEC). This ranges from ground operations to flight operations and is related to aircraft subsystems as well as functioning of the aircraft within for example an airport environment. Some risks are related to maintenance (the fifth category, MTN) of the aircraft. Most commonly, they imply delay of maintenance and thus time, in which the aircraft cannot be used. The last category includes all risks related to end-of-life operations of the mission (EOL). This is especially related to recycling of the aircraft, which is a challenge due to the requirement of having all parts of the aircraft made out of recycled material or being recyclable. However, these risks are not critical and therefore not included here. In addition, it is important to note that the risk identifier convention is the same as in the Baseline Report [42]. The only difference is that only the critical risks and risks that arise during the development phase, are considered here.
Having these risks identified, their respective likelihood and consequence are assessed. For this, a scoring system has been established, giving scores from 1 to 5 for both the likelihood P and the consequence C of each risk. The scoring system for likelihood is explained in Table 5.1 and for the consequence in Table 5.2.

Table 5.1: Scoring system for likelihood of risks

P	Likelihood
1	Negligible (0-5%)
2	Low (5-25%)
3	Medium (25-50%)
4	High (50-75%)
5	Very High (75-100%)

Table 5.2: Scoring system for consequence of risks

C	Consequence
1	System or mission can still run without problems
2	System or mission can still run, but precautions need to be taken
3	System or mission might need to be stopped
4	System or mission cannot continue
5	High probability of fatalities

Using the scoring system, every single risk has been assigned a score for likelihood and consequence. Table 5.3 summarises the results obtained for each risk; for schedule, cost, development, technical, maintenance and end-of-life risks respectively. The results are accompanied by a reasoning behind the assigned likelihood and consequence score.

Table 5.3: Risk description including likelihood and consequences

Risk	P	Explanation for P	C	Explanation for C
RSK-SCD-01: Necessary materials are not available until 2035.	2	Low chances exist that new materials might be needed for further increasing efficiency or for integrating a secondary propulsion unit.	4	The design phase needs to be halted and new materials need to be chosen.
RSK-SCD-02: Necessary tools for manufacturing are not available until 2035.	1	Until 2035, manufacturing techniques as 3D printing will develop further. This allows to produce most possible shapes.	4	The design phase needs to be halted and a new manufacturing technique needs to be chosen.
RSK-SCD-03: Necessary technology is not developed until 2035.	3	There is a medium chance that new engine or energy storage technologies might be needed, that are not ready for use in aircraft in 2035.	4	The design phase needs to be halted and alternative technologies need to be chosen.
RSK-SCD-04: Delays during the production process occur.	4	Often the production of new concepts takes longer than expected as there are no references available.	3	Customers might lose interest in purchasing the aircraft if the expected production time cannot be met.
RSK-CST-01: Necessary materials are too expensive.	3	As the aircraft should be fully recyclable, so new expensive materials might be needed to replace non-recyclable composites.	3	The budget will be exceeded and the aircraft will be less competitive. Thus, customers might choose not to buy this aircraft.
RSK-CST-02: Developing and manufacturing costs are too high.	1	It is unlikely that introduction of a hybrid aircraft will cause an excessive increase in production costs.	3	The budget will be exceeded and the aircraft will be less competitive. Thus, customers might choose not to buy this aircraft.
RSK-CST-03: The customer cannot afford a new aircraft anymore.	1	There is a very low chance that due to climate change, society will fly less and airlines will operate less aircraft, or will even go bankrupt.	3	The aircraft will not be sold anymore.
RSK-DEV-01: Energy storage technologies add too much weight.	3	If batteries are chosen as secondary energy source, there is a high risk that their weight is too high.	3	Heavier weight of the energy storage allows for less payload and therefore reduces competitiveness of the aircraft.
RSK-DEV-02: The energy storage volume is too high.	3	If hydrogen is chosen as secondary energy source, there is a high risk that hydrogen tanks will need an excessive increase in fuel storage volume.	3	Larger hydrogen tanks either require a larger aircraft structure and therefore higher weight, or reduce competitiveness of the aircraft due to reduced payload capacity.
RSK-DEV-03: The use of multiple propulsion systems increases weight substantially.	4	The use of two separate propulsion systems will very likely be needed to implement hybrid propulsion.	2	Higher weight of the propulsion system allows for less payload and therefore reduces the competitiveness of the aircraft to some extent.
RSK-DEV-04: It is not possible to reach a sufficient level of recyclable aircraft parts.	4	Composites are commonly used in aircraft structures as fuselages but are very difficult to recycle.	3	The customer might not buy the aircraft as its requirements regarding recyclability are not met.
RSK-TEC-01: Airport infrastructure is not compatible with aircraft needs.	3	Infrastructure for refuelling with new energy sources might not be present at every airport, which is especially likely for smaller airports.	4	The aircraft cannot take off again due to unavailability of fuel at the airport.

Risk	P	Explanation for P	C	Explanation for C
RSK-TEC-03: Required but uncommon secondary energy source is not available on the airport.	3	A new emission-free secondary propulsion unit is likely to require energy from a source which is not commonly available at all airports.	4	Aircraft cannot take off again due to unavailability of fuel on the airport.
RSK-TEC-10: An onboard fire occurs.	2	An onboard fire could always occur, even though it is unlikely to happen due to extensive safety regulations.	5	The aircraft needs to land immediately. There is a high probability of fatalities occurring.
RSK-TEC-15-A: Sensors on the aircraft fail.	2	Sensors are regularly checked during inspection or walk-around and are therefore unlikely to be damaged during flight. Sensors also have redundancy.	5	Aircraft states cannot be measured anymore, which can lead to fatalities in case the pilot or autopilot is not noticing dangerous flight conditions.
RSK-TEC-15-B: Sensors on the aircraft fail.	3	There is a medium chance that dirt picked up for example during take-off might cause malfunctioning of a sensor.	5	Aircraft states cannot be measured anymore, which can lead to fatalities in case the pilot or autopilot is not noticing dangerous flight conditions.
RSK-TEC-19: The landing gear does not extend before landing.	2	Landing gear mechanisms are regularly inspected and therefore unlikely to fail during flight.	5	The aircraft has to land by sliding on the fuselage. Due to friction, high temperatures are achieved in the fuel tanks, possibly causing fire and resulting in fatalities.
RSK-TEC-20: Electricity failure occurs during flight.	2	The critical moment for the electrical system is at start-up, so at that moment the probability of failure is highest. However, failure is still very unlikely. In addition, the chances of a short circuit during flight are even smaller.	5	All aircraft systems that rely on electricity shut down, which is even more problematic in a fly-by-wire aircraft. This could cause fatalities.
RSK-MTN-02: The hangar is occupied.	4	Waiting time at a hangar is likely to occur, if multiple aircraft need to undergo maintenance in the same time-frame.	3	Delays are experienced due to waiting time at the hangar.
RSK-MTN-05: Damage is not detected during inspection.	4	Small damages can be easily overlooked if inspection or non-destructive testing are not performed correctly.	5	The damage might increase and lead to fatalities during flight.

After having all risks, their likelihood as well as their consequence are discussed, the results can be plotted in a risk map. Figure 5.1 shows the initial version of the risk map before mitigation on the left. A colour scheme was defined for the risks, ranging from minor risks not affecting the design significantly, to major risks that need to be mitigated. As can be seen in the initial risk map, most risks are minor and manageable and can therefore be accepted. However, there are 10 risks that need to be mitigated if possible and 2 major risks that need to be mitigated under all circumstances. Possible mitigation strategies for theses risks will therefore be described in Section 5.2. Conveniently, no design killer was found for the aircraft.

5.2. Risk Mitigation

Christoph, Lisa, Annemijn

In the previous section, a risk map was constructed to identify which risks form a significant threat to the mission. Subsequently, risk mitigation will be performed to move unacceptable risks to an acceptable risk level. Four strategies can be used: accepting, treating, transferring and terminating the risk. Accepting is to be avoided for the risks with an unacceptable risk level, as this could be critical during design or operation of the aircraft. As termination of the risk is also difficult to achieve, treating or transferring risks are the preferred solutions. From the risk map in Figure 5.1, an unacceptable risk level is observed for RSK-SCD-[03, 04], RSK-DEV-04, RSK-TEC-[01, 03, 10, 15-A, 15-B, 19, 20] and RSK-MTN-[02, 05]. Table 5.4 therefore proposes mitigation strategies as well as the new likelihood P and consequence C of the identified risks.

Table 5.4: Risk mitigation

Risk ID	Mitigation strategy	P	C
RSK-SCD-03	The risk of necessary technology not being ready by 2035 can be mitigated by utilising technologies which are likely to be available by 2035. By using already existing technology and researching technology readiness level. This could help to decrease the risk likelihood to 2.	2	4
RSK-SCD-04	Including a margin in production time of one year & implementing cellular manufacturing can help reduce the risk of having delivery delays. Risk likelihood can be reduced from 4 to 2.	2	3
RSK-DEV-04	The likelihood of this risk is not easily reducible as, for example, composites are needed but difficult to recycle. The consequence of this risk is reduced from 3 to 2 by discussing and negotiating with the customer the severity of the recyclability requirement.	4	2
RSK-TEC-01	As the aircraft will be new to the market, not all airports are prepared for its operation at release. To ensure proper ground operations the aircraft needs to be designed to use universal ground connection as much as possible. This reduces likelihood of this risk from 3 to 2.	2	4
RSK-TEC-03	As the aircraft requires a 'green' type of propulsion for take-off and landing, an uncommon fuel will probably be used. Risk likelihood can be mitigated from 3 to 2 by advising and helping airports, both monetarily and expertise-wise, on how to adapt their infrastructure and operation 5 years prior to launch.	2	4
RSK-TEC-10	In addition to the safety regulation present on luggage, crew and passengers, some parameters can also be established on the aircraft structure itself. To avoid the spread of a fire, all compartments of the aircraft should be closed-off by fire-proof structure and flame retardant materials used. Additionally, integral part of the structure should resist fire and heat for sufficient time for a safety landing. This could help reduce consequence of a fire from 5 to 4.	2	4
RSK-TEC-15-A, RSK-TEC-15-B	To ensure that a vital sensor functions during flight and taking into account that some damage may be overlooked during inspection, important sensors are installed at 3 different locations on the aircraft. If one fails, this will be automatically identified as the other two sensors produce different results. Thus reducing the consequence of a failing sensor from 5 to 2.	2(A), 3(B)	2
RSK-TEC-19	A non-extending landing gear will always have fatal consequences for the aircraft. Therefore, likelihood of this risk needs to be reduced as much as possible by imposing frequent aircraft inspection to the operator and by increasing importance of landing gear inspection during walk-around before departure of each flight. Likelihood of this risk can consequently decrease from 2 to 1.	1	5
RSK-TEC-20	Having no electricity will make most systems in the cockpit unusable, thus making the aircraft (especially if it is fly-by-wire) uncontrollable for the pilot. Therefore, as for every other aircraft, an auxiliary power unit will be used to reduce risk likelihood from 2 to 1.	1	5
RSK-MTN-02	The risk of having the maintenance hangar occupied when needing inspection can be reduced by designing the aircraft to be able to undergo maintenance in already available maintenance hangars. This can be achieved by maximising possible use of widely available maintenance tools. In consequence, likelihood of having all possible maintenance hangars on the airport occupied is reduced from 4 to 2, as hangars of similar-sized aircraft can also be used.	2	3
RSK-MTN-05	In order to reduce the risk of critical damage not being detected during maintenance, a certain margin of damage-tolerance can be imposed on critical structural items of the aircraft. In consequence, smaller damages as for example small cracks on the fuselage or wing skin will not cause immediate failure but are allowed to grow until being sufficiently large for visual detection. Additionally, multiple people should perform inspection independently in order to increase redundancy of not detecting a damage, which would most probably lead to fatalities. Therefore, a damage-tolerance margin largely reduces the likelihood of not detecting critical damage from 4 to 1.	1	5

5.3. Updated Risk Map

Christoph, Lisa, Annemijn

In the previous section, mitigation techniques were described for all risks, which were located initially at an unacceptable risk level. New scores for likelihood and consequence were also assigned to those risks. With those scores, a new risk map can be constructed. The updated risk map is visualised on the right of Figure 5.1. As can be seen, it was possible to move all risks out of the regions of important risks towards a manageable or even minor risks. Most risks are now identified as manageable risks. They are acceptable for further design phases, but need to be considered when making design choices or when assessing reliability of the final design. Finally, the risk map should be updated in case new information or more exact information on specific risk becomes available during later design phases of the aircraft.

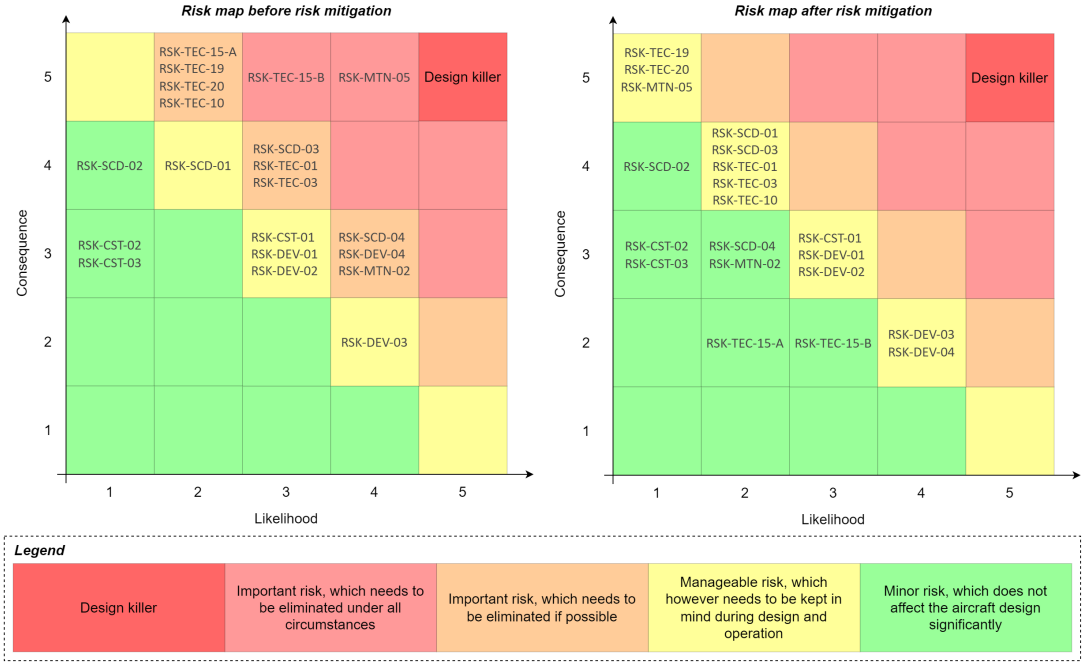

Figure 5.1: Risk map before and after risk mitigation

6 Performance Analysis

Before designing the individual subsystems, general aircraft characteristics have to be estimated with preliminary analysis tools. First, the maximum take-off weight (MTOW) and operative-empty weight (OEW) are estimated using Class I weight estimation in Section 6.1. Next, the payload-range diagram is presented in Section 6.2. Afterwards, the maximum load factor is obtained with manoeuvre and gust load envelopes in Section 6.3. Lastly, a design point for thrust and wing loading is established in Section 6.4, which will provide inputs for aerodynamic and propulsion system designs.

6.1. Class I Weight Estimation

Igor, Constança

In order to conduct a flight performance analysis on the aircraft, the first step is to conduct a Class I weight estimation. This takes into account the maximum take-off weight (W_{TO}), the empty weight (W_E), the mission fuel weight (W_F), the total payload weight (W_{PLtot}) and the weight of trapped fuel and oil (W_{tfo}). Their relation can be seen in Equation 6.1:

$$W_{TO} = W_E + W_F + W_{PLtot} + W_{tfo} \tag{6.1}$$

W_E, determined using Equation 6.2, is derived from a linear regression of reference aircraft weight data. It is approximated that a and b equal 0.4863 and 5054.21, respectively. The payload weight is extracted from the customer requirements and is equal to $20\,500$ kg.

$$W_E = aW_{TO} + b \tag{6.2}$$

Equation 6.3 calculates the fuel weight. This parameter depends on the fuel used during the mission (W_{fused}) and the required fuel reserve (W_{fres}). The required fuel reserve is indicated as a fraction of the mission fuel. 5% is specified by the airworthiness regulations as the minimum amount of fuel reserve the aircraft should carry. The mission fuel weight is estimated using the fuel-fraction method. The weight fractions are derived from statistical values, except for the most fuel intensive phases of the mission which are estimated using the Brequet equations [8].

$$W_F = W_{fused} + W_{fres} = W_{fused} + 0.05 \cdot W_{fused} = 1.05(M_{used} \cdot W_{TO}) = 1.05((1 - M_{ff}) \cdot W_{TO}) \tag{6.3}$$

After combining the above equations and taking W_{tfo} to be 0.5% of W_{TO}, the maximum take-off mass was calculated to be $85\,290$ kg.

6.2. Payload Range Diagram

Igor, Constança

As can be seen from Figure 6.1a, there are four key points in the payload-range diagram. Point A, the initial point, presents the location at which the aircraft carries its MTOW and has not begun operation (zero range). Point B depicts the maximum range when the aircraft is transporting a maximum payload of $20\,500$ kg, which equals 5000 km. Point C presents maximum range for the design payload. The design payload was taken to be $18\,000$ kg, given that the aircraft holds 180 passengers and allocating a weight of 100 kg to each, including luggage. Lastly, point D locates the maximum range for zero payload, also known as ferry range, equalling approximately 8435 km.

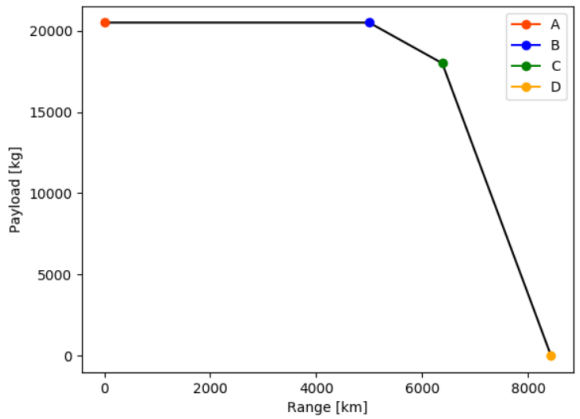

(a) Payload Range Diagram: indicating the initial point (A), and the range at maximum payload (B), design payload (C) and zero payload (D)

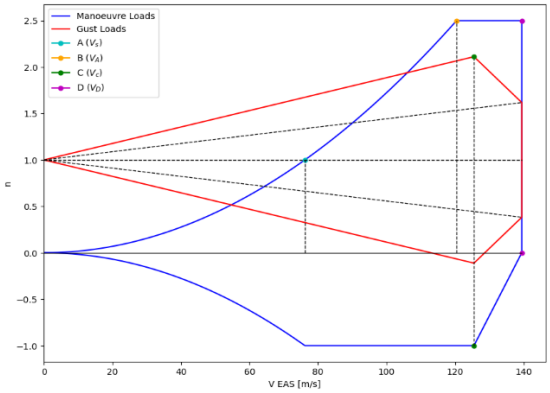

(b) Manoeuvre and Gust Load Diagram

Figure 6.1: Flight Performance Diagrams

6.3. V-n Diagrams

Jenny

The V-n diagram is the load factor (n) versus speed (V) graph throughout the aircraft mission. Figure 6.1b shows the V-n diagram displaying the manoeuvre loads and the gust loads experienced for the decided cruise altitude of $11\,000$ m and cruise speed of 230 m/s in true airspeed (TAS). The velocities are given as equivalent airspeed (EAS). The contour with maximum positive load factor shown in blue is the flight load envelope. For positive values of the load factor, which is the ratio between the lift and weight of an aircraft, the 'Design Manoeuvring Speed' V_A, or the speed at which the critical load n_{max} is reached, was calculated to be 120 m/s. The maximum velocity allowed, called the 'dive speed' V_D is the velocity reached if the aircraft were to dive in a steep descent, and is shown as the speed corresponding to the vertical, blue line. As the dive speed should not come close to Mach 1.0 for a commercial aircraft, the dive speed was set so that the cruise speed did not exceed $\frac{V_C}{0.9}$, as opposed to $\frac{V_C}{0.8}$ as stipulated in CS25 regulations, which resulted in a dive speed that was less close to Mach 1.0. This resulted in the dive speed of 139 m/s. The stall speed V_S is the velocity at which the plane must fly in order to produce lift. This occurs at a load factor of one and the velocity is 76 m/s. Lastly, the cruise speed V_c as defined is shown as the bottom right inflection of the blue curve and has a value of 126 m/s at EAS. The load factor increases linearly between the cruise velocity and $n = 0$ at V_D.

In Figure 6.1b, the gust loads are depicted in red. The characteristic velocities are V_B, V_C and V_D, where V_C and V_D are previously defined cruise and dive velocity respectively. V_B is named the 'Turbulence Penetration Airspeed', the design speed for maximum gust intensity. CS25 regulations for large aircraft define the gust velocities that should be withstood by the aircraft which vary with cruise altitude. As regulations were only present for the gust velocity between the airspeeds of V_B and V_D, V_B is present in the first linear region of the diamond shape gust curve shown in red and takes the value of 94 m/s. The maximum load factor in the overlay of the two plots becomes the limiting factor. Therefore the highest value of $n_{max} = 2.5$ becomes the critical load factor to be used in the Class-II weight estimation.

6.4. Thrust and Wing Loading Diagram

Lisa

A useful tool when sizing for performance is the Thrust and Wing Loading Diagram. In this diagram, the wing loading (W/S) is related to the thrust loading (T/W). Therefore it can also be referred to as a T/W - W/S diagram. The ultimate goal is to identify a design point; a coordinate corresponding to a certain thrust and wing loading, from which, the necessary amount of thrust and wing surface area can be obtained. Ideally the wing loading is as high as possible, meaning that more wing surface area and thus more lift can be acquired for a certain MTOW. At the same time, it is desired to have the thrust loading as low as possible, meaning that less thrust is needed for a certain MTOW. For the LEAF aircraft, the lowest possible thrust loading is more important than the highest possible wing loading. When less thrust is needed, the amount of fuel needed and thus the amount of harmful emissions produced will be decreased significantly. The LEAF aircraft is designed specifically to fulfill the need of aircraft pollution reduction. That is why the lowest possible thrust loading is deemed most important. However, the choice of the design point is constrained by performance requirements. These are requirements regarding take-off, landing, cruise and climb performance. The T/W - W/S diagram is meant for a jet aircraft. At the time of constructing this diagram it was already clear that the chosen design concept would be a jet aircraft and not a propeller aircraft (which would require a different diagram).

For take-off, the performance constraint can be obtained from Equation 6.4 [8].

$$\left(\frac{T}{W}\right)_{TO} = \frac{1}{(TOP)_{jet} \cdot C_{L_{TO}} \cdot \sigma} \cdot \left(\frac{W}{S}\right)_{TO} \tag{6.4}$$

Here, σ is the density ratio between the air densities at sea level and at the chosen airport. For a first estimation, it is assumed that the airport is located at sea level, resulting in $\sigma = 1.0$. In addition, $(TOP)_{jet}$ is the Take-Off Parameter. This parameter is estimated by making use of a method described by Daniel Raymer [8]. The take-off distance is assumed using requirement RAP-SYS-PERF-04 [42], stating that the aircraft shall be able to take-off and land on a runway of $2150\,m$. It is assumed that the take-off distance is 90% of the total runway distance. Using this value for the method in [8], the corresponding value for $(TOP)_{jet}$ is obtained. In the diagram, Equation 6.4 is plotted for various values of the lift coefficient for takeoff $C_{L_{TO}}$, such that the limiting value would become apparent.

For landing, the performance constraint is given in Equation 6.5:

$$\left(\frac{W}{S}\right)_{TO} = \frac{C_{L_{max}} \cdot \rho_0 \cdot V_{s_{land}}^2}{2f} \tag{6.5}$$

Here, ρ_0 is the air density at sea level. $V_{s_{land}}$, the stall speed at landing, is derived from the approach velocity. The approach speed follows from requirement RAP-AL-PERF-01 [42], stating that the flight performance of the aircraft shall be comparable to that of an Airbus A320. Therefore, the approach speed of the A320 was taken, and found in [43]. The stall speed at landing was then assumed to be lower than the approach speed by a factor of 1.2. In addition, f is the weight ratio between the landing weight and take-off weight. This ratio is used so that the wing loading for take-off weight would be obtained, allowing it to be plotted. The landing performance constraint is plotted for various values of $C_{L_{max}}$, such that the limiting value can be identified.

For cruise, it is assumed that the thrust force equals the drag. Therefore, the performance constraint is:

$$\frac{T}{W} = \frac{\frac{1}{2} \cdot \rho_{cruise} \cdot V_{cruise}^2 \cdot C_{D_0}}{\frac{W}{S}} + \frac{\frac{W}{S}}{\frac{1}{2} \cdot \rho_{cruise} \cdot V_{cruise}^2 \cdot \pi \cdot AR \cdot e} \tag{6.6}$$

Here, the zero-lift drag coefficient C_{D_0} and the efficiency factor e are obtained from the Class-I weight estimation Section 6.1. ρ_{cruise} is the air density at cruise altitude. The cruise altitude is stated in requirement RAP-SYS-PERF-02 [42]. The cruise speed V_{cruise} is stated in requirement RAP-SYS-PERF-01. In order to be able to plot the cruise constraint in the T/W - W/S diagram, the thrust at cruise altitude has to be converted to equivalent thrust at take-off using Equation 6.7:

$$T = T_{TO} \left(\frac{\rho_{cruise}}{\rho_0}\right)^{\frac{3}{4}} \tag{6.7}$$

Lastly, as a first estimation it is assumed that during cruise a thrust setting of 90% is used and that the average aircraft weight during cruise is 80% of the MTOW. The cruise performance constraint is plotted in the diagram for multiple values of the aspect ratio AR, so that the limiting value can be found.

For climb rate performance, the constraint can be calculated with Equation 6.8. Additionally, for the climb gradient the dependency in Equation 6.9 is derived.

$$\left(\frac{T}{W}\right)_{TO} = \frac{c}{\sqrt{\left(\frac{W}{S}\right)_{TO}} \cdot \sqrt{\frac{2}{\rho_0 C_L}}} + \frac{C_D}{C_L} \tag{6.8}$$

$$\left(\frac{T}{W}\right)_{TO} = \frac{c}{V_{climb}} + \frac{C_D}{C_L} \tag{6.9}$$

It can be derived that for maximising the climb rate, $\frac{C_L^{\frac{3}{2}}}{C_D}$ has to be maximised. This leads to the following expressions for C_L and C_D:

$$C_L = \sqrt{3 C_{D_0} \pi A R e} \tag{6.10}$$

$$C_D = 4 C_{D_0} \tag{6.11}$$

The climb rate c is assumed to be equal to the climb rate of an Airbus A320 [1], as per requirement RAP-AL-PERF-01. As stated before, C_{D_0} and e are obtained from the Class-I weight estimation. Just as for the cruise

[1] URL https://contentzone.eurocontrol.int/aircraftperformance/details.aspx?ICAO=A320 [cited 15 May 2022]

constraint, the climb rate constraint curves are plotted for multiple values of AR.

The climb velocity V_{climb} also follows from requirement RAP-AL-PERF-01. It can be derived that the optimum climb gradient is reached at maximum $\frac{L}{D}$. This leads to the following expressions for C_L and C_D:

$$C_L = \sqrt{C_{D_0} \pi A R e} \qquad (6.12) \qquad\qquad C_D = 2C_{D_0} \qquad (6.13)$$

The climb gradient constraint is also plotted for various values of AR, in order to find the limiting value.
Now that all constraining curves are defined, the design point can be chosen. A good location for a design point would be at an intersection of multiple different constraining curves. This would be good because it shows that there is not one constraining performance parameter that greatly limits the other performance parameters. The T/W - W/S diagram with the chosen design point is shown in Figure 6.2. As a reference, the design point of the Airbus A320 is also displayed [44].

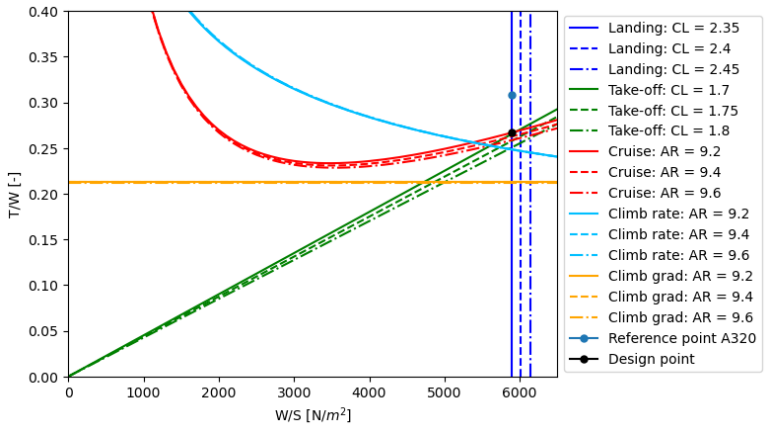

Figure 6.2: Thrust and Wing Loading Diagram

In the design point, $\frac{W}{S} = 5891$ and $\frac{T}{W} = 0.267$. Comparing this design point with the one from the A320, it shows that the LEAF aircraft has a 13.5% lower thrust loading. This means that for every kilogram of aircraft mass, the LEAF aircraft will need 13.5% less thrust to propel this kilogram forward, compared to the A320. Consequently, the LEAF aircraft will need less fuel and thus produce less harmful emissions for every kilogram of aircraft mass than an A320, making it more efficient and sustainable. Furthermore, the LEAF aircraft and the A320 have approximately the same wing loading. Using the Class-I estimation of the MTOW, a thrust T of $219\,\text{kN}$ and a wing surface area S of $139.5\,\text{m}^2$ are found for the LEAF aircraft. The wing surface area and aspect ratio will form the fundamentals of the wing planform design. The lift coefficients for take-off and landing are leading for the sizing of the high-lift devices.

7

Aerodynamic Characteristics

An important part of aerodynamic analysis is the wing design. After the design point is selected from the T/W - W/S diagram, it is possible to generate a preliminary wing design. In Section 7.1, an initial wing planform design is obtained. Section 7.2 covers the airfoil selection. In Section 7.3, lift and drag estimations are performed. Section 7.4 covers the sizing of the mobile surfaces on the wing, consisting of control surfaces and high lift devices. Section 7.6 covers the newly developed sharkskin technology to be implemented in the aircraft to increase efficiency.

7.1. Wing Planform

Lisa

Since the aircraft will operate near the transonic region during cruise, it is wise to incorporate sweep in the wing planform. The quarter-chord sweep angle ($\Lambda_{c/4}$) can be estimated using Equation 7.1, which is based on statistics of transport aircraft [45]. After, another relation based on statistics is used to determine the taper ratio λ [46]:

$$\cos \Lambda_{0.25c} = 0.75 \frac{M^{\dagger}}{M_{dd}} \tag{7.1}$$

$$\lambda = 0.2(2 - \Lambda_{0.25c} \cdot \frac{\pi}{180}) \tag{7.2}$$

In Equation 7.1, $M^{\dagger}$ is a technology factor for supercritical airfoils equal to 0.935. M_{dd} is the drag divergence Mach number, equal to $M_{cruise} + 0.03$. M_{cruise} was calculated to be 0.78. Together, Equation 7.1 yields in a quarter-chord sweep angle of $29.98\,°$.

The taper ratio λ is the ratio between the tip chord c_t and the root chord c_r. For the wing planform, a design consisting of two trapezoids is preferred over a design consisting of a single trapezoid. A reason for this is that more space for storing the main landing gear can be created. Another reason is that the root chord can be enlarged by using two trapezoids. This is beneficial for the wing structure, since more load paths can be created and bending stresses can be reduced. Finally, the lift reduction at the root due to fuselage interference can be limited by enlarging the wing area at the root locally, allowing for a local increase in lift.

It was decided that the leading edge sweep would be kept constant for both trapezoids. In addition, the trailing edge sweep of the inboard trapezoid is chosen to be close to $0\,°$, but still slightly positive. A positive sweep angle corresponds to backward sweep. The wingspan is obtained from the aspect ratio and wing surface area, following from the design point chosen in Section 6.4. This design point is also chosen based on requirement RAP-SYS-GO-06, stating that the aircraft shall be operable at airports that can cater aircraft with Aerodrome Reference Code 4C [42]. This reference code implies that the wingspan of the aircraft shall be below $36\,m$[1]. Therefore, a fitting combination between the wing surface area and the aspect ratio was obtained. Based on statistics of reference aircraft, it was decided that the inboard trapezoid would cover 35% of the wingspan [43]. This value will alter slightly once the engine placement is known, as in the case of wing-mounted engines it is desired to position the engine close to the trapezoid border. Since the wing surface area is known, an iterative process was set up in order to obtain a wing planform that fulfills all set requirements. The resulting wing planform design of the right wing is shown in Figure 7.3, in Subsection 7.4.2.

In Figure 7.3, an estimation of the wingbox boundaries is displayed. Here, it was assumed that the front spar is located at 15% of the chord in the outboard trapezoid, measured from the leading edge. In addition, the rear spar location was estimated to be at 65% of the chord in the outboard trapezoid, and at 70% of the root chord. These values were deemed typical and are therefore a good basis for a first estimation. Lastly, a fuselage boundary is estimated in order to have an idea of what part of the wing planform will actually be visible from the outside of the aircraft. A summary of the dimensions and defining parameters of the wing planform are given in Table 7.1.

[1] URL `https://skybrary.aero/articles/icao-aerodrome-reference-code` [cited 25 May 2022]

Table 7.1: Wing planform parameters

Parameter	$S_{1/2}$	$b_{1/2}$	b_{in}	b_{out}	AR	c_r	c_{kink}	c_t	λ_{tot}	$\Lambda_{c/4}$	Λ_{LE}	$\Lambda_{TE_{in}}$	$\Lambda_{TE_{out}}$
Value	69.74	17.91	6.27	11.64	9.2	7.51	3.72	2.22	0.30	29.98	32.45	1.79	26.89
Unit	m	m	m	m	-	m	m	m	-	deg	deg	deg	deg

In order to verify the iterative process used to build the wing planform, intermediate checks were built in the process to keep track whether only the intended variables changed their value throughout the iteration. After the iteration provided a final wing planform design, the dimensions were saved. The planform was then constructed in a coordinate system, and the taper ratio and total wing surface area were calculated by hand using geometric relations and the outputted chord lengths and wingspan. These values were compared to the taper ratio and wing surface area outputted by the code, and found to differ by only rounding errors. This leads to the conclusion that the iterative process provides reliable wing planform dimensions. Therefore, its working is verified.

7.2. Airfoil Selection

Constança

Table 7.2: Criteria definition and weights for airfoil selection trade-off

Parameter	Weight	Justification
$C_{l_{max}}$	0.30	It is important to have a high $C_{l_{max}}$, as it is a measure of how well the airfoil produces lift.
$C_{d_{min}}$	0.30	It is crucial to have a low $C_{d_{min}}$, as it indicates that the wing produces low drag, hence less thrust required.
$(C_l/C_d)_{max}$	0.15	Also, an important parameter to consider as the higher the $(C_l/C_d)_{max}$ the more efficient the wing airfoil.
C_m at $C_{l_{des}}$	0.15	A C_m at $C_{l_{des}}$ close to zero is desired as it requires less trim, hence less drag.
C_l at zero angle of attack (AoA)	0.10	Relevant to compare the airfoils' C_l at zero AoA to the $C_{l_{des}}$. The closer they are to each other, the more optimal the airfoil is.

Airfoils with a thickness to chord ratio of 15% were selected as this is the minimum required thickness needed to support the wing. Furthermore, after conducting a literature study on airfoil characteristics, 10 airfoils were selected to run an analysis. Table 7.3 shows the top seven choices that were considered in greater detail. The parameter *Stall characteristics*, is ranked from A to C, with A being the best and C the worst.

Table 7.3: Trade-off for airfoil options (qualitative scores and sorted by final score)

Criteria / Airfoil	C_l at AoA=0	$C_{l_{max}}$	Stall characteristics	$C_{d_{min}}$	$(C_l/C_d)_{max}$	C_m at $C_{l_{des}}$	**SCORE**
NACA 63(2)-615	**(3)** 0.5215	**(3)** 1.581	**(4)** A	**(3)** 0.0063	**(3)** 134.40	**(2)** -0.117	2.85
NLF(1)-0215F	**(3)** 0.6355	**(4)** 1.676	**(4)** A	**(2)** 0.0066	**(3)** 139.71	**(2)** -0.140	2.85
NLF(1)-1015	**(2)** 0.7676	**(3)** 1.528	**(4)** A	**(3)** 0.0064	**(4)** 167.74	**(1)** -0.181	2.75
NACA 4415	**(4)** 0.4380	**(3)** 1.552	**(4)** A	**(1)** 0.0070	**(2)** 122.00	**(3)** -0.0880	2.35
NACA 64(2)-415	**(1)** 0.3472	**(2)** 1.427	**(3)** A	**(3)** 0.0063	**(2)** 120.62	**(3)** -0.0793	2.35
NACA 65(2)-215	**(1)** 0.1739	**(1)** 1.250	**(3)** B	**(4)** 0.0061	**(1)** 96.43	**(3)** -0.0427	2.20
NACA 23015	**(1)** 0.1317	**(3)** 1.559	**(4)** A	**(1)** 0.0072	**(1)** 90.95	**(4)** -0.00435	2.05

After conducting the airfoil trade-off present in Table 7.3, two optimal airfoils were found; NACA 63(2)-615 and NLF(1)-0215F. It is important to note that the ranking number of each criteria is multiplied by the weight presented in Table 7.2. To determine which one out of the two would be better, a more thorough analysis was run in XFLR5 using a Reynolds number of 120 million. There is a minimal difference between the two airfoils across the plots, however for the C_m-Alpha plot, the NACA 63(2)-615 considerably performs better but for the remaining four plots the supercritical airfoil performs better. Additionally, the Mach Drag divergence number (M_{dd}), calculated using Equation 7.3, for the NLF(1)-0215F airfoil is considerably higher than for the NACA

63(2)-615. Hence, considering the above analysis, the NLF(1)-0215F is chosen as the baseline airfoil.

$$M_{dd} = K - \frac{C_{l_{des}}}{10} - \left(\frac{t}{c}\right) \tag{7.3}$$

Where K equals 0.87 for a NACA 6-series and 0.95 for a supercritical airfoil.

As a rule of thumb, the thickness of the tails should be equal or less than the thickness of the main wing. For symmetrical airfoils C_l at zero angle of attack is zero, hence it is not taken into consideration for the trade-off.

Table 7.4: Trade-off for airfoil options (qualitative scores)

Tail	Criteria / Airfoil	$C_{l_{max}}$	$C_{d_{min}}$	$(C_l/C_d)_{max}$	C_m at $C_{l_{des}}$	**SCORE**
Horizontal	**NACA 0012**	**(4)** 1.3892	**(3)** 0.0054	**(4)** 75.60	**(2)** 0.0067	3.0
Horizontal	**NACA 0012-64**	**(3)** 1.3431	**(4)** 0.0047	**(3)** 63.00	**(1)** 0.0110	2.7
Horizontal	**NACA 0012-34**	**(2)** 0.9256	**(4)** 0.0046	**(2)** 56.42	**(2)** 0.0062	2.4
Vertical	**NACA 0015**	**(4)** 1.4029	**(2)** 0.0063	**(4)** 77.88	**(4)** 0.0037	3.0

7.3. Lift and Drag Estimations

Constança

An important part of aerodynamic analysis is the lift and drag estimation of the wing. This is achieved by determining both the lift and drag coefficients using the DATCOM Method. The most important input parameters are specified in Table 7.5. Both the angle of attack at zero-lift (α_0) and $C_{l_{max}}$ are airfoil characteristics retrieved from XFLR5.

Table 7.5: Input Parameters for Lift and Drag Estimation

$(\alpha_0)_{cruise}$	$(\alpha_0)_{TO}$	$(\alpha_0)_{land}$	M_{cruise}	M_{TO}	M_{land}	$(C_{l_{max}})_{TO}$	$(C_{l_{max}})_{land}$
-5.00°	-5.82°	-5.82°	0.78	0.30	0.17	2.126	2.080

Wing Lift Coefficient

To analyse the lift coefficient at different angles of attack, the wing lift curve slope for take-off, landing and cruise was computed and plotted in Figure 7.1a. To determine the wing lift curve slope Equation 7.4 [8] was used. The cruise lift curve slope was calculated to determine the trim angle (α_{trim}). α_{trim} is the angle where the design C_L meets the lift curve.

$$\frac{dC_L}{d\alpha} = C_{L_\alpha} = 2\pi AR \div \left[2 + \sqrt{4 + \left(\frac{AR\sqrt{1-M^2}}{\mu}\right)^2 \cdot \left(1 + \frac{\tan^2(\Lambda_{0.5C})}{1-M^2}\right)}\right] \tag{7.4}$$

Where AR is the aspect ratio of the wing, retrieved from the planform design, M the Mach number, μ the airfoil efficiency taken to be 0.95 from literature [8], and $\Lambda_{0.5C}$ the half-chord sweep angle.

Furthermore, the take-off maximum lift coefficient ($C_{L_{max}}$) and stall angle (α_s) are computed for clean configuration and implemented into the lift curve slope as seen in Figure 7.1a. These parameters lay a fundamental baseline for the sizing of the high-lift devices. The $C_{L_{max}}$ for both take-off and landing was determined using Equation 7.5 and equals 1.65828. α_s was calculated using Equation 7.6 and is approximately 17°.

$$C_{L_{max}} = \left[\frac{C_{L_{max}}}{C_{l_{max}}}\right] C_{l_{max}} + \Delta C_{L_{max}} \tag{7.5}$$

$$\alpha_s = \frac{C_{L_{max}}}{C_{L_\alpha}} + \alpha_{0_L} + \Delta\alpha_{CL_{max}} \tag{7.6}$$

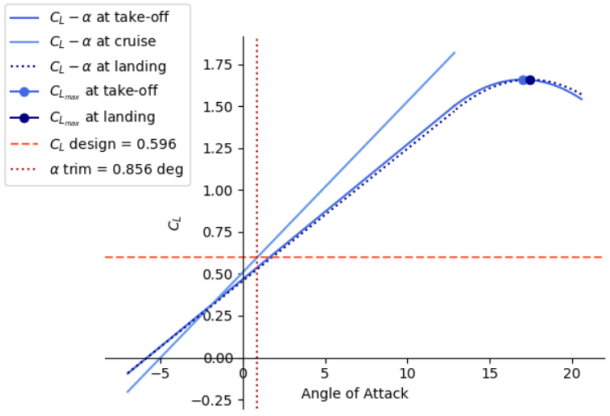

(a) C_L vs. Angle of Attack for clean configuration

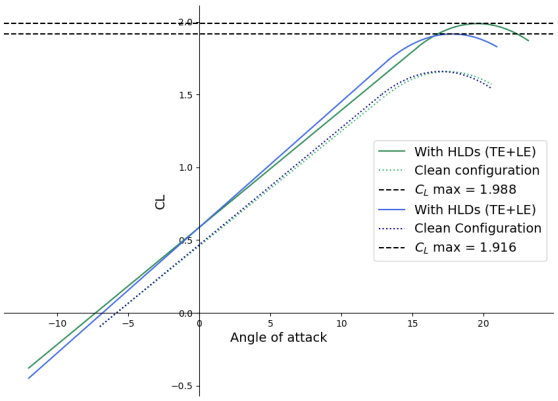

(b) CL vs. Angle of Attack with high-lift devices

Figure 7.1: Coefficient of lift versus angle of attack in degrees for cruise, take-off and landing

$$\Delta C_{L_{max}} = 0.9 \Delta C_{l_{max}} \frac{Swf}{S} \cos(\Lambda_{hinge-line}) \qquad (7.7) \qquad \Delta\alpha_{0L} = (\Delta\alpha_{0L})_{airfoil} \frac{Swf}{S} \cos(\Lambda_{hinge-line}) \qquad (7.8)$$

Equation 7.7, $\Delta C_{l_{max}}$ is a function of the HLD type, for Krueger flap it equals 0.3 and for Fowler flap it equals $1.3c'/c$ (when they are fully deployed). The effect of LE devices on alpha zero lift can be neglected. So this step is actually required only for TE devices. $(\Delta\alpha_{0l})_{airfoil}$ is approximately $-15\,^\circ$ at landing and $-10\,^\circ$ at take-off. Furthermore, given that the trailing edge device increases the wing surface area $C_{L\alpha_{flapped}}$ is equal to S'/S times the clean $C_{L\alpha}$, where S' is the increased surface area by the extended flaps. Combining these contributions with the clean lift estimation yields Figure 7.1b.

Drag Coefficient

After the lift analysis was conducted, the drag coefficient was determined using Equation 7.9 [8]. A preliminary estimation for the zero-lift drag coefficient (C_{D_0}) was performed for take-off, landing and cruise. Their respective values equal 0.0147, 0.0143, and 0.0085. Figure 7.2b shows the drag coefficient trend as angle of attack increases for three phases: cruise, take-off and landing.

$$C_D = C_{D_0} + \frac{C_L^2}{\pi ARe} \longrightarrow C_{D_0} = \frac{1}{S_{ref}} \sum C_{f_c} \cdot FF_c \cdot IF_c \cdot S_{wet_c} + \sum C_{D_{misc}} \qquad (7.9)$$

Where C_L is retrieved from the lift coefficient estimation, e is the Oswald efficiency, which is determined using Equation 7.10. C_{D_0} depends on the flat plate skin friction coefficient (C_f), component form factor (FF), interference factor (IF), the component wetted area (S_{wet}), and miscellaneous drag $C_{D_{misc}}$ [2], and subscript c denotes the component analysed.

$$e = 4.61(1 - 0.045AR^{0.68})(\cos(\Lambda_{LE}))^{0.15} - 3.1 \qquad (7.10)$$

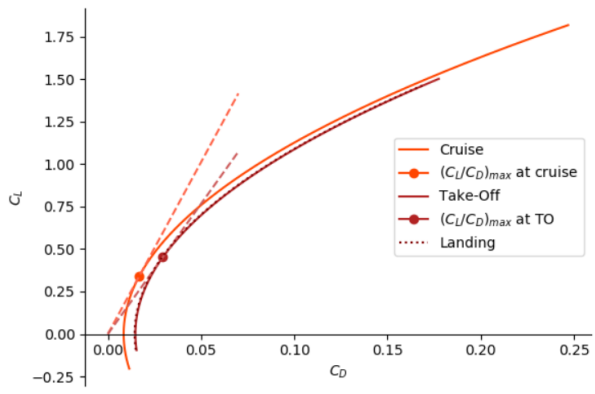

(a) Lift Drag Polar

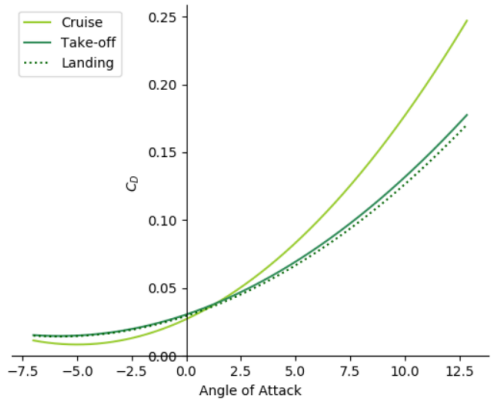

(b) CD versus Angle of Attack Plot

Figure 7.2: Lift and Drag Plots for Cruise, Take-off and Landing

[2] Miscellaneous drag includes wave drag, landing gear, and flap-induced drag.

After calculating both the lift and drag coefficient, the lift drag polar was plotted as demonstrated in Figure 7.2a. The lift-drag polar shows the variation in drag with varying lift coefficient. Computing the lift-over-drag ratio yields the aerodynamic efficiency of the wing. For both cruise and take-off and using Figure 7.2a, the maximum lift-to-drag coefficient ratios were located. For cruise it equals 20.48 and for take-off 15.40. These values describe the most efficient point at which the aircraft should fly.

7.4. Mobile Surfaces on the Wing *Lisa*

After the wing planform is designed and the airfoil is selected, the mobile surfaces on the wing can be sized. Subsection 7.4.1 covers the sizing of the ailerons, and Subsection 7.4.2 elaborates on the sizing of the high lift devices.

7.4.1. Control Surfaces

The requirements specified for the aircraft do not include a specific requirement regarding roll control. However, there are some regulations of which a requirement can be derived. The aircraft can be regarded as a medium-weight, low-to-medium manoeuvrability aircraft. Regulations state that this aircraft class should be able to perform a $45°$ bank angle within 1.4 s [47]. This requirement forms the basis of the control surface sizing. The most straightforward choice of control surfaces is the aileron. Therefore this is the chosen option. The aircraft steady state roll rate P can be calculated as follows [48]:

$$P = -\frac{C_{l_{\delta\alpha}}}{C_{l_p}}\delta\alpha\left(\frac{2V}{b}\right) \tag{7.11}$$

Here, $C_{l_{\delta\alpha}}$ is the aileron control derivative, and C_{l_p} is the roll damping coefficient. These values can be calculated using the following formulas [48]:

$$C_{l_{\delta\alpha}} = \frac{2c_{l_\alpha}\tau}{Sb}\int_{b_1}^{b_2} c(y)y\,dy \tag{7.12}$$

$$C_{l_p} = -\frac{4(c_{l_\alpha}+c_{d_0})}{Sb^2}\int_0^{b_{1/2}} c(y)y^2\,dy \tag{7.13}$$

In these formulas, c_{l_α} is the lift curve slope of the airfoil selected in Section 7.2. In addition, τ is the aileron effectiveness, which is a function of the ratio between the aileron chord and wing chord. This ratio was chosen to be 0.3, based on an estimation. The corresponding value for τ was found to be 0.52 [48]. The chord length as a function of wingspan $c(y)$ was obtained by subtracting the leading edge function from the trailing edge function. Since the ailerons are expected to be located on the outboard trapezoid, the trailing edge function of this trapezoid was used. The LE and TE functions were already known from the wing planform design in Section 7.1. The integral boundaries b_1 and b_2 are the aileron boundaries on the wingspan. It was decided to fix the value of b_2 at 92% of the wingspan, allowing for tailoring the value of b_1 such that the roll rate requirement is satisfied. Lastly, c_{d_0} is the drag coefficient of the selected airfoil.

Looking back at Equation 7.11, $\delta\alpha$ is the aileron deflection. For this aircraft, the decision was made to make use of differential ailerons. These ailerons can be used to minimise the adverse yaw effect, where roll to one direction leads to yaw in opposite direction. For differential ailerons, the down-going aileron deflects with 75% of the up-going aileron deflection. The average aileron deflection is then considered when calculating the resulting roll rate P.

In order to obtain the complete aileron design, an iterative process was set up where the spanwise position b_1 was altered until the roll rate requirement was just met, thereby omitting the possibility of over-designed ailerons. A summary of the aileron dimensions and defining parameters can be found in Table 7.6. In addition, the aileron is shown in the wing planform in Figure 7.3, in Subsection 7.4.2.

Table 7.6: Aileron parameters

Parameter	$\frac{c_{aileron}}{c}$	b_1	b_2	$c_{aileron_1}$	$c_{aileron_2}$	P_{req}	$P_{achieved}$	Δt_{req}	$\Delta t_{achieved}$
Value	0.30	14.69	16.48	2.63	2.40	0.56	0.60	1.40	1.31
Unit	-	m	m	m	m	rad/s	rad/s	s	s

7.4.2. High-Lift Devices

The difference in lift coefficient achieved in clean configuration and needed for take-off and landing configuration ($\Delta C_{L_{max}}$) must be overcome by the use of high lift devices (HLDs). The following relation for $\Delta C_{L_{max}}$ is used for

HLDs sizing [8]:

$$\Delta C_{L_{max}} = 0.9 \Delta C_{l_{max}} \frac{S_{wf}}{S} \cos \Lambda_{hingeline} \tag{7.14}$$

Here, $\Delta C_{l_{max}}$ is HLD-specific, and a method for calculating this value for every type is given by Raymer [8]. $\frac{S_{wf}}{S}$ is the ratio between the flapped wing surface area and the total area. Equation 7.14 can be rewritten such that the ratio $\frac{S_{wf}}{S}$ is obtained. From this, the part of the wingspan occupied by high lift devices can be deduced. The hingeline sweep angle $\Lambda_{hingeline}$ is the sweep angle at the location where the high lift devices are fixed to the wing. For leading edge (LE) HLDs, it is decided that this location is at 15% of the local chord and for trailing edge (TE) HLDs, this location is at 75% of the local chord. $\Delta C_{L_{max}}$ is obtained from the design point selection in the T/W vs. W/S diagram, as this design point specifies $C_{L_{max}}$ for landing and take-off. Subtracting the $C_{L_{max}}$ for clean configuration found in Equation 7.5 leads to the required $\Delta C_{L_{max}}$. The required $\Delta C_{L_{max}}$ for landing is found to be the constraining factor, since the landing configuration required a higher lift coefficient. That is why the HLDs are sized for landing.

It was decided that 80% of the required $\Delta C_{L_{max}}$ will be generated by the TE devices, and the remaining 20% by the LE devices. In addition, a constant ratio between HLD chord and local chord is assumed, as this enables the option to find the total chord length after full deployment of the HLDs [46]. This is needed in order to determine the HLD-specific $\Delta C_{l_{max}}$. Now, it is possible to find the flapped surface area and the corresponding spanwise flap length.

Initially, the TE devices were designed such that flaps would be placed on both the inboard and outboard trapezoids. However, it was found that the spanwise flap length of the inboard flaps in particular was very small. Therefore, the decision was made to only place flaps on the outboard trapezoid. An advantage of this choice is that there will be no interference between flaps and landing gear storage space. In addition, the effect of fuselage interference on the flaps will be limited since the flaps are located further away from the fuselage. Following from this, it was decided to let the LE devices start at 20% of the wingspan and the TE devices at 10% of the span of the outboard trapezoid.

After performing all necessary calculations, 6 feasible design options were found:

- **Design option 1**: Fowler (single slotted) + Leading edge flap
- **Design option 2**: Double slotted (variable geometry) + Leading edge flap
- **Design option 3**: Fowler (triple slotted) + Leading edge flap
- **Design option 4**: Fowler (single slotted) + Krueger flap
- **Design option 5**: Double slotted (variable geometry) + Krueger flap
- **Design option 6**: Fowler (triple slotted) + Krueger flap

A trade-off is performed to determine the most suitable configuration. The selection criteria are:

- **Design complexity** (30%): Costs and failure rates increase when design complexity is increased. Ideally, the costs and failure rates are kept to a minimum.
- **Efficiency** (25%): Efficiency is defined here as flap weight per unit span compared with its increase in lift coefficient. When a design is not efficient, this leads to a higher structural weight and possibly more costs.
- **Occupied wingspan** (25%): All design options are already verified to be feasible within the allocated wingspan. However, less occupied wingspan allows for more flexibility regarding sudden design changes.
- **Maintenance** (20%): Ideally, the ease of maintenance is as high as possible to allow for fast maintenance. In addition, the risk of overlooking damage during inspection is limited.

Table 7.7: Trade-off for HLDs (qualitative scores)

Criteria / Option	Design complexity	Efficiency	Occupied wingspan	Maintenance	SCORE
Design 1	(3)	(4)	(2)	(4)	3.2
Design 2	(2)	(3)	(3)	(3)	2.7
Design 3	(1)	(2)	(4)	(2)	2.2
Design 4	(4)	(4)	(2)	(4)	3.5
Design 5	(3)	(3)	(3)	(3)	3
Design 6	(1)	(2)	(4)	(2)	2.2

From the trade-off, it can be concluded that design option 4, the single slotted Fowler flap at the TE with a Krueger flap at the LE, is the most suitable option. The only difference in score with design option 1 comes from the design complexity, since a leading edge flap is a bit more complicated than a Kruger flap and is more suitable for improving the transonic manoeuvring performance of high-speed fighters. The complete wing planform design with the high lift devices included is show in Figure 7.3. A summary of the HLD dimensions and defining parameters can be found in Table 7.8.

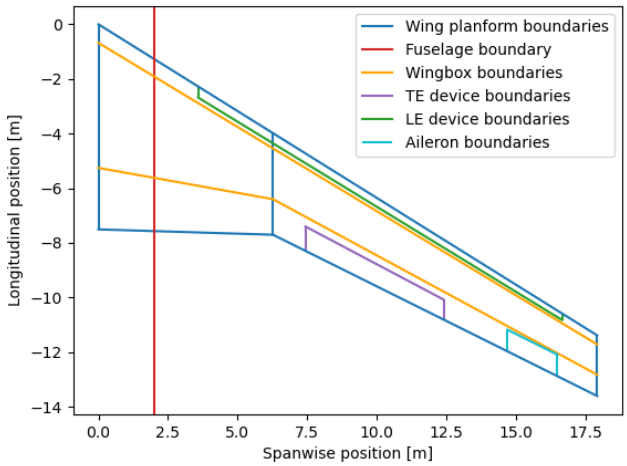

Figure 7.3: Complete Wing Planform with High Lift Devices

Table 7.8: HLDs Parameters

Parameter	Value LE device	Value TE device	Unit
$\frac{c_{flap}}{c}$	0.1	0.25	-
b_{start}	3.58	7.43	m
b_{flap}	13.06	4.97	m
$\Lambda_{hingeline}$	31.92	28.34	deg

It is worth noting that the trailing edge flap only occupies part of the wingspan, which is different than for conventional passenger aircraft like the Airbus A320. The main reason for this difference is that the difference in lift coefficient for which this aircraft is designed, is considerably lower than for the A320 [44]. Logically, it follows that this aircraft needs smaller high lift devices than the A320.

7.5. Winglets

Constança

Reduces total wing drag by creating a forward lifting force. Reduces tip vortex generation, results in less induced drag on the wing. Main disadvantage is the added weight to the wing structure. With this further reduction in drag, fuel consumption reduces, presenting a possible 6% and 8% decrease in CO_2 and NO_x emissions, respectively [49]. Winglet design is chosen based on literature, more specifically computational analysis based scientific reports with analyses on the winglets lift coefficient and lift-to-drag ratio.

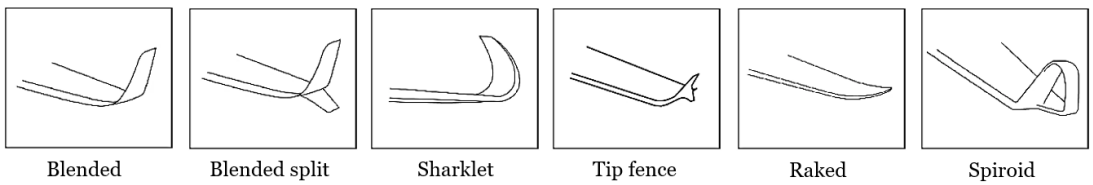

Figure 7.4: Winglet Options for the Wing [50]

The following steps were taken in order to determine the best winglet option. First, research was conducted to identify currently-existing winglets with the highest performance. Figure 7.4 shows the six different winglets that were further analysed with respect to the lift and drag that they produce. Two university thesis on aircraft winglet design that perform a computational fluid dynamics (CFD) analysis and present the results per winglet type were used in order to determine the best winglet for the LEAF aircraft. Both analysis ran the simulation

for Mach 0.8, which is almost identical to the cruise speed of Mach 0.78, and an angle of attack of $2\,°$. It is important to note that the values extracted from both analyses were only used for comparison purposes.

Table 7.9: Trade-off for winglet options (qualitative scores) [51] [52]

Criteria \ Winglet	Blended	Split	Sharklet	Tip fence	Raked	Spiroid
Lift [N]	**(3)** 14.01	**(4)** 14.69	**(3)** 13.92	**(1)** 12.91	**(2)** 13.38	**(2)** 13.21
Drag [N]	**(3)** 2.12	**(2)** 2.27	**(4)** 2.03	**(3)** 2.13	**(1)** 2.41	**(2)** 2.23
L/D	**(4)** 6.61	**(3)** 6.47	**(4)** 6.86	**(2)** 6.06	**(1)** 5.56	**(2)** 5.92
SCORE	3.33	3.00	3.67	2.00	1.33	2.00

From the trade-off conducted in Table 7.9, the sharklet was the best design with respect to lift and drag. Sharklets are fin-like winglets, resembling the dorsal fin of a shark, developed by Airbus. One of its main advantages is its smooth chord transition between the wing and the winglet. In addition to increasing the lift and reducing drag, Airbus estimates that with sharklets the fuel burned per flight can be decreased by 3.4% [51]. This further reduces the emissions per flight.

$$\Delta \text{AR} = 1.9(\text{h/b}) \cdot \text{AR} \tag{7.15}$$

Using Equation 7.15 the increase in aspect ratio of the wing can be calculate based on the height (h) of the winglet and the span (b) of the wing. For preliminary sizing, the height of the A320-NEO aircraft sharklet is used and corresponds to $2.40\,$m [53]. This generates in a ΔAR of 1.17, resulting in an effective aspect ratio of 10.37.

7.6. Riblet Technology

Constança

To reduce complexity and focus on hydrogen technology, passive flow control devices were analysed. First, miniature vortex generators were investigated. However, given that the aircraft is flying at Mach 0.78, attempting to delay transition will be hard due to the presence of shock waves. The shock wave generates turbulent flow in the aft side of the shock. Second, at these cruise speeds, 90% of the wing boundary layer will be turbulent, hence no vortex generators are needed. Thirdly, riblet technology has been shown to reduce drag when there is turbulent flow. And given the predominantly turbulent boundary layer at cruise, riblets are a good solution for the aircraft been designed.

To mitigate the drag increase caused by the turbulent boundary layer, a type of passive flow control device using sharkskin technology called Riblets can be used. Riblets are small surface groves micrometre sized, aligned in the airflow direction that reduce the turbulent skin-friction drag by up to 5% in full-scale conditions [55]. This technology further reduces aircraft emissions and fuel consumption during operations. Since riblets are only effective at reducing the turbulent skin friction drag, and the boundary around the main aircraft subsystems is predominantly turbulent, there exists a potential drag and fuel reduction benefit from applying them.

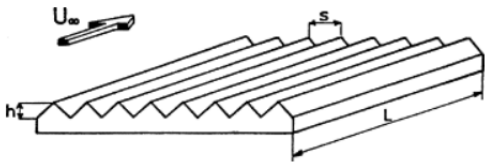

Figure 7.5: Riblet surface scheme [54]

An adjustment to the turbulence skin-friction coefficient by Spalart and McLean is implemented and the results can be seen in Table 7.10.

Table 7.10: Riblet drag reduction percentage

Reduction in skin friction coefficient due to riblets		
Take-off [M=0.18]	**Cruise** [M=0.78]	**Landing** [M=0.30]
4.088%	4.070%	4.191%

Lufthansa and BASF, a chemicals and coatings manufacturer, have co-developed a ribbed textured film with small protrusions, riblets [3]. This film contains millions of prism-shaped riblets and can be easily applied. The

[3] URL `https://www.lufthansa-technik.com/aeroshark` [cited 07 June 2022]

film is aligned with the airflow and a zoomed in schematic is seen in Figure 7.5.

Due to logistical factors such as connection joints and ease of maintenance, only the wings are coated with riblets. Other potential operational considerations are that external factors such as exposure to strong UV radiation, large temperature and pressure fluctuations, and bug splatters or dirt, can all cause damage to riblets. Fortunately, the technology used in the riblet film developed by BASF works in such a way to protect the riblets from these external factors. Hence, no extra cleaning cost is necessary compared to a normal aircraft cleaning schedule. Additionally, due to the part having a high complexity, the maintenance and fabrication costs are relatively high.

Riblets have three main advantages sustainability, scalability, and cost-effectiveness.

7.7. Recommendations

Constança

First and foremost, to increase both the accurateness and reliability of the wing aerodynamic design a computational fluid dynamics (CFD) analysis should be conducted. This is a vital tool for development analysis, optimisation and verification. A CFD analysis not only determines the lift and drag characteristics of the wing, but also the contribution of the other aircraft components. Secondly, in order to validate the findings in this report from both XFLR5 and Python, a wind-tunnel experiment should be conducted. Principal advantage of performing a wind-tunnel experiment is its accurate results while minimising assumptions.

Further research can be performed on variable cant angle winglets. This not only has the potential of increasing the aircrafts flight range but also the maximum payload [49]. Furthermore, the implementation of wing twist should be analysed in order to further evade wing tip stall. Another option for avoiding this is to use a variable thickness airfoil with the maximum C_L near the tip of the wingspan. To increase the efficiency of the aircraft, miniature vortex generators should be investigated as a form of additional passive flow control. Miniature vortex generators delay turbulent flow transition over a surface near the leading edge of the wing. In the spanwise direction, miniature vortex generators create a streaky boundary layer with alternating low and high speed streaks.

8

Fuselage Sizing and Energy Storage

Luke

In this chapter, the cabin configuration is shown in Section 8.1, then the hydrogen tank design process is illustrated. The tank design is divided into two parts including tank thermal design (Section 8.2) and tank geometry design (Section 8.3). In which, detailed design process including trade-off between different insulation method, insulation material tank sizing and other concerns are shown respectively in Subsection 8.2.1, Subsection 8.2.2,Subsection 8.3.1, and Subsection 8.4.2. Finally, the tank geometry is shown in Subsection 8.3.2.

8.1. Interior Design

It is initially considered in the design process that the cross-sectional diameter of the fuselage must be increased in order to be able to place the hydrogen tanks in the rear of the aircraft, without increasing its length beyond that of an A320-200. This would mean that the interior configuration of the seats would differ quite substantially from that of an A320-200. The conventional *three seats - one aisle - three seats* configuration would then have to become a *two seats - one aisle - three seats - one aisle - two seats* configuration. Two aisles would be necessary in this case in order to comply with the seating configuration safety regulations set by EASA [56]. This would mean that an extra aisle and an extra seat should be added along the width of the cabin. It is important to note that one of the stakeholder requirements is that the passenger experience shall not differ much from that of an A320-200. Also, the airline wants to operate the aircraft as if it would be an A320-200. This means that the airline prefers to load and unload passengers the same way as they do now with an A320. In addition, it is desired in general to have a slenderness ratio (length-to-diameter) of the fuselage of approximately 10 in order to minimise the profile drag [57]. This means that for relatively short aircraft, like the A320-200, the diameter cannot be 'considerably big'. Considering these three negative effects of increasing the amount of seats abreast, it has been decided to use a conventional seating configuration of an A320-200 for this aircraft, thereby increasing the length of the fuselage.

With the *3 seats - 1 aisle - 3 seats* configuration used for the interior design of the aircraft, it is possible to start estimating the outer dimensions of the entire fuselage and the cargo compartment. The cargo compartment is fitted with typical cargo containers used for the A320-200. All the seats, armrests and aisle dimensions are designed to comply with EASA's regulations. Figure 8.1 shows the final cross sectional design of the fuselage cabin-cargo cross-section. From this cross-section it can be deduced that the minimum inner diameter of the fuselage cross-section required is 4.05 m.

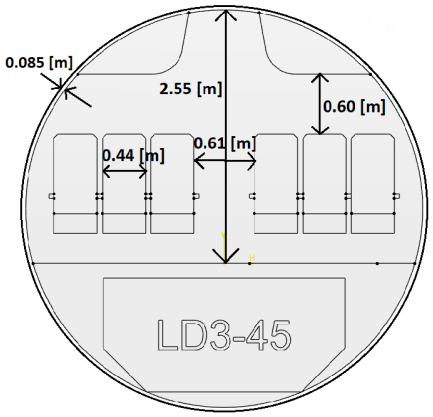

Figure 8.1: Cabin and cargo hold cross-section with dimensions in metres

8.2. Tank Thermal Design

There are three ways of heat transfer including conduction, convection and radiation. To address heat conduction, either a foam or a vacuum layer can be used due to their low heat conductivity and due to the super-low-to-non free molecule characteristic, the heat transfer by conduction is also eliminated. As for the heat flow by radiation, due to the complexity of the surrounding heating environment and the scope of this design, a special coating will be applied to reduce heat captured via radiation and thus eliminated from consideration. Also, at this early design phase, due to the uncertainty in dimension and location of the cut-outs on the tank for liquid hydrogen to flow in and out, an extra 20% of heat flow is considered.

It is assumed that the content of the tank (hydrogen gaseous-liquid mixture) is quasi-uniform as the vibration or acceleration of the aircraft will increase the level of uniformity in the mixture and as a result, the internal heat

transfer is neglected.

8.2.1. Trade-off between using vacuum or foam to insulate

As mentioned above, either foam or vacuum can be used to minimise heat transfer by conduction and convection from the outside environment. Either method has its advantage and disadvantage and a more detailed table is listed below in Table 8.1. Condensation of oxygen is critical to the safety of this aircraft due to the high flammability of hydrogen at rich oxygen environment. Extreme case including leakage of hydrogen and condensation should be avoided. To design a double metal layered vacuum tank system, it is crucial to fix the middle tank in place while not compromising the insulation performance of the system, the addition of supporting struts will increase local stress and further increase the mass performance and complexity in designing such structure. As a result, foam is selected as the insulation layer.

Table 8.1: Advantages and disadvantages of foam and vacuum

	Outgassing	**Condensation**	**Mass**	**Volume**	**Structural complexity**
Foam	Not a concern given that this insulation method does not depend on molecule absence	Considerable concern due to environmental gas flow in. Can be tackled by decreasing the connection between tank and foam	Better, due to the low density perform of the foam	Bigger, due to the required amount of foam to keep cryogenic temperature	Less complex due to that the foam will uniformly support the metal inner tank
Vacuum	Will reduce performance, however can be tackled by more frequent maintenance and regeneration of vacuum environment	Maybe a issue if the regeneration of the vacuum environment is not frequent enough	Heavier, due to more heavy metal structures required	Better, due to vacuum layer can be effectively thin when well designed	More complex due to connection structural part needed to connect inner and outer tank and also vacuum regeneration method

8.2.2. Insulation Material

The material is required to meet various requirements including thermal conductivity, density, minimum service temperature, flammability and etc in order to be selected. The chosen material for this tank is reticulated vitreous carbon foam (RVC). This material is designed for cryogenic insulation and has good thermal conductivity performance (0.04 W/mK [58]), high service temperature range including the cryogenic part needed, relative low density to Young's modulus ratio. Super insulation foil will be added to the foam layer to further reduce thermal conductivity.

8.3. Tank Geometry Design

Considering that the liquid hydrogen tank needs to carry the alternative fuel for the most energy consuming flight profile, an alternative approach to size the mass of the total hydrogen needed is performed based on the total energy contained in the current A320 using Equation 8.1. Here, V is the total volume of the tank of the A320 $27\,200$ L, $\rho_{\text{JET–A1}}$ is the density of the kerosene being used (0.804 kg/m^3), $e_{\text{JET–A1}}$ is the gravimetric energy density of the kerosene (42 MJ/kg) and finally $\eta_{\text{A320–engine}}$ is the efficiency of the current jet engine assumed to be 35%. As a result, the total energy stored in the current A320 is $321\,500$ MJ.

$$E = \frac{V \cdot \rho_{\text{JET–A1}} \cdot e_{\text{JET–A1}}}{\eta_{\text{A320–engine}}} \tag{8.1}$$

To reduce the total energy consumption by 10% and to perform 30% of the flight using hydrogen, a factor of $90\% \cdot 30\%$ is applied to the above calculated total energy with a result of $86\,800$ MJ. Since the number is based on the full tank capacity of the current A320, it should already contain the extra amount to counter extreme situations and thus only 5% is added to ensure the continuity of the design process. The total mass of the hydrogen is calculated using Equation 8.2, in which the energy density is 120 MJ/kg and efficiency is assumed to be 45%. As a result, the total mass of hydrogen needed is 1687.72 kg.

$$m_{\text{liquid–hydrogen}} = \frac{E_{\text{alternative–source}}}{e_{\text{liquid–hydrogen}} \cdot \eta_{\text{Hydrogen–engine}}} \tag{8.2}$$

In order to achieve maximum volume-to-surface area ratio and pressure performance, a spherical shaped tank is firstly considered, however, due to the large amount of hydrogen needed to be stored and the limit radius can be provided by the fuselage, the full sphere option is adapted to cylinder with hemispheres on each side.

8.3.1. Tank Sizing

The foam insulated liquid hydrogen tank includes three layers, the inner shell for holding pressure, the foam for insulation and the fairing to protect the foam. The respective thickness of each layer must be optimised. In the midterm report[59], the tank is assumed to be filled with 80% liquid hydrogen and the remaining with 20% of one bar of gaseous hydrogen. With heat flow in, the liquid hydrogen will start to boil off and turn into gaseous while increasing the internal pressure. The amount of total heat is calculated based on the latent heat of hydrogen evaporation by over-simplifying the high pressure effect on hydrogen gas-liquid mixture and the further condensation of subcooled hydrogen. The new method being used focuses more on the internal energy change of the hydrogen inside of the tank as a whole by using hydrogen's thermodynamic property with the first law of thermodynamics. The internal energy data with varying pressure and density is acquired from Reference Fluid Thermodynamic and Transport Properties (RefProp) [1]. For each mixture density step, step increment of pressure will be set as independent variable, and the internal energy will be generated as state dependent variable. By repeating the process for different mixture density, a complete relationship of internal energy at different pressure level and mixture can be acquired, and by finding the difference of internal energy at different density level, the internal energy increment due to heat flow in can be calculated (Equation 8.3). Density is set constant for each level is because of the fixed volume of the hydrogen storage tank.

$$Q = \Delta U = U_{after} - U_{initial} \tag{8.3}$$

The dormancy of the hydrogen tank is a crucial performance parameter in designing the hydrogen tank, with extended exposure time or extreme temperature conditions, a higher pressure will be accumulated inside the pressure wall and to ensure the safety of the tank, excessive pressure will be released by venting out unused gaseous hydrogen into the surrounding environment and thus wasted. Also, to ensure the safety of the tank, safety coefficient respective to pressure is set to 2.

The thickness of the inner wall is calculated based on pressure and shown in Equation 8.4, in which the P is internal pressure, r is the radius and σ_{yield} is the yield stress of the high performance Aluminium 7068-T6511 being used, which has a yield strength of 648 MPa and density of 2.85 kg/m^3. Similarly, the foam thickness is calculated based on the internal and environmental temperature difference ΔT, surface area of the inner tank S_{shell}, the mission time, the thermal conductivity of the selected foam α_{foam} and the total input energy Q. The equation is shown in Equation 8.5. It is worth noticing that the tensile strength of aluminium will be enhanced due to low temperature condition, which provides an extra safety margin. In addition, due to the aluminium alloying contain magnesium which could react with hydrogen in unlikely event, a coating will be applied to the inner side of the tank to prevent activity.

$$t_{wall} = \frac{P \cdot r}{\sigma_{yield}} \tag{8.4}$$

$$t_{foam} = \frac{\Delta T \cdot S_{shell} \cdot time \cdot \alpha_{foam}}{Q} \tag{8.5}$$

With varying mixture density, allowed pressure and length to radius ratio of the cylinder part, sets of required tank wall thickness, foam thickness and the total volume and mass can be generated. The mixture density range is set to be from 40 kg/m^3 to 59 kg/m^3, allowed pressure is set to be from 0.1 MPa to 3.0 MPa and l to r ratio is set to be from 0.0 to 3.0. As a result, the calculated total mass, total volume, total length and outer radius variation are illustrated in the format of heat map and shown in Figure 8.2. Moreover due to small step size in pressure axis, scattered dots may resemble a continuous line. Options are filtered with geometry and mass constraint in order to fit in the fuselage given by the previous result while also not causing extreme loads.

It can be seen in Figure 8.2a, considering mass only, a lower internal pressure is favoured given that the pressure is the main component contributing to the total weight. With a high pressure of up to 3.0 MPa, the whole tank can weigh up to more than seven tons. Also, indicated by Figure 8.2b, it can be seen that the possible total volume varies from around 48 m^3 to more than 60 m^3. In which, a higher pressure and higher density will give a lower total volume. A higher total density will result in lower hydrogen volume while higher allowed pressure will allow more hydrogen expansion, which leads to an increased amount of allowed heat and thus smaller foam thickness is needed for insulation. with respect to the total length and outer radius output shown respectively in Figure 8.2c and Figure 8.2d and aside from the length to radius ratio, a higher pressure will lower the outcome, which is in line with the volume analysis.
Based on the above outcome, the optimum design point can be chosen.

[1] URL `https://www.nist.gov/srd/refprop` [cited: 02 June 2022]

8.3.2. Sizing result

As a result, the hydrogen inner tank parameters chosen are 56 kg/m^3 for mixture density, 2.67 MPa for maximum allowed pressure and 3.5 for l-to-r ratio. The total volume of the assembly is 50.81 m^3, total mass is 2644.83 kg, outer diameter is 3.15 m and total length is 7.55 m. In which, the inner tank wall thickness and mass are 10.4 mm and 1605.95 kg, respectively. For the foam layer, the thickness is 292.98 mm and mass is 941.41 kg and for the faring, its thickness is chosen to be 15.7 mm [60] and its mass is 97.47 kg. At this point, the geometry is optimised for fitting in the tail cone and will result in minimum extra fuselage length.

8.4. Other concerns and recommendations

8.4.1. Delamination

Because of the low temperature the tank will operate at, the thermal strain will shrink the inner tank and thus possible delamination between the inner tank and the foam layer could occur. The maximum thermal strain of the tank is calculated by multiplying the thermal expansion coefficient and the service temperature difference and a result of -0.007 strain is calculated. While the maximum strain caused by pressure loading is calculated by dividing the metal yield strength by its Young's Modulus and a number -0.0022 strain is calculated. The strain caused by cryogenic temperature is greater than the strain caused by pressure loading and thus the tank will over all shrink the tank and the combined shrinkage will be the multiplication of inner tank radius by total strain and a result of 6 mm is calculated for each half side. The thermal strain of the foam is 0.0001 strain when assuming uniformly decrease of temperature from outside in and because of the lower thickness of the foam and lower magnitude in strain, this part of deformation is neglected. When assuming all the tank deformation is deformed by the foam layer, a strain can be calculated by dividing the displacement by the foam thickness which is mentioned in the previous section and as a result, a strain of 0.020 strain is calculated in the foam. To calculate the pressure that the adhesive will sustain, the foam strain is multiplied with foam's Young's modulus and as a result, a pressure of $63\,500$ Pa is calculated. This first level pressure estimation on the adhesive layer is proved not high for typical adhesive bond and the load between the tank and foam is fully in tension. The most dangerous case would be on ground when the inner tank is under cryogenic temperature while no pressure is applied (tank is empty). However, more study on the type of adhesive to be used and their performance under cryogenic temperature should be closely investigated.

8.4.2. Fatigue

There are additional loads within the tank system including load caused by self-weight or fatigue load that should also be considered. As the safety factor used for the pressure tank is 2, the maximum actual operational stress will not exceed 324 MPa. The load cycle due to use of hydrogen will result in maximum pressure 26.7 bar and vary during each mission cycle depending on operation method. The estimated number of load cycle for the whole aircraft would go up to 50,000 because of the long operating life-span, a first level estimation on fatigue load is performed based on fatigue data provided by aluminium manufacture[2]. It can be seen that the material can sustain a maximum load of 100,000 cycles when the stress ratio is 0.5 or approximately 10,000 cycles when the stress ratio is 0. When operating the aircraft, for short flights, the tank will not be fully filled, which will result in a lower pressure accumulation. Also, during turnover time and refuelling, the tank will not be fully emptied thus with the combined operating mode optimised, the hydrogen tank will not fail under fatigue. However, due to the long life span, and lack of further study on this cryogenic tank, a more frequent inspection is recommended. As for the weight of the inner tank combined with hydrogen inside, due to the large contacting surface with foam, the pressure caused by self-weight on foam is nearly negligible and the deformation is thus also negligible.

8.4.3. Cut-out consideration

Cutouts will be applied to the tank in order for hydrogen to flow in and out. In addition, a heating rod will be placed inside to regulate the pressure which requires a connection to an outside control system. To minimise the impact of pressure and thermal performance, the openings will be placed on the hemispherical part of the tank. As the gaseous hydrogen will be extracted and used, a first cutout on the near cabin side, top half of the hemisphere is applied. Then, as the heating rod will be placed inside the liquid part to ensure maximum contact, a cutout in the lower half is required. Also placed at near fuselage side, an opening in the middle, near tail side will be applied for liquid hydrogen to flow in. Further investigation in thermal insulation is needed on the cutout locations as well as stress analysis due to stress concentration. Extra weight consideration has been taken into account during the previous design phase as the stress caused by pressure will be halved in the hemisphere part comparing with the cylindrical part, while the thickness in the previous design is kept the same. Moreover, due to the pipelines' circular cross-section, the stress concentration factor will not be considerably larger and

[2]URL `https://online.kaiseraluminum.com/depot/PublicProductInformation/Document/1027/Kaiser_Aluminum_7068_Rod_and_Bar.pdf` [cited 14 June 2022]

as a result, further optimisation of the round openings will not drastically increase the weight or volume of the whole assembly.

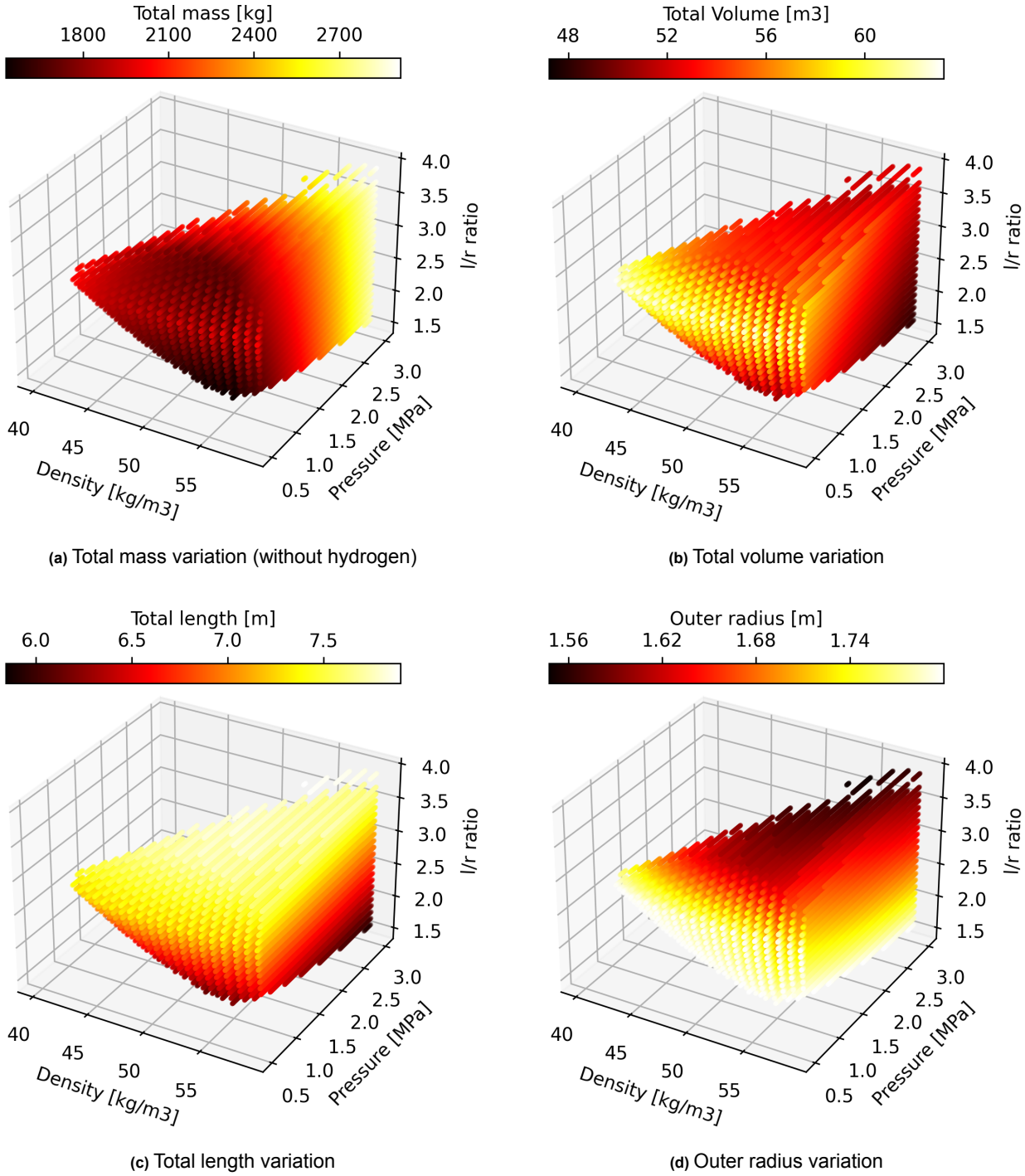

(a) Total mass variation (without hydrogen)

(b) Total volume variation

(c) Total length variation

(d) Outer radius variation

Figure 8.2: Total mass, total volume, total length and outer radius as a result of varying mixture density, allowed pressure and length to radius ratio (darker is better)

9

Power and Propulsion

Power and propulsion systems are crucial in design of the LEAF aircraft as they are the main factor differentiating the design from conventional airliners and directing the design into the more sustainable route. In this chapter the design method and taken assumptions are presented in Section 9.1, followed by the verification of the model in Section 9.2. Next, the engine architecture is discussed in Section 9.3. Lastly, the emissions of the propulsion system are quantified by using a simulation, presented in Section 9.4.

9.1. Method & Assumptions

Jelle, Igor

9.1.1. Analysis Method

The propulsion system is designed to create the required thrust using as little energy (i.e. fuel) as possible. In a situation without any energy loss due to inefficiencies, a jet engine can be described as an ideal Brayton cycle [61]. In this cycle, a fluid is first isentropically compressed, after which heat is added isobarically. The fluid then expands isentropically and finally, the heat is transferred isobarically. The isentropic compression requires power, which can be received from the isentropic expansion. The latter stage releases more energy than required by the compression stage. This energy can then be used to propel the aircraft. For the isentropic processes, the pressure and temperature can be determined using Equation 9.1 and Equation 9.2[61].

$$\frac{p_2}{p_1} = \Pi \qquad (9.1) \qquad \frac{T_2}{T_1} = \Pi^{\frac{K}{K-1}} \qquad (9.2) \qquad \dot{Q} = \dot{m} \cdot c_p \cdot (T_2 - T_1) \qquad (9.3)$$

However, there are losses due to inefficiency. This means that the steps described above are no longer isentropic or isobaric. The compression stage now generates some additional heat for the same compression, as well as entropy. Some pressure is lost during the heating stage. The inefficiency in the turbine means that more heat needs to be extracted for a certain amount of energy. Finally, the inlet and nozzle are not adiabatic, which means that energy is lost there as well. Using the method from [62], the performance of the engine can be analysed.

To analyse the performance of a jet engine, it is divided into five sections. These sections are the inlet, the compressor stages, the combustion chamber, the turbine stages and the nozzle. Whilst numerous different engine designs are possible, it can be analysed as a different combination of these stages.
The inlet is the part of the engine where the air flows in. Depending on how fast the aircraft is flying, the total pressure can increase (when flying faster than air speed at the end of the inlet) or decrease with respect to the ambient pressure. Since there is no work done on the air, the total (or stagnation) temperature remains the same. There is some pressure loss due to inefficiency as well. Equation 9.4 shows the total temperature at the end of inlet section. T_0 is the ambient temperature, $T_{0,0}$ and $T_{0,2}$ are the total temperature outside the engine and at the end of the inlet, respectively. M_0 is the Mach number of the aircraft. Equation 9.5 is the expression for the total temperature at the end of the inlet. p_0 is the ambient pressure and η_{inlet} is the inlet efficiency. Equation 9.6 is used to determine the amount of air that flows through the engine per second. Here, A is the area of the inlet, V is the velocity and R the specific gas constant.

$$T_{0,2} = T_{0,0} = T_0 \cdot (1 + \frac{K-1}{2 \cdot c_p} M_0^2) \qquad (9.4) \qquad p_{0,2} = p_0 \cdot (1 + \eta_{inlet} \cdot \frac{K-1}{2} \cdot M_0^2)^{\frac{K}{K-1}} \qquad (9.5)$$

$$\dot{m} = A \cdot \frac{p_2}{T_2 \cdot R} \cdot V \qquad (9.6)$$

As explained earlier in this section, in an ideal Brayton cycle the fluid would be compressed isentropically. Since the compressor is designed for a certain compression ratio, Equation 9.1 is still used to determine the pressure after the compressor. However, the temperature in the real compressor rises further than in an ideal compressor, as seen in Equation 9.7. The work required for this compression is calculated using Equation 9.8. In the case of a turbofan, the fan is comparable to the compressor stage. After the fan, the flow of air is split in two. One flow goes through the other compressor, combustion chamber and turbine, i.e. the core. Since this

flow of air is heated, it is called the hot flow. The air that does not pass through the core is called the cold flow. The bypass ratio indicates how many parts of air are in the cold flow per part of air in the hot flow.

$$T_2 = T_1 \cdot (1 + \frac{1}{\eta_{comp}} \cdot (\Pi^{\frac{K-1}{K}} - 1)) \quad (9.7) \qquad \dot{W} = \dot{m} \cdot c_p \cdot (T_2 - T_1) \quad (9.8)$$

In the combustion chamber, fuel is burned to increase the temperature of the flow. Since a different fluid is added to the flow, the properties such as c_p and $\dot{m}$ can change. Furthermore, there are some pressure losses, e.g., due to swirling inside the chamber. The new mass flow is simply the fuel flow added to the air flow. To get c_p for a mixture of two fluids, Equation 9.9 can be used. The amount of energy added by the fuel is also calculated. Unfortunately, some of the energy is lost due to inefficiency. As a result, the final temperature is lower than it would be otherwise. The temperature at the end of the combustion chamber can be calculated using Equation 9.10. η_{cc} indicates the efficiency of the combustion chamber. The pressure change is determined using Equation 9.1.

$$c_{p_{mix}} = \frac{c_{p_1} \cdot \dot{m}_1 + c_{p_2} \cdot \dot{m}_2}{\dot{m}_1 + \dot{m}_2} \quad (9.9) \qquad T_2 = T_1 + \frac{\dot{m}_f \cdot LHV_f}{\dot{m} \cdot c_{p_{mix}} \cdot \eta_{cc}} \quad (9.10)$$

In the case of a jet engine, the turbine is connected to at least one of the compressor stages. The turbine needs to extract a certain amount of energy per second to power the compressor(s) to which it is attached. Since the connection is not 100% efficient, there is some additional power required to overcome this loss. Equation 9.11 and Equation 9.12 show how the temperature and pressure after the turbine stage is determined.

$$T_2 = T_1 - \frac{\dot{W}_{comp}}{\eta_{mech} \cdot \dot{m} \cdot c_p} \quad (9.11) \qquad p_2 = p_1 \cdot (1 - \frac{1}{\eta_{turb}} \cdot (1 - \frac{T_2}{T_1})^{\frac{K}{K-1}}) \quad (9.12)$$

In the end of the jet engine, the mass is exhausted through the nozzle. If the pressure difference is too large, the exhausted flow becomes choked. This means that the mass flow cannot be increased any further. A flow becomes choked if $\frac{p^*}{p_{upstream}}$ is larger than $\frac{p_{downstream}}{p_{upstream}}$. In this case, the pressure will equal the critical pressure. The temperature and exhaust velocity are then calculated using Equation 9.13 and Equation 9.14. Otherwise, these values are calculated using Equation 9.15 and Equation 9.16. The total thrust is calculated using Equation 9.17 if the flow is not choked, and using Equation 9.18 otherwise.

$$T_2 = \frac{2 \cdot T_1}{K - 1} \quad (9.13) \qquad V_{exhaust} = a = \sqrt{K \cdot R \cdot T_2} \quad (9.14)$$

$$T_2 = T_1 \cdot (1 - \eta_{nozzle} \cdot (1 - \frac{p_0}{p_1}^{\frac{K-1}{K}})) \quad (9.15) \qquad V_{exhaust} = \sqrt{2 \cdot c_p \cdot (T_2 - T_1)} \quad (9.16)$$

$$F = \dot{m} \cdot (V_{exhaust} - V_0) \quad (9.17) \qquad F = \dot{m} \cdot (V_{exhaust} - V_0) + A \cdot (p^* - p_0) \quad (9.18)$$

9.1.2. Assumptions

Conducting an analysis of engine thermodynamic cycle requires a variety of input parameters. Due to engine development being largely an industry secret, accurate data is very scarce. Therefore values for certain parameters need to be assumed. Most importantly, efficiencies of individual engine stages need to be estimated, based on state-of-the-art values of the current engines used in comparable aircraft. A summary of assumed values for efficiencies is presented in Table 9.1.

Table 9.1: Assumed efficiencies for engine components

η_{inlet}	η_{fan}	$\eta_{gearbox}$	η_{comp}	η_{cc}	$\eta_{turbine}$	η_{mech}	η_{bypass}	η_{core}
0.97	0.90	0.975	0.90	0.965	0.90	0.98	0.95	0.96

Whilst it is possible to achieve higher efficiencies for the turbomachinery for a certain design point [63], the engine will operate at varying loads and altitudes. It should be noted that in case of more than one component of the same type, the same efficiency is assumed for all of them. Aside from the efficiencies, pressure ratios for the inlet and combustion chamber are assumed (Π_{inlet} and Π_{cc} respectively), as during the design optimisation they will be kept constant. Their values are summarised in Table 9.2.

Table 9.2: Fixed pressure ratios for the engine

Π_{inlet}	Π_{cc}
0.97	0.98

Additionally, for the purpose of the analysis, further assumptions are taken, relating to the airflow and combustion properties. The assumptions include:

- **Standard Atmosphere:** all atmospheric properties of the ambient flow are calculated according to the International Standard Atmosphere.
- **Efficiencies are constant:** The efficiencies of the components are independent of the mass flow, temperature, pressure or other variables.
- **Same combustion chamber for hydrogen and kerosene:** Kerosene and hydrogen can be combusted in the same combustion chamber with the same efficiency. However, the change to the upper and lower flammability limits is taken into account.
- **Rule of mixtures:** Properties of the pre-mixed fuels, such as c_p, K (specific heat ratio) and stoichiometric ratio are determined using the rule of mixtures

9.1.3. Engine Development Constraints

In practice, the engine is constrained in some areas, meaning that not all design options are possible. The constraints originate from physical limitations in the engine design, for instance material durability or compressibility effects. The main considerations for the engine design include the temperature in the turbines section, overall engine pressure ratio and speed of the tip of the fan blades.

Temperature and pressure limits

The temperature at the end of the combustion chamber and thus at the entry of the high pressure turbine is possibly the most important design constraint. The temperatures depend on the amount of fuel being burned, as well as the type of fuel. The temperature limit for the engine has been set to $2000\,\mathrm{K}$ for normal operation in accordance with current state-of-the-art technologies used for turbine blades [63]. This is possible since the blades are cooled using compressed air taken from the high pressure compressor. This air is expelled through tiny holes in the turbine blade, after which it forms a relatively cool film on the turbine blade, insulating it from the hot flow. In case of an emergency, this temperature limit can be exceeded to $2200\,\mathrm{K}$.
The overall pressure ratio is limited to be 60 at most. This is similar to modern engines. Whilst it would be possible to achieve a higher pressure ratio, the extra weight required would offset the benefit.

Combustion Limits

The amount of fuel burned in the engine will determine the emission profile of the aircraft, further discussed in Section 9.4. An influential parameter for engine performance and its exhaust composition is the equivalence ratio φ, defined in Equation 9.19. Depending on the type of fuel, there exist lower and upper bounds for equivalence ratio, outside which combustion will not occur. For the engine design, primarily the lower limit will be considered, as lean combustion is beneficial for fuel efficiency as well as reducing emissions.

$$\varphi = \frac{(\mathrm{A/F})_{\mathrm{stoich}}}{(\mathrm{A/F})_{\mathrm{actual}}} \tag{9.19}$$

the Equivalence ratio constraint is characterised by the Lower Flammability Limit (LFL) of the fuel, determined by volume percentage. The values for LFL are 0.7% for kerosene and 4% for hydrogen [64]. These correspond to equivalence ratios of approximately 0.55 and 0.1, for combustion in air. Enriching the kerosene with hydrogen can contribute to lowering the equivalence ratio required for a successful and stable burn [65]. These limits are presented in Figure 9.1. The values for λ, corresponding to $\frac{1}{\varphi}$, will be introduced as additional constraints to the engine calculations. That way the engine can be ensured to always be operating at the setting that provides the most beneficial emission characteristics. Using these relations, the usage strategy for fuels can be determined in order to ensure minimised emissions of harmful compounds.

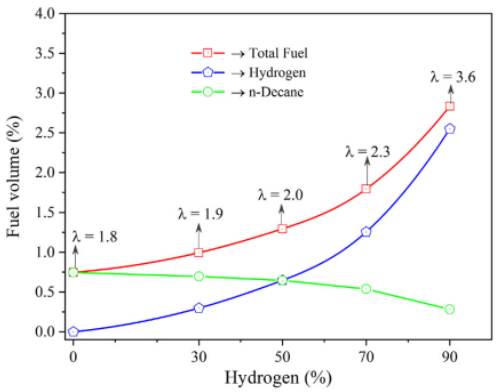

Figure 9.1: Equivalence Ratio limits for different kerosene-hydrogen mixtures

Rotational velocity

The rotational velocity of the shafts is limited by the speed at the tip of the blades compared to the fluid flowing through the system. In other words, it is the combination of the velocity of the air flowing through the system and the rotation of the blade. While there is no rotation in a stator, a significant component of the flow velocity is tangential to the axial flow due to the rotor. This means that the relative blade velocity at a stator can be limiting as well.

Multiple factors influence the maximum tip speed, such as noise limits and centrifugal forces in the blades. The formation of shock waves can also be a limiting factor. However, the shock waves can also be used to further compress the airflow, at relatively little efficiency loss. With current design and material options, relative mach numbers at the tip of the blades of 1.6 are possible. This enables a compression ratio of two or more with a single set of a rotor and a stator.

The internal forces in the rotors should also be taken into account. Together with the temperature, these forces can cause creep, where the blade is deformed over time. For high forces, it could even lead to failure of the material. However, since the internal stress depends on the design of the rotor blades, it is chosen to not investigate the limit here.

To determine the required blade speed, Equation 9.20 can be used [63]. Here U is the mean blade speed, i.e., the speed at the average radius of the blade. Ψ is the stage loading coefficient. It is an indication of how much change in enthalpy can be generated in a stage for a certain rotational velocity. Equation 9.21 and Equation 9.22 can be used to calculate the speed of the blade and the relative mach number at the tip, respectively. From Equation 9.20 it can be seen that a higher blade speed leads to a higher compression ratio.

$$U = \sqrt{((\frac{P_{02}}{P_{01}})^{\frac{K-1}{K \cdot \eta_p}} - 1) * \frac{c_p \cdot T_{01}}{\Psi}} \quad (9.20) \qquad U_{tip} = U \cdot \frac{r_{upper}}{r_{mean}} \quad (9.21) \qquad M_{rel_{tip}} = \frac{\sqrt{U_{tip}^2 + v_{flow}^2}}{a} \quad (9.22)$$

9.2. Model Verification

Igor

The calculations for the thermodynamic cycle of the engine need to be verified to confirm the credibility of the results. For that purpose, input values for an engine with known values for thermodynamic cycles can be used in the method to verify whether the output will correspond to the literature values. It should be noted that the correspondence will not be exact as the engine model used for verification was evaluated for a given set temperature at the combustion chamber while in the model used for analysis the temperature was estimated from the amount of fuel needed to provide the thrust required by the critical flight condition. The comparison of thermal cycles from literature (red) and outputted by the model (blue) are presented in Figure 9.2.

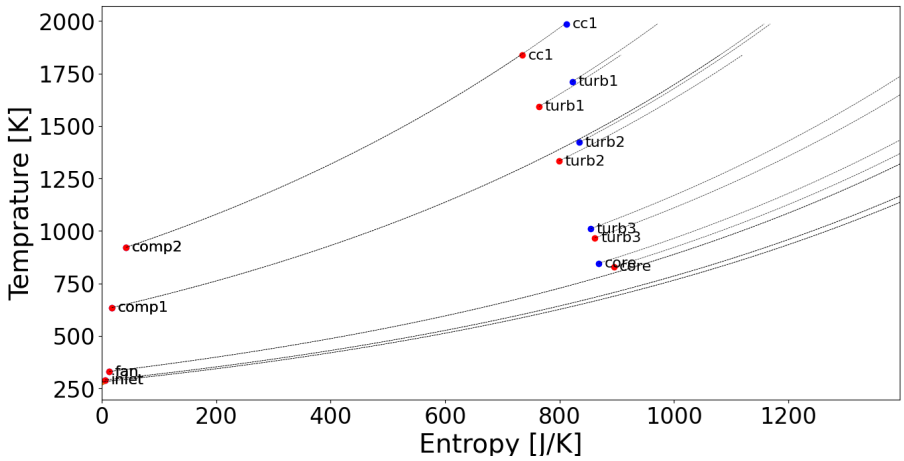

Figure 9.2: Verification of the propulsion system model

9.3. Engine Architecture

Jelle

Three different turbofan engines were considered: A geared twin spool design with a mixed combustion chamber, a geared twin spool design with two combustion chambers in series, and a triple spool design

- **Twin spool:** This design is the most similar to the engine currently used by the A320neo. The gearbox allows the fan to spin at a different speed than the compressors, making a more optimized design possible.

- **Two combustion chambers:** This design allows the combustion chambers to be optimised for each fuel type. Furthermore, the residual heat from the first chamber can help combust the fuel in the second chamber. However, since the aircraft will be able to fly on only hydrogen, it would mean that one combustion chamber in each engine would remain unused for take-off. The hydrogen combustion chamber would also be much larger than required during cruise. This adds weight to the engine, which means more energy is required to fly. Finally, if the second combustion chamber is not operative, there are still losses that occur there, further increasing the energy required. Therefore, this design was eliminated, as it is estimated that the benefit of more optimized combustion chambers is less than the drawbacks.

- **Triple spool:** In contrast to the twin spool design where a gear allowed the fan and the low pressure compressor to spin at different speeds, these compressors are not connected. This also means that the rotational velocity of the low pressure turbine can be more optimised, since there is now a third turbine. However, this optimisation is estimated to not be enough to offset the higher efficiency of a gearbox compared to a turbine. Therefore, this design is not chosen.

The design optimisation is done by using the method described in Section 9.1. The optimal engine configuration is considered to be the configuration with the lowest fuel consumption at the design thrust, as this would both reduce emissions and increase the energy efficiency. To determine the fuel consumption, the power required by the compressors was determined. It is assumed that this power comes from the combustion of the fuel. The fuel flow can then be set so that the flow of energy ($\dot{m} \cdot \mathrm{LHV}_f$) is at least equal to the power extracted by the turbines. If the required thrust is not met for a certain design, the pressure ratios of the fan and compressors is increased, corresponding with an increased fuel flow. Furthermore, if one of the restrictions mentioned in Section 9.1 is exceeded, the configuration is deemed unfeasible.

The different configurations were different combinations of fan diameter and bypass ratio. As expected, higher bypass ratios are more efficient. Since the core flow is smaller for a larger bypass ratio, the flow will be heated up more for a certain fuel flow. This means that there is an upper limit on the bypass ratio. This limit increases with increases to the fan diameter, since the needed compression ratio to reach the target thrust is lower while the mass flow is higher.

However, there is no such limit on the fan diameter. Whilst there is a limit on the tip speed, this limit is reached by increasing the pressure ratio. Since the relative mach number at the tip requires a large rotational velocity, which in turn requires a large pressure ratio, whilst a large diameter means that the pressure ratio can be lower. Furthermore, a larger diameter will mean more weight and parasitic drag, and therefore a higher thrust requirement, but that is not taken into account since the effect for this will be difficult to estimate accurately. A

larger diameter engine also means that reaching a sufficient ground clearance will require a larger landing gear, further increasing the weight of the aircraft. For these reasons, it was chosen to limit the fan diameter to 2.35 m, with a maximum cowling diameter of 2.50 m.
The dimensions and specifications of the engine can be found in Table 9.3. This design is found to be the most fuel efficient at the design condition of 90 kN at sea level, whilst still being able to deliver the required peak thrust in case of a one-engine-out emergency. It is also capable of operating at cruise conditions. In Figure 9.3, the temperature and entropy change can be seen for each stage of the engine. The engine itself can be seen in Figure 9.4.

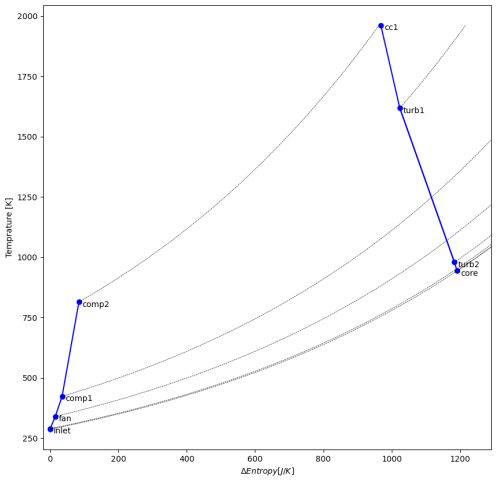

Figure 9.3: Entropy change - Temperature in the engine at take-off conditions

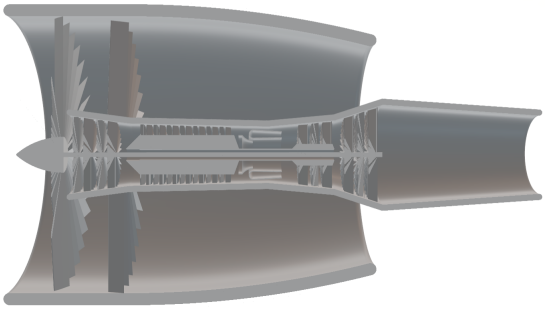

Figure 9.4: Side view of the engine

Table 9.3: Engine dimensions and specifications

Fan diameter [m]	Bypass Ratio [-]	Π_{fan} [-]	Π_{LPC} [-]	Π_{HPC} [-]	F_{bypass} [N]	F_{core} [N]	stage layout
2.35	11.5	1.663	2.02	8.316	83187	6814	1-G-2-6-CC-1-2

Material selection

Like the fan blades of the PW1100G engine, used by the A320neo, the fan blades will mostly be constructed from an aluminium-lithium alloy, such as EN AW-8009 [66]. The leading edge will be constructed from a titanium alloy, such as Ti-4Al-6V, to reduce erosion due to cloud droplets [66], as well as reduce the damage in case of a bird strike or other foreign object damage [67]. Using metal alloys in the blade has multiple advantages compared to carbon fibres. It is recycleable, cheaper to manufacture, and it is possible to have a thinner leading and trailing edge, which can reduce the drag and noise emissions. For the compressor blades, the temperatures are too high for aluminium alloys. For these, a titanium alloy such as Ti-4Al-6V will be used.
To increase the efficiency of the combustion chamber, the thermal conductivity of the material should be minimised. The chamber should also be able to withstand the high pressure. Because of this, a titanium alloy with a ceramic coating will be used.
The blades of the high pressure turbine need to withstand a flow temperature of 2000 K, whilst also needing to withstand high stresses due to centrifugal and aerodynamic forces. To be able to withstand the high temperatures, the core of the blades will be made from a Nickel-Cobalt alloy, whilst the surface will be made from a ceramic coating such as Zirconia. Whilst Zirconia is not recyclable, it is needed to allow for the higher temperature required for efficient operation. For the low pressure turbine, the blades will use the same alloy as the high pressure blades, but the ceramic coating is not required.
The fan casing, fairing and nacelle will be constructed from the same material as the fuselage of the aircraft, as they do not experience a significant increase in temperature or pressure. The spinner will be constructed from the same aluminium as the blades.

9.4. Emission Profile

Igor

The emission profile is a crucial aspect of the design, as it places the LEAF aircraft at the forefront of energy transition towards a more sustainable aviation. Emission of the aircraft can be quantified by a simulation of a full flight profile combined with chemical analysis of the combustion reaction of fuel used at a time.

Types of Emissions

Reduction of emitted ultra-fine particles and other harmful or greenhouse gases is the main objective of the mission. Therefore the engine combustion should be performed in a way to reduce these emissions as much as possible. In terms of reducing CO_2, it can be achieved by burning hydrogen, as it does not contain carbon, eliminating the CO_2 created in the process. Similarly, burning a mixture of hydrogen and kerosene can reduce the amount of CO_2 emitted by the engine by an amount strongly correlated with the proportions in the mixture.

NOx emissions are a significant climate forcer, while presenting significant health effects to the near-airport population. They are the main contributor to the ultra-fine particles emitted. The main formation mechanism of NOx is Zeldovich mechanism [68], described by Equation 9.23 and Equation 9.24.

$$O + N_2 \longrightarrow NO + N \tag{9.23}$$

$$N + O_2 \longrightarrow NO + O \tag{9.24}$$

Lowering NOx emissions is more complex than reducing CO_2, as burning hydrogen also emits nitrogen oxides. Emitted NOx is reduced for leaner combustion in the engine i.e. lower equivalence ratio [69]. This trend holds for both kerosene and hydrogen combustion, but hydrogen can be combusted at φ of as low as 0.1, compared to 0.55 for kerosene. This limit can be lowered by pre-mixing the fuels, as shown in Figure 9.1. Therefore, leaner combustion can be achieved, reducing health and environmental effects. Precise fuel composition for the most optimal emission profile will be determined later in the section.

Another emitted compound during flight is water vapour. While not harmful to humans, H_2O can be a powerful greenhouse gas due to formation of contrails, especially in high-humidity areas [41]. Hydrogen combustion emits more water vapour than kerosene combustion, but it should be noted that a large proportion of hydrogen will be used at lower altitudes, at which the lifetime of water vapour in the atmosphere is considerably lower [70]. While water vapour emission can be estimated, contrail formation is a complex phenomenon, for which the 95% confidence interval for value of Effective Radiative Forcing ranges as wide as 17 to $98\,\mathrm{mW/m^2}$ for a conventional kerosene-powered fleet. Due to such high uncertainty, more detailed analysis of contrails has thus been classified as outside of the scope of this project.

Emission Composition

The exact composition of products of the combustion of desired fuel is a consequence of the combustion reaction occurring in the engine. Reactions for combustion of kerosene and hydrogen are given by Equation 9.25 and Equation 9.26 respectively.

$$C_{12}H_{24} + 18\,O_2 \longrightarrow 12\,CO_2 + 12\,H_2O \tag{9.25}$$

$$2\,H_2 + O_2 \longrightarrow 2\,H_2O \tag{9.26}$$

However, there are secondary chemical reactions taking place. The compounds formed also depend on the temperature and pressure. Additionally, if the fuels are pre-mixed, more complex reactions occur which are difficult to predict with simple stoichometry. Therefore, to estimate the emission composition of combustion, Chemical Equilibrium and Applications (CEA) software developed by NASA is used [3]. Example compositions of products of combustion for varying equivalence ratios are presented in Figure 9.5 and Figure 9.6.

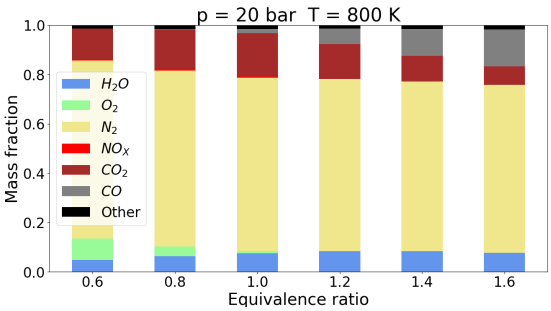

Figure 9.5: Emission composition for kerosene

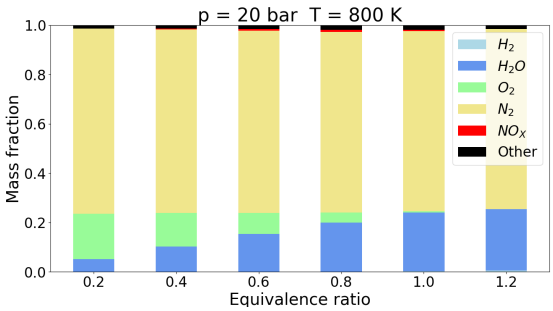

Figure 9.6: Emission composition for hydrogen

Flight Profile Simulation

Flight profile for LEAF aircraft is similar to standard flight profile for jet airliners, as its targeting the same customer base as the aircraft like A320. The approximate flight profile can be seen in Figure 9.7. The simulation discretises the whole mission profile in order to estimate the flight parameters at each point in time. From the flight parameters the engine settings can be obtained, followed by emission characteristics. For each flight stage certain parameters are assumed, in order for the aircraft to comply with flight regulations. The assumed values for their respective flight stages are summarised in Table 9.4.

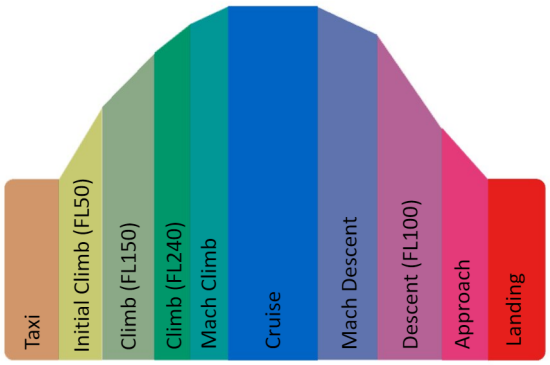

Figure 9.7: Flight profile

Table 9.4: Assumed values for flight stages

Flight Stage	Assumed Parameter	Assumed Value
Initial Climb	Rate of Climb	2500 ft/m
Climb (FL150)	Rate of Climb	2000 ft/m
Climb (FL240)	Rate of Climb	1400 ft/m
Mach Climb	Rate of Climb	1000 ft/m
Mach Descent	Rate of Descent	1000 ft/m
Descent	Glide Slope	3 deg
Approach	Glide Slope	3 deg

Assuming a division of flight into these stages with mentioned climb and descent a whole flight profile can be simulated, featuring characteristics like altitude, speed and fuel consumption at a given point. The time step in the simulation is 10 s for climb and descent phases and 60 s for cruise phase. Such time step is believed to be fine enough to accurately assess the desired characteristics over the whole flight. Resulting plots of altitude and velocity over the flight duration can be seen in Figure 9.8 and Figure 9.9. For clarity, only climb and descent stages with a small part of cruise are shown, due to these parameters being uniform throughout cruise. Apart from the assumptions, the flight profiles has been verified with flight data from actual flight performed by the A320. Flights used for comparison were EJU7904, BAW493 and JZR123, all flown on the 8th of June 2022. The flight data was taken from FlightAware website [1]. Sufficient resemblance with the flight profiles have been found to consider the simulation credible. It should be noted that for real flight the exact flight profile always differs depending on atmospheric conditions, airport surrounding and current air traffic, while the simulation aims to quantify flight characteristics for an average route, of an aircraft carrying maximum payload over the range of 5000 km. For determining the aerodynamic forces the equations of motion are evaluated at each point in time. The aircraft configuration is assumed to change when entering a new flight stage, which is determined by the altitude reached, with the exception for cruise which ends as soon as the aircraft covers the desired range. The configuration includes flap and landing gear extensions, which influence the drag coefficient. The exact values for the coefficients are taken from drag estimation.

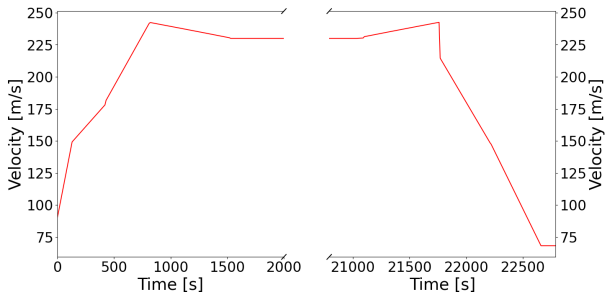

Figure 9.8: Velocity over the flight

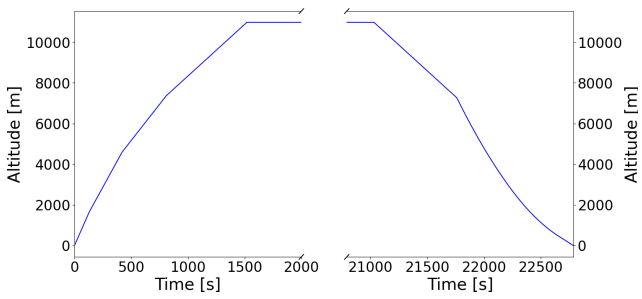

Figure 9.9: Altitude over the flight

Emission Quantification

Aside from velocity and altitude, the simulation can quantify the required thrust and determine the approximate engine setting at a given point in flight. From the engine setting the fuel flow and thus characteristics of combustion can be derived. With combustion characteristics known the composition of emissions can be calculated using the CEA software. As the mission objective is to reduce emissions at low altitudes, the amount of emitted compounds can be quantified at each altitude level, with steps of 1000 m. Emissions that will be considered are H_2O, CO_2 and NOx, as they are deemed the most important for the mission due to health effects and en-

[1] URL `https://uk.flightaware.com/` [cited 8 June 2022]

vironmental forcing. The requirements and top-level design dictates that hydrogen is used for lower altitudes. The simulation is investigated for that case, as well as for the case of performing the climb and descent phase using only kerosene, for comparison. The resulting emissions are shown in Figure 9.10. They are expressed as a ratio of aggregate emissions from hydrogen combustion compared to kerosene combustion. It can be seen that while H_2O values are comparable or even higher for hydrogen, the amount of CO_2 is negligible and it is only present due to the CO_2 already contained in the air as the method of analysis outputs the complete products of combustion. The amount of NOx is also greatly reduced due to lean burn enabled by hydrogen.

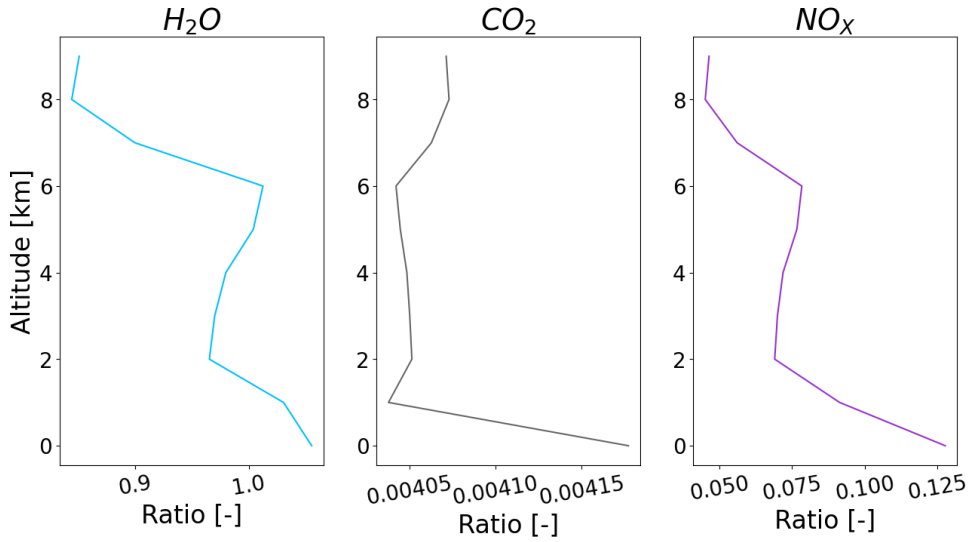

Figure 9.10: Emissions for climb and descent phases using hydrogen compared to kerosene

However, the amount of hydrogen stored on board is more than required for climb and descent alone, as approximately 30% of the total energy needed for flight comes from hydrogen. Therefore, the rest of hydrogen can be used at higher altitudes and during cruise. Various strategies of hydrogen usage can be adopted, including pre-mixing the hydrogen with kerosene with different proportions, ranging from 30% to 90% of hydrogen mass fraction, or alternatively burning pure hydrogen fuel until its depletion and then switching to kerosene. Higher proportion of hydrogen in the fuel allows for a leaner burn, reducing the NOX emissions, but also implies faster depletion. As the emissions and speed of hydrogen usage do not scale linearly the simulation is run for different proportions of pre-mixed fuel to determine which strategy yields the most favourable emissions characteristics. The comparison is presented in Figure 9.11.

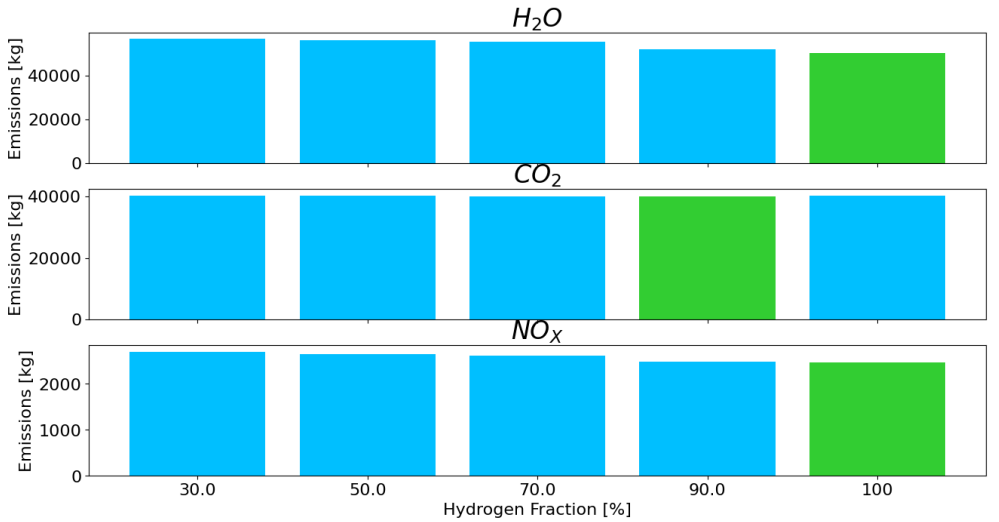

Figure 9.11: Comparison of total emissions for different hydrogen usage strategies. The option with the least emissions is indicated in green.

The mixtures giving the lowest emission totals for a given compound are marked with green. It can be clearly

seen that in terms of H_2O and NOX emissions it is best to first burn all hydrogen and switch to kerosene afterwards.On the other hand, from the perspective of CO_2 emissions the best strategy is to pre-mix the fuels with 70% hydrogen and 30% kerosene, as it allows for a later switch to pure kerosene. As the relative difference for CO_2 emissions is lower than for NOX and H_2O emissions, combined with the fact that NOX is the main contributor to ultra-fine particles, which the mission aims to reduce, the strategy best optimised for the LEAF aircraft is to first burn up all of the stored hydrogen and switch to kerosene for the later part of the cruise. This option implies switching the fuels after covering just under 20% of the flight distance. It should be noted that a margin is always left such that hydrogen can still be used for descent and approach at lower altitudes, so that the harmful emissions at lower altitudes can be minimised.

9.5. Auxiliary Power Unit *Guillermo*

The auxiliary power unit, or APU, of the LEAF aircraft will be a hydrogen fuel cell instead of a conventional APU of an A320 which is powered by the combustion of kerosene. By making it possible to start spinning the shaft of the turbofan engines electrically it is possible to reduce the emissions during ground operations even more. Before placing this APU fuel cell it is necessary to size it. The amount of power that a fuel cell needs to generate determines the size and weight of the fuel cell. The current APU of an A320, the Pratt & Whitney APS3200, uses 90 kW of power to spin the shaft enough to make the airflow through the engines high enough to burn kerosene without overheating the engine [71]. Because there is no reference aircraft that currently starts its turbofan engines using a fuel cell it is assumed that the amount of power that these fuel cells need to generate is at also 90 kW. Note that this value is an upper boundary for the amount of power that needs to be generated. This is because current APUs rotate the shaft by letting bleed air flow into the engine, which is a more inefficient way of starting the engine than by directly applying a torque to the shaft electrically. Using an expected power of a fuel cell in the the coming ten years of 0.85 kW/L and 0.85 kW/kg it can be calculated that the volume of the fuel cell will be $0.106\,m^3$ and the mass will be 106 kg[72].

Now that the mass and size of the APU hydrogen fuel cell is known it is possible to find the most optimal location for this. Because the fuel cell needs to get hydrogen from the liquid hydrogen tank and provide power to the engines it is desired to place it between these two parts of the aircraft. It is desired to minimise the amount of pipelines that contain hydrogen, therefore it has been decided to place the APU as close as possible to the hydrogen tank. Taking these two constraints into consideration it has been decided to place the APU hydrogen fuel cell in the location shown in Figure 9.16.

9.6. Electric Motors and Regenerative Braking *Guillermo*

In order to reduce the emissions during ground operations by 100% and also drastically reduce noise emissions the option of having electric motors in the hub of the main landing gear wheels to drive the aircraft around is being analysed and designed. Also, the energy that can be obtained from magnetic regenerative braking in the wheels will be calculated in order to minimise the energy consumption of the aircraft.

9.6.1. Energy ground operations

In order to make an estimation for the amount of energy that is needed for the electric motors to fully operate by themselves during ground operations the total work to go from the runway to the gate and back is calculated. Using the equations below this needed energy, E_{needed}, can be calculated. First, in Equation 9.27, the total force forward by the motors F_{motors} is calculated by taking the MTOW, lift during taxiing L_{taxi}, rolling resistant coefficient μ_R and drag during taxiing D_{taxi} into account. For the rolling resistant coefficient the value 0.014 is used which is a common value used for rubber tires on asphalt [2]. In Equation 9.28 the total work and energy needed to accelerate the aircraft to taxi speed V_{taxi}, 9.7 m/s, is calculated. To calculate the total work a taxi distance s_{taxi} of 6900 m in every direction is used, which is the maximum distance an aircraft would taxi on an airport where A320 type aircraft operate [73]. On top of this an efficiency of converting electrical energy into kinetic energy by the electric motors μ_{motor} is applied which is assumed to be 90% at this stage.

$$F_{motors} = (MTOW - L_{taxi}) \cdot \mu_R + D_{taxi} \tag{9.27}$$

$$E_{needed} = \frac{F_{motors} \cdot s_{taxi} \cdot 2 + \frac{1}{2} \cdot MTOM \cdot V_{taxi}^2}{\eta_{motor}} \tag{9.28}$$

It is estimated from these equations that the total amount of energy that is needed to taxi the aircraft around the airport per turnaround is $167\,141$ kJ. This energy can be stored in batteries and capacitors which will be

[2] URL https://skill-lync.com/student-projects/project-1-powertrain-for-aircraft-in-runways-90 [cited 12 June 2022]

described in more detail in the next sections.

9.6.2. Electric motor sizing

In order to size the electric motors in the main landing gear wheels it is needed to size the main landing gear wheels first. The number of main wheels needed for the same type of aircraft as the LEAF aircraft is four or eight [74]. Since every main wheel will contain an electric motor and every electric motor adds weight to the aircraft it is desired to have the least amount of main wheels as possible. Therefore, it has been decided to choose four main landing gear wheels for now in the analysis of the amount of power that each electric motor would need to use.

To size the main wheels the diagram in Figure 9.12 is used. Since it is required that the main wheels carry 92% of the static load of the aircraft and there are four main wheels the static load on each wheel will become 172.2 kN or 1790 kg. From Figure 9.12 it can be seen that the required wheel dimensions are (1.27 x 0.400 - 0.559) in metres, which describe the total diameter, width and inner diameter respectively. Because the electric motors can only be placed in the inner part of the wheel, the maximum diameter of the electric motor will be 0.50 m when taking a margin of 3.0 cm on each side into account. Taking the same margin for the width of the electric motor results in a width of 0.34 m.

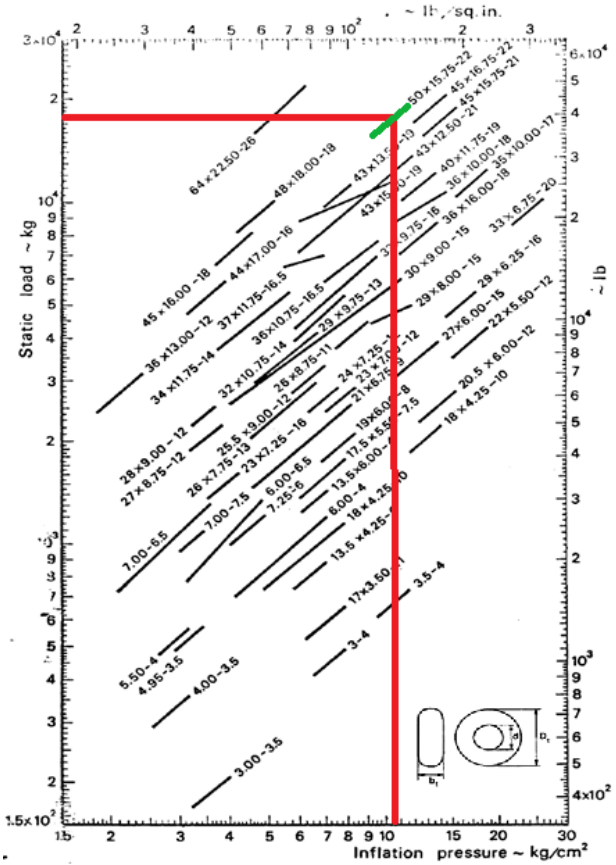

Figure 9.12: Sizing diagram of landing gear wheels in inches for a certain inflation pressure and static load [46]

Now that it is known what the maximum dimensions of the electric motor are it is possible to calculate the amount of torque that each electric motor needs to generate during operations. There are two occasions where the torque needed to be generated by the electric motors is relatively high: braking during landing and accelerating the aircraft to taxi speed. In Figure 9.13 the amount of torque that the electric motors need to generate per ground operation phase is illustrated over time. This torque is calculated by multiplying the force that the electric motors need to overcome with the radius of the main landing gear wheels where the motors are in. From Figure 9.13 it can be seen that the highest amount of absolute torque that needs to be generated by the electric motors is during braking of the aircraft when landing. $12\,500$ Nm of negative torque needs to be generated per electric motor during this phase. The maximum amount of positive torque is 8400 Nm for accelerating the aircraft from standstill to taxi speed.

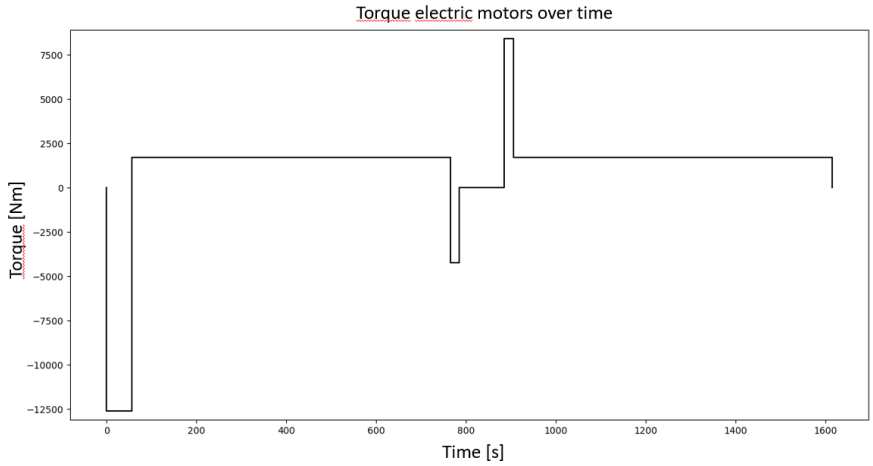

Figure 9.13: The torque that needs to be generated per electric motor over time. The horizontal lines with different values represent the following ground operations in this order: braking during landing, taxiing to the gate, decelerating to a full stop, stand still at the gate (placeholder length of 100 seconds chosen), acceleration to taxi speed, taxiing to the runway. Note that a negative torque means that the electric motors are acting as brakes on the aircraft.

9.6.3. Regenerative braking and energy storage

In order to reduce the amount of energy the aircraft consumes it has been decided to implement regenerative braking as mentioned before to gain energy from braking the aircraft using the electric motors. Electric motors are able to rotate coils by changing the magnetic field created by these coils just at the right time. This magnetic field comes from a current going through the coil and exactly opposes the magnetic field of the magnet. During regenerative braking the coils are already rotating from the start due to the kinetic energy of the wheels. The rotating coils in the magnetic field start then to generate a current and therefore convert kinetic energy into electrical energy. This current can then be used to charge up an energy source, so that the aircraft can use this energy during taxiing.

The maximum amount of energy that you can get from regenerative braking is estimated by multiplying the average power generated by the electric motor during landing with the time the entire landing takes. Equation 9.29 and Equation 9.30 show the calculations of the electric power generated, $P_{electric}$, and the electric energy you get from it, $E_{electric}$. Using the previously calculated $12\,500$ Nm for the braking torque $T_{braking}$, the average rounds per second of the main wheels during landing ω_{wheel} and the electric motor efficiency η_{motor} the total electric energy is calculated to be $26\,820$ kJ per electric motor. The efficiency of the electric motor is assumed to be 70% which is the maximum efficiency of state-of-the-art regenerative braking systems [75].

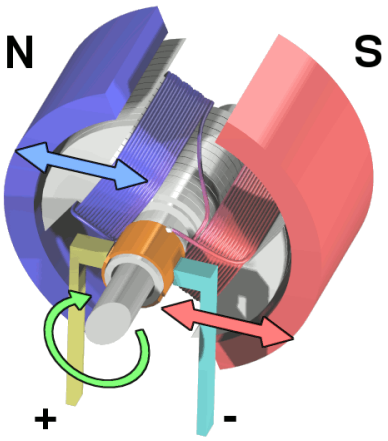

Figure 9.14: Animation of the principle of an electric motor that will also be used in the main wheels of the LEAF aircraft, created by Wapclapet in Blender.

$$P_{electric} = T_{braking} \cdot \omega_{wheel} \cdot \eta_{motor} \tag{9.29}$$

$$E_{electric} = P_{electric} \cdot t_{landing} \tag{9.30}$$

It should be noted that slipping of the tires is not taken into account during the analysis of the electric motors. It is assumed that the wheels have 100% traction control over the surface. The total amount of energy generated by regenerative braking can be obtained by multiplying $38\,314$ kJ with the number of electric motors on the aircraft, which is four. Therefore, the total amount of energy generated using regenerative braking is $107\,279$ kJ. To check if this value is in the right order of magnitude it can be compared with the total kinetic energy of the aircraft just before landing. This total kinetic energy of the aircraft is calculated to be $181\,353$ kJ. This means that 59% of the kinetic energy is converted to electrical energy during regenerative braking, which is in the neighborhood of other regenerative braking systems [75].

Using this $107\,279$ kJ of energy it can be concluded that about 64% of the maximum energy needed for ground operations can be obtained from regenerative braking. All of this energy needs to be stored somewhere on

the aircraft. In order to size the energy storage the diagram in Figure 9.15 [3] is used. From this diagram it can be seen that in general batteries have a high energy density, while ultracapacitors have a high power density. Because the entire energy storage unit needs to be charged within the time the aircraft takes on the runway, it is not feasible to use batteries to store the energy from regenerative braking. According to the figure a maximum value of 10 Wh/kg must be used for the gravimetric energy density of the ultracapacitors. This results in a total added mass of 2980 kg to the mass of the aircraft. However, the possibility of ultracapacitors with a gravimetric density of 47.3 Wh/kg has been proven [76]. These ultracapacitors are not on the market yet, but they are being developed and probably ready by 2035. With this new gravimetric density the total added mass of the ultracapacitors to the aircraft will be substantially lower: 634 kg.

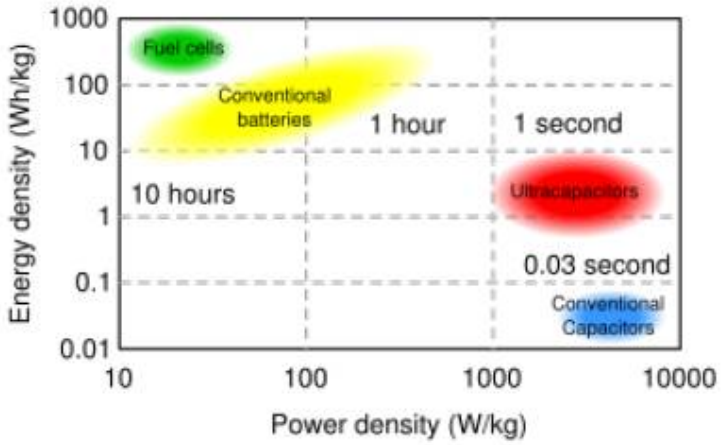

Figure 9.15: Power and energy densities for different forms of energy storage [76].

Now that the weight of the ultracapacitor is known, it is possible to determine its dimensions and placement. Janardhanan R. Rani et al. [76] also obtained a volumetric energy density of the newly developed ultracapacitors, this would be 49.66 Wh/L [76]. From this it can be calculated that the total volume of the ultracapacitor will be $0.60\,\mathrm{m}^3$. By minimising the distance the current has to travel from the electric motors to the ultracapacitor the resistance in the cables is minimised as well. That is why it has been decided to place the ultracapacitor above the retracted main landing gear wheels at the root of the wing as illustrated in Figure 9.16.

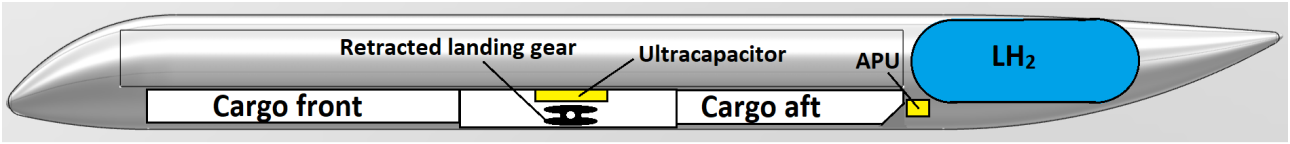

Figure 9.16: Longitudinal placement of ultracapacitor and APU hydrogen fuel cell in the fuselage.

When there is no energy left in the ultracapacitors to perform ground operations the electric motors will get their energy from the APU hdyrogen fuel cell. In Figure 9.17 a flow diagram is shown with all the components needed to drive the electric motors with their respective efficiencies. However, from all the power values given in Table 9.5 it can be seen that the amount of power coming from the APU is about 40% of the maximum power needed by the electric motors. This means that the acceleration time to the taxi speed from stand still of the aircraft will be 50 seconds instead of 20 seconds when the aircraft is driving using only the APU hydrogen fuel cell. This problem could be fixed by always making sure that the electric motors are powered by both the fuel cell as well as the ultracapacitor.

[3] URL www.futurebridge.com/industry/perspectives-mobility/supercapacitors-a-viable-alternative-to-lithium-ion-battery-technology/ [cited 14 June 2022]

Table 9.5: Table showing efficiencies, power in- and output and AC/DC in- and output per component in the electric motor system.

Property/Component	Electric Motor	Ultracapacitor	APU hydrogen fuel cell
Efficiency	90%	90%	40%
Maximum power input	58.7 [kW]	2736 [kW]	-
Maximum power output	684 [kW]	234.8 [kW]	90 [kW]
AC/DC output	DC	DC	DC
AC/DC input	DC	AC	-

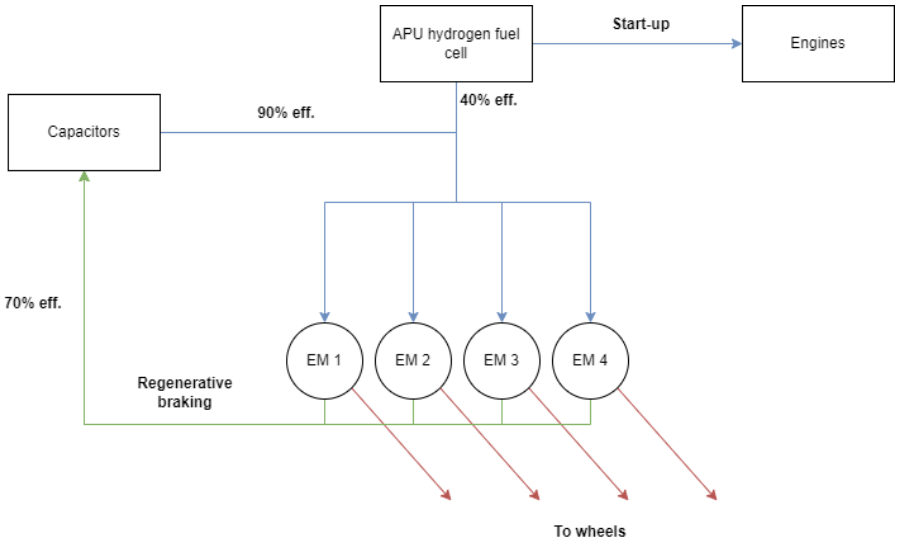

Figure 9.17: Flow of energy between all the components that drive the electric motors with their respective efficiencies.

To ensure that the aircraft is able to brake safely while the electric motors do not work properly for some reason a conventional pneumatic braking system is also installed in the main landing gear wheels as a backup. This braking system will be implemented inside the rotating axis of the electric motor, but the brake disc must be made of ferromagnetic metal to make sure that it does not interfere with the magnetic field of the electric motor. This brake disc will therefore be made of cast iron.

The electric motors are designed as a way to minimise noise emissions and reduce pollution during ground operations to 0%. Not only does this technology reduce emissions it also lowers the general energy consumption of the LEAF aircraft in general. This section and the previous ones show that this is feasible by analysing the energy generated and the power required. The implementation of this technology into the LEAF aircraft would contribute therefore to the general goal of the design process.

9.7. Recommendations

Jelle, Igor

Propulsion system of LEAF aircraft is the system requiring the highest degree of development of new and existing technologies. Combusting hydrogen and kerosene in the same combustion chamber brings forward many aspects which need to be investigated in more detail before such engine can enter production and testing phases. Likewise, the simulation and emission quantification can be refined for more accurate predictions.

For engine development, the analysis in this chapter was conducted primarily from a thermodynamic perspective. While a preliminary value was derived for the number of stages for compressors and turbines, further investigation should be performed into the airflow of the engine to optimise the configuration of rotor and stator blades for the most efficient engine operation. Furthermore, specific parts required to accommodate hydrogen combustion should be considered, for instance flashback protection shall be investigated, as it is needed to avoid damage to the fuel feed system and other parts of the engine. The fuel feed system for hydrogen needs to be sized as well, taking into account the its interface with the kerosene feed system and the limited space. It is a possibility that the engine would need to be lengthened to house both fuel systems, alternatively the nacelle could be enlarged but it may imply integration issues.

The engine has at this time been optimised for conditions at take-off and landing speeds at low altitude. This is

done to minimise the impact the LEAF aircraft has on surroundings of airports, but the engine is currently not optimised for cruise conditions.

At this point, no analysis is done for future materials and technologies. As new materials are discovered, the upper limit on temperature inside the engine might increase, allowing for a larger bypass ratio. Stronger materials or more efficient cooling mechanisms could also be employed to allow for the storage of more hydrogen. These advancements would lead to a further reduction of the emissions.
Considering analysis of emissions, a more refined model can be implemented for the simulation. The drag of the aircraft can be refined from wind tunnel experiments and computational fluid dynamics simulations, in order to estimate the thrust and thus fuel flows better. A more refined model for estimating the emissions themselves can be employed as well. As contrail formation is a significant climate forcer, their formation along the typical flight paths should be investigated to estimate the environmental effects better. Noise emitted by the engine also needs to be analysed. If the noise level is deemed too loud, a method of reducing it needs to be determined, such as chevrons.

10 Structural and Material Characteristics

An important aspect in the design of the aircraft are the structures and material design. The structure is the integration between all different parts of the aircraft and will prevent failures by having enough strength. Loads flow in a lot of directions so a careful study has to be done to analyse how strong a material must be at certain places. Besides that, requirements stated in Subsection 10.1.1 have to be met. A difference with already existing aircraft is that now 90% of the aircraft has to be recycled, so this will be taken into account throughout the chapter next to the fact that it should be as efficient and thus as light as possible. Then the analysis of the loads can be seen in Subsection 10.1.3 and further structure analysis in Section 10.2. Furthermore additions to the structure such as stringer and spars will be selected in Section 10.3. Material options will be analysed and a material will be chosen for the main parts in Section 10.4. Finally in the final design after an iteration will be discussed in Section 10.5.

10.1. Structural Set-up

To make sure the aircraft has the lowest possible impact on the environment, extra requirements are set that take into account recyclability, next to regular loading and structures requirements. After that the size constraints will be explained in Subsection 10.1.2. Using these constraints and environmental values set before, loading diagrams are made for different loading cases which are shown inSubsection 10.1.3. While doing calculation for these diagrams a consistent coordinate system is used which can be seen in Figure 10.1:

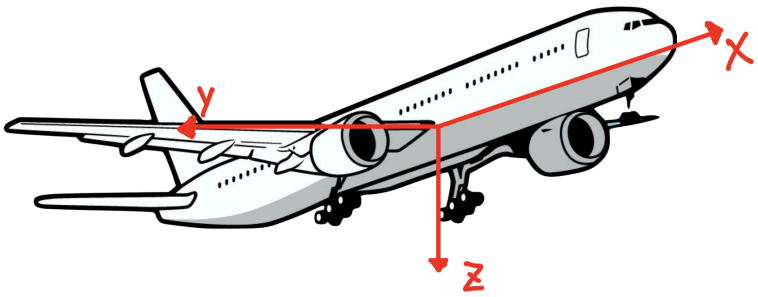

Figure 10.1: Aircraft coordinate system

10.1.1. Requirements

Giorgio, Annemijn, Christoph

In order to get the best possible design, it is important to prepare a set of requirements that will shape the final product. For the structures, these requirements have been divided first into general requirements found in Table 10.1. Then more specific requirements will be explained in Table 10.2 for the main wing structure, followed by the empennage requirements found in Table 10.3, and finally, the requirements for the fuselage in Table 10.4. On top of all requirements come the main requirements about sustainability that at least 90% should be recycled and at least 5% of all parts should be reused.

Table 10.1: General requirements for aircraft structures

Identifier	Requirement
LEAF-ENV-SUS-04	At least 90% of the aircraft parts shall be recyclable at end-of-life.
LEAF-ENV-SUS-05	At least 5% of the aircraft parts shall be reusable at end-of-life.

LEAF-SYS-ST-01-07	All structural parts of the aircraft shall withstand all the loads generated through out the duration of the flight.
LEAF-SYS-ST-08	All structural parts of the aircraft shall withstand the previously mentioned loads during 60,000 cycles (Same as A320).
LEAF-SYS-SAF-05	All structural elements should account for a safety margin of 1.5.

Table 10.2: Requirements for wing structure

Identifier	Requirement
LEAF-SYS-MAN-R1	The wingbox shall have a trapezoidal shape.
LEAF-SYS-MAN-R2	The wingbox shall fit within the airfoil shape.
LEAF-SYS-MAN-R3	The wingbox shall not interfere with the high-lift devices and control surfaces of the wing.
LEAF-SYS-MAN-R4	The wingbox shall allow for storage of 17136L of fuel.
LEAF-SYS-WING-R5	The materials used for the wingbox shall not corrode in contact with fuel.
LEAF-SYS-WING-R6	The tip displacement shall not exceed 15% of the wingspan.
LEAF-SYS-WING-R7	The wing tip twist shall not exceed ± 10 [deg].
LEAF-SYS-WING-R8	The wing structure shall allow for integration of landing gear.
LEAF-SYS-WING-R9	The wing structure shall keep the airfoil shape intact through out the duration of the flight.

Table 10.3: Requirements for Empennage structure

Identifier	Requirement
LEAF-SYS-EMP-R1	The empennage wingboxes shall have a trapezoidal shape.
LEAF-SYS-EMP-R2	The empennage wingboxes shall fit within the airfoils shape.
LEAF-SYS-EMP-R3	The empennage structure shall keep the airfoils shape intact through out the duration of the flight.
LEAF-SYS-EMP-R4	The vertical and horizontal tail wingboxes shall fit inside the airfoil shape.
LEAF-SYS-EMP-R5	The vertical tail tip displacement shall not exceed 15% of the wingspan of the vertical tail.
LEAF-SYS-EMP-R6	The horizontal tail tip displacement shall not exceed 15% of the wingspan of the horizontal tail.
LEAF-SYS-EMP-R7	The vertical tail tip twist shall not exceed ± 10 [deg].
LEAF-SYS-EMP-R8	The horizontal tail tip twist shall not exceed ± 10 [deg].

Table 10.4: Requirements for Fuselage structure

Identifier	Requirement
LEAF-SYS-FUS-R1	At cruise altitude of 11km, the fuselage should allow pressurisation to conditions equivalent to a height of 2.4km.
LEAF-SYS-FUS-R2	Fuselage bending shall be limited to a maximum deflection of 0.5% of the fuselage length.
LEAF-SYS-FUS-R3	The fuselage structure shall account for all necessary openings for operation.
LEAF-SYS-FUS-R4	The fuselage structure shall allow for integration of a center wingbox connecting the wingboxes of both wings.
LEAF-SYS-FUS-R5	The fuselage structure shall allow for integration of the empennage in the aircraft structure.

10.1.2. Size Constraints *Giorgio*

In order to optimise the volume capacity and the aerodynamic performance of the aircraft, the structure of the aircraft needs to be designed in such a way that they are integrated in the fuselage and wing sections.

Wing

For aerodynamic reasons, the wingbox will be integrated inside the wing shape, which will define most design boundaries. In Figure 10.2 the top view of the wing is observed with the wingbox boundaries, which are for the aft spar 65% of the chord and for the front spar 15% of the chord. Furthermore, the vertical boundaries will be the thickness of the wing at every chord section. This boundary will result in the top, and bottom panels will also act as the wing skin. Therefore it will need to have a smooth surface on the exterior side, and all the possible strength adding devices will need to be installed on the inside of the wingbox. The final cross-section of the wingbox can be seen in Figure 10.3:

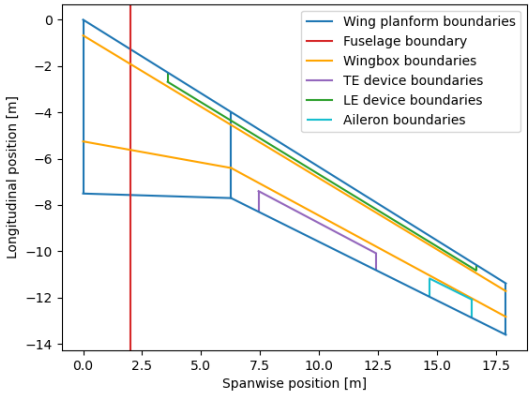

Figure 10.2: Top view of the wing

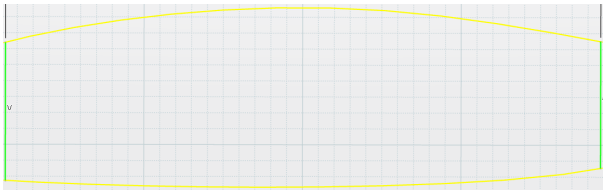

Figure 10.3: Wingbox sideview

Empennage

The empennage is a similar structure to the main wing, as both will have wingboxes integrated inside the wing shape. The front and aft spars will again be located at 15% and 65% of the chord, and will run through the entirety of the wing span. The aft limit is especially important, as it is required to leave space for the control surfaces for both vertical and horizontal stabilisers.

Fuselage

Finally, for the fuselage, a very important requirement is that the interior volume is unobstructed. This will allow to optimise the space for commercial use. Therefore the structure in the fuselage will have to be located around the diameter, which in previous sections has been set to 4.05 meters. Furthermore, the fuselage needs to integrate other structures such as the wingbox for the main wing, the wingbox for the empennage and the hydrogen storage tank situated in the tail of the aircraft. Finally, the airframe will need to be able to have cutouts for all the required openings such as cargo and passenger doors, windows, or the doors for the landing gear.

10.1.3. Loading Diagrams

Annemijn, Giorgio, Christoph

For the design the loads are analysed for the three main parts: fuselage, wings and empennage. Using the weight of the parts and the sizes estimated, the stresses acting on the parts can be simulated. Then various cases are used to calculate the load for these parts in python and are then merged in diagrams. For this analysis, seven general load cases were created in order to find the most critical situations which the structure will face:

- **LC-1** Taxi: aircraft on the ground with MTOW
- **LC-2** Takeoff: flaps deployed and weight equals MTOW
- **LC-3** Cruise: 20% of the kerosene used, and 40% of the hydrogen used
- **LC-4** Approach: flaps deployed, & 70% of the kerosene and 80% of the hydrogen used
- **LC-5** Landing: same weight as the approach, and a 2g impact on touchdown
- **LC-6** Pull up manoeuvre with the maximum n loading
- **LC-7** Nose dive with the most negative n loading

Wing loads

The first step in analysing any structure is to display all the possible forces acting on that specific part. In the wing there are two main forces that act via a point-load or a distributed load on the wing. First there is the weight of the wing and all the parts on the wing like the landing gear and engines which cause downwards shear and a bending moment. All the possible forces which will act on the wing during its lifespan in this direction are displayed in the free body diagram found in Figure 10.4. Secondly, the drag during flight causes shear and a bending moment in the wing in x-direction. The forces in this direction are shown in the free body diagram of Figure 10.5.

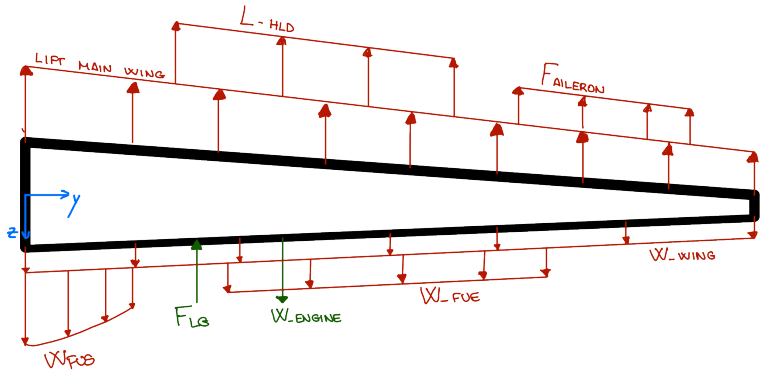

Figure 10.4: Free body diagram of the wingbox in yz-plane

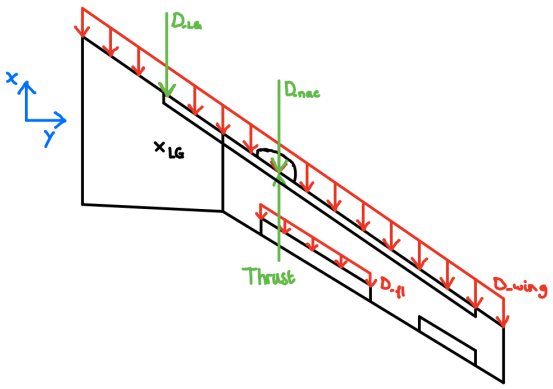

Figure 10.5: Free body diagram of the wingbox in xy-plane

In order to complete the loading diagram of the wingbox, two extra loading cases have been added to show the influence of the ailerons:

- **LCW-1** Cruise situation (LC-3) with full aileron actuation
- **LCW-2** Approach situation (LC-4) with full aileron actuation

The results of the analysis of forces in z-direction are displayed in Figure 10.6 to 10.10 for the shear, bending and torsion through the wingbox:

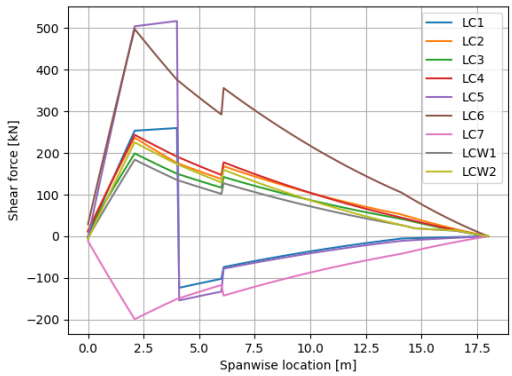

Figure 10.6: Shear through wingbox for different load cases

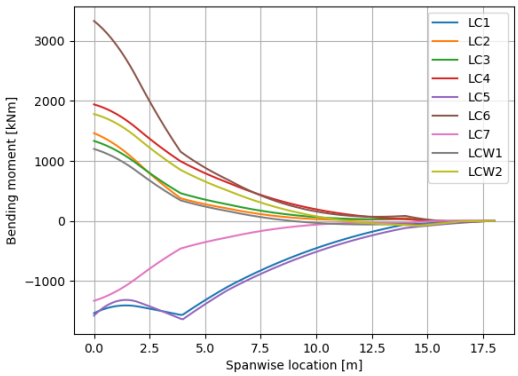

Figure 10.7: Bending through wingbox for different load cases

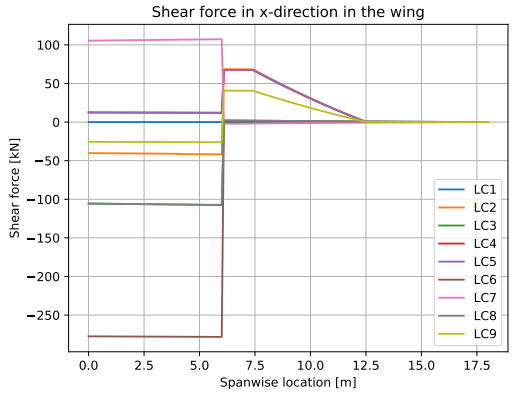

Figure 10.8: Shear due to forces in x-direction in the wing

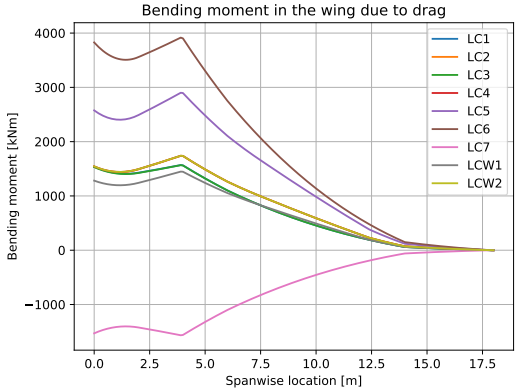

Figure 10.9: Bending moment due to forces in x-direction in the wing

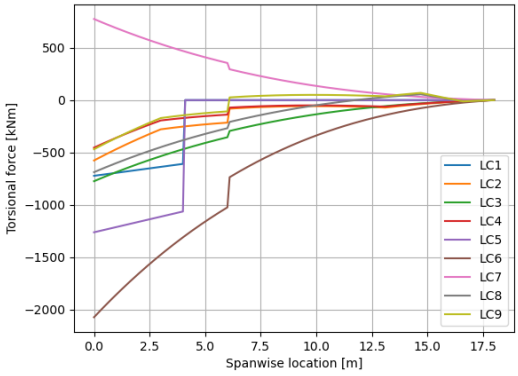

Figure 10.10: Torsion through wingbox for different load cases

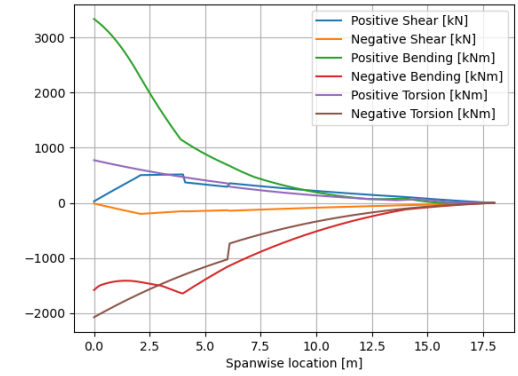

Figure 10.11: Maximum values for shear, bending and torsion

As seen on the graphs, the loading changes throughout the span of the wing. For the next steps, it is important to know the most critical forces at each section of the wing. For this reason, the most critical shear, bending and torsion forces have been displayed in Figure 10.11. These values will then help to calculate the stresses found in the wingbox.

Empennage loads

For the empennage, both the horizontal and vertical tail are analysed. For the horizontal, there are two shear forces and bending moments present. In Figure 10.12 the force due to the weight of the horizontal tail is drawn on the horizontal tail and on the vertical tail the loads in y-direction because of the rudder are drawn. The drag acting on both the horizontal and vertical tail is drawn in Figure 10.13. The forces in y-direction in the vertical

tail have two causes: the deflections of the rudder and the sideslip force. For all combinations of these, the shear force is analysed. The combinations are:

- Case 1: rudder to left, positive sideslip force
- Case 2: rudder in centre, positive sideslip force
- Case 3: rudder to right, positive sideslip force
- Case 4: rudder to left, no sideslip force
- Case 5: rudder in centre, no sideslip force
- Case 6: rudder to right, no sideslip force
- Case 7: rudder to left, negative sideslip force
- Case 8: rudder in centre, negative sideslip force
- Case 9: rudder to right, negative sideslip force

The shear force and bending moment because of the weight of the horizontal tail can be seen in Figure 10.14 and Figure 10.15. It can be seen that both increase when going from the tip to the root. The shear flows in z-direction and this bending moment is in the yz-plane. The loading diagram for the other shear force and bending moment, due to the drag that acts on the horizontal tail, is visualised in Figure 10.16 (x-direction) and Figure 10.17 (xy-plane).

For the vertical tail the shear forces caused by the rudder deflection and sideslip force which goes in y-direction are shown in Figure 10.19 for the cases listed above. Then in Figure 10.18 the shear due to the drag is plotted for the LC-1 to LC-7, these loads flows in x-direction.

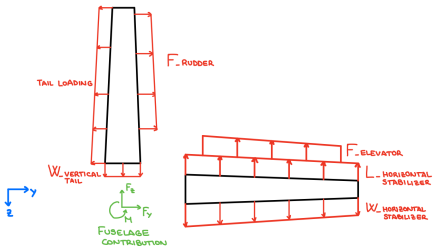

Figure 10.12: Free body diagram of the empennage in yz-plane

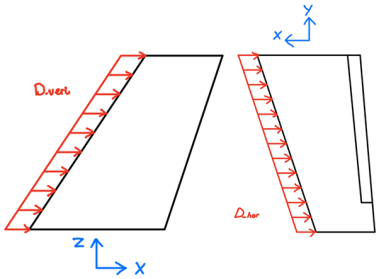

Figure 10.13: Free body diagram of the empennage due to drag

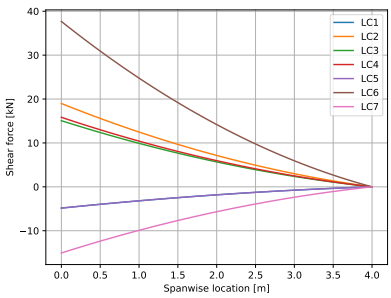

Figure 10.14: Shear force due to weight in the horizontal tail

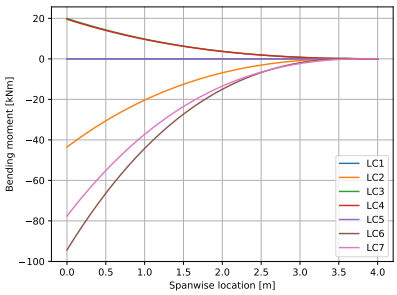

Figure 10.15: Bending moment due to weight in horizontal tail

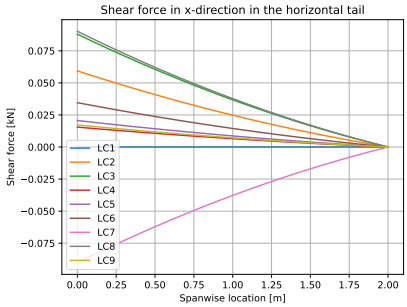

Figure 10.16: Shear force due to drag in the horizontal tail

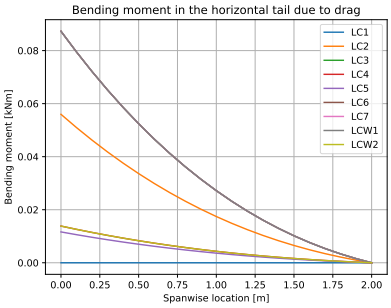

Figure 10.17: Bending moment due to drag in horizontal tail

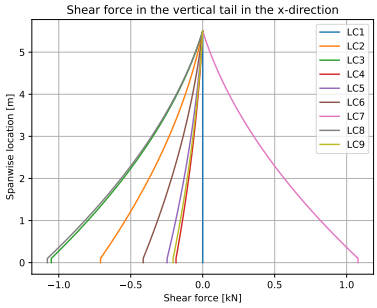

Figure 10.18: Shear force due to drag in the vertical tail

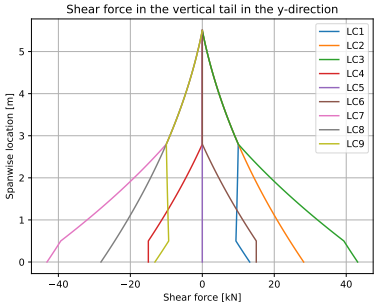

Figure 10.19: Shear force due to rudder deflections and sideslip force in vertical tail

Fuselage loads

The connecting structure of all parts is the fuselage, which means it has to carry multiple loads as seen in Figure 10.20. Different loading cases are considered for different forces acting on the fuselage. For the shear force in z-direction and the bending moment around the y-axis, which are shown in Figure 10.22 and Figure 10.23, the seven base loading cases from Subsection 10.1.3 as for the wings are used, as the main forces in that direction are the weight of the components and the lift of wing and horizontal tail. For the shear force in y-direction, the bending moment around the z-axis and the torsion moment, which are shown in Figure 10.24 to 10.26, the same loading cases as in the empennage are used, as the empennage exerts the main load for those loading cases.

For easier understanding of the loading cases, Figure 10.20 shows a free body diagram for all loads acting in z-direction and Figure 10.21 for all loads in y-direction on the fuselage. It must however be noted that the loads in y-direction were heavily simplified, due to the limited amount of time available and need to be calculated more in detail in future design stages. All the load from the side forces on the fuselage and tail were assumed to be transferred to the wing, even though parts of these forces should be transferred to the fuselage structure itself as well. However, this is a reasonable approximation still allowing a good overall image of the maximum loads acting on the fuselage, which are shown in Figure 10.27

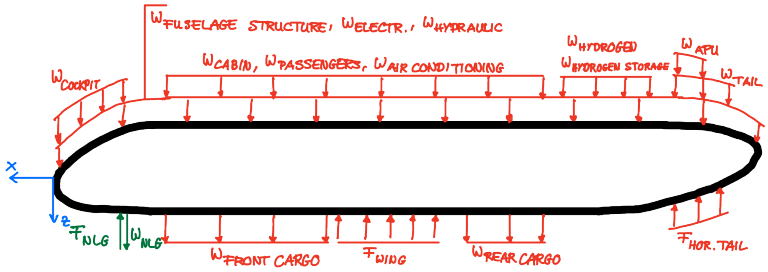

Figure 10.20: Free-body-diagram of the fuselage side-view

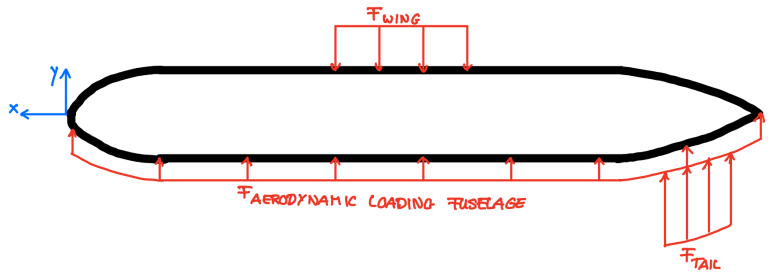

Figure 10.21: Free-body-diagram of the fuselage top-view

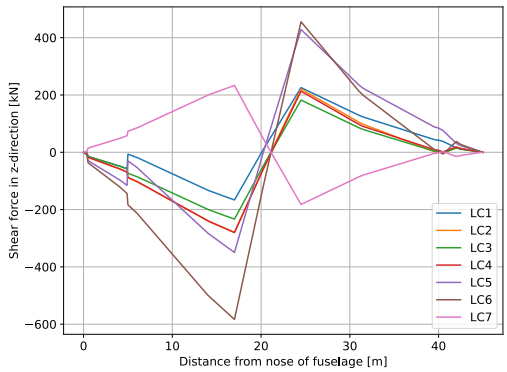

Figure 10.22: Shear force in z-direction acting on the fuselage

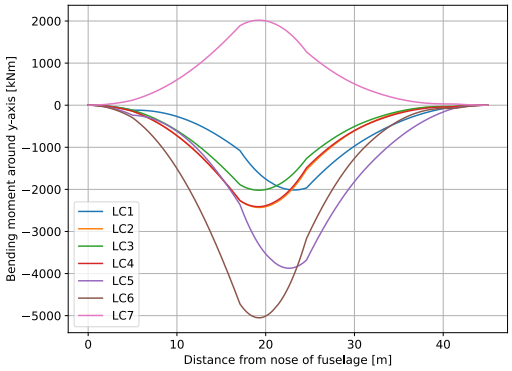

Figure 10.23: Bending moment around y-axis acting on the fuselage

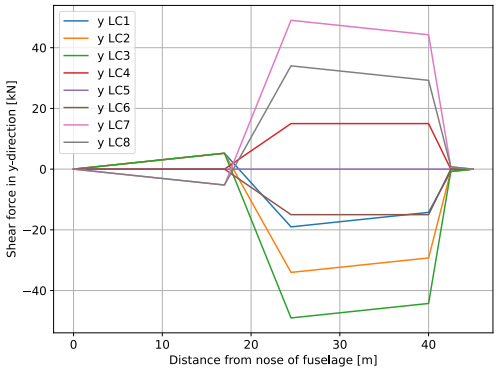

Figure 10.24: Shear force in y-direction acting on the fuselage

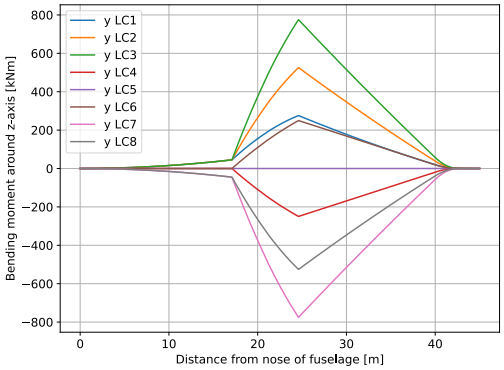

Figure 10.25: Bending moment around z-axis acting on the fuselage

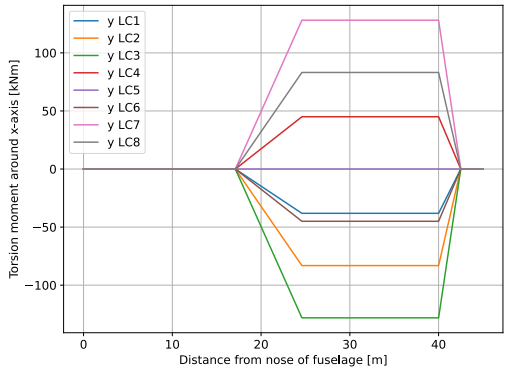

Figure 10.26: Torsion moment around x-axis acting on the fuselage

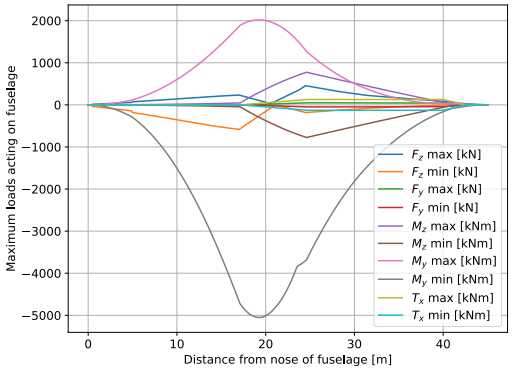

Figure 10.27: Maximum loads acting on the fuselage

Verification

It is crucial that along the designing process, the work done is verified in order to guarantee that the final design meets our expectations. For the structure of the aircraft, the first part of the code to be verified is the loading diagrams. In this section, the loads calculated will be compared to a simplified equation which will be calculated manually.

For the wingbox loading, the shear produced by vertical forces were analysed. For this, all the forces acting in the z-direction were summed and compared to the output of the program at the position y = 0. Through manual calculations, the value for the shear loads was 245 kN, while for the code, 249 kN. This difference is acceptable, as in the python program a lot more decimals are calculated at every step, resulting in a more precise value. A similar process was done with the bending loads, were the difference between numerical and computational

values were less than 8%.

For the fuselage, working of the loading diagrams has been verified by applying a simple point and distributed load (1200 N at 3 m and 2000 N from 5 m to 8 m) to the fuselage and calculating manually the shear force and bending moment from those forces at 10 m from the nose. Calculating by hand, at 10 m an internal shear force of 3200 N and a bending moment of $15\,400$ Nm was obtained, which is in line with the results shown in Figure 10.28 and Figure 10.29. As the complete loading diagrams are constructed with the same simplified method but a more complete list of the loads for the full fuselage, this method of verification was deemed sufficient to confirm working of the code. For the torsion diagram, the same method of verification was used, now applying a moment arm of 1.5 m for all forces. This gave a torsion moment of 4800 Nm at 10 m from the nose, which is again in line with the results produced by the code.

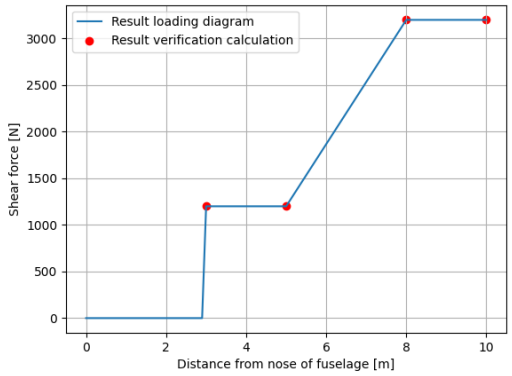

Figure 10.28: Verification of the shear force diagram

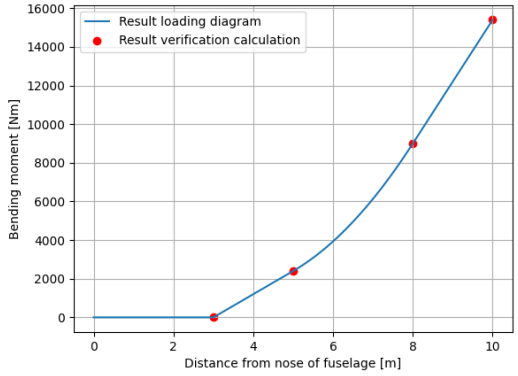

Figure 10.29: Verification of the bending moment diagram

10.2. Structural Analysis Procedure

After analysing carefully all the loads that are applied to the different sections of the aircraft, it is time to carefully design a structure capable of sustaining these loads to ensure the safety throughout the life cycle.
In order to design the best performing design, the maximum possible loads at every section from the different load cases were determined. A safety factor of 1.5 was then applied to these loads in order to account for possible manufacturing defects or for other random evens that could impact the structure. In the following sections, a more detailed look at every section will be explained, focusing on the required formulas and assumptions that will be used to come up with the final design.

10.2.1. Fuselage *Christoph*

Designing of the fuselage requires multiple different steps. First, the general design of the fuselage needs to be made. This consists of the fuselage skin thickness as well as the reinforcing elements, which consist both of stringers and frames. Furthermore, the cut-outs of the fuselage need to be designed. The most important cut-outs are necessary for the windows, the passenger doors (including the emergency exits) and the cargo doors. Finally, structural reinforcement is needed at specific locations in the fuselage in order to transfer the weight of the structural elements in the fuselage to the general fuselage structure.

Applied stresses on the fuselage skin

The fuselage is subject to different possible modes of failure. They can be divided in the modes of failure for the fuselage skin, the stringers as well as the frames in the fuselage. For the skin, the following modes of failure are analysed: the maximum shear strength of the skin, the ultimate strength of the material for sections of the skin loaded in tension, shear buckling as well as compression buckling of skin sections and crack propagation of possible undetected damage in the fuselage structure.

First, regarding shear strength and ultimate strength of the material, the maximum applied shear stress and ultimate stress on the skin is simply required to be lower than the maximum shear strength and yield strength of the skin material. The maximum stress in the skin is determined using equation 10.1 [77], where M is the applied moment on the fuselage, y is the distance of the skin to the neutral axis of the aircraft (which lies in the centre of the fuselage for an assumed symmetrical fuselage) and I is the moment of inertial of the fuselage structure with respect to the axis over which the bending moment is applied.

$$\sigma = \frac{M \cdot y}{I} \tag{10.1}$$

The applied shear stress on the skin is determined using a structural idealisation of the fuselage. For this, the stringers were modelled as booms which are carrying all normal stresses and the fuselage skin panels were assumed to carry all the shear stresses. For this idealised structure, 3 different shear flows could be calculated: The shear flow from a shear force V_y and V_z in y- and z-direction as well as the shear flow from a torque T applied on the fuselage.

The shear flow calculations from a shear force will be explained for a shear force V_z in the z-direction, but the method is the same for V_y. The method from [77] is used. For a shear force applied on the fuselage vertically in z-direction, the shear flow is first of all assumed to be 0 at the top center of the aircraft, which is in line with the applied shear force. Consequently, boom (which model the stringers) by boom, an additional shear flow Δq is added to the total shear flow. Δq for each boom is calculated using equation 10.2 [77], where I_{xx} is the moment of inertia about the x-axis, B_r is the area of the respective idealised boom (which is assumed to be equal to the stringer area) and y is the distance of the respective boom to centre line of the aircraft. If the method works correctly, after adding the shear flows for all booms, the shear flow should also be 0 for the centre bottom of the fuselage, as it was already for the centre top of the fuselage.

$$\Delta q_V = -\frac{V_y}{I_{xx}} \cdot B_r \cdot y \tag{10.2}$$

As was mentioned before, the same method is used for a shear force V_y in y-direction. Regarding the shear flow from a torque T applied on the fuselage, it can be simply calculated using equation 10.3. The area A used in this formula is equal to the enclosed area of the fuselage.

$$q_T = \frac{T}{2 \cdot A} \tag{10.3}$$

Having all 3 contributions for the shear flow calculated, the total shear flow of the fuselage can simply be calculated by summing all contributions as shown in equation 10.4. Finally, the shear stress applied on the skin will be calculate using equation 10.5 [77].

$$q_{total} = q_{V_y} + q_{V_z} + q_T \tag{10.4}$$

$$\tau = \frac{q}{t} \tag{10.5}$$

In addition to the stresses from shear, the fuselage is also subjected to stresses from pressurisation, most importantly in circumferential direction. This can be calculated using equation 10.6 [77], where Δp is the pressure difference applied to the fuselage, D is the diameter of the fuselage and t is the thickness of the fuselage. The used pressure difference Δp is equal to the difference of pressure between an altitude of $2400\,\text{m}$ and $11\,000\,\text{m}$.

$$\sigma_y = \frac{\Delta p \cdot D}{2 \cdot t} \tag{10.6}$$

Critical skin buckling stresses

Now, having the applied stresses determined, the critical stresses for buckling can be calculated. The formula for compression buckling of the aircraft skin is shown in equation 10.7 [77]. In this equation, η is the plasticity correction factor, which is equal to 1 in the linear elastic region. k is the compression buckling coefficient, which is equal to 8 for skin panels with an aspect ratio of more than 3. If the frame spacing is not 3 times larger than the stringer spacing, a new factor k needs to be chosen from [77]. Additionally, in order to determine the factor k, the edges of the skin panels in buckling are assumed to clamped both on the loaded and unloaded edge by the frames and stingers. Furthermore, E is equal to the modulus of elasticity and ν is the Poisson's ratio of the skin material. Finally, t is equal to the skin thickness and b is equal to the shorter side of the skin panel, which is the distance between two stringers on the fuselage.

$$\sigma_{CR} = \frac{\eta \cdot k_c \cdot \pi^2 \cdot E}{12 \cdot (1-\nu^2)} \cdot (\frac{t}{b})^2 \qquad (10.7)$$

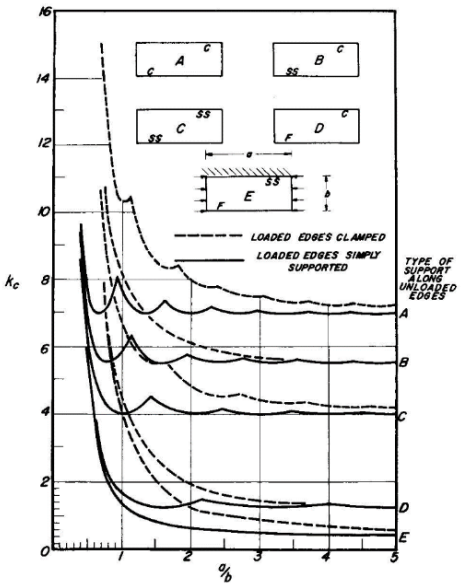

Figure 10.30: Buckling coefficients for plates under compression [78]

For the shear buckling, a similar equation is used. The critical shear buckling stress can be determined using equation 10.8. Most of the variables are still the same than for equation 10.7, but a different shear buckling coefficient k is used now. For a skin panel with clamped edges (which are assumed as already for the compression buckling coefficient) with an aspect ratio higher than 3, a shear buckling coefficient of 9.6 is found from [77].

$$\tau_{CR} = \frac{k_s \cdot \pi^2 \cdot E}{12 \cdot (1-\nu^2)} \cdot (\frac{t}{b})^2 \qquad (10.8)$$

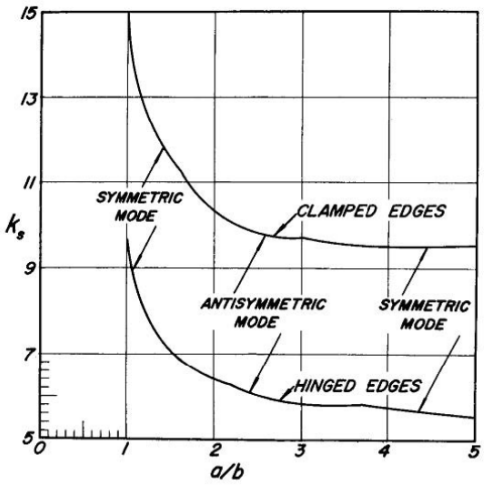

Figure 10.31: Buckling coefficients for plates under shear [78]

Fuselage skin crack propagation failure stress
Finally, next to the material strength and buckling resistance, also the possibility of undetected damage needs to be considered. In order to determine the critical failure stress at which the crack suddenly starts to propagate, equation 10.9 [79] is used. In this equation, K_1 is the fracture toughness of the skin material and c is equal to half of the width of the undetected crack.

$$\sigma = \frac{K_1}{\sqrt{\pi * c}} \qquad (10.9)$$

Applies stresses on the fuselage stringers
After having considered the different failure modes of the skin, now the stringers of fuselage are considered. The tension and compression stresses in the fuselage stringers are assumed to mainly originate from the bending moments M_x and M_y which are applied on the fuselage. Again, equation 10.1 can be used in order

to determine the bending stress acting on a stringer at the distance y from the neutral axis, with I being the moment of inertia of the fuselage cross-section. The applied stress on the stringer can then be compared to the tensile yield strength of the stringer material. For stringers in compression, the applied stress can be compared to the critical column buckling stress of a stringer, which will be discussed in the next subsubsection.

Critical column buckling stresses of fuselage stringers
In order to determine the critical column buckling stress of fuselage stringers, equation 10.10 [77] and 10.11 can be used. In equation 10.10, E is the modulus of elasticity of the stringer material, I is the moment of inertia of the stringer around its bending axis and l_e is the effective length of the stringer. The length considered in the case of the fuselage is the distance between 2 frames, to which the stringers are joint and do not only pass through using a cut-out in the frame. As the stringers are assumed to be pinned by the frames, a correction factor of 1 needs to be applied in order to obtain the effective length from the previously described length.

$$P_{cr} = \frac{\pi^2 \cdot E \cdot I}{l_e^2} \tag{10.10}$$

Equation 10.11 is then used, in order to determine the critical column buckling stress from the critical applied force on the stringers. In this equation, B is equal to the cross-section area of the considered stringer.

$$\sigma_{cr} = \frac{P_{cr}}{B} \tag{10.11}$$

Applied stresses on the fuselage frames
The fuselage frames are used for multiple purposes. They are spaced in order to limit column buckling loads of the stringers and section stringers and fuselage skin, but they also need to transfer the loads from all elements inside of the fuselage (as for example the cabin, the cargo, the hydrogen tank, etc.) to the fuselage structure and thus the stringers and skin. Thus, the frame is sized in order to resist all these loads.

In a first step, the shear and normal forces which are applied to the fuselage frame are calculated. Every force applied on the frame can be split into a shear and normal force component, according to the circumferential position at which the force is applied in the frame. In a next step, the shear stress from the internal shear force in the frame can be calculated, in order to determine if the frame can resist its applied loads. The shear stress can be determined using equation 10.12, 10.13 and 10.5. In equation 10.12, V is the internal shear force, Q can be determined using 10.13 and I is the moment of inertia of the frame. In equation 10.13, $\bar{y}$ is the distance from neutral axis of the stringer to the center of mass of the considered area for calculating the shear flow and A is the considered area. The maximum shear flow for symmetric stringers is expected on the neutral axis of the stringer, and therefore the top half of the stringer can be considered for equation 10.13.

$$q = \frac{V \cdot Q}{I} \tag{10.12}$$

$$Q = \bar{y} \cdot A \tag{10.13}$$

Hydrogen tank support structure
After having discussed the design of the fuselage frames, the hydrogen tank support structure can be discussed, which uses similar principles than the frame design. Different to all other frames, the frames around the fuselage are extended up until the fuselage skin in order to transfer the loads immediately from the fairing of the hydrogen tank to the fuselage skin and stringers. The frames therefore act like walls placed in the fuselage between tank and outer skin. The weight can then be simply transferred through the web of the frame. Therefore, in order to design the tank support structure, the same principles as for the frames are used, which were discussed in the previous subsubsection.

Bulkhead design
The bulkhead is designed in order to be able to resist the same pressure difference as the fuselage, as it is the end of the pressure cabin. Therefore, again the applied pressure difference is equal to the pressure difference between an altitude of $2400\,\text{m}$ and $11\,000\,\text{m}$. In order to determine the required thickness of the bulkhead, 10.14 and 10.15 [1] were used. In equation 10.14, P is equal to the applied pressure difference, D is equal to the fuselage diameter, K is determined using equation 10.15, S is the yield stress of the bulkhead material and E is the joint efficiency which is equal to 1. For equation 10.15, D is again equal to the fuselage diameter and h is the depth of the bulkhead.

$$t = \frac{P \cdot D \cdot K}{2 \cdot S \cdot E - 0.2 \cdot P} \tag{10.14}$$

$$K = \frac{1}{6} * 2 \left(2 + \left(\frac{D}{2 \cdot h} \right)^2 \right) \tag{10.15}$$

[1] URL https://www.cis-inspector.com/asme-code-calculation-elliptical-head.html [cited 15 June 2022]

Design of Fuselage Cut-Outs

In order to determine the reinforcements needed for cut-outs, the method explained in [77] is used. This method consists of changing the skin thickness of the panels around the cut-out and adding additional reinforcements around the cut-out to transfer the loads. As can be seen in Figure 10.32, first the general shear flow of the section of the cut-out q_{avg} is considered. From that, the shear flow of all panels around the cut-out is determined. First, the shear flow of the panels left and right as well as above and below of the cut-out is determined. This will be done by cutting the global panel over the cut-out, as can be seen in Figure 10.33. If the top and bottom as well as left and right panel have the same height or width respectively, the top and bottom as well as left and right panel are assumed to have the same shear flow. Therefore, q_2 and q_6 are calculated using equation 10.16. q_4 and q_8 can then be determined using the same method.

$$q_2 = q_6 = \frac{q_{avg} * (h_1 + h_2 + h_3)}{(h_1 + h_3)} \tag{10.16}$$

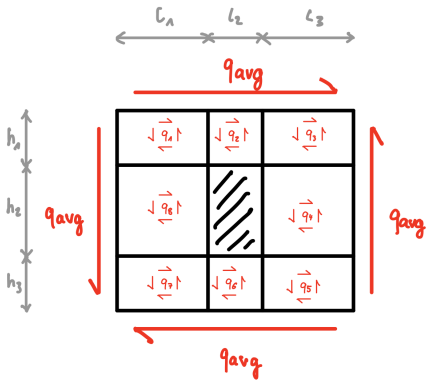

Figure 10.32: Overall image of example cut-out

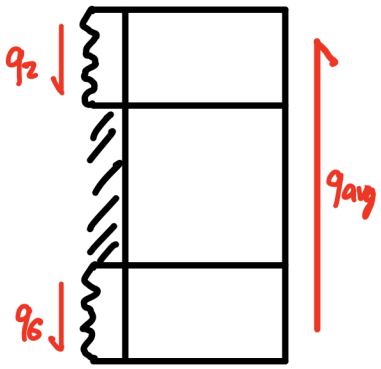

Figure 10.33: First cut of example cut-out to determine q_2 and q_6

If the width and height around the cut-out is constant, all corner panels have the same shear flow. It can be determined by cutting the side panels, as shown in Figure 10.34. Knowing q_4 already, q_3 and q_5 can be calculated using equation 10.17. The other corner panels have the same shear flow, as the cut-out has symmetric reinforcing.

$$q_3 = q_5 = \frac{q_{avg} * (h_1 + h_2 + h_3) - q_4 \cdot h_2}{(h_1 + h_3)} \tag{10.17}$$

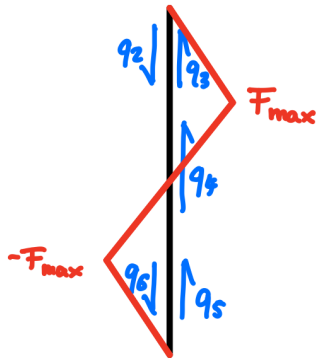

Figure 10.34: Second cut of example cut-out to determine q_3 and q_5

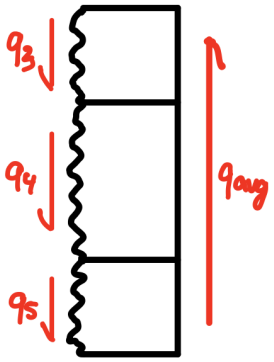

Figure 10.35: Force distribution in reinforcing stiffener next to cut-out

Finally, the force in the reinforcing stiffeners around the cut-out can be determined. This is done by adding up the shear flow from the touching panels multiplied by the height of the panels. The resulting force distribution is shown in Figure 10.35. The maximum force in the reinforcing stiffeners can be calculated using equation 10.18.

$$F_{max} = (q_2 - q_3) * h_1 \tag{10.18}$$

From the shear flows determined around the cut-out as well as the maximum forces of the reinforcing stiffeners around the cut-out, the structural elements can be designed. The thickness t of the panels can be determined using 10.5. Finally, the cross-sectional area A of the reinforcing stiffeners is determined using 10.19.

$$\sigma = \frac{F_{max}}{A} \tag{10.19}$$

10.2.2. Wingbox *Giorgio*

The main structure of a wing is called a wingbox due to its rectangular cross-section. This structure runs throughout the wingspan of the wing, and it transfers all the possible loads to the fuselage. A wingbox consists of a thin skin, stiffened by a combination of stringers, ribs and spar webs. This structure is present in all the wings present in the aircraft, so this process will be valid for the main wing and horizontal and vertical stabilisers.

As explained previously in Subsection 10.1.2, the wingbox will have to fit inside of the shape of the wing, therefore the top and bottom skins will coincide with the contour of the airfoil, and it will be closed off with a front and rear spars located at 15% and 65% of the chord to allow for the mounting of systems such as ailerons, high lift devices or landing gear mountings. The final cross-section of the main wing is displayed in Figure 10.3. This cross-section will be then extruded to complete the wing shape. Due to aerodynamic reasons, the wing shape has been given a sweep and a dihedral angle which will bring a certain level of complexity, which needs to be studied in more detail.

Sweep effect

The sweep of a wingbox results in the wing loads being at a bigger distance from the flexural axis, which means that most of these loads will be partly transformed into torsion. In order to help with the structural analysis, this effect will be simplified in order to get a first estimate of the wingbox geometry. It will be assumed that the wingbox is clamped to a structure which already accounts for the sweep as seen in Figure 10.36. This procedure will allow to analyse the structure as a straight wing while still retaining the correct angles of all the forces acting on it as seen in Figure 10.37.

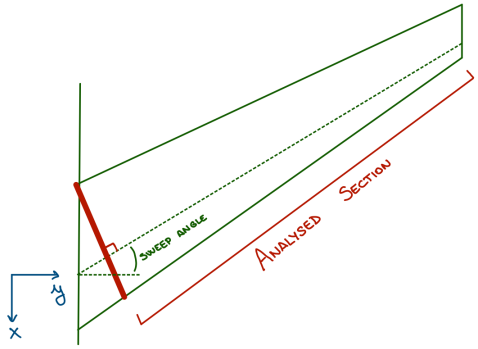

Figure 10.36: Top view of the Wingbox displaying the section used in structural analysis

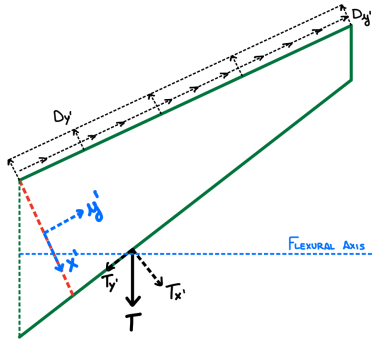

Figure 10.37: Example on the decomposition of forces acting on the wing

After applying this process to account for the sweep, these are the new moments with the new coordinate system that act on the wingbox which will be used to design the structure:

$$M_{y'} = M_y + M_x * \sin(\text{sweep}) + M_z * \sin(\text{dihedral}) \tag{10.20}$$

$$M_{x'} = M_x * \cos(\text{sweep}) \tag{10.21}$$

$$M_{z'} = M_z * \cos(\text{dihedral}) \tag{10.22}$$

The characteristics structure of the wingbox will be calculated looking at all the possible failure modes with a similar process to the fuselage. The first failure case would be regarding the maximum shear allowable shear flow. Using Equation 10.23, it is possible to calculate the minimum skin thickness of the wingbox:

$$\tau_{allow} = \frac{q_{tot}}{t} \tag{10.23}$$

$$q_{tot} = q_{torsion} + q_{shear_y} + q_{shear_x} \tag{10.24}$$

The next step is to check for web buckling. This will size the web plates in the front and the back of the wingbox. This analysis will output the required skin thickness and the number of required ribs throughout the span. For this the Equation 10.8, and the graph in Figure 10.31 are used. In order to find the buckling coefficient K_s, the a/b aspect ratio is used, which represents the ratio between the spacing between ribs and the height of the wingbox. The critical shear comes from the maximum shear in the z-direction (including the safety-margin).
Finally, some stringers are needed to prevent skin buckling. For this, the Equation 10.7 is used. Similarly to the web buckling, the coefficient K_c is derived with the a/b ratio. However, in this case, a refers to the distance between ribs, and b is the space between stringers.

10.3. Geometry

Geometry selection is of special importance when selecting the stringers, frames and ribs which will be used in the wingbox, fuselage and empennage structure. However, the choice will differ between the fuselage and the wingbox and empennage. Therefore, they will be treated separately in this section. Subsection 10.3.1 will first discuss the stringers and frame geometry used in the fuselage. Subsequently, Subsection 10.3.2 will discuss the geometry of the stringers and ribs in the wingbox.

10.3.1. Geometry in Fuselage *Christoph*

For the fuselage, mainly a geometry for the stringer and for the frame need to be selected. Different criteria were set up, in order to choose a good geometry. First of all, it was chosen that the stringers as well as the frames need to be manufactureable using simple sheet forming, in order to reduce manufacturing costs. Therfore, for example I-stringers were excluded from the beginning, as they cannot be manufactured from a continuous sheet. Another requirement was that every part of the stringer and frame, except the joining surface, shall be visible and inspectable and that no hidden surfaces should be present in the geometry. Most importantly, for both the frame and the stringer geometry, a geometry with a high moment of inertia for its size were required, in order to stiffen the structure as much as possible while adding the least weight possible.

Furthermore, the geometries should be easy to join, by having sufficiently large contact surfaces to which joints or adhesives can be applied. It should also be considered, that the stringers should be able to pass through the frame webs. Therefore, the frames were required to be at least 3 times higher than the stringers, in order to not be weakened too much by the required cut-outs. Finally, the overall height of the structure around the fuselage was limited to 10 cm, in order to not add too much to the diameter of the fuselage. Therefore, the frame was limited to a height of 8.5 cm, in order to allow for enough thickness for the fuselage skin and especially for the cabin wall. Respecting all the previously mentioned criteria, the stringer and frame shape shown in Figure 10.38 and Figure 10.39 are selected.

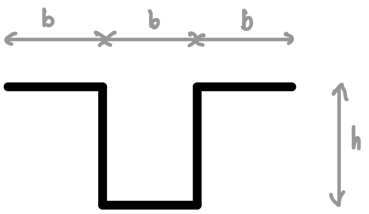

Figure 10.38: Fuselage stringer geometry

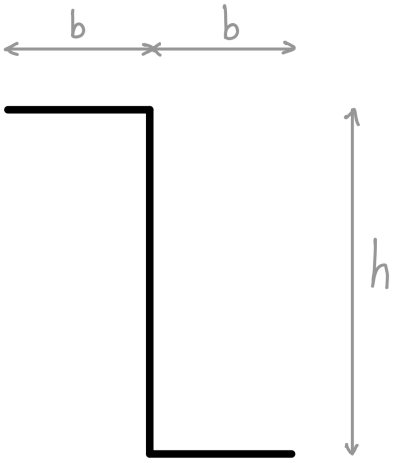

Figure 10.39: Fuselage frame geometry

Regarding the stringer, as shown in Figure 10.38, it can be seen that due to the top and bottom flanges, the moment of inertia is increased even for a small height of the webs. Additionally, another advantage of this stringer design is that no secondary bending is induced to the stringer due to its symmetric shape. The width b of all flanges was selected to be equal to 2 cm and the height h was limited to 2.5 cm, to have relatively small cut-outs in the frames. For the frame, the geometry shown in Figure 10.39 is chosen. Due to its height and the flanges on top and bottom, the geometry can have a relatively large moment of inertia for a small thickness and consequently weight. Furthermore, it was decided to only have one web on the stringer in order to easily design cut-outs in the frames. The width b of the flanges was now selected to be equal to 3.5 cm, whereas the height h was limited to the previously mentioned 8.5 cm, in order to allow for enough space for the fuselage skin and cabin wall, while still keeping the structural thickness of the fuselage below 10 cm.

10.3.2. Geometry in Windbox *Giorgio*

As explained previously in Subsection 10.2.2, a wingbox has different stiffening adding elements, mainly ribs and stringers. In this chapter both elements will be analysed in order to find the best possible design that will bring the best possible performance.

Stringers for wingbox
The main use of a stringer is to stiffen the wing skin to prevent buckling. This is done by increasing the mass moment of inertia. In Figure 10.40, some of the most used shapes for stringers are displayed. For the wingbox, the most used in the industry is the L-shape since it is a very simple shape to produce and install. Given the complicated nature of the wingbox assembly, the easy installation of L-shaped stringers would decrease the material and assembly cost, while still retaining the required performance.

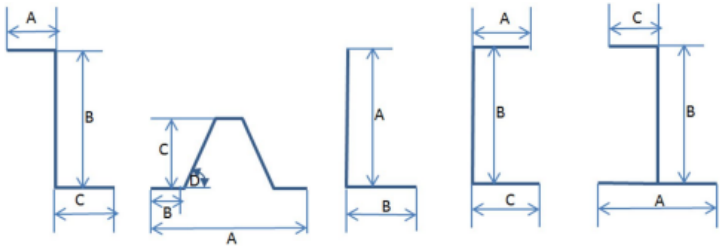

Figure 10.40: Possible shapes for stringers [80]

Ribs for wingbox
The ribs of the wingbox will be constructed with cross-section C-shape again to keep the manufacturing costs low and to reduce material waste. Furthermore, since the kerosene needs to flow through the wingbox, the ribs need to allow the passage of fluids. To solve this issue, the ribs will have cutouts as seen in Figure 10.41:

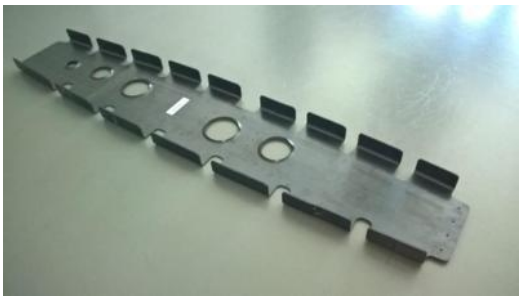

Figure 10.41: Structural rib[2]

10.4. Material

Annemijn

Material selection is of significant importance for the design of this aircraft. Besides the standard requirements that the material should be able to handle the loads on that specific part where the material is applied, sustainability requirements have to be met. To design as environmentally friendly as possible, it has to comply with requirements RAP-ENV-SUS-04 and RAP-ENV-SUS-05 in Table 10.1. These requirements state that at least 90% of the aircraft parts shall be recyclable and 5% of the aircraft parts shall be reusable at end-of-life. So, it is desired that the materials used have an end-of-life option that is in the upper side of the table of Figure 10.42.

10.4.1. Material Options

It is known that the aircraft requires light and also strong materials. The extra requirement that the LEAF aircraft has is that now 90% of its mass must also be recyclable. The amount of material required varies by aircraft part, and is frequently determined by the item's maximum load. First a selection is done using Granta EduPack [58] by comparing the following specific properties (E being the Young's modulus and G being the shear modulus) in the charts:

- $E^{1/2}/\rho$
- G/ρ

End-of-Life option	Description
Reuse	Extension of product life
Re-engineer	Incorporation of re-engineered part into new product
Recycle	Reprocessing of material into primary supply chain
Downcycle	Reprocessing into a lower grade material
Combustion	Recovery of the calorific content of the material
Landfill	Disposal of material

Environmental burden increase

Figure 10.42: for parts at end-of-life phase as stated in the EduPack software [58]

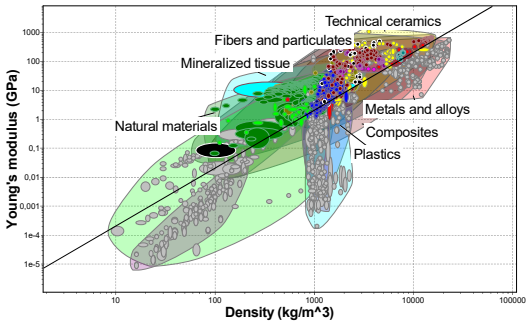

Figure 10.43: Material plot with line indicating $E^{1/2}/\rho$

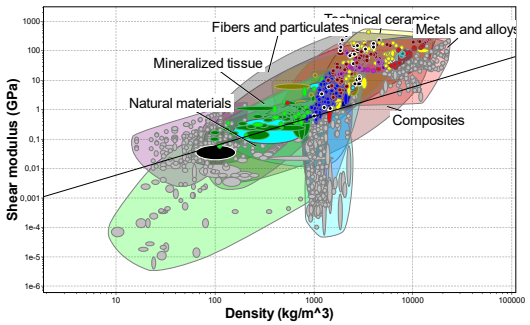

Figure 10.44: Material plot with line indicating G/ρ

Now, in a Python file with material properties, the group of materials that perform well in both properties will be presented as input. These values are tested with load cases for different parts of the aircraft.

10.4.2. Recyclability of the Materials

When the end-of-life phase is reached, the aircraft must be dismantled carefully so that all parts can be sorted per alloy or composite, or complete part. The options for the sorted materials are then again the same as in Figure 10.42. Ideally, a part would be reused because it uses the least amount of energy. However, if this is not possible and the material can be recycled, it will be recycled.

Metal Alloys

One of the main reasons why recycling of materials is important if for instance, aluminium production from a recycled element costs 2.8 KWh/kg while raw aluminium production costs approximately 45 KWh/kg [81]. The problem with employing a secondary metal is that it may have impurities that do not adhere to the rigorous criteria. Additional processes are used to get rid of these impurities. The chance of imperfections can also be reduced by using paint or coverage which does not affect the material and can be removed in the end. Often clad metals are used to have a better resistance to corrosion. When melting a metal after end-of-life, two different alloys are mixed, which results in it not being recyclable for the same purpose. This method of having a good resistance to corrosion will thus be avoided.

Composites

Because the technology for recycling composites is still in its infancy, the simplest solution would be to use metal alloys. However, using carbon-reinforced composites can make the aircraft significantly lighter so this would increase the efficiency which is desired. Therefore methods to recycle composites are investigated. For the material selection upcoming methods are reviewed to estimate which composites have the possibility of being recycled by 2035. Various methods are found [3] so it could be possible that recycling will be possible for some fibers and resins by 2035. Recycable resins that exist are eco-resin, silicone resin, and epoxy resin [4]. At the same time, there are three type of resins used for carbon fibre composites: epoxy, vinylester and polyester resins. Because epoxy is the only one recyclable and with best properties, this resin would be used for composites in the aircraft [5]. As a result, it is uncertain whether recycling procedures will be fully developed by 2035, hence it will score lower in the trade-off than materials that can already be recycled.

Downcycling

Finally, there are a few materials that cannot be recycled aircraft use, so they will be down-cycled. These are the rubber of the tires, windows, wire plastic covering and interior components such as the curtains, overhead bins and safety gears. Nevertheless, for example the curtains and overhead bins can be made of recycled material or biodegradable material, thus complying with the objective statement. For every part that has to be downcycled, a solution will be investigated to make it from recycled or biodegradable material.

10.4.3. Reusable parts

To fulfil the requirement that 5% of the aircraft parts shall be reused at the end-of-life, reusable purposes for reuse must be investigated. Many structural sections contribute to the end-of-life of the aircraft because they

[3] URL `https://www.aviationtoday.com/2021/03/15/new-research-improve-recycling-remanufacturing-commercial%2Dairplane-carbon-fiber/` [cited 13 June 2022]

[4] URL `https://www.conserve-energy-future.com/is-resin-recyclable.php` [cited 13 June 2022]

[5] URL `https://www.sollercomposites.com/EpoxyResinChoice.html` [cited 13 June 2022]

have reached the end of their fatigue cycle and can no longer be used. As a result, parts that are still functional towards the end of life must be considered. The interior is frequently still in good condition. The seats may need to be reupholstered, but the frame can be reused in a new plane. Some cockpit measurement instruments are also the same as they were years ago, thus they can be utilised in modern aircraft if their technology has not changed. Safety measures such as escape slides and oxygen masks can be reused if they have not been use and are inspected and updated as needed.

10.4.4. Selection of Materials

For the final selection of a material, a trade-off is performed. The criteria set are the density, Young's-modulus, shear-modulus, costs, corrosion resistance and the ability of recycling. The columns in the trade-off table are scaled according to the weight of the criteria. The values where the scores are based on are retrieved from the material data base [58]. The cost is an estimation of the properties *E/(specific cost per kg)* and of *G/(specific cost per kg)*.

Table 10.5: Trade-off for materials

Option \ Criteria	Density	E-modulus	G-modulus	Cost	Corrosion resistance	Recyclability	CO_2-footprint	Score
Al 7075 T6	(3)	(3)	(3)	(3)	(2)	(4)	(4)	3.05
AL 2024 T3	(3)	(3)	(3)	(3)	(1)	(4)	(4)	2.9
AL 7149-T73	(3)	(3)	(3)	(3)	(3)	(4)	(4)	3.2
AL 7085-T7452	(3)	(3)	(3)	(3)	(3)	(4)	(4)	3.2
Stainless steel, 304	(1)	(4)	(4)	(4)	(2)	(4)	(4)	2.95
Stainless steel, 304L	(1)	(4)	(4)	(4)	(2)	(4)	(4)	2.95
Stainless steel, 15 5PH	(1)	(4)	(3)	(4)	(4)	(4)	(4)	3.1
Ti6Al4V	(2)	(4)	(3)	(2)	(2)	(4)	(3)	2.75
Ti8Al1Mo1V	(2)	(4)	(3)	(2)	(3)	(4)	(3)	2.9
Ti6Al2Sn4Zr2Mo	(2)	(4)	(3)	(2)	(3)	(4)	(3)	2.9
Ti5Al2Sn2Zr4Cr4	(2)	(4)	(3)	(2)	(2)	(4)	(3)	2.75
Ti15V3Cr3Sn3Al	(2)	(4)	(3)	(2)	(2)	(4)	(2)	2.65
Ti10V2Fe3Al	(2)	(4)	(3)	(2)	(2)	(4)	(2)	2.65
Epoxy/CF 1	(4)	(3)	(2)	(1)	(4)	(1)	(1)	2.65
Epoxy/CF 2	(4)	(3)	(2)	(1)	(4)	(1)	(1)	2.65
Epoxy/CF 3	(4)	(3)	(2)	(1)	(4)	(1)	(1)	2.65
Epoxy/CF 4	(4)	(3)	(2)	(2)	(4)	(1)	(1)	2.9
Epoxy/CF 5	(4)	(3)	(2)	(1)	(4)	(1)	(1)	2.65
Epoxy/CF 6	(4)	(3)	(2)	(2)	(4)	(1)	(1)	2.75

Multiple materials emerged as one of the best-suited materials as a result of the material trade-off. Not all parts need to be made out of the same material of course, but to stay in the scope of the project the aircraft is divided in three main components. These are the fuselage, wingbox and the empennage. As can be seen, carbon-epoxy composites would perform well on an aircraft due to their low weight and high strength. However, with the current technology, they cannot be recycled and still have an undesirably high footprint.

Fuselage

For the fuselage, Al 7075 T6 is chosen as best material. This may not immediately be clear from the table due to a lower corrosion resistance compared to other forms of aluminium. However, the fuselage will be coated with paint, to ensure that the fuselage's skin is resistant to corrosion caused by water or chemicals in possible spilled fuel thus this property will not be disadvantageous in this case. When looking better into materials that scored high, this material has the highest yield strength which is desired for a fuselage. It is therefore concluded to use Al 7075 T6 for the fuselage.

Wingbox and empennage
Not every part of the wingbox is exposed to the environment, however this means that not every part is covered in paint. This material thus has to have a higher resistance to corrosion than for the fuselage. Four aluminium alloys have an excellent resistance to corrosion as can be seen in Table 10.5. Out of these four aluminium alloys, Al 7149 has the highest Young's modulus and shear-modulus, hence it is selected as the wingbox material. For the same reasons and with assumption for now that empennage requires high Young's modulus and shear-modulus as well and having to cope with corrosion, Al 7149 is chosen for the empennage likewise.

Table 10.6: The best materials from the trade-off

Property / Material	**Density** [kg/m^3]	**E-modulus** [GPa]	**G-modulus** [GPa]	**Cost** [€/kg]	**Poisson ratio**	**Yield strength** [MPa]	**Shear strength** [MPa]	K_{Ic} [MPa]
Al7075 T6	2770	69	26	3.32	0.325	460	331	26.6
Al7149	2840	70	27	3.32	0.33	379	379	25
Al7085	2850	69.6	26.9	3.35	0.33	427	254	29.6

10.4.5. Sensitivity Analysis
To verify that the outcome of the trade-off for the material selection is acceptable and to show how stable the trade-off is, a sensitivity analysis was conducted. In the sensitivity analysis simulation, two parameters were changed compared to the original trade-off in Subsection 10.4.4. These parameters that change are the weights and the criteria. For the weights all possible combinations of dividing the total weight of one over all criteria are analysed. For varying criteria, combinations are made were different criteria are left out and then used for the trade-off. The result of the analysis for varying weights and criteria is shown in Figure 10.45 and Figure 10.46 respectively. The orange horizontal lines show the average after varying weight and it can be seen that this influences the outcome quite a lot. These fluctuations are ought to be caused by having many options and criteria. To avoid this, there could have been multiple, more specific trade-offs, for example one for aluminium alloys, one for stainless steels etc. This is advised for later design to get trade-offs that are more stable.

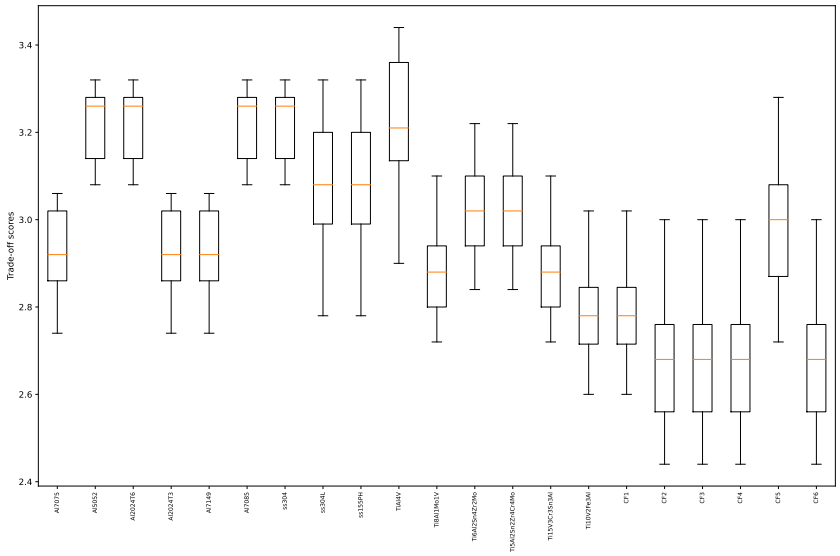

Figure 10.45: Plot of trade-off outcomes when varying weights

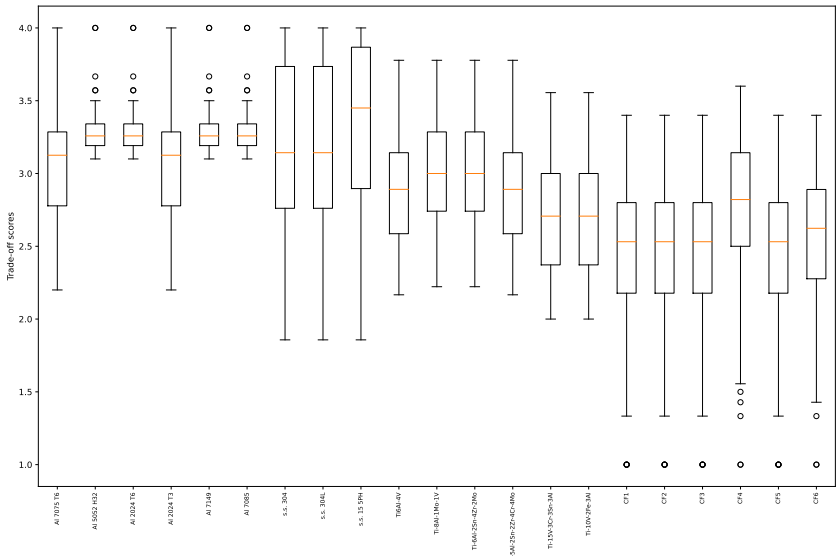

Figure 10.46: Plot of trade-off outcomes when varying criteria

10.5. Final Design

Having all the loads on the fuselage calculated, the methods for designing the geometry defined and the materials and geometries selected, the final aircraft structure can be developed. In this section, first the fuselage design is discussed in Subsection 10.5.1. Subsequently, Subsection 10.5.2 presents the wingbox and empennage design.

10.5.1. Fuselage Design *Christoph*

In Subsection 10.2.1, the methods for designing the fuselage structure are described. In this subsection, the flow of designing the fuselage structure will be described. Furthermore, the verification procedure of the design tools is presented. Finally, the final fuselage structure and mass distribution is shown.

Design Procedure

The first step of designing the structure of the fuselage is to define the skin thickness as well as the stringer placing and thickness. The skin and stringer set-up was chosen to be constant around the fuselage circumference, in order to resist all possible loading cases in all directions. The considered failure modes at this step were yield and shear strength of the skin, crack propagation on the skin, as well as shear buckling of the skin. The choice of configuration has been done in an iterative procedure. For a specific range of stringer thicknesses and distance between stringers, the minimal skin thickness was determined. From all the generated options, the option with the lowest total mass per meter of fuselage was determined and was chosen as configuration.

It must be noted that the fuselage was split in 5 sections with different skin thicknesses, as the loads were observed to be lower on the front part of the fuselage than on the rear part, where the loads from the tail are introduced. However, the stringer configuration is constant, in order to have continuous stringers over the fuselage. In general, the fuselage is sectioned after the tail-cone, before the wing root leading edge, after the wing root trailing edge and at the bulkhead, in order to allow the hydrogen tank behind the bulkhead to be easily replaced by just separating the fuselage again where it was joined.

In a next step, the frames are placed (but not sized yet) along the fuselage. This is done in order to avoid compression buckling of the skin as well as column buckling of the stringers. Additionally, some frame locations are required already by the internal configuration of the aircraft, such as at the end of the cockpit, around the hydrogen tank, at the location of galleys in the aircraft. These are considered when placing all remaining frames.

Having placed all the frames, theses can now be sized according to the load they are introducing in the fuselage structure. This can be done by calculating the shear and normal forces in the frames, as was described previously, determining the maximum shear flow and thus determining the required thickness from the shear strength of the material. A different frame size was chosen for the frames before and after the bulkhead, as they are required to transfer very different loads. It was also considered, that the radius of the fuselage decreases

at the tip and tail of the fuselage.

Having all the skin, the stringers and the frames designed, the required reinforcements for cut-outs can be sized. This is done according to the method described previously and the size of the respective cut-outs. The reinforcements were designed for the windows, the passenger doors, the emergency exits and the cargo doors. Finally, the bulkhead thickness was determined, in order to finalise the fuselage structure.

Verification

Before determining the final design, the code for fuselage design needed to be verified. First, the code for calculating the shear flow distribution around the fuselage was verified. For this, an example cross-section of the fuselage was subjected to a vertical shear force of 1000 N and a torsion moment of 400 Nm. This cross-section was simplified with a radius of 2 m and consisted of 8 booms with a cross-section area of 0.0001m^2 at $30\,°$, $60\,°$, $120\,°$,$150\,°$, $210\,°$, $240\,°$, $300\,°$ and $330\,°$ from the top of the fuselage. The shear flow distribution around the fuselage was then calculated by hand and it was seen that the shear flow from torsion is equal to 15.9 N/mm, the first boom adds a shear flow of 108.3 N/mm and the second boom a shear flow of 62.5 N/mm. This leads to the same maximum shear flow of 186.7 N/mm as produced by the code and seen in Figure 10.47. Furthermore, the shear flow was plotted for the whole fuselage under the applied loads in Figure 10.48. As expected, the highest shear flows are located at and behind the wing root. Furthermore, the shear flow is lowest in front of the wing, which was expected beforehand. Therefore, the code is considered to provide a reasonable output.

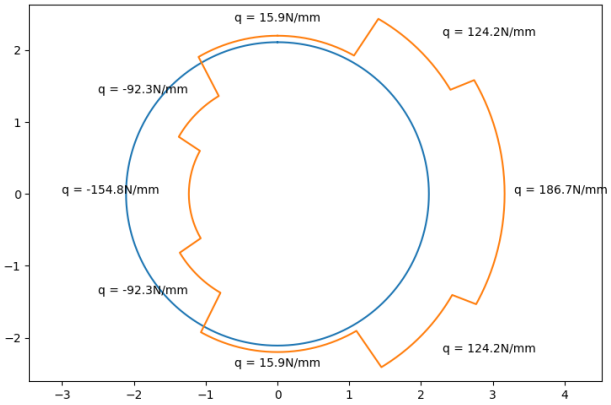

Figure 10.47: Shear flow diagram for verification

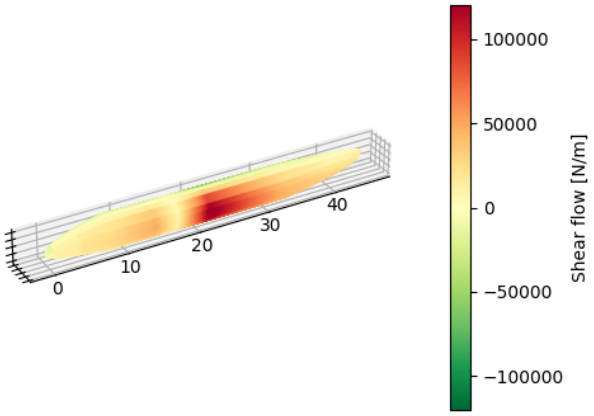

Figure 10.48: Shear flow distribution on fuselage

Next to the code for the shear flow, also the code for the stresses in the stringers from bending of the fuselage need to be verified. This was done by calculating the stresses for selected stringers in an example cross-section of a fuselage (8 stringers with a cross-section of 100mm^2 ($30\,°$, $60\,°$, $120\,°$,$150\,°$, $210\,°$, $240\,°$, $300\,°$ and $330\,°$ from the top of the fuselage), radius of 2 m and thickness of 0.001 mm) using the methods from [77] for a moment of 1000 Nm. The stresses in stringer at $30\,°$ were calculated to be equal to 64.837 kPa and in the stringer at $60\,°$ equal to 37.434 kPa, both by hand and in the code. This consistency of results verified that the stresses for bending moments in the stringers are correctly calculated for the fuselage cross-sections.

Regarding the buckling formulas, they were verified by calculating the critical buckling loads for random skin panel sizes as well as stringer geometries. The results from the buckling functions implemented in the code were then compared to the results by calculating the critical buckling loads by hand, using the equation from [77]. Both methods showed the same results and the buckling functions were concluded to be verified.

Furthermore, the method for calculating the shear and normal stresses in a fuselage frame needed to be verified. This was done by assuming a weight of 6000 N which is connected at 6 equally spaced locations to the frame ($0\,°$, $60\,°$, $120\,°$, $180\,°$, $240\,°$ and $300\,°$ from the top centre). At all locations, it inserts a vertical force of 1000 N in the frame. The resulting shear and normal forces in the frame are shown in Figure 10.49. At $0\,°$, a force of 1000 N is inserted, which is equally distributed over the left and right part. Therefore a shear force of 500 N is observed in the plot. The shear force is increased at $60\,°$ to 1000 N, as $1000\text{N} \cdot \cos(60°)$ of the force is inserted as a shear force, the remaining part of the force ($1000\text{N} \cdot \sin(60°)$) explains the jump in the normal force of the frame. The slopes observed in the curve of the normal force are explained by the continuous transferred forces between the frame and the fuselage skin and stringers. The calculation for the shear flow in the frame itself was verified by calculating the shear flow by hand using the methods from [77] and comparing it to the output of the code.

Finally, the calculation for the reinforcements around the cut-outs needed to be verified. This was done by

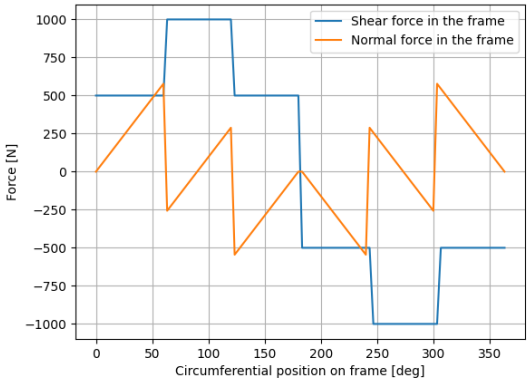

Figure 10.49: Verification of the internal forces in the frame

checking static equilibrium of all forces around the cut-out for an example cut-out, which was chosen to be the cut-out of a window. The verification procedure confirmed static equilibrium of all forces in the reinforcing stringers and skin panels around the cut-out and therefore demonstrated correct working of this code.

Final Fuselage Design

The final structural design of the fuselage has been determined according to the methods described in the previous sections and subsections. It consists of a circular fuselage with 108 stringers equally spaced around the fuselage. The stringers have the shape shown in Figure 10.38 and a thickness of 0.8 mm. The thickness and minimum required frame spacing is varying over the fuselage length over the five different sections, as shown in Table 10.7.

Table 10.7: Fuselage lay-out for 5 sections

Section	0m - 8m	8m - 12m	12m - 23m	23m - 32m	32m - 45m
Skin thickness [mm]	0.942	1.069	1.535	1.473	1.109
Required minimum frame spacing [m]	2.026	1.346	0.991	1.123	1.845

Regarding the frames, a constant frame spacing was chosen for the part in front and behind the bulkhead respectively. The minimum required frame spacing, as shown in Table 10.7, only shows the frames to which the stringers need to be pinned, in order to avoid column buckling. More frames might, however, be needed to ensure structural integrity of the aircraft. Therefore, for the part before the bulkhead, a frame spacing of 0.495 [m] was chosen, in order to have one frame between all windows. The stringers are pinned to every second frame, every other frame simply uses cut-outs. Table 10.7 suggests that the stringers only need to be pinned at every fourth section in the cockpit. However, the stringers in the cockpit section need to resist more compression loading from the frontal loads on the cockpit and are therefore also pinned to every second frame. Finally, for the part behind the fuselage, the frame spacing is equal to 0.649 [m] and the stringers are pinned to every third frame.

For the size of the frames, a thickness of 0.118 mm was determined to be required for the frames in front of the bulkhead and of 0.160 mm for the frames behind the bulkhead. However, such a small thickness was considered to be very difficult to manufacture. Therefore, it was decided to use the same thickness than for the stringers (0.8 mm), also in order to reduce the amount of different metal sheets required. The same thickness was also used for the 7 frames which are used as hydrogen tank support structure and transfer the loads from the hydrogen tank to the outer fuselage structure.

Furthermore, Table 10.8 shows the design of the cut-outs in the fuselage. It shows both the outer dimensions of the cut-out and the outer dimensions of the reinforced section. Additionally, it shows the thickness of the panels above and below the panel, right and left of the panel, in the corner panels as well as the cross-section area of the 2 horizontal and 2 vertical reinforcement stringers around the cut-out. Finally, the bulkhead has been determined to have a required thickness of 2.857 mm due to the maximum pressure difference applied to it.

Table 10.9 summarises the most critical failure modes for the different structural components of the fuselage.

As can be seen, often buckling is the most critical, especially for the fuselage skin. This is beneficial for operation, as it is easy to observe while not creating critical damage to the structure immediately. Additionally, this table can be useful, in order to know what failure mode could require special attention during inspection.

Table 10.8: Cut-out reinforcements

Cut-out	Width Reinf. [m]	Height Reinf. [m]	Width Cut-O. [m]	Height Cut.-O. [m]	Thickness top/ bottom [mm]	Thickness left/ right [mm]	Thickness corner [mm]	Area reinf. hor. stringer [mm^2]	Area reinf. vert. stringer [mm^2]
Windows Section 1	0.945	0.491	0.258	0.368	1.391	1.324	0.963	17.292	20.624
Windows Section 2	0.945	0.491	0.258	0.368	1.566	1.489	1.075	26.294	31.359
Windows Section 3	0.945	0.491	0.258	0.368	2.201	2.087	1.477	83.930	100.099
Windows Section 4	0.945	0.491	0.258	0.368	2.116	2.007	1.423	73.562	87.734
Front PAX door	1.485	2.210	0.990	2.087	2.046	1.464	2.392	251.785	167.602
Rear PAX door	1.485	2.210	0.980	2.087	3.178	2.221	3.701	1060.284	698.868
Emergency exit	0.990	1.105	0.500	0.982	2.715	2.065	2.344	324.844	257.811
Cargo front	2.475	1.719	1.820	1.596	2.161	1.765	2.772	555.658	245.466
Cargo rear	2.475	1.719	1.820	1.596	2.954	2.396	3.814	1554.552	686.734

Table 10.9: Critical failure modes of fuselage structural components

Structural element	Critical failure mode
Fuselage skin	Shear buckling
Stringers	Column buckling
Frames	Exceeding maximum shear strength
Bulkhead	Exceeding yield strength
Cut-out	Shear buckling
Hydrogen tank support	Column buckling

Finally, Figure 10.50 shows the mass distribution of all the different components of the fuselage structure. As can be seen, the fuselage skin is with 2100.17 kg by far the heaviest part of the structure. Stringers and frames both have a weight about 1000 kg. The bulkhead as well as the support structure of the tank have negligible weights smaller than 150 kg. The distribution of the structural weights is comparable as well to those of an A320, which has a weight of 2196 kg for the skin panels, 598 kg for the stringers and 1399 kg for the frames[6]. Additionally, it must be noted that the reinforcements for the cut-outs even slightly decrease the weight by 49 kg. However, the weight will be significantly increased again, when adding the weight of the windows and doors themselves, which are however considered out of the scope of this report. Finally, the fuselage has an outer diameter of 4.22 m and a overall length of 45 m.

[6]URL https://www.dlr.de/fa/Portaldata/17/Resources/dokumente/institut/srw_10.pdf [cited 16/06/2022]

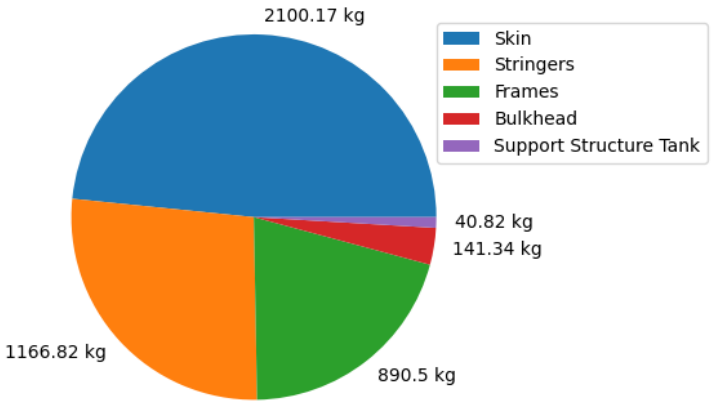

Figure 10.50: Mass distribution of fuselage structure components

10.5.2. Wingbox Design

Giorgio

After carefully selecting all the elements for the wingbox construction, the analysis explained in Subsection 10.2.2 can start. First all the structure regarding the main wing will be explained, followed by the design for the empennage.

Main wing

The first step is to calculate the minimum required thickness in order to withstand shear flow. This is done with the Equation 10.23, and the results give an average thickness throughout the span of 0.6 mm, with a maximum value at the root of the wing of 1.2 mm. This thickness distribution can be seen in Figure 10.51.

Next, the spar webs were sized, resulting also in the amount of ribs needed in order to withstand the bending moment produced by the vertical forces such as lift or weight of the engines and wing. In order to optimise the design, the thickness of the spar webs was decided to 8 mm in order to get the optimal amount of ribs such as to have the lightest possible design. The rib distribution can be seen in Figure 10.52.

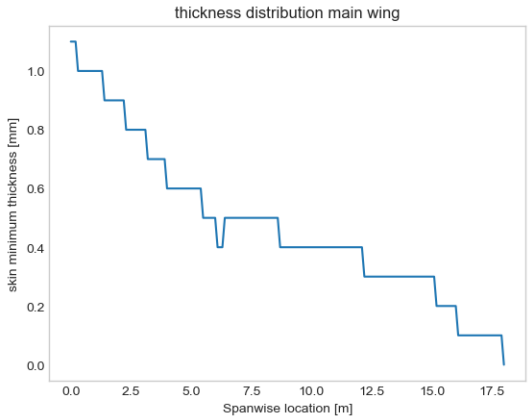

Figure 10.51: Required thickness distribution according to shear flow calculations

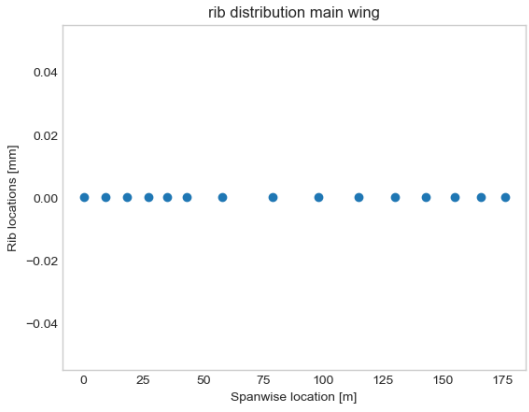

Figure 10.52: Required rib distribution according to bending stresses

Finally, in order to prevent skin buckling, the stringers will be placed both on the top and bottom skins. Given that the loads at the tip and at the root of the wing will be different, the number of stringers will vary through the span. For this, the wingbox will be divided into sections, and the ribs will be used as divider between them. Similarly, the top and bottom skins will have different critical loads, therefore they will have a different amount of stringers in each section. Finally, similarly to the spar webs, the skin thickness calculated for the shearflow will not be enough to prevent buckling, so the skin has been increased to 2 mm on both the top and bottom sides. The final stringer distribution can be found in Table 10.10:

Table 10.10: Main wing wingbox stringer layout

Section	Number of stringers (top)	Number of stringers (bottom)
0m - 0.9m	28	27
0.9m - 1.8m	27	26
1.8m - 2.7m	25	26
2.7m - 3.5m	23	28
3.5m - 4.3m	21	29
4.3m - 5.8m	19	28
5.8m - 7.9m	17	25
7.9m - 9.8m	15	23
9.8m - 11.5m	14	21
11.5m - 13m	13	18
13m - 14.3m	13	16
14.3m - 15.5m	11	7
15.5m - 16.9m	7	11
16.9m - 17.6m	6	9

This final design has the following weight distribution:

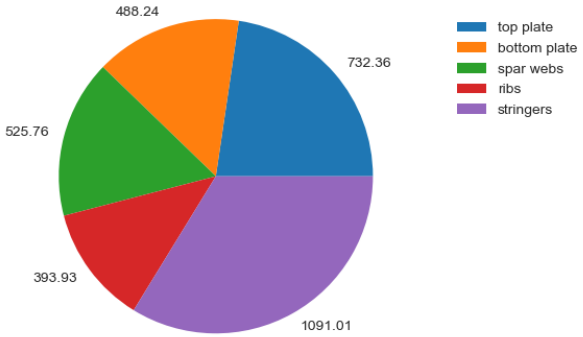

Figure 10.53: Mass distribution of the wing [kg]

Empennage

As explained previously, the empennage uses the same design process as the wingbox for the wing. Therefore in this section the results from the same process but with the empennage data will be displayed in this section. Starting with the required number of ribs showed in Figure 10.54 and 10.55:

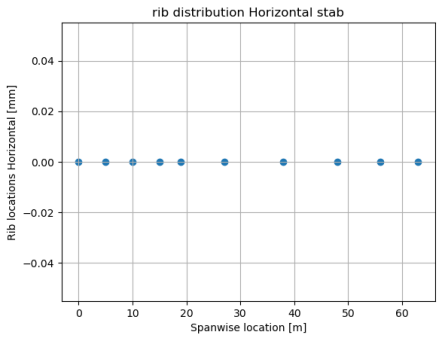

Figure 10.54: Required rib distribution for horizontal stabilizer

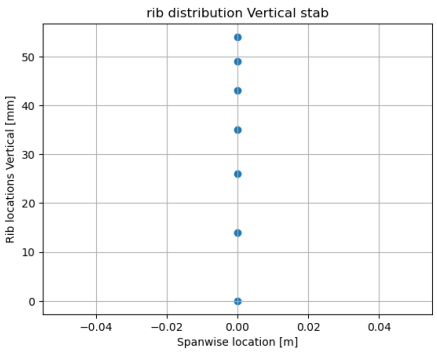

Figure 10.55: Required rib distribution for vertical tail

Next, the stringer distribution in each section of the wingboxes of the horizontal and vertical tails will be displayed in Table 10.11 & 10.12. As seen in those tables, there is no difference between top and bottom stringers because the airfoil is symmetric, and the critical loads are equal both on positive and negative z-direction.

Table 10.11: Horizontal stabilizer wingbox stringer layout

Section	Number of stringers
0m - 0.5m	2
0.5m - 1m	2
1.5m - 1.9m	2
1.9m - 2.7m	2
2.7m - 3.8m	2
3.8m - 4.8m	2
4.8m - 5.6m	2
5.6m - 6.3m	2

Table 10.12: Vertical stabilizer wingbox stringer layout

Section	Number of stringers
0m - 1.4m	3
1.4m - 2.6m	3
2.6m - 3.5m	3
3.5m - 4.3m	3
4.3m - 4.9m	3
4.9m - 5.4m	3

Finally, the weight distribution of the horizontal stabiliser is found in Figure 10.56, and for the vertical tail in Figure 10.57

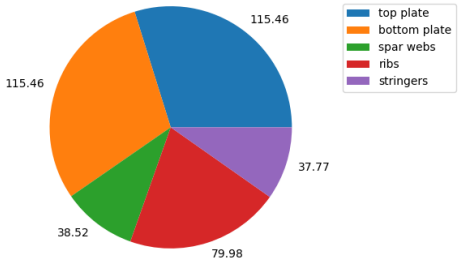

Figure 10.56: Mass distribution of the horizontal stabilizer [kg]

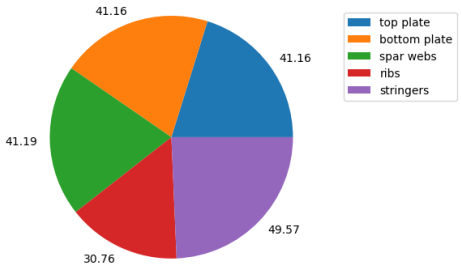

Figure 10.57: Mass distribution of the vertical tail [kg]

10.6. Validation

Giorgio

The final step of a structural design is the validation process. The validation procedure will be very similar to the aviation standard structures test, which consists in creating a rig that surrounds the aircraft, and with the help of pulleys, the expected critical loads will be applied throughout the aircraft as seen in Figure 10.58 [7].

Figure 10.58: Wing test from the Boeing 787

As seen in this figure, the structure is pushed to the limits, therefore it is important to make sure that it has not suffered any damage in the process. For this reason, the most critical points in the structure will be fitted with various strain gauges to monitor the deflection of the panels. Furthermore, after the test, the whole structure will undergo further non-destructive tests such as an ultrasound to check for the presence of possible cracks.

10.7. Recommendations

Christoph, Annemijn

Different recommendations can be made after designing the full aircraft structure, in order to obtain an even better structure in future steps of the design process. First of all, regarding loading of the aircraft, the loading diagrams from forces in the y-direction can further be refined. Due to the limit in available time, all aerodynamic loads on the wing and vertical tail were considered to be transferred in the wing. However, they are also partly transferred in the fuselage structure, which can be investigated in order to obtain a more precise load distribu-

[7] URL `https://www.flightglobal.com/picture-boeing-completes-787-ultimate-load-wing-flex-test/92688.article` [cited 16 June 2022]

tion.

As a further recommendation, for the materials, methods for recycling composites can be investigated. More research on this approach is recommended as it would save a substantial amount of weight and make the aircraft more efficient. In general, research can be conducted on various recycling techniques. Therefore, the most environmentally friendly approach must be adopted to ensure that the end-of-life operations are as green as possible. The footprint of production is now included in the material selection, but the CO_2-footprint of all manufacturing can still be investigated. This analysis is beyond the scope of this project but is recommended to be pursued as further work.

11

Stability, Control and Balance Characteristics

Stability, controllability and aircraft balance are essential for both the flight and ground operations of an aircraft. This chapter covers all aspects related to this topic. A method to obtain the aircraft's centre of gravity limits is described in Section 11.1. The stability and controllability limits of the aircraft are shown in Section 11.2. The constraints for longitudinal landing gear positioning are discussed in Section 11.3. The analysis process for the optimal longitudinal landing gear position, taking into account the information in the aforementioned sections, is established in Section 11.4. The lateral landing gear positioning is then described in Section 11.5. Lastly, the horizontal and vertical tailplane designs are discussed in sections 11.6 and 11.7 respectively.

11.1. Aircraft Balance: Loading Diagram and CG Range Diagram *Lisa*

The first step in determining the balance of an aircraft, is to obtain its center of gravity (cg) limits. This can be done by constructing a Loading Diagram, not to be confused with the loading diagrams discussed in Chapter 10. This type of Loading Diagram shows the variation of the longitudinal cg position X_{cg} relative to the MAC during the loading of cargo, passengers and fuel on the aircraft. The cg position at the aircraft OEW is taken as starting point.

First, the cargo is loaded. It is assumed that the cargo is placed in two cargo holds: one in front of the wing and one after the wing. This determines their cg positions. The weight of the cargo holds is estimated by taking into account their volumes, the volume of a suitcase and the maximum allowed weight per suitcase as determined by airliners[1].

Second, the passengers are loaded. The cabin layout and location are established and an average passenger weight of 100 kg is used. The loading is done in three 'shifts: first the window seats, then the middle seats and finally the aisle seats.

Lastly, the fuel is loaded onto the aircraft. The liquid hydrogen will be placed in the hydrogen tank in the back of the fuselage, and the SAF will be placed in the fuel tanks in the wings.

For all stages, two options have to be considered. The cargo and passengers can either be loaded from front to back, or from back to front. For the fuel, either the hydrogen or SAF can be loaded first. Both options need to be analysed in order to determine the most forward and aft cg positions of the aircraft.

The starting point of the Loading Diagram is highly dependent on the aircraft wing position. One reason for this is that a different wing position leads to a different absolute cg position at OEW. Another, more important reason is that in the diagram, the cg position is displayed at relative to the MAC. The MAC position varies along with the wing position, while the change in cg position is always less than the change in wing position. Therefore, the ratio $\frac{X_{cg}}{MAC}$ takes on quite different values for different wing positions. The shape of the Loading Diagram depends mostly on the absolute cg position at OEW. When the OEW cg position is close to the tail, the loading of cargo, passengers and fuel will shift the cg strongly forward, thereby causing a large cg range. On the other hand, when the OEW cg position is close to the cockpit, the loading of cargo, passengers and fuel will shift the cg strongly backward. This also leads to a large cg range. Ideally, the cg range is kept as small as possible to make balancing, stability and controllability easier. Therefore, the desired absolute cg position at OEW is such that the cg position after loading is close to the OEW cg position.

[1] URL `https://www.skyscanner.nl/nieuws/regels-bagage-overzicht-afmetingen-en-gewicht-voor-handbagage` [cited 14 June 2022]

In Figure 11.1, three examples of a Loading Diagram are given. These examples visualise the shape difference as a result of the OEW cg position, as discussed above. In addition, they show the general layout of a Loading Diagram that takes into account both loading from front to back and from back to front. The fact that the examples show the described principles means that the program written to generate these diagrams is consistent with the theory and expected outcome. Therefore, the generation of these examples can be seen as a system test to verify the working of the program. Since the system test is passed, it is justified to state that the functionality of the program is verified.

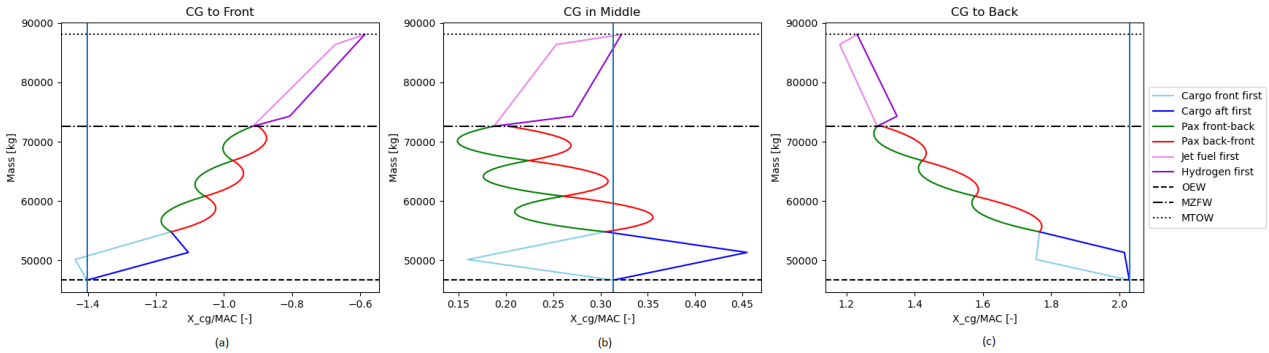

Figure 11.1: Loading Diagrams for Foward, Middle and Aft CG OEW Positions

As stated before, the wing position influences the absolute OEW position and the position relative to MAC. For the LEAF aircraft, a cg position of the entire aircraft without the wing at OEW is obtained from the Class-II weight estimation described in Section 13.1. For any given wing position, the total cg position of the aircraft at OEW can be calculated. It is important to note that since the cg position of the aircraft without wing is fixed, the total cg position will vary only to some extent when the wing is added. Therefore, the Loading Diagram shape corresponding to each wing position will not be as extreme as Figure 11.1a and Figure 11.1c. This means that the cg range will not vary as much in width. However, the relative position of the total cg with respect to the MAC will vary significantly. This can be visualised in a CG Range Diagram. For any longitudinal wing position, a Loading diagram can be produced. The most forward and aft relative cg positions are then documented for each wing position. The variation in cg range and relative position for each wing position is displayed in the CG Range Diagram. The wing position is denoted by $\frac{X_{LEMAC}}{l_{fus}}$, which is the ratio between the longitudinal position of the start of the MAC and the total fuselage length. Part of the full CG Range Diagram for the LEAF aircraft is shown in Figure 11.2. In this figure, the wing position is varied between 30 and 60% of the fuselage length, and the results are displayed.

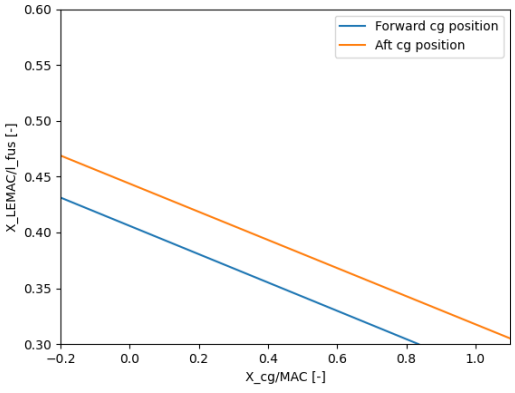

Figure 11.2: CG Range Diagram for the LEAF Aircraft

As expected, Figure 11.2 shows that $\frac{X_{cg}}{MAC}$ increases when the wing moves more towards the cockpit. This is because for a forward wing position, the MAC is also located forward. However, the total aircraft cg will not have moved as much as the MAC. Thereby, from the wing's perspective the cg position will move backwards and thus the ratio between the cg position and the MAC will increase.

11.2. Aircraft Stability and Control

Lisa

CS25 regulations specify that a large aircraft must be longitudinally, directionally and laterally stable [82]. In addition, the aircraft must be controllable at all times. This means that everywhere within the aircraft's cg range, the stability and controllability constraints must be satisfied. In order to satisfy these constraints, the horizontal tailplane area must be large enough. The size of the horizontal tailplane as a fraction of the wing surface area $\frac{S_h}{S}$ can be determined by constructing a so-called Scissor Plot. This plot shows the stability and controllability constraints for every aircraft cg position relative to the MAC. It therefore has the same x-axis as the Loading Diagram and CG Range Diagram discussed in Section 11.1, which allows for alignment of these diagrams. This will be important later.

The stability constraint follows from the position of the stick-fixed neutral point relative to the MAC ($\bar{x}_{np}$), as a function of the horizontal tail size. A stability margin of 5% is assumed, meaning that the position of the aircraft cg relative to the MAC ($\bar{x}_{cg}$) is 5% in front of the neutral point relative to the MAC. This allows for directly relating the aircraft cg position to the horizontal tailplane area. The relationship is described in Equation 11.1:

$$\bar{x}_{cg} = \bar{x}_{ac} + \frac{C_{L\alpha_h}}{C_{L_{\alpha_{A-h}}}} \cdot \left(1 - \frac{d\varepsilon}{d\alpha}\right) \cdot \frac{S_h l_h}{S\bar{c}} \cdot \left(\frac{V_h}{V}\right)^2 - 0.05 \tag{11.1}$$

Here, $\bar{x}_{ac}$ is the position of the aerodynamic center relative to the wing MAC. $C_{L\alpha_h}$ is the lift slope of the horizontal tail, while $C_{L_{\alpha_{A-h}}}$ is the lift slope of the aircraft without tail. The factor $\left(1 - \frac{d\varepsilon}{d\alpha}\right)$ accounts for the downwash influence. Furthermore, l_h is the tail arm, or the distance between the aerodynamic center of the wing and the horizontal tail. $\bar{c}$ is the MAC of the wing, and $\left(\frac{V_h}{V}\right)$ is the ratio between the air velocity over the horizontal tail and the wing. The relationship in Equation 11.1 can be rewritten such that $\bar{x}_{cg}$ is expressed in $\frac{S_h}{S}$, allowing the equation to be displayed in the Scissor Plot in Figure 11.3.

The controllability constraint follows from the trim equation. This equation describes the condition that must be satisfied for an aircraft to be trimmed. It can be written in the same form as Equation 11.1, so that the aircraft cg position and the horizontal tailplane area are directly related:

$$\bar{x}_{cg} = \bar{x}_{ac} - \frac{C_{m_{ac}}}{C_{L_{A-h}}} + \frac{C_{L_h}}{C_{L_{A-h}}} \cdot \frac{S_h l_h}{S\bar{c}} \cdot \left(\frac{V_h}{V}\right)^2 \tag{11.2}$$

Here, $C_{m_{ac}}$ is the aircraft moment coefficient in the aerodynamic center. All other variables are also used in Equation 11.1. Similar to that equation, Equation 11.2 can be rewritten to allow for displaying it in the Scissor Plot. The Scissor Plot belonging to the LEAF aircraft is shown in Figure 11.3. The controllability constraint defines the most forward cg position of the aircraft, as every cg position in front of that corresponds to an uncontrollable aircraft. On the other hand, the stability constraint defines the most aft cg position of the aircraft. Every cg position behind this constraint, for a certain value of $\frac{S_h}{S}$, corresponds to an unstable aircraft.

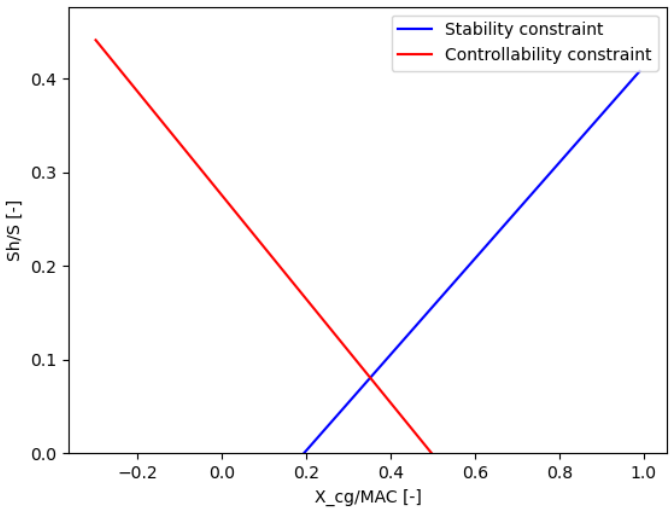

Figure 11.3: Scissor plot showing the stability and controllability constraints

For a certain wing position, the aircraft has a certain cg range. When this cg range is indicated in the Scissor Plot, it will intersect with both the stability or controllability curve for different values of $\frac{S_h}{S}$. The highest found value of $\frac{S_h}{S}$ is then the value for which the horizontal tailplane has to be sized, since the corresponding constraint is found to be limiting. The minimal horizontal tailplane area is found when the cg range intersects both the stability and controllability curve at exactly the same value of $\frac{S_h}{S}$. This means that both constraints are limiting at the same time, and that the horizontal tailplane is not over-designed for one of the two.

11.3. Constraints for Longitudinal Landing Gear Positioning *Lisa*

For the longitudinal positioning of the nose and main landing gear, there are a few requirements that the obtained landing gear positions must comply with. The first requirement states that the static load on the nose wheels should be between 8 and 15% of the total aircraft weight at all times. This means that the static load condition on the nose wheels must be checked for both the most forward and aft cg positions of the aircraft. This condition can be formulated as follows:

$$(x_{cg_{aft}} - x_{nw}) * f_{aft} = (x_{mw} - x_{cg_{aft}}) * (1 - f_{aft}) \tag{11.3}$$

$$(x_{cg_{fwd}} - x_{nw}) * f_{fwd} = (x_{mw} - x_{cg_{fwd}}) * (1 - f_{fwd}) \tag{11.4}$$

For every longitudinal nose wheel position x_{nw}, main wheel position x_{mw} and aft or forward cg position x_{cg}, the static load factor f on the nose wheel can be calculated and checked against the requirement of $0.08 < f < 0.15$.

Another requirement is that the main landing gear must be placed between the rear spar and trailing edge of the wing, to allow for main landing gear storage. This means that the wing position of the aircraft is very important for landing gear positioning.
In addition, it must be possible to retract the nose wheels forward, so that the nose landing gear extension happens rearward. The reason for this is that in extended position, the nose gears are locked in place. If the nose landing gear is extended forward, it might happen that the touchdown of the nose wheels during landing generates a moment in the direction of retraction, meaning that the landing gear might suddenly retract during landing. Since this is highly undesirable, the nose landing gear will be positioned such that it allows for forward retraction.

Furthermore, the length of the landing gear must be such that the aircraft can take off and land without hitting its tail on the runway. A scrape angle is defined to prevent this from happening. The scrape angle is taken to be 13 degrees, which is a reasonable value at this stage of the design phase according to Roskam [83]. A line with the slope of $\tan(13°)$ is drawn tangent to the tailcone, to visualise the minimum length of the main landing gear that allows for rotating $13°$ around the main wheels. Lastly, longitudinal tip-over of the aircraft must be prevented at all times. Longitudinal tip-over happens when the aircraft cg gets too close to the main landing gear position. This can happen for example when loading the aircraft, if the actual cg position exceeds the calculated $x_{cg_{aft}}$. The longitudinal tip-over angle indicates the minimum needed clearance between $x_{cg_{aft}}$ and x_{mw}. The tip-over constraint can be drawn as a line deviating 15° from the vertical axis (counterclockwise), while passing through the aft cg position of the aircraft. This tip-over angle should always be bigger than the scrape angle. At this stage of the design phase, the tip-over angle should be taken to be the largest value, being either 15° or the take-off angle of attack [8]. The take-off angle of attack will be less than or equal to 13 degrees since it should be less than the scrape angle. Therefore, a longitudinal tip-over angle of 15 degrees is used. A visualisation of the scrape and tip-over constraints is shown in Figure 11.4. The blue line indicates the scrape constraint, while the orange line indicates the tip-over constraint. At the intersection of the two lines, the main landing gear can be placed while adhering to both constraints.

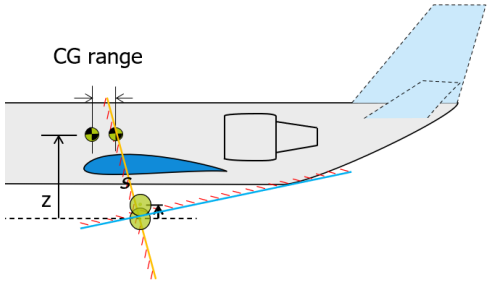

Figure 11.4: The scrape and tip-over constraints for the main landing gear [84] (modified)

11.4. Analysis Process for Optimal Longitudinal Position *Lisa*

Since the constraints for the longitudinal landing gear positioning are identified, they can be used to position the landing gear. However, it is important to note that the static load on the nose and main wheels, as well as the tip-over constraint, are dependent on the cg range and absolute cg positions of the total aircraft. Now, say for example that the wing is positioned somewhere on the fuselage, and that the most forward and aft cg positions of the aircraft are calculated. The scrape and tip-over constraints indicate the main landing gear position and the nose landing gear is then positioned such that the static load requirement and nose gear retraction requirements are met. So far, so good. However, it becomes clear that the wing is positioned such that the main landing gear cannot be placed between the rear spar and trailing edge of the wing for the given main gear position. It also becomes apparent that changing the main gear position such that it fits in the wing, violates either the scrape and tip-over or the static load constraint. This means that for the given wing position, the landing gear cannot be placed such that all requirements are met. The next proposed solution is to change the wing position instead of the main gear position, so that it fits in the wing. However, changing the wing position to make the main landing gear fit in, will shift the cg range and cg positions of the aircraft because the cg position of the wing is altered. This change in total cg position might then cause the static load constraint or tip-over constraint to be exceeded, leading again to an infeasible landing gear position. This example illustrates how sensitive the landing gear positioning is to the wing position and cg positions.

That is why an iterative analysis process was set-up to find the best possible wing and landing gear positions, that are in accordance with the constraints. The starting point of the analysis is a fixed value for the cg position of the OEW of the aircraft without the wing. Then, for every possible wing position along the fuselage, the total cg position of the aircraft OEW is calculated. This cg position is then used as starting point on the Loading Diagram, discussed in Section 11.1. The Loading Diagram corresponding to this particular wing position is generated, and the most forward and aft cg positions of the aircraft are obtained. The tip-over line is drawn through the aft cg position and the intersection with the scrape constraint is found. For this analysis, the upper and lower tailcone borders are approximated by parabolic functions, making sure that the hydrogen tank fits in the tailcone. The scrape line is then drawn tangent to the lower tailcone parabola. The intersection point defines the location of the main landing gear and its length. The nosewheel is then located such that it allows for forward retraction. In short, for every possible wing position along the fuselage, the unique forward and aft cg positions of the aircraft, and the unique landing gear positions are found. Now, it has to be checked if the landing gear positions meet all requirements specified in Section 11.3.

First, for every unique case, it is checked whether the main landing gear fits in the wing. All of the possible wing positions that allow for main landing gear storage are documented along with their respective forward and aft aircraft cg positions and landing gear positions. The wing positions that do not pass this check are discarded. Then, using Equations (11.3) and (11.4), the percentage of static load on the nosewheels is calculated for the remaining unique cases. If the static load is found to be out of the allowed range of 8-15%, the wing position leads to impossible landing gear positioning and is discarded. On the other hand, if the static load is found to be within the allowed range, the constraint is satisfied and the wing position along with its corresponding values are documented.

The unique cases that are now left, comply with all requirements for longitudinal landing gear positioning. This means that all cases represent a possibility for landing gear positioning. However, an optimal case can be selected, based on the required horizontal tail size. The forward and aft cg positions relative to the MAC are used to find the corresponding horizontal tailplane surface area in the Scissor Plot described in Section 11.2. Then, the unique case leading to the smallest ratio between the horizontal tail and wing surface area is selected as optimal case. This means that the selected longitudinal landing gear position and wing position not only satisfies the constraints, but also allows for the smallest possible horizontal tailplane surface area.

The results of this analysis are shown in Figure 11.5. The figure is generated automatically for the optimal case determined in the analysis. In Figure 11.5a, the Loading Diagram for the corresponding wing position is shown. The CG Range Diagram in Figure 11.5b and the Scissor Plot in Figure 11.5c are the same as Figure 11.2 and Figure 11.3 respectively. Here however, the cg range found in the Loading diagram is indicated by two vertical lines, and the intersection with the graphs is shown. This allows for identification of the wing position in the CG Range Diagram and for the horizontal tailplane size in the Scissor Plot. The Scissor Plot shows that the controllability constraint is limiting for the LEAF aircraft. Lastly, the scrape and tip-over constraints are visualised in Figure 11.5d, allowing for indication of the main landing gear position at the intersection of the two constraints.

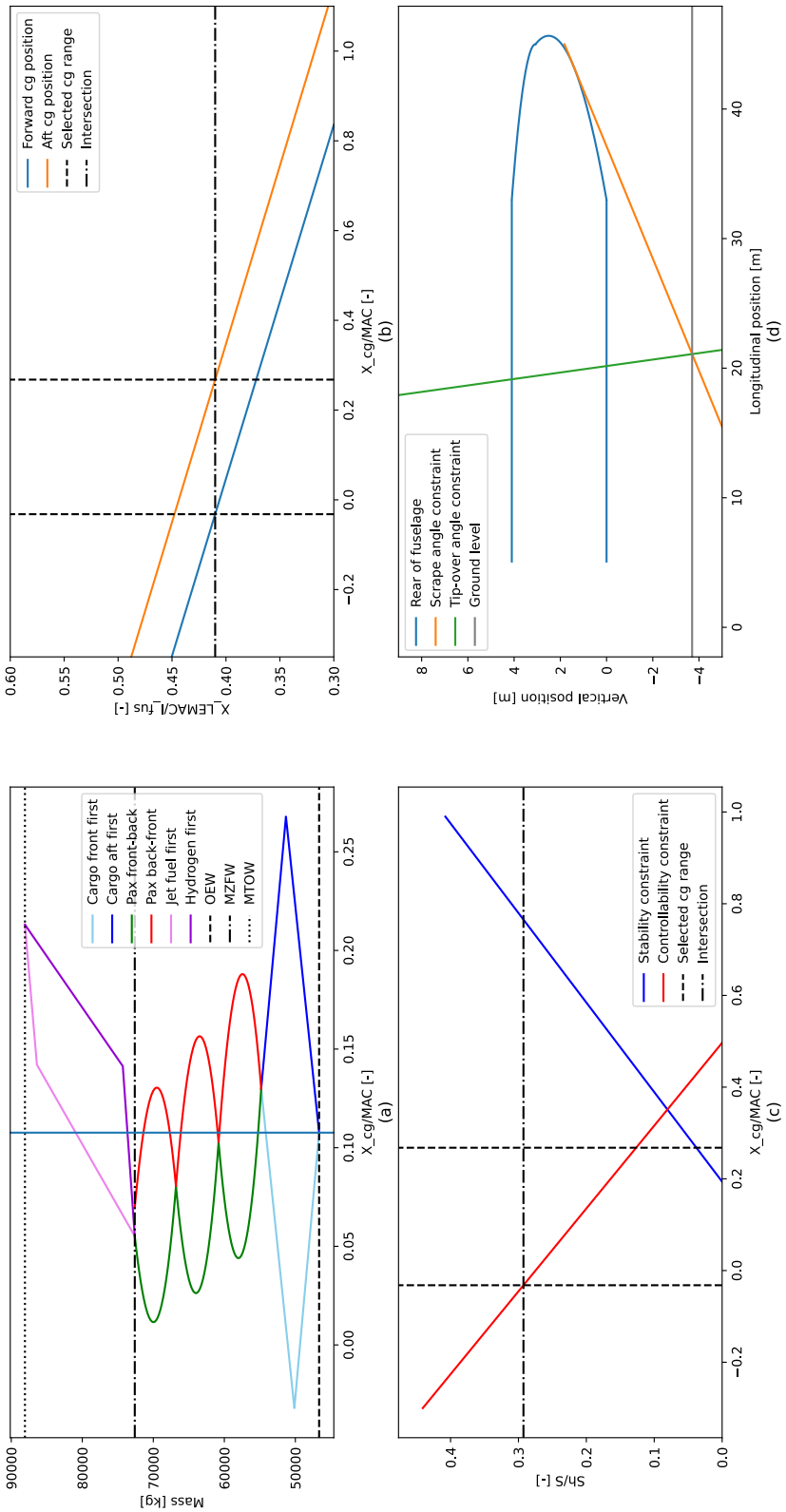

Figure 11.5: Loading Diagram, CG Range Diagram, Scissor Plot and Longitudinal Landing Gear Positioning for optimal case

11.5. Lateral Landing Gear Positioning *Lisa*

The lateral position of the main landing gear has to comply with constraints, similar to the longitudinal position. The first requirement states that there should be sufficient engine clearance. The engine clearance is defined as a line tangent to the engine, while passing through the main landing gear position on the ground. The angle between the ground and this line is the engine clearance angle. Torenbeek states that this angle should be at least 8° [46]. However, it was decided to increase this constraint to 10°, to allow for some margin in the design. The engine is positioned at 35% of the semi-span of the wing. The second requirement states that the lateral position of the main landing gear must be such that it can be retracted inwards without interfering with the nose gear and the main gear on the other wing half. A margin of 30 cm is included for this. Another imposed constraint is that there must be a lateral distance of at least 50 cm between the outer main wheel and the engine nacelle. This constraint is imposed to avoid the possibility of the main landing gear ending up behind the exhaust of the engine. The final requirement included the turnover angle. This angle is a measure to check whether the aircraft cg is guaranteed to be located within the 'landing gear triangle' connecting the nose and main landing gear. It also shows whether the aircraft is stable during a sharp turn and will not turn over. The turnover angle is dependent on the longitudinal and lateral position of the main landing gear with respect to the nose landing gear, and should not exceed 55° [46].

An iterative process was set-up, to calculate for every possible lateral main landing gear positions (from the nose gear position on the centerline towards the engine nacelle) whether all requirements were met. The lateral positions that met all requirements, were documented. Then, the required landing gear length was calculated for all possible positions. The lateral position corresponding to the smallest landing gear length was selected as optimal lateral position.

The analysis described in Section 11.5 provided an optimal longitudinal landing gear position. From this position, the minimum required landing gear length can be derived, including an extra 10 cm to allow for integration in the wing. This length is then compared to the minimum required length obtained from the lateral landing gear position. The highest value of the two is then the adopted value of the landing gear length, since this value is limiting. For the LEAF aircraft, it was found that the landing gear length for longitudinal position is limiting, so this length now has to be considered for the lateral positioning. It was checked whether the landing gear is still retractable inwards without any interference, now that the length is longer than required for lateral positioning. It was found that this requirement is still met, meaning that the initially obtained lateral position is still appropriate.

The analysis outcome is visualised in Figure 11.6. A schematic front view of the aircraft is provided, including the engine clearance constraint and the final obtained landing gear length.

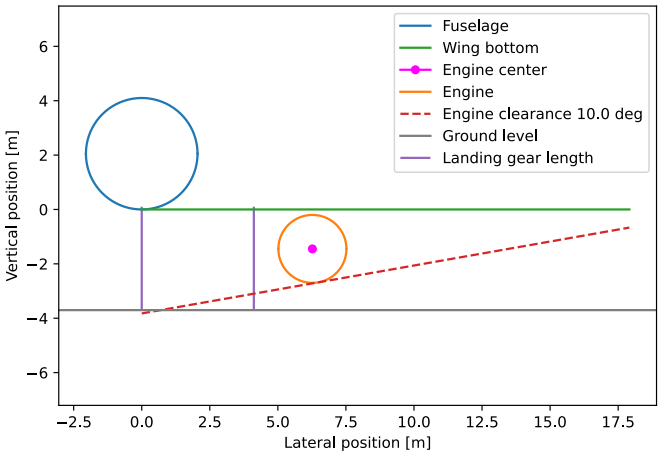

Figure 11.6: Schematic front-view of the aircraft after completion of the lateral landing gear positioning analysis

An overview of the parameter values obtained during the entire landing gear positioning, is given in Table 11.1. The longitudinal distances are expressed along the x-axis, and measured from the aircraft nose. The lateral position of the main landing gear is expressed along the y-axis, and measured from the aircraft centerline.

Table 11.1: Overview of landing gear positioning analysis outcome

Parameter	$x_{cg_{fwd}}$	$x_{cg_{aft}}$	x_{LEMAC}	x_{nw}	x_{mw}	y_{mlg}	l_{lg}	$\frac{S_h}{S}$
Value	18.31 m	19.64 m	18.45 m	4.00 m	21.09 m	4.12 m	3.80 m	0.293

11.6. Horizontal Tailplane Design

Lisa

As stated in Section 11.4, the analysis conducted results in a horizontal tailplane surface area. Typical ratios between the horizontal tail and wing surface area for existing jet airliners, are between 0.15 and 0.35 [46]. The ratio of the LEAF aircraft falls within this ratio and is therefore deemed acceptable. The horizontal tailplane surface area forms the basis of the horizontal tail planform design. According to Raymer, the exact planform of the tail surfaces is not very critical in the early stages of the design process [8]. The tail geometries are revised during later analytical and wind-tunnel studies. However, a preliminary estimate of the horizontal tail planform can be obtained.

The leading-edge sweep of the horizontal tail is usually set to about 5 deg more than the leading edge wing sweep. This tends to make the tail stall after the wing, and also provides the tail with a higher critical Mach number than the wing. This avoids loss of elevator effectiveness due to shock formation. According to Raymer, the horizontal tail aspect ratio AR_h has a value between 3 and 5 [8]. It directly influences the lift-curve slope of the horizontal tail, with a higher AR_h being favourable for stability. However, for the LEAF aircraft, not stability but controllability is the limiting constraint, as shown in Figure 11.5. This means that the horizontal tail is to be designed for controllability rather than stability. Therefore, a lower value for AR_h will be sufficient. A lower AR_h implies a shorter wingspan. This is preferred for structural reasons, to minimise the structural weight. However, the wingspan should be large enough to fit the elevators. Typical values of AR_h for other civil jet aircraft were considered and it was found that all values were quite close to 4 [46]. Therefore, an AR_h value of 4 is taken for the aircraft at this stage of the design.
The taper ratio typically has values between 0.3 and 0.6 [8]. A smaller value is preferred to save structural weight. Similar as for the aspect ratio, the taper ratio of other civil jet aircraft were used as reference [46]. From this, a taper ratio of 0.35 is assumed at this stage of the design.
Now that the surface area, aspect ratio and taper ratio are determined, the horizontal tail planform can be designed. The planform is shown in Figure 11.7.

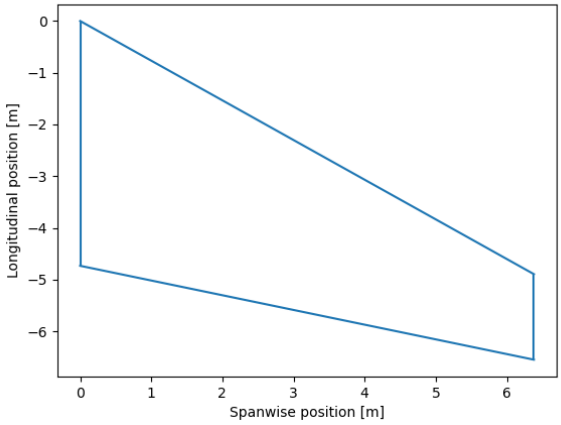

Figure 11.7: Horizontal tail planform design

The defining parameters and values are documented in Table 11.2:

Table 11.2: Defining parameters and values of the horizontail tail planform

Parameter	Λ_{LE_h}	Λ_{TE_h}	$S_{h_{half}}$	AR_h	λ_h	$b_{h_{half}}$	c_{root_h}	c_{tip_h}
Value	37.49 °	15.88 °	20.41 m^2	4	0.35	6.39 m	4.73 m	1.66 m

11.7. Vertical Tailplane Sizing

Guillermo, Jenny

The requirement that the aircraft should still be able to fly safely with one engine inoperative is a key requirement that sizes the vertical tailplane. In order to analyse this a static analysis has been done of the aircraft in this situation. Figure 11.8 shows the force needed, F_v, to be generated by the vertical tail in order to counteract

the induced yawing moment generated by the one engine that is operative. This will be analysed for a most aft CG location, because for that a larger force by the vertical tail is needed. When looking at the aircraft from behind the blades of the engine will rotate in clockwise direction. This means that the right side of each engine will generate more thrust, T_r, than the left side, which causes the right engine to have a larger arm, y_e, with the fuselage centerline than the left engine. Therefore, for sizing the vertical tail for one engine inoperative there will only be looked at the generated yawing moment of the right engine.

In order for the aircraft in Figure 11.8 to be in static equilibrium Equation 11.5 needs to be satisfied. From this the required surface area of the vertical tail plane on one side can be calculated using the lift formula as shown in Equation 11.6. In this equation C_{L_V} is the lift coefficient of the vertical tail plane's symmetrical airfoil at a given angle of attack relative to the incoming flow due to the yawing moment from the operative engine. In Figure 11.8 this angle is shown as β and is the same as the maximum allowable side slip angle which is 15 degrees as specified in CS25 [82].

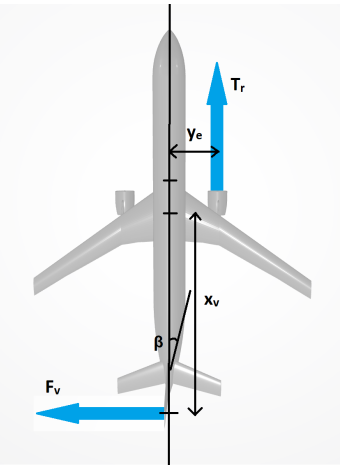

Figure 11.8: Top view of the aircraft with the forces acting on it while the left engine is inoperative

$$F_v = \frac{y_e \cdot T_R}{x_v} \qquad (11.5) \qquad S_V = \frac{F_V}{\frac{1}{2} \cdot \rho_0 \cdot V_s^2 \cdot C_{L_V}} \qquad (11.6)$$

In order to calculate C_{L_V} the equation below is used. For the vertical tail, values for the aspect ratio and half chord sweep angle were estimated using statistical data for aircraft of similar size [74]. Because the airfoil used for the vertical tail should be symmetrical, the intercept for the $\frac{dC_L}{d\alpha}$ curve with the C_L axis is zero, as zero angle of attack causes zero lift. Therefore, the lift coefficient was found by simply multiplying $\frac{dC_L}{d\alpha}$ with the 15 degrees of angle of attack. Substituting these values into Equation 11.6 yields a surface area S_V for both sides of the tail of $41.03\,m^2$.

$$\frac{dC_L}{d\alpha} = C_{L_\alpha} = 2\pi AR \div \left[2 + \sqrt{4 + \left(\frac{AR\sqrt{1-M^2}}{\mu}\right)^2 \cdot \left(1 + \frac{\tan^2(\Lambda_{0.5C})}{1-M^2}\right)}\right] \qquad (11.7)$$

It should be noted that this vertical tail plane surface area will actually be smaller after sizing the rudder. The rudder is a control surface that can change the shape of the vertical in such a way that it generates a larger force for a smaller surface area.

The defining parameters and values for the vertical tail are documented in Table 11.3:

Table 11.3: Defining parameters and values of the vertical tail planform

Parameter	Λ_{LE_v}	S_v	AR_v	λ_v	b_h	c_{root_v}	c_{tip_v}
Value	$35\,°$	$14.59\,m^2$	2	0.28	$5.54\,m$	$4.13\,m$	$1.15\,m$

11.8. Recommendations

Guillermo

In terms of stability and control there are several recommendations for further analysis of the LEAF aircraft. The first thing that should be analysed and designed are the control surfaces of the empennage: the rudder and the elevator. These control surfaces could be designed based on a dynamic analysis of certain pitch and yaw manoeuvres that the aircraft should perform. After this, the trim settings and trim drag of the elevators can be analysed in order to ensure longitudinal stability at all times. Also, a further analysis of the ailerons must be done to make it possible for the aircraft to perform specified rolling manoeuvres. An analysis on the effect of the lift generated by the fuselage on the stability of the aircraft is needed as well to ensure stability in further design stages.

12
Aircraft Systems

There are various systems in the modern aircraft that enable it to operate fully. In this chapter, the proposed configuration for the hardware block system, electrical block diagram, fuel system, hydraulic system, pneumatic system, software block system, and the communication flow diagram are indicated in Section 12.1, Section 12.2, Section 12.3, Section 12.4, Section 12.5, Section 12.6 and Section 12.7 respectively.

12.1. Hardware Block Diagram

Christoph, Luke

The hardware block diagram shown in Figure 12.6 gives an overview of all hardware components in the aircraft. The hardware components are split in 5 different groups. First, the cockpit group and cabin group are separated. The control group contains all control surfaces of the aircraft. Additionally, there is a power and propulsion group as well as an external group, which contains all elements of the aircraft in contact with the environment. Finally, the mechanical groups contain the hydraulic and pneumatic system. All groups are connected using different links. Theses can be either electric links, hydraulic fluid, data cable, bleed air, hydrogen, kerosene, water and direct connections, as most importantly for rotating elements such as the engine and wheel with their respective generator for producing electricity. The A320 flight briefing manual for pilots gave inspiration for multiple components of the aircraft shown in the hardware diagram[1]. Finally, it must be said that this diagram should only give a general overview of the hardware components. More detailed system diagrams can be found in the subsequent subsections.

12.2. Electrical Block Diagram

Igor, Luke

Electrical system is one of the essential systems for the aircraft to function. The design is largely based on modern airliners, like the A320, featuring two separate power buses as well as the third, essential power bus. Main bus powers hydraulic actuators, fuel pumps, engine starter and lighting systems. Avionics bus supplies the navigation and guidance as well as communication systems. Essential bus provides power for flight computer and flight data recorder, as they need to function even if other electrical components were to fail. The power during flight is provided by alternators connected to the engines. Left engine alternator provides power to the main bus and the essential bus, while right engine alternator powers the avionics bus. Main power bus can also be supplied from an external energy source to which the aircraft will be connected while stationing at the airport as well as the APU, which produces power using fuel cells. Furthermore, an extra emergency power generator is included using power provided by ram air turbine (RAT) for essential bus, and two batteries are charged by the power generators in case extra power is needed. Furthermore, regenerative braking included landing gear is feeding the power back into the main bus, improving the overall efficiency of the aircraft.

[1] URL `https://www.smartcockpit.com/docs/A320_Flight_Deck_and_Systems_Briefing_For_Pilots.pdf` [cited 15 June 2022]

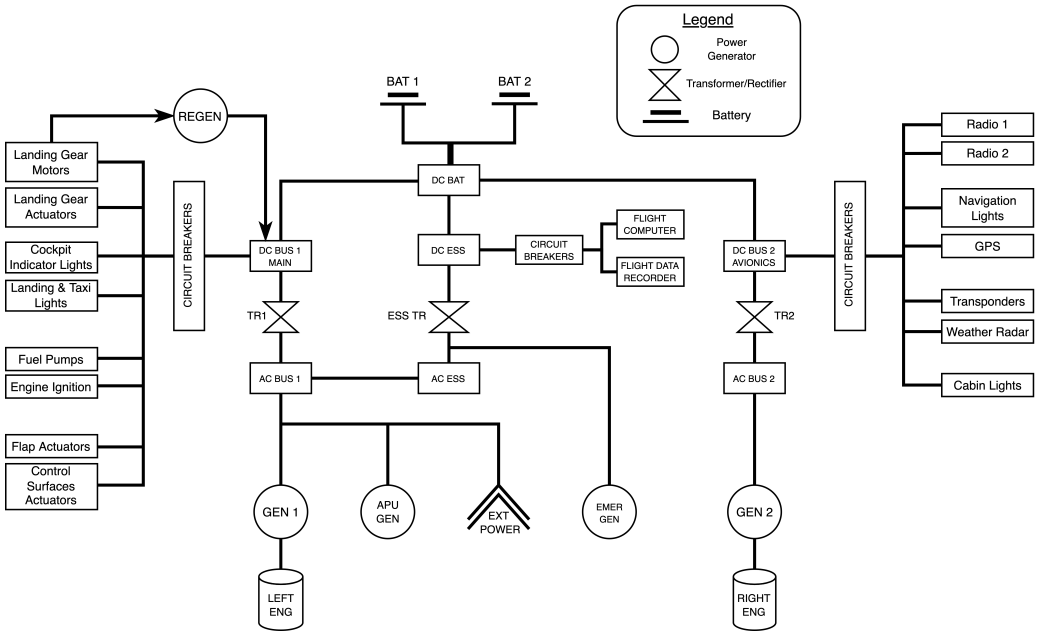

Figure 12.1: Electrical Block Diagram

12.3. Fuel System Layout *Luke*

The fuel system are divided into the primary kerosene fuel system as shown in Figure 12.2 and secondary hydrogen fuel system as shown in Figure 12.3. The kerosene system is similar with the current A320, with a center tank, and two inner tanks. With the reduced amount of kerosene carried onboard, a pair of outer tanks are chosen to be optional as airline customers can choose to install and further extend the range based on their operation profile. Each tank is equipped with fuel level sensor and two sets of pumps to monitor the status of the fuel and minimise the probability of failure. In case of extreme situations, the cross-feed valve will balance the fuel pressure fed to each engine. The same single refueling port is inherited to minimise implication with respect to ground operation.

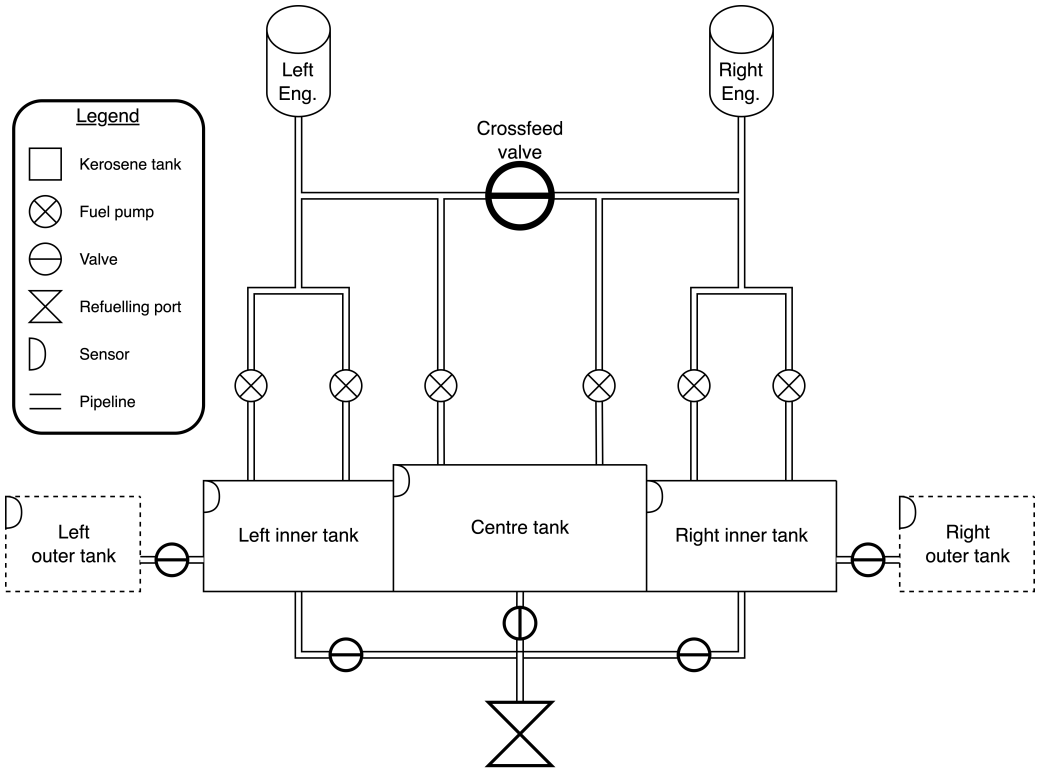

Figure 12.2: Kerosene fuel system

The hydrogen fuel system is designed based on tank structural and operation needs. Three cutouts are

made to allow liquid hydrogen to flow in, gaseous hydrogen to flow out and access for heating components. The pipeline on the image are differentiated to liquid (in cyan) and gaseous hydrogen (in black). The hydrogen tank will act as reaction vessel in changing the state of hydrogen from liquid to gaseous. When refuelling the tank, two trucks will feed liquid hydrogen into the tank through flow regulators to minimise damage caused by turbulence. When refueling, because the constant volume of the tank, excessive boiled off hydrogen will be vented through refuelling pressure release valve and recollected via primary truck. The boiled off hydrogen will then be transferred back to the liquefaction plant and be used in later cycles. An emergency pressure release valve is also installed in the gaseous hydrogen outlet, in case of extended exposure time or other operation needs, the pressure can be released to ensure the safety of the tank assembly.The hydrogen gas will then be separated into the main system and the APU (fuel cell) which will then be transferred into energy to power the aircraft. Heat will be recaptured from the engine and feed to the heating system. When excessive heat is needed to regulate the hydrogen, heat can be generated from the fuel cell and power the heating system. The heating component inside the tank will vary temperature to avoid thermal shock and better control the hydrogen flow.

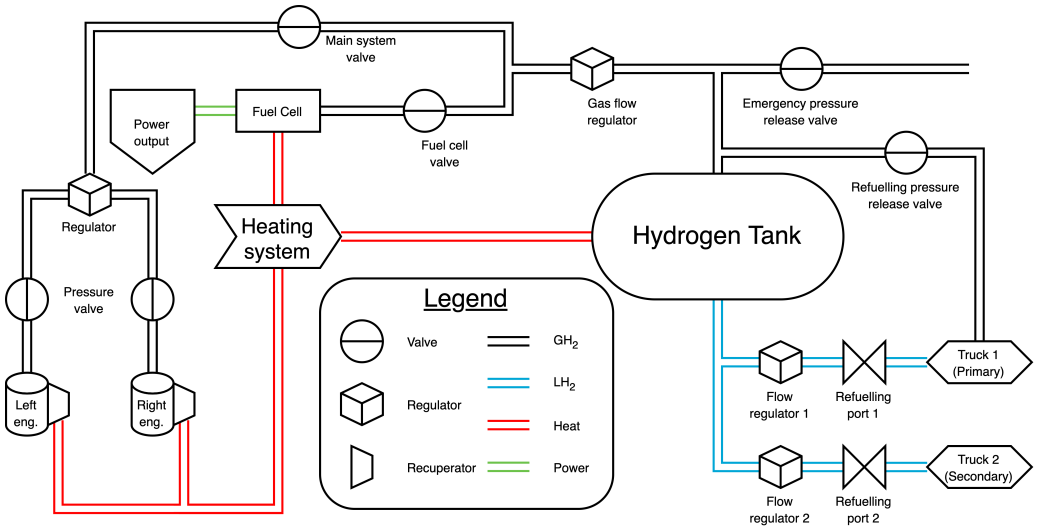

Figure 12.3: Hydrogen fuel system

12.4. Hydraulic System Layout *Luke*

The hydraulic system on the aircraft is used for moving and actuating the landing gear, control surfaces and brakes. For current A320s, the hydraulic system consists of three parts including the green, blue and yellow system[2]. Each system has its own reservoir and relatively individual pipeline system in which the fluid is not interchangeable, however, transfer power is possible between systems using Power Transfer Unit (PTU).The hydraulics are driven by the engines, and the auxiliary power unit in the beginning or end of the flight phase or a Ram Air Turbine (RAT) in case of both engine failure. Fluids are then used to transmit power through pipes and control devices. Advantages of hydraulics are ease of application of force, ability to increase force, easy routing of pipelines and no backlash between components.

For the design of this ultra-high efficient aircraft, the design philosophy of the current A320 is mostly kept with modifications to meet the requirements. The three system architecture is kept with three systems as illustrated below in Figure 12.4. The green and yellow systems are mainly powered by the two hybrid engines while the blue system is mainly made for emergency use with the deployment of RAT. Electric pumps are powered by hydrogen power cell or ground power unit. The three systems will power the various systems in the aircraft including brakes, control surfaces, landing gears and etc.. Each system will act as backup for each other to ensure safety. A hand pump is also placed in the yellow system to ensure cargo door availability when parking without GPU, and with the addition of hydrogen fuel cell, the gas intake needed to be considered due to high oxygen needed for the reaction.

[2]URL `https://safetyfirst.airbus.com/app/themes/mh_newsdesk/documents/archives/a320-dual-hydraulic-loss.pdf` [cited 16 May 2022]

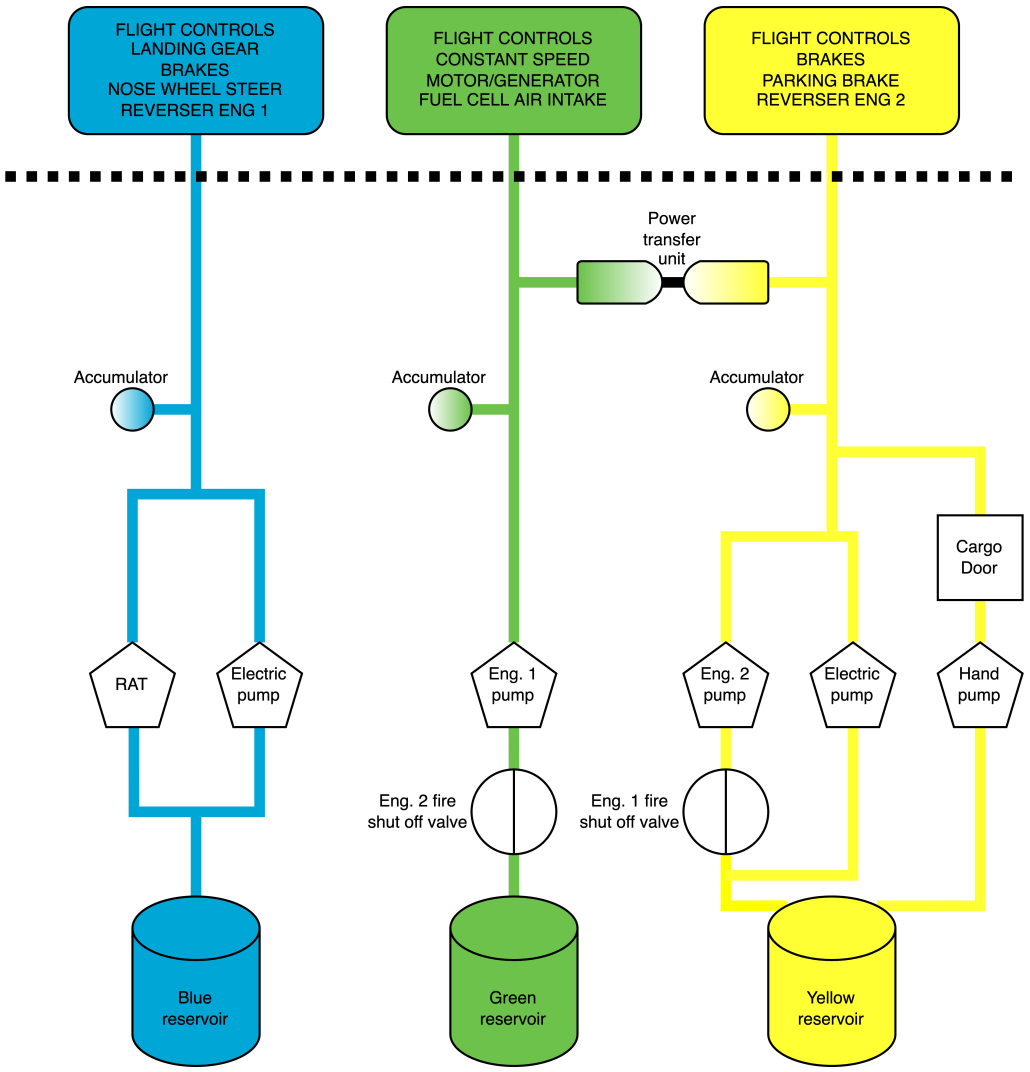

Figure 12.4: Hydraulic system layout

12.5. Pneumatic System Layout

Pneumatic System Layout *Luke* A pneumatic system is presented based on the current A320 aircraft, as shown in Figure 12.5. The bleed air is taken in from different stages of the main engine turbines. The high pressure valve allows air to flow from High Pressure (HP) stage to the system when there is not enough pressure in the Intermediate Pressure (IP) stage. The bleed air is regulated by the heat regulator to a desired temperature. The heat can then be used to power the heater for hydrogen handling system or anti-ice and de-ice systems. The cooled air is then regulated by cross-bleed valve and may power the environment control system onboard. When on ground, the engines are turned off and ground air input unit is used to provide the needed air for the cabin and engine. With the development in technology, the current B787 jet does not use bleed air to power the air conditioning system on board or anti-ice and de-ice system, instead, a small turbine in the engines will generate electricity to power these systems. However, due to the complexity of the combined fuel source engine, the feasibility of this option needed to be further considered.

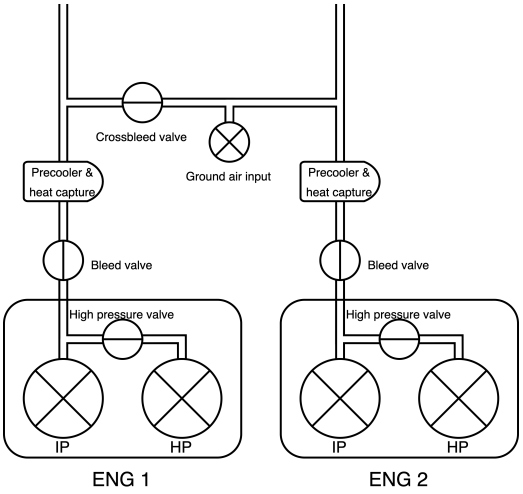

Figure 12.5: Pneumatic system layout

12.6. Software Block Diagram *Igor*

Functionality of avionics of an aircraft is largely handled by software. In modern aircraft, competitive on the market, software is one of the most important components of many systems, ranging from navigation and communication to controlling wing movable surfaces. Software block diagram presented in Figure 12.7 shows the flow and interactions between the main software components. They are categorised based on purpose, such as navigation or communication as well as type of the component, for instance sensor or control system. The aircraft will use software systems akin to what is implemented in modern airliners with the most expanded part of the software being the fuel control system, which needs to control and indicate the quantity, distribution and flows of both hydrogen and kerosene as well as accommodate the switch between fuels when set margins are reached.

12.7. Communication Flow Diagram *Christoph, Luke*

The communication flow diagram is shown in Figure 12.8. It contains all important elements of the internal as well as external communication of the aircraft. In order to make the diagram easier to understand, it also shows the boundaries of the aircraft, the cockpit as well as the radio system. Additionally, the most important people on the aircraft (pilot, crew, passengers) are easily identifiable in the diagram. The communication diagram was made based on the current airline communication types [3]. It was also decided to include the most current standard of 4G and 5G communication for a better experience of the aircraft passengers [4]. Finally, the choice of high and very high frequency radio communication was designed to resemble the one of an A320 [5].

[3] URL `https://events.windriver.com/wrcd01/wrcm/2016/10/Airline-Communications-Types-White-Paper.pdf` [cited 15 June 2022]

[4] URL `https://www.icao.int/Meetings/anconf13/Documents/WP/wp_244_en.pdf` [cited 15 June 2022]

[5] URL `https://www.smartcockpit.com/docs/A320-Communications.pdf` [cited 15 June 2022]

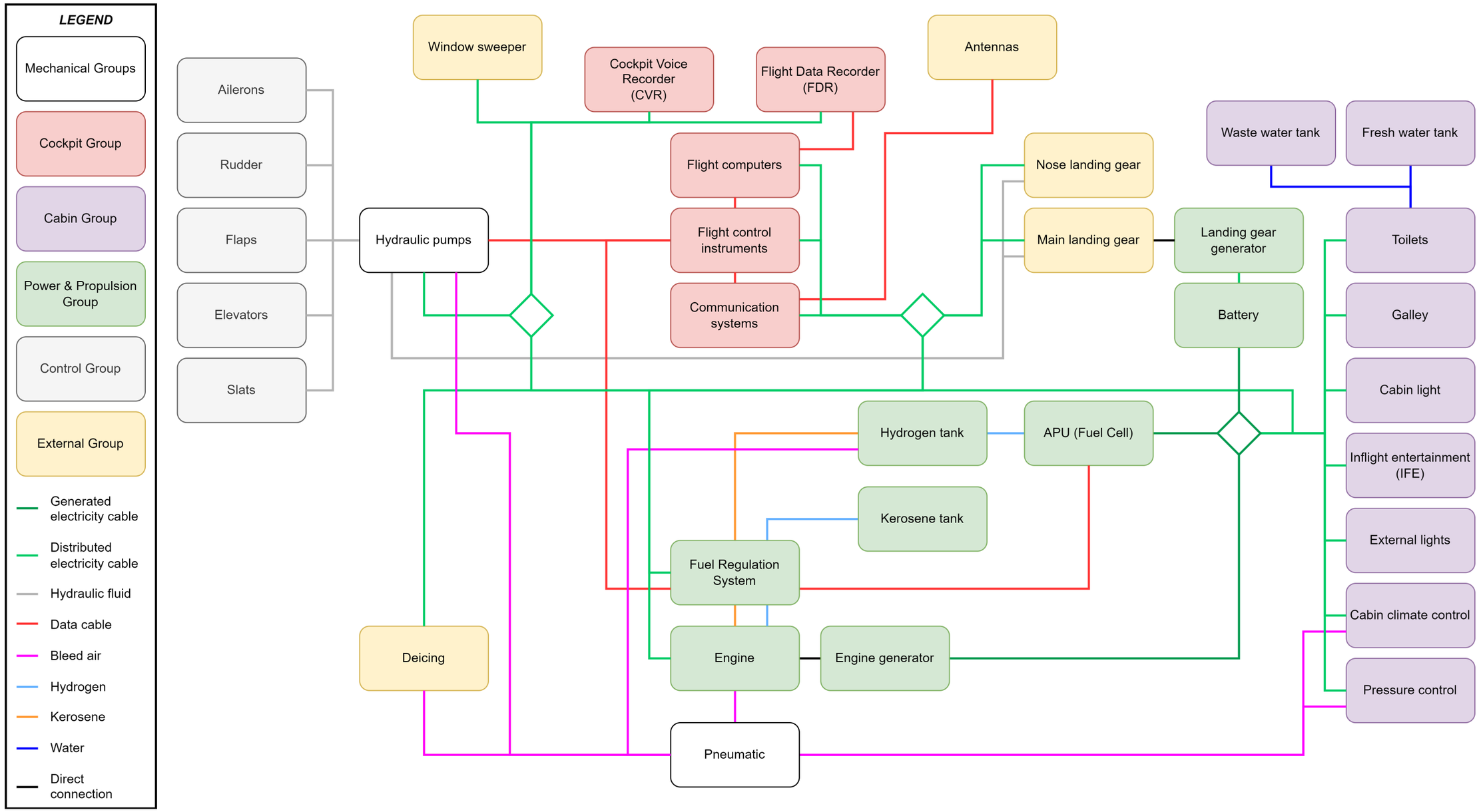

Figure 12.6: Hardware Diagram

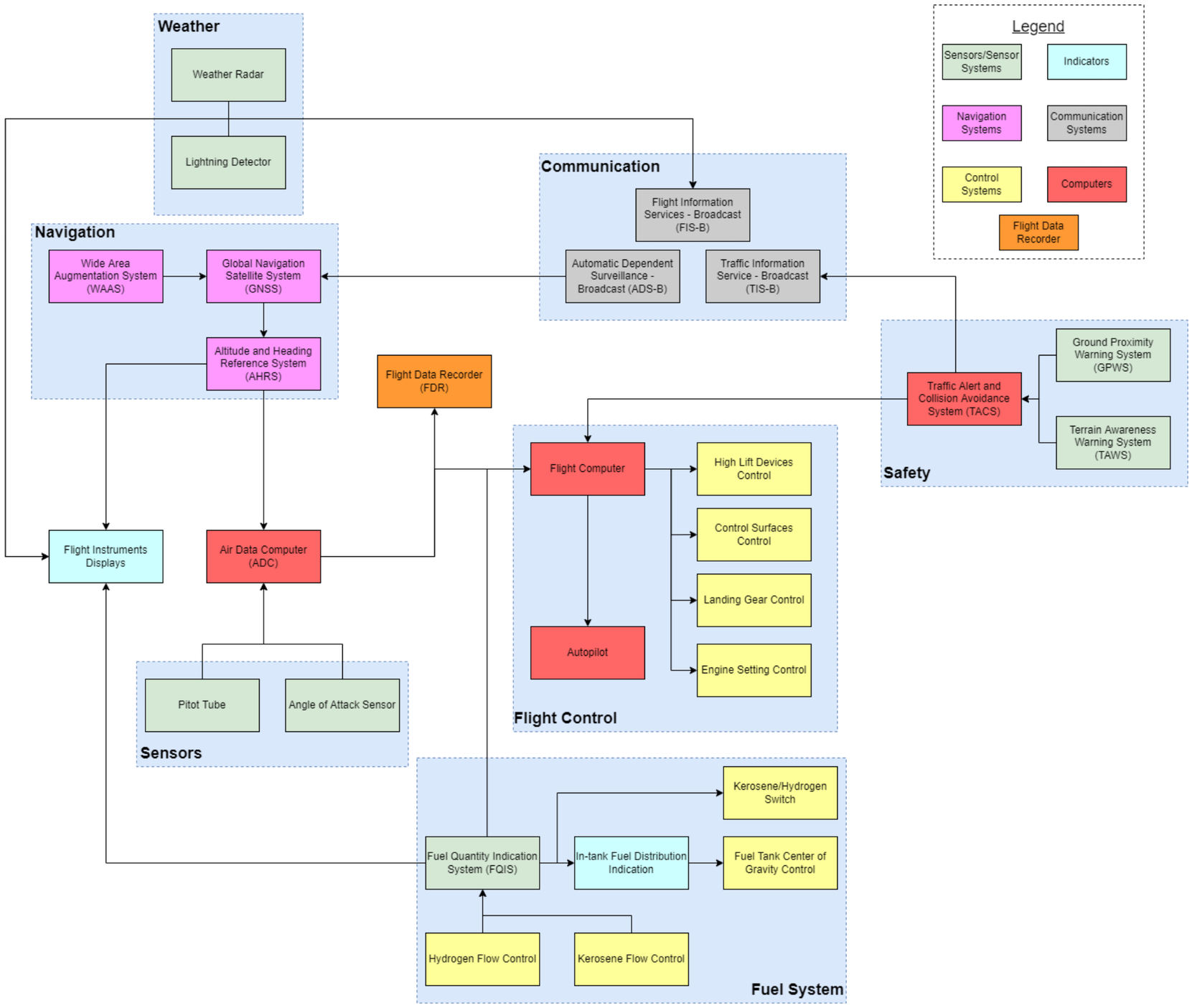

Figure 12.7: Software Block Diagram

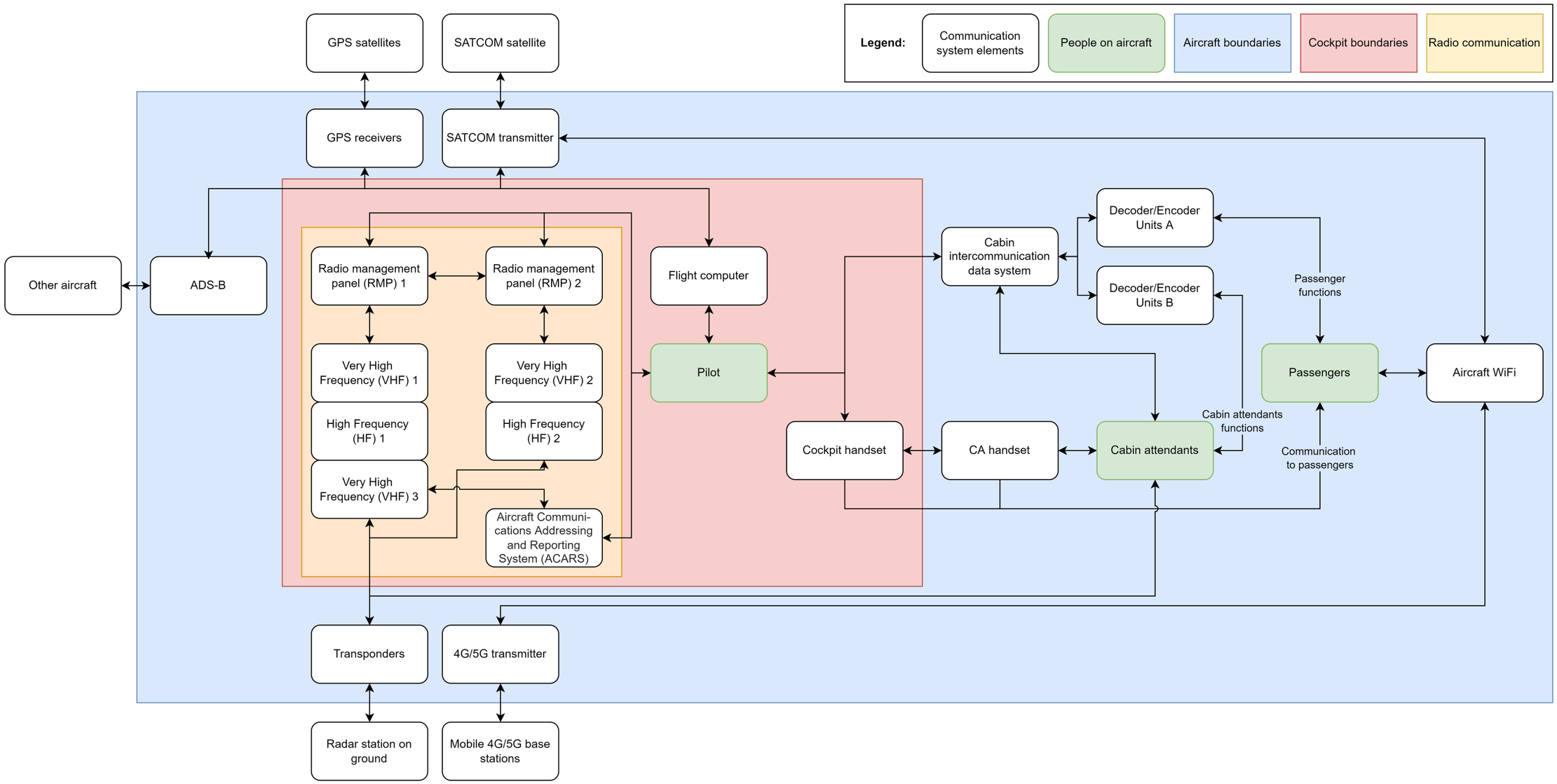

Figure 12.8: Communication Flow Diagram

13

Final Weight Estimation and Reiteration of Design

Jenny

13.1. Class-II Weight Estimation

Once parameters for components from each design department are established, a class-II weight estimation can be performed. A class-II weight estimation is used to estimate the weight of component groups, as these are easily influenced by parameter variations during the design process. The formulas used to derive the component weights are empirical relations based on statistical databases of existing aircraft weights given by Roskam [85]. It should be noted that as the LEAF aircraft is not a conventional aircraft that exists in existing databases due to the inclusion of the hydrogen tank and fuel system, as well as the increased fuselage length to account for this, that the weight estimation cannot estimate the desired weights precisely. The weight estimation method was adapted to include the weight of the hydrogen tank in the maximum take-off weight of the aircraft. Details in how this was done can be found in Subsection 13.1.1. In order to size hydrogen powered aircraft in the future, a new class-II weight estimation method should be devised for this aircraft category.

13.1.1. Hydrogen Tank Weight Estimation

In order to size the hydrogen tank as part of class-II weight estimation, the gravimetric index (GI) of hydrogen was used. The gravimetric index is a measure of the mass of a fuel as a proportion of the total tank weight (structural weight and fuel). Current estimates for the gravimetric index of hydrogen are around the value of 0.2. This value of GI signifies that 20% of the total tank and hydrogen mass is hydrogen, so of 100 kg of total mass, 20 kg of that is hydrogen and the remaining 80 kg is the structural tank mass. A GI of 0.35 is currently considered ambitious; however, it is estimated that by 2035, this value will be achievable.

13.1.2. Results of First Calculation of Class-II

The pie chart shown in Figure 13.1 shows the results of the first iteration of the class-II weight estimation, and the respective percentages of MTOW for each component group when the percentage exceeded 3%.

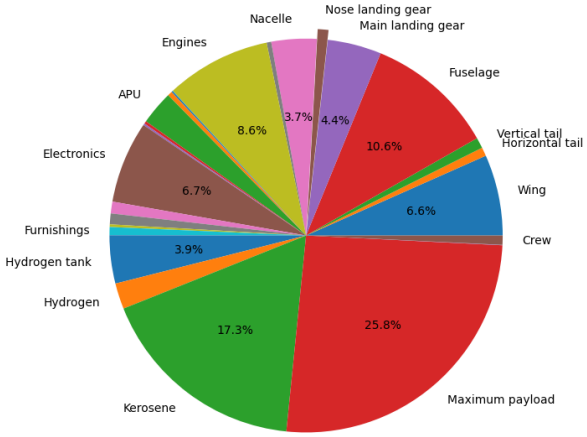

Figure 13.1: Class-II distribution of weights as a percentage of MTOW after first calculation

13.2. Results of First Full Design Iteration

Once the OEW of the class-II weight estimation is obtained, the first design is complete. However, the outcomes are not yet optimal. To optimise the design process and converge to a lighter design, the entire process must be iterated in accordance with the previously generated N2 diagram, as given in chapter 4 of the midterm report [59]. With the new returned values from each department, output parameters for each department must be recalculated in succession. As this is a laborious process, one iteration of the full design will be conducted in this section, and therefore the design will not converge fully to the optimum. If the aircraft concept is continued in further design, this iteration process should be repeated until the result for the OEW converges to the point where the difference in successive iterations < 2%.

13.2.1. Performance diagrams, aerodynamic analysis and planform sizing

Updated values from Class-I weight estimation led to a different Thrust-Wing Loading Diagram. It was found that the initially chosen design point can be maintained, at the expense of needing to size for a $C_{L_{max}}$ of 2.4 for landing, instead of the initial 2.35. Additionally, it turns out that the cruise performance constraint is not limiting anymore, leaving only the take-off and landing performance constraints as limiting factors. The aspect ratio is chosen to be kept equal to the initial value, to assure a wingspan smaller than 36 m as required. Since the value of MTOW is obtained from the iterated Class-I weight estimation and is decreased because of the iteration, the required wing surface area and thrust are also decreased.

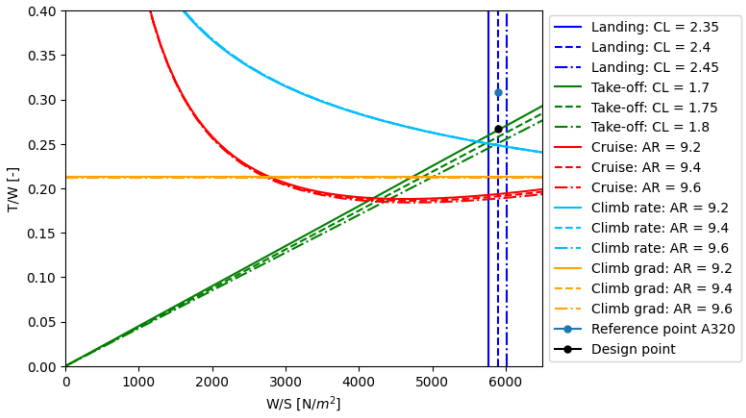

Figure 13.2: Updated Thrust-Wing-Loading Diagram After First Iteration

The changed values of S (and AR) have a direct influence on the wing planform layout and dimensions. In

addition, the increase in $C_{L_{max}}$ for landing requires bigger areas of the high lift devices to compensate for this. It was found that keeping the initial high lift device placement was impossible, since the leading edge flaps would then exceed the wingspan. Therefore, it was chosen to increase the $\Delta C_{L_{max}}$ generated by the trailing edge flaps from 80 to 85%. This allows for smaller leading edge flaps. The new dimensions of the planform and mobile surfaces are shown in Table 13.1.

Table 13.1: Table containing parameter values for wing planform sizing before and after first full iteration

Parameter	Before Iteration	After Iteration	Unit
OEW	457678.55	426246.16	N
MOTW	799095.34	775057.34	N
$W_{F_{used}}$	159760.67	136981.80	N
$C_{L_{max_{landing}}}$	2.35	2.4	-
S	139.49	131.56	m^2
T_{max}	219249.24	206940.31	N
MAC	4.44	4.31	m
y_{mac}	7.14	6.93	m
b_{tot}	35.82	34.79	m
S_{in}	35.18	33.19	m^2
S_{out}	34.55	32.59	m^2
$c_{tip_{wing}}$	2.21	2.15	m
$c_{root_{wing}}$	7.50	7.29	m
$c_{kink_{wing}}$	3.71	3.61	m
$y_{aileron_{inner}}$	14.68	14.26	m
$y_{aileron_{outer}}$	16.47	16.00	m
S_{csw}	2.76	2.55	m
$y_{flap_{TE_{inner}}}$	7.43	7.21	m
$b_{flap_{TE}}$	4.97	5.58	m
$y_{flap_{TE_{outer}}}$	12.40	12,79	m
Swf_{TE}	16.14	17.35	m^2
Swf_{LE}	42.10	31.93	m^2

Hydrogen Fuel Tank and Fuselage Sizing

The fuel tank should be designed to carry the required amount of hydrogen onboard. The volume and dimensions of the tank are derived from the iterated weight of fuel used during flight from the class-I weight estimation. As the amount of fuel burnt during flight decreases with the first iteration, the aircraft can be considered more sustainable. Furthermore, this effect will continue as the lower the amount of fuel that is carried on board, the less of it will be required during flight. To estimate the new amount of fuel required of each type, the ratio of the calculated new fuel used to the old value was used to scale the exact fuel weights. The effect of requiring less fuel is that the hydrogen tank can be made smaller. There is freedom in the tank design as the volume may not necessarily be a fixed value, and the geometry can be altered. Therefore this process is very variable, and to achieve optimum results this should be optimised manually through the use of modelling software. In this iteration, the size of the tank will remain constant as redesign would require a more in-depth analysis. Due to the passenger requirement of 180 passengers and the fixed sizing of the cabin components from modelling, the size (length and diameter) of the cockpit and the cabin did not change with iteration. The fuselage length however is dictated by the sizing, shape and placement of the hydrogen fuel tank. In practice, the tank would be made shorter to approach a more spherical shape, which is the optimum shape, which in turn would decrease the length of the fuselage and therefore the weight of the entire aircraft. Decreasing the weight of the entire aircraft also would reduce the amount of fuel burned, and therefore has positive effects on sustainability. It should be noted that reducing weight in the rear of the fuselage has effects on the position of the centre of gravity location of the aircraft. As less weight is concentrated further aft, less force would need to be delivered by the horizontal tail plane in order to manoeuvre and therefore it is likely to be made smaller. Reduction in tail plane size contributes to the lower aircraft weight, which would also reduce the the amount of fuel required during flight, thus also having a positive effect on stability. It is important that the process of tank redesign is investigated in detail in the future as it has potential to affect design iterations considerably.

Engine Sizing

The engines have been sized to be able to provide the required take-off thrust of $90.000\,\mathrm{N}$, and therefore the newly calculated amount of fuel used during flight is not required to resize the engine. The engine was designed

to satisfy take-off requirements as this was the constraining flight phase. In addition, it was optimised for this flight phase and therefore optimised to minimise the emissions in and around airports. Future recommendations in the area of engine design would be to further optimise the design while considering optimisation for cruise conditions, which can take into account the decreased fuel burned as calculated by the reiteration of the class-I estimation. Making the engine as efficient as possible for these flight phases and fuel use would positively affect sustainability.

Mass, Balance and Stability
Due to the change in fuel weight and subsequently the OEW and MTOW, the position of the aft centre of gravity shifted further aft when calculating the new aircraft balance. This is likely in part due to the fact that less fuel weight is stored in the wing. It could also be affected by the unaltered tank size relative to the change in fuel weight, and for this again the tank should be redesigned. For this reason, the position of the wing is shifted rearwards. Due to the change in range of centre of gravity location, the surface of the horizontal tail plane will change. The limiting factor, the aft centre of gravity, means that a shift backwards should cause and increase in vertical tail plane and the horizontal tail should increase. However, due to the reduced thrust as calculated from the class-I weight estimation, the surface area of the vertical tail plane can be made relatively smaller in the limiting one engine inoperative condition, as the vertical tail would be required to deliver less force to counteract the yawing moment. Furthermore, the horizontal tail plane can be made relatively smaller as the load at the aft of the aircraft is reduced. The results of the iteration of the aircraft mass, balance, stability and control and impacts on empennage sizing can be found in Table 13.2.

Table 13.2: Table containing parameter values for wing planform sizing before and after first full iteration

Parameter	Before Iteration	After Iteration	Unit
$x_{w_{r_{LE}}}$	13.90	14.48	m
x_{LEMAC}	18.45	18.90	m
x_{mlg}	21.08	21.53	m
x_{nlg}	4.00	3.90	m
$cg_{mac_{forward}}$	-0.032	-0.051	-
$cg_{mac_{aft}}$	0.26	0.27	-
S_v	14.592	16.96	m^2
S_h	‘40.23	32.88	m^2

13.2.2. Results of First Full Design Iteration
At the end of the full iteration, the class-II weight estimation can be re-performed to give the redistributed weights. Figure 13.3 shows the results of the iteration. As the fuel weight is decreased, the proportion of fuel decreases relative to the components constituting the OEW. This can be seen as all components except for fuel increase in weight share. For further design, the full iteration process should be repeated until the design converges to a reduced OEW and MTOW so that the design is optimised.

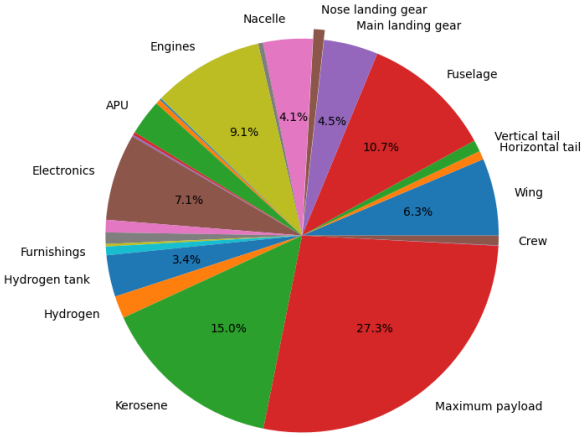

Figure 13.3: Class-II distribution of weights as a percentage of MTOW after first full iteration

14

Operations and Logistics

Given that a hybrid aircraft is a new aviation concept, adjustments must be made to airports in order for the LEAF aircraft to operate. Zero-emission ground vehicles are for example required to comply with the mission statement. In particular, new airport infrastructure is needed to allow for hydrogen refuelling. Section 14.1 details the operations and logistics of the LEAF aircraft. More specifically it details the hydrogen and kerosene refuelling system, passenger and cargo loading and unloading and maintenance operations. Section 14.2 presents the reliability, availability, maintainability, and safety analysis.

14.1. Operations and Logistics Concept

Constança, Guillermo

To reduce the emissions of ground operations by 100%, all operations must be performed using an alternative energy source. Figure 14.1 shows the ground operation segments of the LEAF aircraft. It includes the hydrogen and kerosene refuelling in green, loading of passengers, cargo and service items in blue and operational trucks in orange.

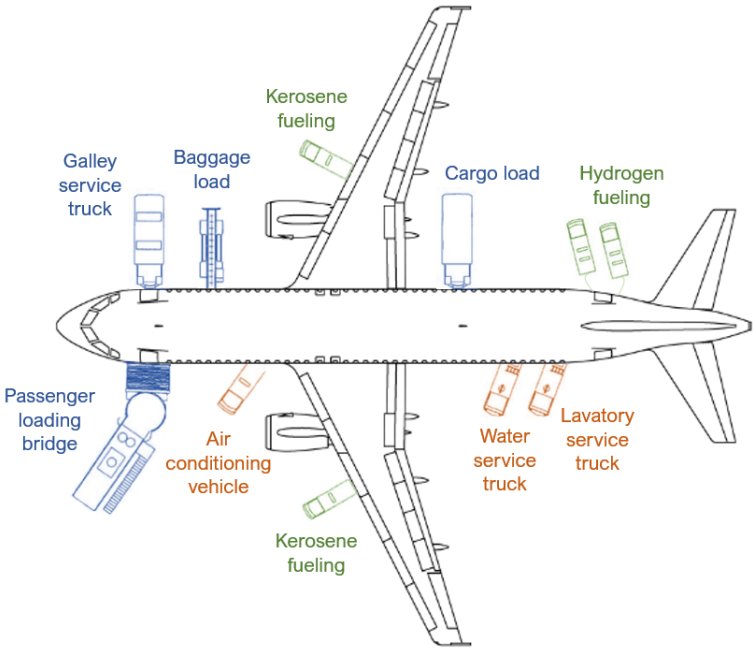

Figure 14.1: Ground handling arrangement [4] [5] [6]

Hydrogen Refuelling

Using liquid hydrogen as a fuel in the aviation industry has not only substantial implications in the fuel supply chain but also on the airports infrastructure, operations and logistics. The aircraft's hydrogen tanks will be refuelled with hydrogen by separate trucks that connect through insulated pipelines to the aircraft [59]. These trucks are refuelled at a remote location near the airport to minimise boiloff during transport, in a large hydrogen storage location. The liquid hydrogen refueling trucks will be considerably different compared to the existing refueling trucks in airports, and will require specialised training and a safety assurance framework for aircraft personnel [86]. However, these are manageable changes for the airport given the increase in hydrogen demand and expertise. Figure 14.2 demonstrates the supply chain of the liquid hydrogen from its energy source to the aircraft refueling.

As mentioned in Chapter 8, there are certain operation requirements imposed on thermal and fatigue design regarding the refuelling the hydrogen tank. During overnight or extended stay, the tank internal temperature will increase as well as the internal pressure, and to protect the structure from delamination, the tank should either be drained to a state which only has limited amount of hydrogen or the pressure needed to be released through the pressure release valve. Also, to avoid fatigue fracture, in daily operation, during refueling, the pressure of the tank should not be completely emptied and some hydrogen should be kept inside to provide the pressure. For each flight duration, the amount of liquid hydrogen should be calculated based on mission time, range,

payload and etc. to minimise impact on tank structure. When operating short-haul flight, the tank will not need to be fully filled, thus one refuelling truck might be needed for the refuelling work to lower operation cost.

To ensure that the mission is sustainable as whole, it is of paramount importance that green hydrogen is used. In other words, that hydrogen originates from a clean energy source that does not pollute the environment. The most common production method is renewable energy powered water electrolysis [86]. After production, the hydrogen must be liquefied and transported to a storage area, from where it will be transported in refueling trucks to the airport.

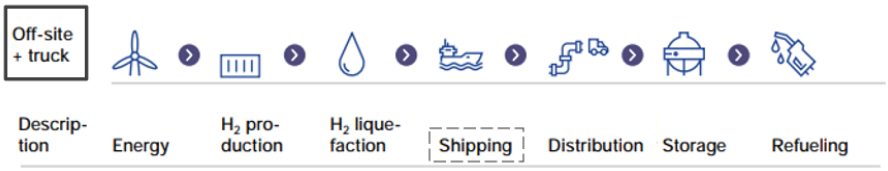

Figure 14.2: Fuel Supply Chain for Liquid Hydrogen

Kerosene Refuelling

Refuelling the kerosene tanks will be conducted in a conventional way, in order to make the operations of the aircraft resemble as much as possible as that of an A320-200. Fuel is pumped into the tanks through a secure and sealed connection in the wing. The aircraft will be primarily refueled using underground kerosene fuel hydrants to facilitate ground operations. If required in smaller airports, refuelling kerosene trucks can be used as shown in Figure 14.1. In Figure 14.5 an overview of all the operations needed to be taken by the airport and its personnel is shown. Under function F4 are all the chronological steps shown needed to refuel the aircraft.

Passengers and Cargo

The interior and cabin doors of the LEAF aircraft are designed to resemble an A320-200 as much as possible so that the change in airlines operational structure is minimised. The aircraft should be refueled, at least for the liquid hydrogen refuelling, when all the passengers are away from the aircraft in order to minimise the consequences of a possible problem during refuelling of the very flammable liquid hydrogen. Furthermore, loading and unloading of the cargo should be done after refuelling the aircraft with at least the liquid hydrogen, because the airport personnel that deals with this will be relatively close to the hydrogen tanks. This is also shown in Figure 14.5 under function F5. Main differences to the ground operations of a typical aircraft is the addition of the liquid hydrogen fueling operation and the removal of the towing truck due to the addition of regenerative braking in the landing gear.

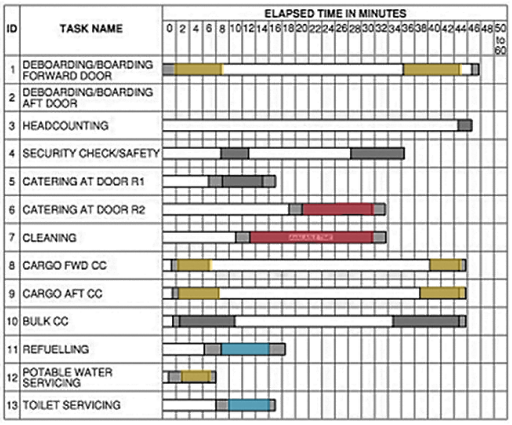

Figure 14.3: Turnaround time schedule for an A320 [87]

Turnaround Time

According to a study from the Technical University of Dresden the turnaround time for an A320 is approximately 48 minutes. The time schedule per ground operations task for the A320, that make up the total turnaround time, can be seen in Figure 14.3. Given the similarities of the LEAF aircraft compared to an A320, the boarding and un-boarding of the passengers in addition to all other ground operations tasks shown in Figure 14.1, except for refueling, are identical to the A320.

Given the uniqueness of the LEAF's aircraft refueling operation, it will be discussed further. First, approximately $13\,777$ kg ($6,888$ kg per wing) of kerosene must be refueled. On average kerosene is refueled 1,500 Liters per minute [88]. Hence, refueling both kerosene tanks at the same time yields a fueling time of approximately six minutes. This value is slightly lower than for the A320 given that the LEAF aircraft transports less kerosene due to its hybrid nature.

Furthermore, liquid hydrogen refueling hoses can attain 900 Liters per minute [86]. However, as hydrogen usage becomes increasingly more popular, the industry is striving to reach flow rates of above 1,000 Liters per minute [86]. In order to meet the required turnaround time, the amount of refueling ports are doubled. Given that

the aircraft carries 1687 kg or $23\,760$ Liters, the refueling time is 13.2 minutes using two ports. Key challenges still remain with respect to refueling safety and precautions needed. This will impact the ability to run parallel operations in-between flights. It is also important to note that liquid hydrogen hoses have a considerably heavy weight and low manoeuvrability, complicating the refueling operation of hydrogen.

Two turnaround times are calculated for the LEAF aircraft. A first, 'worst case scenario', turnaround time is devised, taking into account that no other operations can be conducted in parallel with liquid hydrogen refueling. This yielded a turnaround time of 66 minutes, which is 38% higher than that of an A320. A second turnaround time was calculated taking using two hoses for hydrogen refueling, and running the aircraft cleaning at the same time as the liquid hydrogen refueling. This can be accomplished by adopting robot cleaning, which reduces the risk to humans. By doing so, a turnaround time of 48 minutes can be achieved, meeting the requirement that the LEAF's turnaround time must not be greater than that of an A320.

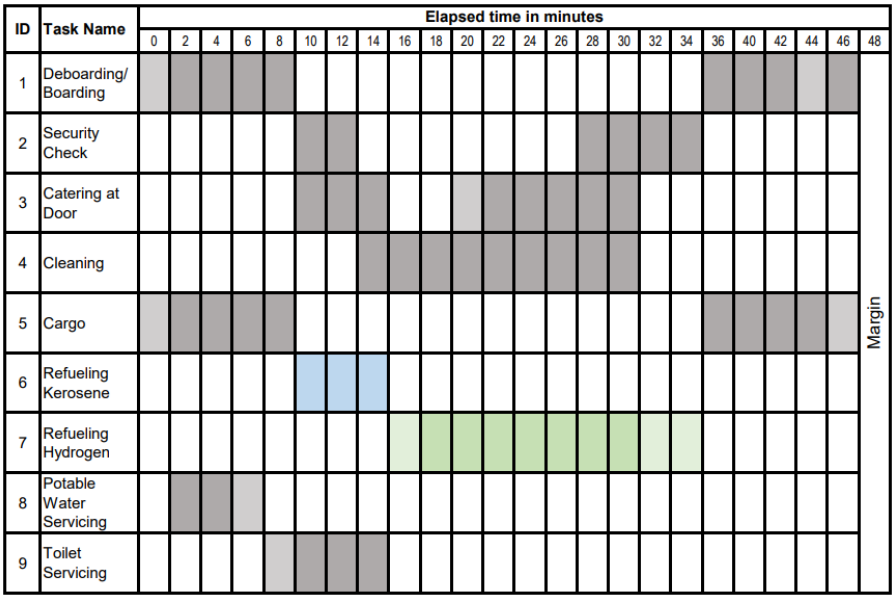

Figure 14.4: Turnaround time schedule for the LEAF aircraft conducting parallel operations

Maintenance

Maintenance of the aircraft is of paramount importance to ensure the reliability and thus safety of its operation. The maintenance can be split into airframe and engine. The maintenance procedure of the LEAF aircraft will resemble that of an A320-200 class aircraft, except the addition of the liquid hydrogen tank and the modified engine.

According to EASA, four types of inspections should be conducted throughout the lifetime of the aircraft [89]. These are listed as follows:

- **25 hour inspection**: a special inspection should be performed after the first 25 flight hours of the new aircraft.
- **100 hour inspection**: after 100 hours of operation the aircraft shall undergo a complete maintenance check.
- **Annual inspection**: a thorough, complete inspection should be conducted annually.
- **Unscheduled maintenance check**: if the aircraft experiences any unusual activity, a special inspection should be conducted.

At the same time, a replacement schedule should be implemented for certain components such as the the rubber dampers in the landing gear and the batteries every X amount of years.

Each component of the aircraft is comprised of a unique material and is under a specific load during operation. Table 14.1 details the failure or malfunctions that should not be identified for each aircraft item. Furthermore, several key failure modes can be identified visually or by using non-destructive testing. With respect to the airframe, the fuselage items should be checked with the metal parts inspection parameters from Table 14.1. The wing and empennage should also be inspected in the same manner, in addition to careful inspection of its high-lift devices and control surfaces.

The landing gear is a vital aircraft system that requires close inspection of the following items. Check the overall condition, including possible cracks and damage. The tires should not only be pressure-checked but also visually inspected for excessive wear and cuts. The fuel, oil, cooling or any other type of liquid system should be closely inspected for leakages, attachment and security malfunctions. Load intensive components, such as the engine mount, should be thoroughly be checked for fatigue, cracks, bending, corrosion and distortion. Additional systems to be inspected are the cockpit group, in addition to operational and functional check.

Table 14.1: Possible failure modes per aircraft component [89]

Aircraft item	Movable parts	Fluid lines and hoses	Metal parts	Composite parts	Structural fasteners	Wiring
Inspection items	- Security of attachments - Excessive wear - Proper operation & adjustment - Cracked fittings - Deformation - Corrosion	- Leaks & cracks - Twisting - Dents & kinks - Deterioration - Proper routing	- Fatigue cracks - Distortion - Deterioration - Paint condition - Any other apparent damage	- Cracks - Bond separation - Delamination - Wear - Deformation - Pain condition	- Wear - Damage - Stretch	- Defective insulation - Heat deterioration - Terminal corrosion - Chafing - Lose or broken terminals

By performing regular inspection checks, preventive maintenance can be conducted. This not only increases the reliability and safety of the aircraft but also reduces the operational cost of the airline. Furthermore, three operations should be conducted to ensure preventive maintenance.

1. **Hard time**: the concept of removing an aircraft component when it reaches a pre-defined limit [90].
2. **Functional inspection**: to regularly closely monitor the conditions of each aircraft parameter to prevent failure [90].
3. **Functional verification**: requires performing an operational check of hardware function(s) to determine each function's availability if it is normally hidden from the scrutiny of the flight and operating crew.

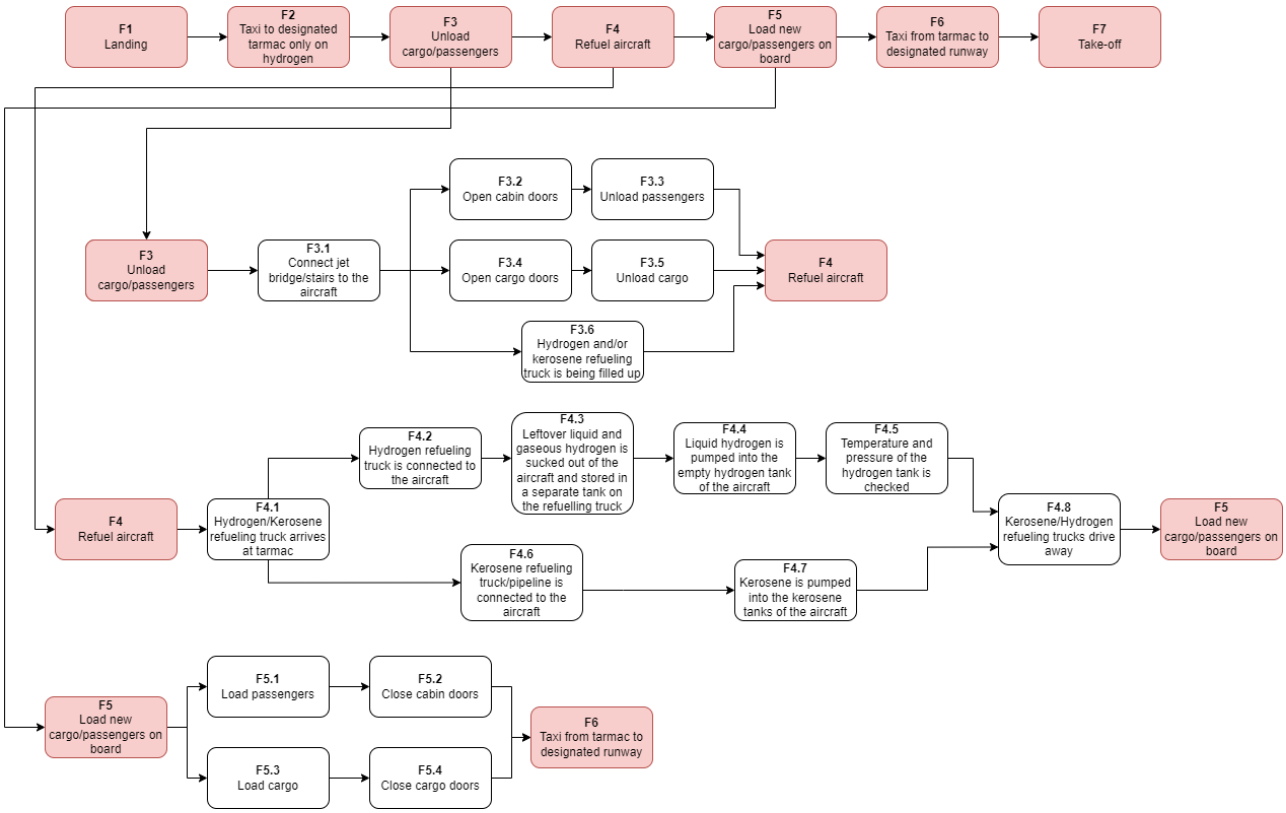

Figure 14.5: Functional flow diagram of all the ground operations needed to be taken by the airport and others from landing of the aircraft until take-off on a typical schedule

14.2. Reliability, Availability, Maintainability and Safety Analysis *Constança*

"The goal of RAMS is to create input data for the assessment of the suitability of a system in a life cycle. That is, to provide data on failure rates of the system, possible failure modes, MDT, maintenance operations, hazards and their consequences, etc."

Reliability

Reliability is the probability that a failure will *not* occur in a given time frame. Failure may occur in each individual subsystem or on the system as a whole. The reliability of the aircraft system is divided into five sub-components. They are listed as follows.

- **Dispatch reliability**: is the likelihood of the aircraft departing on the scheduled time frame.
- **System reliability**: the failure probability of specific aircraft systems is monitored to determine their reliability. In order to do this, a selected number of components is removed in an unscheduled manner [91].
- **Structural reliability**: comprises of monitoring and determining the reliability of each structural component. During maintenance, this can be estimated using non-destructive testing methods and structural health monitoring [1]. In addition, sensors should be integrated in the aircraft to continuously monitor and detect possible failures.
- **Components reliability**: state-of-the-art aircraft are fitted with an onboard maintenance system [91]. Sensors continuously measure technical parameters to detect any possible malfunction during operation.
- **Power system reliability**: the reliability of the power system components can be regularly compiled throughout the operation of the aircraft and then analysed.

The following aircraft systems and components are individually analysed with respect to reliability.

- Engine system
- Control system
- Structures

The engine system comprises of several newly developed technology and recently-designed systems. Given the novelty and low technical readiness level of the liquid hydrogen components and corresponding system, a thorough investigation and testing should be conducted. Nevertheless, preliminary research and failure estimates of hydrogen system components (such as cryogenic valves and sub-components) used in various applications has already been performed by Prof. Fydrych and Prof. Consogno [92]. According to one study, the fuel injection system is considered to be the most critical component, with respect to reliability, in the engine system [93].

In addition, the control system consists of a multitude of vital subsystems for the aircraft. These include directional control systems, longitudinal control systems, flaps, stabilizers, landing gear, and rudders. The control system is of paramount importance as each component is responsible for controlling the aircraft in the x, y and z axes of rotation throughout the flight [93]. Research on *Modeling a reliability analysis of aircraft components and system*, estimated that the trim control system is the least reliable subsystem [93].

Availability

Availability refers to the probability that the aircraft system is accessible and operational when required, with the exception of it being malfunctioning or undergoing maintenance checks [94]. In simple terms, it is the fraction of the aircraft's lifetime for which it is usable to the airline. It is important to maximize this percentage, in order to reduce cost and maximise the airline's revenue from the aircraft availability. Figure 14.6 details the availability schematic of an aircraft, clearly indicating what classifies as operating and non-operating time. It is apparent that availability is a function of both reliability and maintainability.

[1] A system for continuously monitoring the structural health of an aircraft [91]

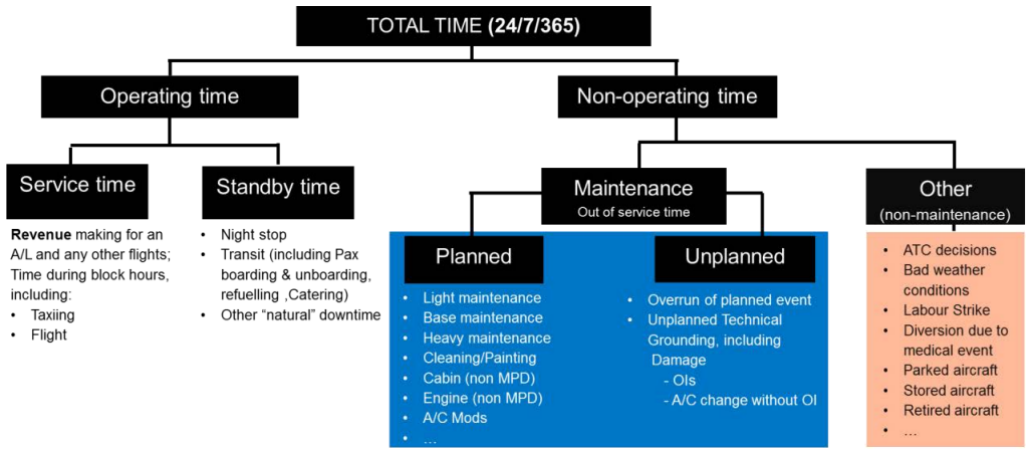

Figure 14.6: Aircraft lifetime availability schematic [94]

All planned and unplanned aircraft maintenance checks, for both technical and non-technical motives, comprises of the "aircraft non-operating time"[94]. First, planned inspections include routine maintenance programs such as the A, B, C, D checks present in Table 14.2. Second, unplanned maintenance procedures occur due to unforeseen aircraft malfunctions or foreign-object damage. These are hard to quantify due to their unpredictable nature. Thirdly, unexpected unavailability periods may occur and contributes to the reduction of available time given that availability time is calculated as follows:

$$\text{Availability time} = \text{Total time} - \text{Unavailability time}$$

Hydrogen Fuel Supply
Given that liquid hydrogen is a novice aviation fuel, currently in development by a multitude of companies, in the beginning operational years hydrogen fuel may not be accessible in certain particular airports. This may impact the operational time of the aircraft. However, the aircraft can operate with reduced performance using solely kerosene given that the engines are hybrid. Thus, only impacting the availability for planned longer route flights. By 2050, it is projected that hydrogen will be more accessible and reliable [86].

Regenerative Braking & Engine
The new liquid hydrogen engine and tank system, in addition to the innovative regenerative braking system are newly developed systems which required increased maintenance checks due to the lack of experience and knowledge with these components (in comparison to mature systems). In addition, in case of failure, these components are an integral part of the aircraft and thus would impact substantially the availability time of the aircraft.

Maintainability

Aircraft maintainability is the capability of the aircraft to operate efficiently and safely while minimising both planned and unplanned maintenance checks. Table 14.2 details the scheduled maintenance checks required by an aircraft.

Table 14.2: Maintenance check intervals [95]

	Pre-flight check	A Check every 150 h	B Check every 750 h	C Check every 3,000 h	D Check every 20,000 h	Unplanned maintenance
Ground time	0 h	8 h	24 h	72 h	21 days	-

Pre-flight check consists of simple visual inspections of the aircraft performed by the pilots and a mechanic right before the flight operation. The A check carried out approximately every 150 flight hours, should include general operational checks of the airframe, engine and its systems. The B check includes the A check parameters plus preventive maintenance, fluid servicing and lubrication [95]. The C check is a more thorough and detailed inspection of each aircraft component, including flight control calibration. The D check is a highly thorough structural maintenance check conducted after removing the cabin interior. Finally, unscheduled maintenance checks may need to be performed in case of anomalies.

Engine, Hydrogen Tank and System
With respect to the fuel storage tanks, in particular the liquid hydrogen tank, must be thoroughly inspected. Measurements such as the pressure, temperature and humidity should be monitored continuously in addition to the consumption and flow rate of the fuel. From these parameters, possible leakages and tank material degradation (such as the foam insulation) can be identified. Due to the liquid hydrogen's cryogenic temperatures, the entire hydrogen system, including tubes and piping, should be extensively examined.

Maintenance Check Procedures
Determining the structural and operational state of each aircraft subsystem, should be the first stage in any maintenance procedure. In order to detect any flaws, visual inspection in combination with non-destructive testing procedures should be conducted. System maintenance checks mainly consist of aircraft operational examinations.

Safety
Safety is a crucial parameter that not only exists to protect the aircraft but also its payload and passengers. According to the Federal Aviation Administration (FAA) the relationship between the severity and probability of failure is classified as follows [96]:

- Failure conditions with no safety effect have no probability requirement
- Minor failure conditions shall be probable
- Major failure conditions shall be no more frequent than extremely remote
- Catastrophic failure conditions shall be extremely improbable

The safety of the several key aircraft systems are discussed in this section.

Hydrogen
As hydrogen is highly flammable and has relative low ignition energy, presence of fire or spark should be fully eliminated when operating this aircraft. This can be done by enforcing a more strict no smoking rule inside the cabin and on the tarmac. When refuelling, both aircraft and the fuel truck should be grounded to prevent static electricity discharge. Refuelling operator should wear anti static personal protective equipment (PPE) and fully discharged when entering the operation site. Also, rich oxygen environment should be avoided when doing refuelling operation.

As liquid hydrogen must transferred from tank to the truck, leakage might happen. Due to the cryogenic temperature, although there are insulation around all pipelines and connections, operator should also add low temperature PPE into consideration to minimise exposure.

As hydrogen is odourless, colourless and tasteless, and highly diffusive, leakage will not be easily seen by visual inspection, and also because of the yet lack of study on large scale application of such hydrogen tank (high pressure, low temperature, etc.) , more often inspection using ultrasound to detect internal damage is required to ensure safety operation.

15 Production

Production plan is an integral part of the aircraft design cycle and a necessary step for it to enter the market and gain certification. A step from design to the physical product is challenging from both logistical and environmental perspective. Therefore a production plan have been devised for the LEAF aircraft where production of individual components as well as their assembly will be evaluated. First, production of structural components is considered in Section 15.1. It is followed by Section 15.2, detailing production of aircraft aerodynamics. Next, production of energy storage and propulsion system is looked at in Section 15.3. Lastly, the final assembly is evaluated in Section 15.4.

15.1. Structures

Giorgio

The production of the structure is a critical part of the project, as any small defect could have an impact on the performance and most importantly the safety of the aircraft. Similarly to the design process, the production plan will be divided between the fuselage, wingboxes and empennage.

15.1.1. Fuselage

As seen in Figure 15.1 [1], the fuselage of the aircraft is made of an aluminium skin strengthened by a set of stringers and ribs distributed throughout the length of the fuselage. Additionally, various cutouts need to be made for the windows and the different doors.

Figure 15.1: Example of a fuselage structure

The aluminum skin will be divided into 5 sections longitudinally, each with their own thickness defined in Figure 10.5.1. Furthermore, as seen in Figure 15.2, the fuselage cross section will be divided into 4 different panels, top, bottom and two sides:

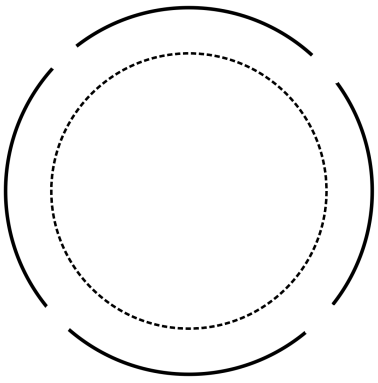

Figure 15.2: Fuselage cross-section displaying the four different panels that will be used for manufacturing

Each of these panels will then be bent into shape with the help of a press brake. The die for the press will need to be designed accounting for the spring back effect that occurs after the load is removed. An advantage of this press system is that the cut-outs for the windows and doors can be produced in the same process. Next, the stringers on every section will be attached using solid rivets with a countersunk head to improve the aerodynamic characteristics. Finally all the sections, together with the floor will be assembled and riveted together. The final result will be the 5 cylindrical sections of the fuselage, which will be joined at the final assembly.

15.1.2. Wing & Empennage

For both the main wing and the empennage structure, the same production process will be used. Similarly to the fuselage, the wingbox skin will be produced in four different sections, which can be seen in Figure 15.3.

[1] URL https://www.hexagonmi.com/nl-nl/solutions/industries/aerospace/aircraft-structure/machine-tool-probing-for-aircraft-fuselage-sections-and-floor-panels [cited 15 June 2022]

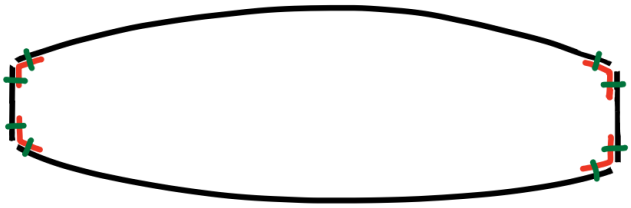

Figure 15.3: Wingbox cross-section displaying all the different elements to create the general shape.

First steps of the wingbox production is to attach all the stringers and ribs to the top and bottom skins with solid countersunk rivets to help with the aerodynamic performance of the wing. The front and aft spar are left for the end, as for the solid rivets, access to both sides of the skin is needed. Once all the quality checks are performed, the wingbox will be closed by attaching both spars. These spars will be attached with blind rivets, which allow the installation without having access to both sides of the spar. Furthermore, the spars will be covered by the airfoil, so the aerodynamic of the rivets is not important.

15.2. Aerodynamics

Giorgio

The aerodynamics production takes the already assembled wingbox explained previously in Subsection 15.1.2 to complete the airfoil shape. Given that this will produce most of the lift of the aircraft, it is crucial that the shape is smooth and well-maintained, without possible imperfections at the surface.

Similarly to the process for bending thin aluminium plates for the structure, a special die will be produced in order to bend the plate into the correct airfoil shape. To retain its shape during the flight, the structural elements for the wing such as ribs and stringers will be riveted into shape. Finally the airfoil will be riveted together with the wingbox to end up with the final wing.

Figure 15.4: Riblet technology installation

With a similar process to the production of the main wing airfoil, the control surfaces airfoils will be produced. Those will be attached to the retraction mechanism which has been previously casted with liquid metal and assembled with all the necessary actuators. The final product can be seen in Figure 15.5[2]:

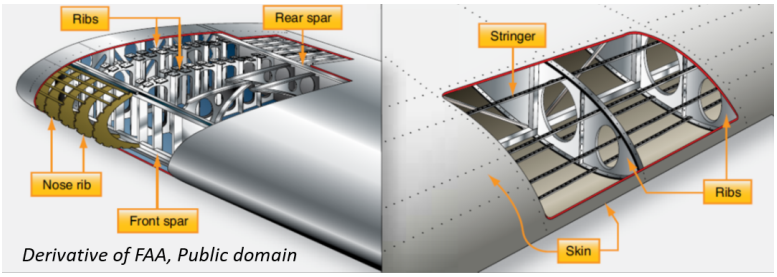

Figure 15.5: Wing structure needed to achieve airfoil shape

Finally when the wingbox is complete, the surface riblets will be installed. This technology is presented as large plastic stickers that are glued into shape. These stickers will be cut with a computer program in order to minimise waste. An example on the riblet installation can be seen in Figure 15.4[3].

15.3. Power & Propulsion

Jelle, Luke

15.3.1. Hydrogen tank

As shown in Chapter 8, there are three layers in constructing the hydrogen tank. The inner shell bearing pressure load is made of aluminium 7068-T6511, the middle layer foam is used for insulation and made of reticulated

[2]URL https://ocw.tudelft.nl/course-readings/3-4-1-introduction-to-wing-structures/ [cited 15 June 2022]
[3]URL https://www.lufthansa-technik.com/aeroshark [cited 15 June 2022]

vitreous carbon foam (density 0.05kg/m^3) and the external fairing is made of aluminium honeycomb to protect the foam.

For the inner tank, the cylindrical part and the hemispherical part are manufactured with different techniques due to its shape difference. To manufacture the cylindrical part, the metal sheet firstly undergoes shape drawing process to the desired thickness, then it is cut to the desired length (the circumference of the tank) and will undergo inner side treatment to prevent corrosion by hydrogen. After that, the edge is processed to a ”V” shape for further connection purpose. Then the processed metal sheet is sent to the rolling machine to form the desired curvature and ultimately to a full cylinder. Finally, the connection is welded. The hemisphere on each side will start with sheet metal at desired thickness, then it will undergo press forming to get the desired curvature. Finally, the surrounding waste material will be removed as well as opening for pipes. After the three parts are processed individually, the whole tank is welded together. It is worth noticing that stress concentration due to the imperfection of the connection technique (welding) needs further investigation as well as the accumulated internal stress during the manufacture process. The outer surface is polished and treated for further adhesive needs.

Regarding the carbon foam layer, it is cut into the desired shapes: two hemisphere caps and one cylindrical part.Furthermore, holes are cut into the hemispherical foam caps, in order to attach the pipes at a later stage. The inner side of the foam is applied with adhesive and then the metal shell is slide in. Similarly, the fairing is rolled into desired shape from whole sheet and welded and bonded with the foam using adhesive. It is worth noticing that during final production of the tank, the environment should be filled with inert gas to avoid future condensation of oxygen.

15.3.2. Engines

The blades on the compressor will be cast, after which they are machined. The turbine blades will be made in the same way. After machining, a ceramic coating is applied. After this, the holes used for creating the cooling film are produced using a laser. The fan blades are cast by first casting the leading edge, after which the remainder of the blade is cast on. This order is used since the material used for the leading edge has a higher melting point. The blade is then machined. The spools will be cast as well.

15.4. Final Assembly

Igor, Christoph

Assembly is a process employed in aircraft manufacturing due to its numerous benefits, which include the ability to parallelise production tasks to speed up the workflow and reduce cost. Assembly also enables easier maintenance, especially when class C or class D checks are performed, as the components can be inspected separately. The aircraft is assembled on the assembly line, divided into stations performing given tasks. An aircraft in production advances to the next station every fixed time interval, referred to as the deliver interval (DI) [97]. Multiple smaller sub-assembly lines will join into the final assembly line at various points. These sub-assemblies include the fuselage section, wingbox and empennage structures as well as engine with nacelles. An example scheme of an assembly components is presented in Figure 15.6.

Assembly Principles

Aircraft assembly is a lengthy and complicated process, which requires detailed planning and adherence to set rules in order to be performed efficiently and within time limits. The most important principles of the assembly line relate to places and types of divisions of the assembly line, station workloads and characteristics of assembly jigs.

Divisions of assembly line into stations are crucial to establish a balanced and efficient workflow. Mounting divisions will mostly be visible in sub-assembly lines, where movable parts required for operations, like control surfaces or high lift devices will be assembled onto their respective structural components. The main assembly line will employ division primarily based on production divisions, enabling equal distribution of the workload at stations and thus no downtime in production. Examples of such divisions include the joining between main sections of the fuselage, as elaborated on in Section 15.1, wing-fuselage and wing-empennage intersections or mounting of the nacelles. Special attention should be paid to the rigid-flexible principle, which states that flexible parts should be joined with rigid parts as they can be adjusted on assembly jigs. It should also be ensured that the divisions are made at natural places in the structure, for instance no division should occur within the door frame.

The assembly itself will take place at individual stations utilising the assembly jigs. The most important features of the jigs include sufficient stiffness and strength to support the parts as well as accessibility to enable easier

assembly. Joining methods for the aircraft components used in assembly of LEAF aircraft will include primarily riveting and bolting with little welding or adhesive bonding as they are deemed not fit for the parts and materials used as well as being less environmentally friendly in case of adhesive bonding. The assembly line will also apply the hole-to-hole principle to eliminate drilling at assembly stations. This requires tight tolerances in part manufacturing of the order of 0.1 mm [97], as the aircraft is made mostly out of metallic components.

Assembly Flow

The assembly flow details the order of activities of the assembly of the complete aircraft from part manufacturing until the roll-out of complete product off the assembly line. The assembly flow diagram is presented in Figure 15.7. Inspiration for the assembly flow diagram was drawn from [97].

Flow of the main assembly line is centered around assembling the sections of the fuselage. It should be noted that the hydrogen tank and its support structure is part of the sub-assembly of the rear fuselage section, which implies that it is fitted and joined before that section is joined with the rest of the fuselage. Once all the fuselage sections are joined the wing sub-assembly is fixed to the assembly followed by the empennage sub-assembly including the vertical and horizontal tail-planes. The sub-assemblies of the respective aerodynamic components will include the movable surfaces such as elevators, flaps or ailerons. The main and nose undercarriages are also parts of the wing and front-fuselage section respectively. The last parts assembled onto the structure from the outside of the aircraft are the engine nacelles, which are attached to the nacelle support structures on the wings.

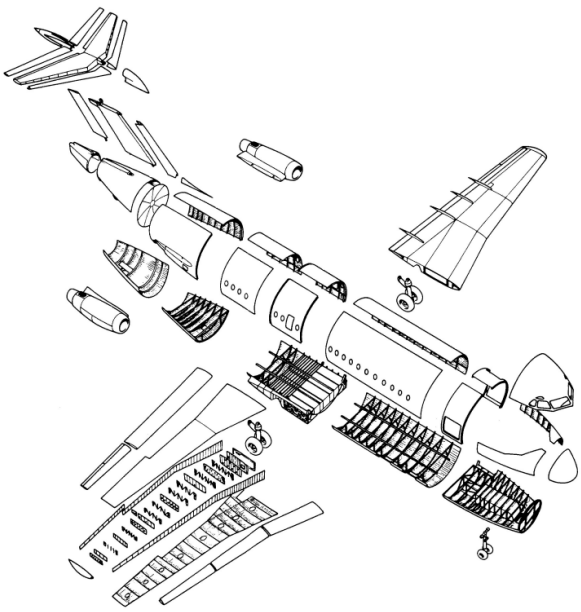

Figure 15.6: Example of an assembly breakdown [97]

Once the airframe has been assembled all of the internal systems can be put into place. While individual parts, such as the hydraulic actuators for wing movable surfaces or landing gear are part of their respective sub-assemblies, aircraft-wide systems such as hydraulic, pneumatic or electrical systems need to be connected together. Furthermore, the hydrogen fuel system surrounding the tank needs to be assembled and connected with the nacelles in order to be ready for integration with the engine. Once the essential aircraft systems are in place, the furnishings of the cabin can be attached inside the fuselage along with the smaller electrical components, which production is outsourced with only the final assembly being carried out by the aircraft manufacturer. At that stage the aircraft will be ready for flight-testing, which will finally determine its airworthiness.

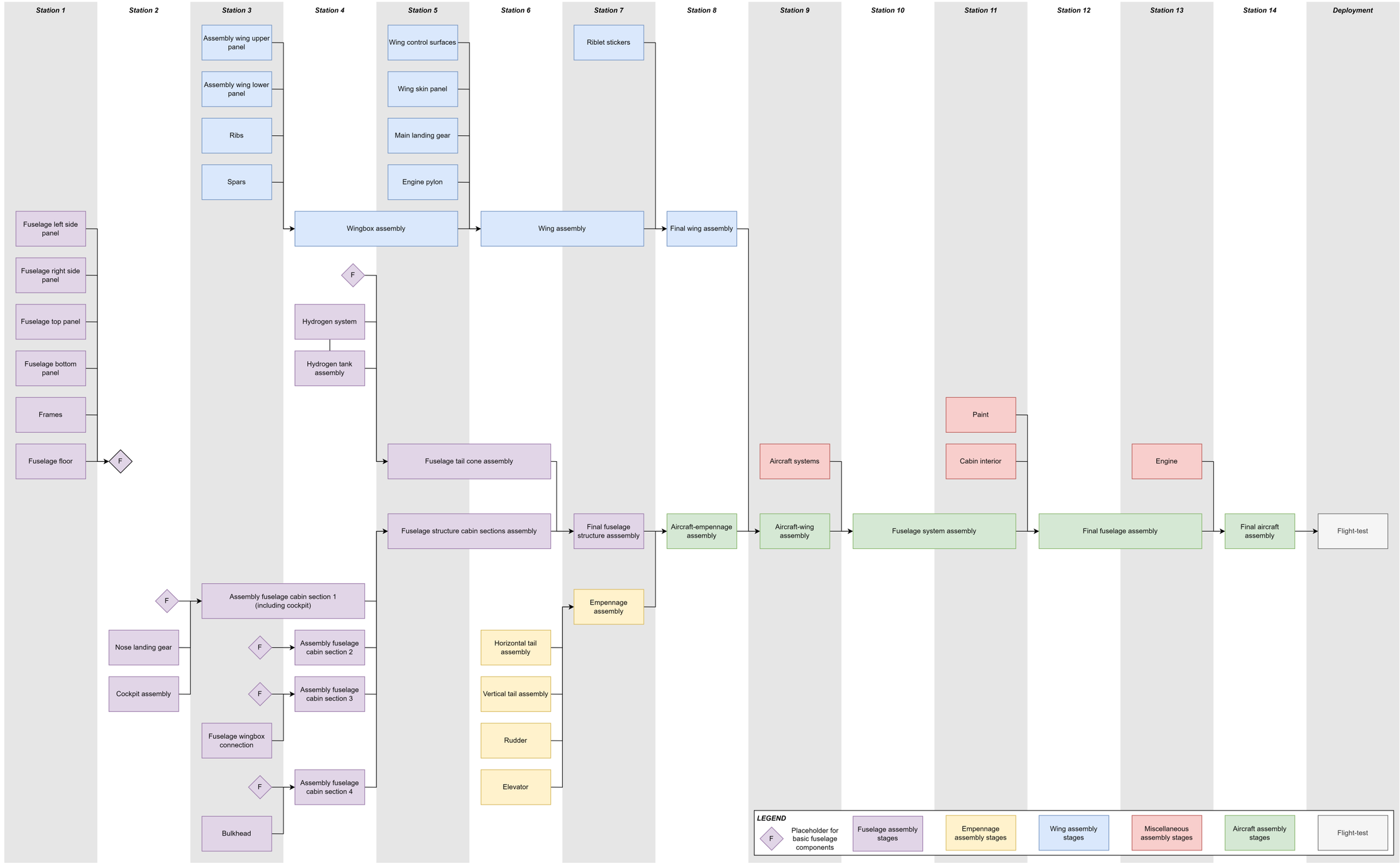

Figure 15.7: Assembly Flow Diagram

16 Project Design and Development

16.1. Project Design and Development Logic

Jenny

After the completion of the DSE, steps should be taken in order to materialise the designed concept into the final completed product which will be available for purchase on the market. The concept will enter the production phase. This chapter will give a short description of the processes that are followed after the completion of the DSE until the product is fit to enter the market.

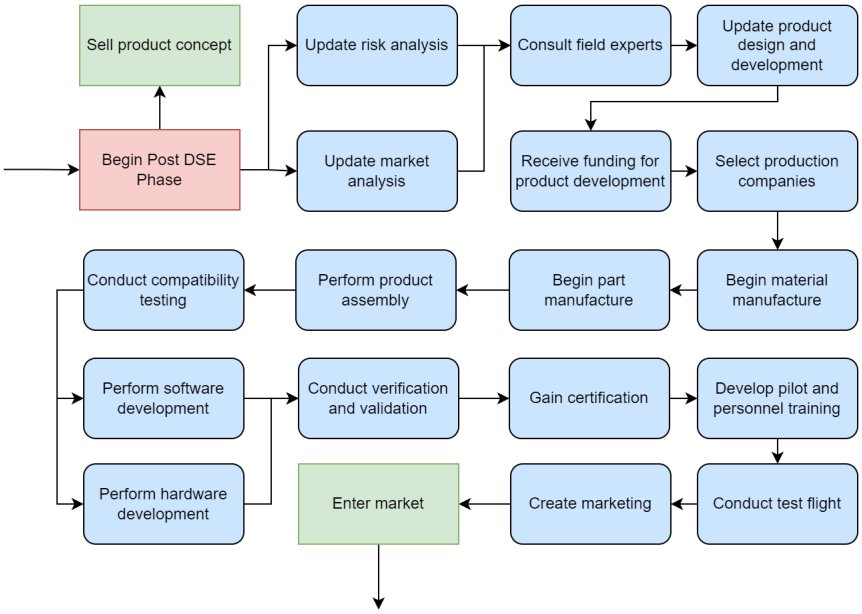

Figure 16.1: Project design and development logic: from beginning post DSE phase to market entry

The first stage of the production phase will be to consolidate the design once more. This is done by updating the risk and market analyses, consulting experts in respective fields and then concluding by updating small aspects of the product design and development based on the feedback of these tasks.

Once funding has been received, material and part production can commence by selecting production companies. As it is likely that the concept will not follow the trajectory of conventional aircraft production, care should be taken in selecting the production companies that are capable of producing the required parts for the design. The aircraft should then undergo assembly, before compatibility testing is conducted to ascertain whether the aircraft complies with existing flight regulation.

Next, hardware and software can be developed in part simultaneously, before these are verified and validated. After gaining fit to fly certification, pilots and personnel can be trained to operate the aircraft; the unconventional aircraft design will require new training which may be unfamiliar so it is important that this is conducted successfully. Lastly a test flight can be conducted and when this is successful, the aircraft will be able to enter the market by 2035.

16.2. Project Gantt Chart

Luke

The future events and tasks after the DSE phase, adapted from Section 16.1, are shown in Figure 16.2. The time phase in the horizontal bar is united in quarters and the total time span of this chart is 10 years.

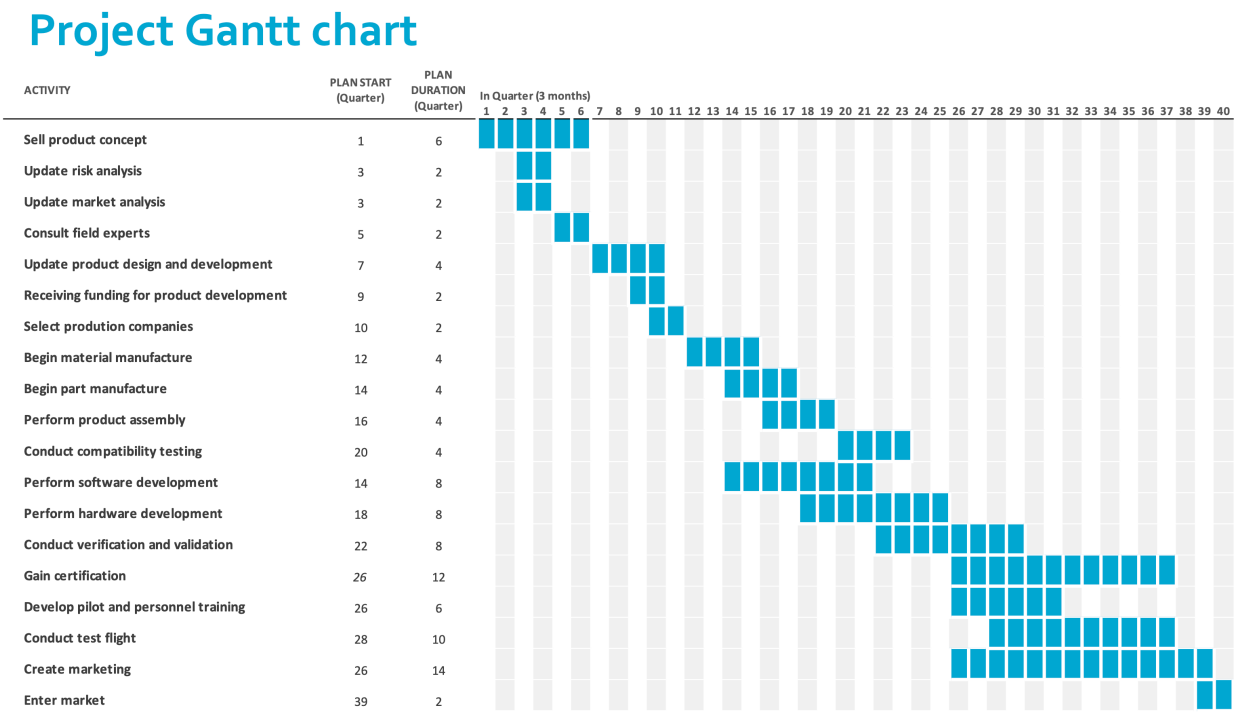

Figure 16.2: Project Gantt chart (each block represents 1 quarter)

17 Financial Analysis

To check if the LEAF aircraft is economically sustainable a financial analysis of the aircraft has been performed. This analysis is subdivided into the acquisition cost, return on investment and direct operational cost.

17.1. Acquisition Cost

Guillermo

In order to estimate the actual acquisition cost of the LEAF aircraft for airlines it is necessary to make a cost breakdown structure, or CBS. The acquisition cost of the LEAF aircraft is divided into three main parts as shown in Figure 17.1: development cost, profit and manufacturing cost, or flyaway cost for unit aircraft. All of the cost estimation formulas used in this section are coming from T. Zhao [7] [7] and Raymer [8].

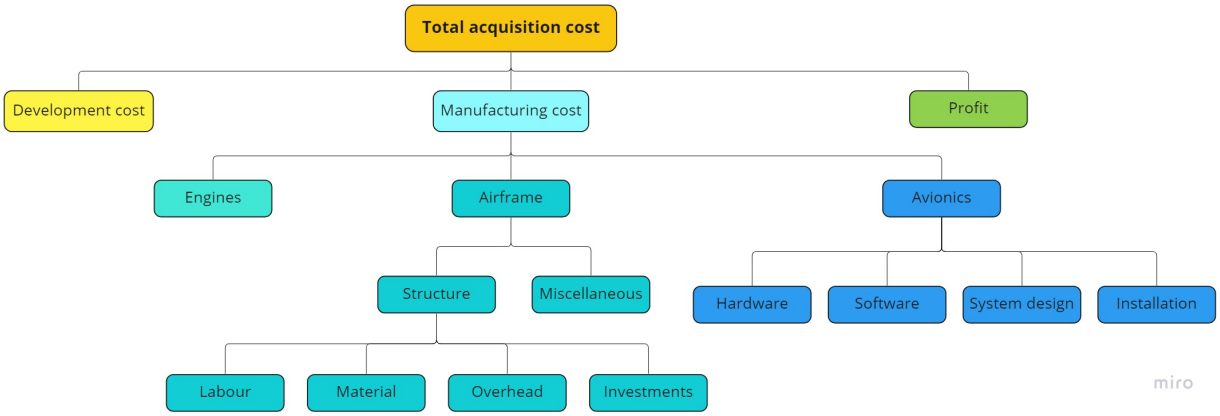

Figure 17.1: Cost breakdown structure for the acquisition cost of the LEAF aircraft.

The development cost of the aircraft is estimated by adding the development cost of an A320, which is €1.85 billion, to the development cost of a new power and propulsion system. Developing a new power and propulsion system costs about €1.0 billion [98]. This means that the total development cost of the LEAF aircraft is estimated at €2.85 billion.

The manufacturing costs are subdivided into three main categories: engines, airframe and avionics. In order to estimate the cost of the engines Equation 17.1 is used [7]. Multiplying this value by two, since there are two engines, an engine cost of €40.9 million is obtained per unit aircraft.

$$C_{engine} = -18.144 + 0.0191 \cdot Thrust_{max} + 0.193 \cdot BPR + 0.011 \cdot T - 12.187 \cdot SFC + 20.174 \cdot M_{cruise} \quad (17.1)$$

As can be seen in the the CBS in Figure 17.1 the airframe costs are subdivided into structures and miscellaneous costs. The structural costs are then again subdivided into material, labour, overhead and investments. The material costs are estimated using Equation 17.2, where the pricing of Al-7075T6 is used as the material [7]. Because almost all the structural material is made of the more expensive and stronger aluminium Al-7075T6, it is a better estimate to use this value than other values. From this equation a total material cost of €1.05 million is estimated per unit aircraft.

$$C_{material} = Mass_{structural} \cdot Price_{Al-7075T6} \cdot F_u \cdot F_m \quad (17.2)$$

In order to calculate the costs of putting labour into the production of components Equation 17.3 can be used [7]. In this formula MHR stands for the man hours put into production and R for the hourly rate of the engineers

and manufacturers. C_{qc} stands for the quality control costs during manufacturing. For this analysis an hourly rate of €49.90 per hour and €79.05 per hour for the manufacturers and engineers is used respectively. From this it can be estimated that the costs for labour during production will be €8.5 million per unit aircraft.

$$C_{labour} = MHR_{ENG} \cdot R_{ENG} + MHR_{MAN} \cdot R_{MAN} + C_{qc} \tag{17.3}$$

The overhead costs are difficult to estimate and depend a lot on the management framework of the company. For this reason it is a formula that depends on the production labour costs of the aircraft as shown in Equation 17.4 [7]. From this formula it is estimated that the total overhead costs will be about €7.23 million per unit aircraft.

$$C_{overhead} = F_{overhead} \cdot C_{labour} \tag{17.4}$$

The last costs related to the structures of the aircraft are the investments, which include the equipment to produce parts, the buildings, facilities etc. These costs also depend heavily on the labour costs during production as can be seen in Equation 17.5 [7]. From this equation it can be estimated that the total investment cost is about €3.19 million per unit aircraft.

$$C_{investment} = F_{tech} \cdot F_{investment} \cdot C_{labour} \tag{17.5}$$

The airframe also has some miscellaneous costs next to the costs related to the structures of the aircraft as can be seen in the CBS in Figure 17.1. These miscellaneous costs include functional systems except avionics and engines. For instance, the landing gears, APU and air conditioning. Equation 17.6 shows how to estimate these costs [7]. It can be seen that these costs are driven heavily by the structural costs which is the sum of the previous four cost estimation formulas. From this equation a miscellaneous cost of €6.0 million per unit aircraft is calculated.

$$C_{miscellaneous} = F_{miscellaneous} \cdot C_{structural} \tag{17.6}$$

Now that the cost of every component related to the airframe is estimated, it is time to estimate the costs of components related to the avionics of the LEAF aircraft. The avionics are divided into four categories: software, hardware, system design and installation. All these costs are estimated based on equations where they are fractions of the base avionics kit of a Boeing 737. The assumed base avionics kit of a Boeing 737 is €2.0 million. From this it is derived that the cost for the software is €3.2 million, the hardware is €1.6 million, the system design is €1.28 million and the installation is €1.6 million. Together with a difficulty judgement factor of 1.5 it means that the avionics contribute a total of €11.52 million to the aircraft's costs per unit.

The profit of the LEAF aircraft is set at 10% of the total acquisition cost. This is a percentage widely used in the industry of passenger jet aircraft [7]. Table 17.1 shows an overview of the cost breakdown with all the corresponding costs and percentages.

Table 17.1: Cost breakdown table with the values of the costs per compartment, profit and development cost

	Cost [M€]	Percentage of acquisition cost [%]
Manufacturing	88.53	75.2
–Airframe	25.97	22.1
—-Structure	19.98	17.0
——Labour	8.5	7.2
——Material	1.05	0.89
——Overhead	7.23	6.1
——Investments	3.19	2.7
—-Miscellaneous	6.00	5.1
–Engines	40.90	34.7
–Avionics	11.52	9.8
—-Hardware	1.60	1.4
—-Software	3.20	2.7
—-System design	1.28	1.1
—-Installation	1.60	1.4
—-Miscellaneous	3.84	3.3
Total costs without profit [M€]	88.53	90.0
Profit	8.85	10.0
Total acquisition cost with profit [M€]	97.38	100.0
Development	2850	-

17.2. Return on Investment

Guillermo

As mentioned before the profit per unit aircraft is 10% of the acquisition cost. However, before selling any aircraft there has already been made a relatively large development cost. In order to know how many units need to be sold over time to break even with the development cost the total cumulative profit is plotted against the amount of aircraft units sold as shown in Figure 17.2. From this plot it can be seen that a total of about 290 LEAF aircraft need to be sold to break even and thus to start making a profit.

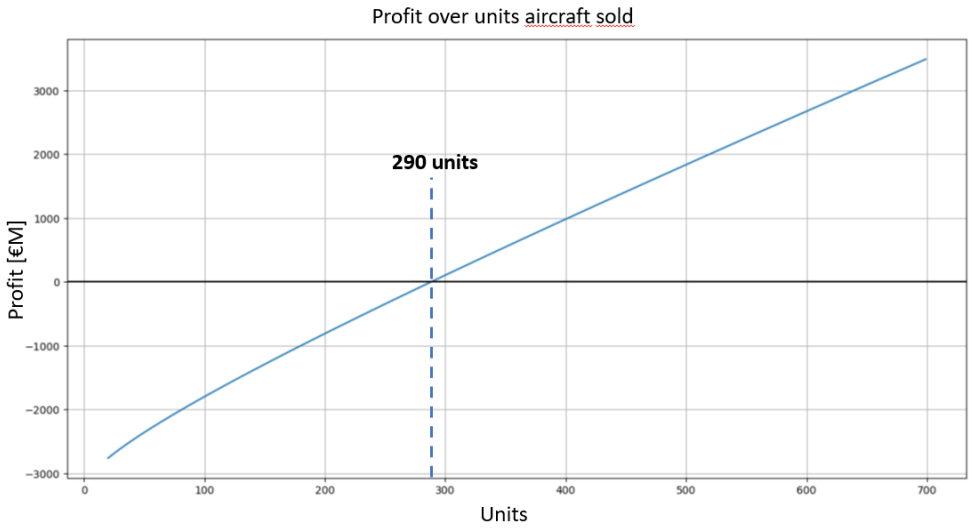

Figure 17.2: Profit of the LEAF aircraft over the amount of units sold. Note that the line is not fully linear. This is because the costs of labour becomes lower when more units are sold, thus the acquisition cost will be lower as well while the profit stays at 10%.

In Figure 17.3 [1] the cumulative deliveries of the A320 and Boeing 737 over time are shown. By assuming that the LEAF aircraft will perform the same way when entering the market as the A320 did, it can be estimated that the amount of time to reach the break even point is about five years. This means that five years after the first unit is sold investors will start getting a positive return out of their invested money.

[1] URL https://theblogbyjavier.com/2019/01/24/boeing-737-vs-airbus-a320-family-deliveries-1967-2018/ [cited 15 June 2022]

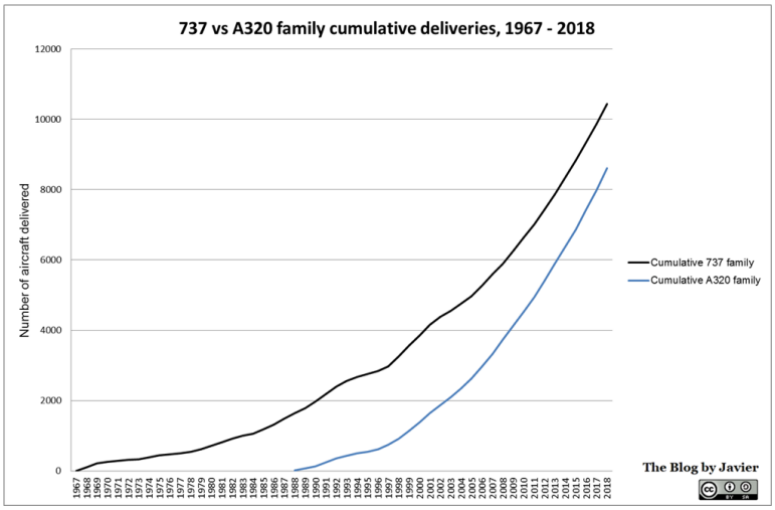

Figure 17.3: Cumulative deliveries of the A320 and Boeing 737 over time [99].

One of the requirements set by the stakeholders is the fact that the acquisition cost of the LEAF aircraft does not exceed 125% of the current acquisition cost of an A320. Since the current acquisition cost of an A320 is €97 million, this means that the LEAF aircraft cannot cost more than €121.25 million to satisfy this requirement. The total acquisition cost, including profit, of the LEAF aircraft is €117.73 million. Therefore, the financial constraint that is put on the acquisition cost is complied with.

17.3. Direct Operational Cost

Constança

An important financial analysis for the airline is the direct operational cost (DOC) of the airline. This is a combination of the following parameters.

DOC = Total financial cost + Total crew cost + Total charges and fees + Total maintenance cost + Fuel cost

Each cost parameter of the DOC will be calculated using the AEA framework based on statistical data [100] and NASA's estimation framework [101]. First, the total investment, a combination of the acquisition cost of the aircraft, the cost of airframe spares cost and the spare propulsion unit cost, will be computed. Input parameters include the engine price taken to be €20.45 million. Total financial cost is the summation of the depreciation, interest and insurance costs calculated using statistical based equations.

First, the utilisation parameter for the LEAF aircraft is computed using Equation 17.7 as it is required to determine the depreciation, interest and insurance cost of the aircraft.

$$U = t_{available}/(t_{block} + TAT) \tag{17.7}$$

where $t_{available}$, the available hours per year, is on average 6500 hours given the LEAF range of 5.000 km, t_{block} is estimated to be 3.7 hours for a medium range flight, and TAT, the TurnAround time is approximately 3 hours.

In order to determine the total financial cost of the aircraft, the total investment of the aircraft is computed. The total investment cost is a summation of the manufacturer's study price, taken to be equal to the acquisition cost, the airframe spares cost and the engine system spares cost. It is estimated to equal € 132 million. With this parameter, the depreciation, interest and insurance cost can be calculated. Moreover, the total financial cost is computed as follows:

Total financial cost = Depreciation + Interest + Insurance

Total crew cost consists of the cockpit crew (CPC) and cabin crew (CAC). These two are differentiated, given the cost disparity of the two.

$$CPC = 380 \cdot t_{block} \tag{17.8}$$

$$CAC = 60 \cdot n_{cab} \cdot t_{block} \tag{17.9}$$

Another component of the DOC of the aircraft are the cost charges by governments and fees by the airport authorities. The cost charges pertain to the navigation charges and are function of the range of the aircraft and maximum take-off weight (MTOW). The landing airport fees are solely a function of the MTOW.

Maintenance costs can be split into airframe and engine maintenance cost. First, airframe cost is a combination of labour (AFL) and material cost (AFM).

$$\text{AFM} = \text{AFP} \cdot (4.2 + 2.2\text{t}_\text{f}) \tag{17.10}$$

where AFP is the airframe price and t_f is the flight time, estimated to be the block time plus 0.25 hours.

$$\text{AFL} = (0.09 \cdot \text{AFW} + 6.7 - (\frac{350}{\text{AFW} + 15})) \cdot (0.8 + 0.68\text{t}_\text{f}) \cdot \text{R}_\text{labor} \tag{17.11}$$

where R_{labor} is the labor rate taken to be approximately €63.4 per hour.

Second, the engines are a crucial maintenance segment which is split between the labour and material cost. The engine material maintenance cost (EMM) is a function of the sea-level engine thrust, the bypass ratio, the overall pressure ratio, and the number of compressor stages. The engine maintenance labour cost is based on the same parameters and on the labour rate.

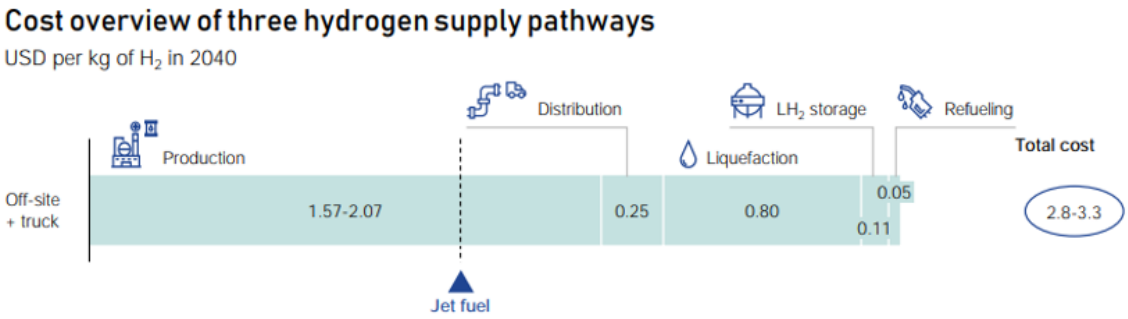

Figure 17.4: Cost of Liquid Hydrogen Breakdown [86]

Last but not least the fuel cost must be implemented. Research on the cost of both aviation kerosene fuel and liquid hydrogen was conducted. In 2035, it is expected that kerosene will reach a price of €0.50 per kilogram and liquid hydrogen €2.80 per kilogram [86]. Figure 17.4 shows the cost-breakdown of liquid hydrogen from production to refueling.

Table 17.2: Direct Operational Cost Breakdown per flight

Ownership cost			Flight					Maintenance			
Depreciation	**Interest**	**Insurance**	**Fuel**	**Cockpit crew**	**Cabin crew**	**Landing fees**	**Navigation charges**	**Airframe: Labour**	**Airframe: Material**	**Engine: Labour**	**Engine: Material**
€10,137	€7,096	€7,281	€10,793	€1,406	€888	€513	€3,270	€3,050	€160	€5,187	€707

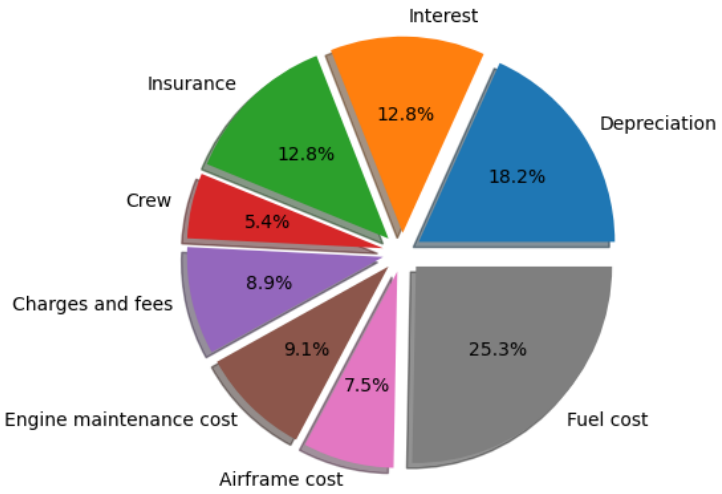

Figure 17.5: Direct operational cost breakdown per division

Per flight, there is a total direct airline flight cost of €16,870.64, approximately €94 per passenger. Adding the ownership and maintenance contributions increases this amount.

18

Compliance of Final Aircraft Design *Guillermo, Annemijn*

The following tables in this chapter show all the stakeholder requirements for the LEAF aircraft with their compliance status and some remarks. In the remarks it is stated where in this report the compliance is justified by referencing a chapter or section. If the requirement is not justified in a specific section a general description of why the requirement is complied with is given in this column as well.

Table 18.2: Stakeholder requirements from the airport

Identifier	Requirement	✓/x	Remarks
RAP-AP-PERF-01	The aircraft shall be able to operate at the same airports as the A320-200.	✓	The dimensions are similar to A320, so will be able to operate at same airports
RAP-AP-PERF-02	The refuelling system shall be possible to be integrated with existing airport infrastructure.	✓	Section 14.1

Table 18.3: Stakeholder requirements from the residents around the airport

Identifier	Requirement	✓/x	Remarks
RAP-RE-SUS-01	The aircraft shall achieve a 90% reduction of harmful non-CO_2 emissions during ground operations.	✓	Section 14.1
RAP-RE-SUS-02	The aircraft shall not produce more noise pollution than an A320-200.		Research if met is a further recommendation Section 9.7

Table 18.4: Stakeholder requirements for passengers

Identifier	Requirement	✓/x	Remarks
RAP-PAX-PERF-01	The general passenger experience shall be comparable to that of an A320-200.	✓	Figure 14.1

Table 18.1: Stakeholder requirements for airline

Identifier	Requirement	✓/x	Remarks
RAP-AP-PERF-02	The refuelling system shall be possible to be integrated with existing airport infrastructure.	✓	Section 14.1
RAP-AL-PERF-01	The flight performance of the aircraft shall be comparable to that of an A320-200	✓	Chapter 6
RAP-AL-PERF-02	The aircraft shall operate with a 10% reduced overall final energy consumption compared to the A320-200.		
RAP-AL-PERF-03	The aircraft shall be able to carry an amount of passengers or amount of cargo that is competitive with the A320-200	✓	Section 8.1
RAP-AL-PERF-04	The total turn around time for the aircraft shall be the same as for an A320-200.	✓	Section 14.1
RAP-AL-SAF-01	The aircraft shall be able to safely land using either energy source.	✓	Section 14.2
RAP-AL-SUS-01	The aircraft shall include an hybrid energy system which is able to be upgraded with more efficient components as the technology evolves.		Section 9.7
RAP-AL-SUS-02	The aircraft shall have a nominal lifetime of 30 years.	✓	
RAP-AL-FIN-01	The acquisition cost shall be maximum 25% above the cost of an A320-200.	✓	Section 17.1
RAP-AL-FIN-02	The operating cost shall not exceed the cost of an A320-200 by more than 25%.	✓	Section 17.3
RAP-AL-FIN-03	The amount of training required for A320-200 pilots to operate the aircraft shall be minimised.	✓	

Table 18.5: Stakeholder requirements for manufacturer

Identifier	Requirement	✓/x	Remarks
RAP-MA-PERF-01	All parts of the aircraft shall be manufacturable with existing manufacturing techniques.	✓	Chapter 15
RAP-MA-PERF-02	The aircraft shall maintain structural integrity at all times.	✓	Chapter 10
RAP-MA-SAF-01	All manufacturing processes will comply with industry safety standards and regulations.	✓	Chapter 15
RAP-MA-SAF-02	The aircraft shall comply with EASA's JAR25.	✓	Throughout the entire design so far, all the decisions have been made after checking with EASA's JAR25 if it is feasible
RAP-MA-FIN-01	The aircraft shall enter service in 2035.	✓	For every component of the aircraft a minimum TRL of 5 is set for the design and production technique

Table 18.6: Stakeholder requirements for airport personnel and environmental organisations

Identifier	Requirement	✓/x	Remarks
RAP-ENV-SUS-01	The aircraft shall achieve an 80% overall reduction of harmful non-CO_2 emissions with respect to the current state of the art.	✓	Section 9.4
RAP-ENV-SUS-02	The aircraft shall achieve a 30% overall reduction of CO_2 emissions with respect to the current state of the art.	✓	Section 9.4
RAP-ENV-SUS-03	The aircraft shall achieve a 100% reduction of CO_2 emissions during ground operations.	✓	Section 14.1
RAP-ENV-SUS-04	At least 90% of the aircraft parts shall be recyclable at end-of-life.	✓	Subsection 10.4.4
RAP-ENV-SUS-05	At least 5% of the aircraft parts shall be reusable at end-of-life.	✓	Subsection 10.4.3

From the tables above it can be seen that all the requirements that are set by the stakeholders are complied with. The reason for this is in part that the killer requirements were identified relatively soon into the project. These killer requirements were discussed with the customer and modified to a more feasible requirement. All the system requirements of the LEAF aircraft come from a stakeholder requirement. Therefore, it can be concluded that all the system requirements are also complied with.

19

Conclusion

Annemijn, Christoph

Near-airport residents are often exposed to a significant amount of emissions of ultra-fine particles, having a severe consequence on their health. It is therefore of high importance to reduce those emissions as much as possible at by tackling the source where they come from. The newly designed Low Emission Alternative Fuel aircraft, or LEAF aircraft, is aiming to reduce those emissions almost completely during ground operations, take-off and landing. In the case of the LEAF aircraft, this will be done using liquid hydrogen kept at cryogenic temperatures as the energy source. During cruise, kerosene will be used. This will allow to reduce total CO_2 emissions by 30%.

Many procedures are taken to produce the design given in this report. After considering trade-offs for the energy source, configuration and type of engine, a preliminary design was made. Different aspects of the aircraft had to be investigated, researched and finally designed. For every part sustainability was a driving factor that was taken into account during the design. For the aerodynamic design, sharkskin technology is used which increases aerodynamic efficiency and thus reduces energy consumption. A new, hybrid engine is designed which will limit the emissions such that the mission need statement is met, and emissions are clearly visualised throughout the report. Structural design was a crucial aspect of the design process, as it allowed for the integration of the essential components as well as ensuring the aircraft's structural integrity. Besides these regular requirements most of the materials are selected to be recycled or even reused, to lower the impact on the environment. Given that a hybrid aircraft is new to the market and because ground emissions should be reduced or completely cut, adjustments should be made to current airports in order for the LEAF aircraft to operate. To make the production feasible, a production plan was written where producing as sustainable as possible was kept in mind at all times. Finally, in a compliance matrix it is seen that almost all requirements are met, except for two for which there still needs to be a calculation added to show their compliance.

In conclusion, this report presents a complete design of a new hybrid LEAF aircraft ready to enter the market in 2035. However, even if for all parts and systems an initial structural design is already presented in this report, still a lot more work needs to be done before starting production of the aircraft. First of all, it is recommended to perform further design iteration in order to arrive at a final converged aircraft design. Furthermore, it is recommended to investigate more of how to help airport to adapt their operation for this new type of aircraft. A final recommendation is to starting testing the engine of the aircraft as soon as possible, as the current design is only based on thermodynamic calculations.

References

[1] Lockheed Martin Corporation, IHI Corp., and Bombardier Inc. *Commercial Aircraft Global Market Report*. The Business Research Company, 2022.

[2] S. Barrett, R. Britter, and I. Waitz. *Global Mortality Attributable to Aircraft Cruise Emissions*. Environmental Science & Technology, 2010.

[3] S. Gordon and B. J. McBride. “Computer Program for Calculation of Complex Chemical Equilibrium Compositions and Applications”. In: *NASA Reference Publication 1311* (1996).

[4] LTU International Airways. “Ground Operations Manual: Airbus A320-A321”. In: 15 (2003).

[5] M. Eroles, J. Ramos, and E.Robayna. *Airport Logistics Operations*. Spain: Springer, 2009.

[6] S. Trabelsi, C. Cosenza, W. Moudani, and F. Mora-Camino. “Mananing Uncertainty at Airports Ground Handling”. In: *Airports in Urban Networks* (2014).

[7] T. Zhao. “Acquisition Cost Estimating Methodology for Aircraft Conceptual Design”. In: *Cranfield University* (2009).

[8] D. Raymer. *Aircraft Design: A Conceptual Approach*. 2nd ed. California: AIAA, 1992.

[9] Group3. *Requirements change request*. Delft, The Netherlands: DSE, 2022.

[10] *Financial Statements I 2020 I*. Airbus, 2020.

[11] D. Fink. *85 dB is Not a Safe Noise Level to Prevent Hearing Loss*. The Hearing Journal, 2019.

[12] B. Graver, D. Rutherford, and S. Zheng. *CO2 Emissions From Commercial Aviation*. Washington DC, USA: International Council on Clean Transportation, 2020.

[13] M. Winther and K. Rypdal. *EMEP/EEA air pollutant emission inventory guidebook*. European Environment Agency, 2019.

[14] EASA Certification Noise Levels. *Jet aeroplanes noise database*. EASA, 2022.

[15] Boeing. *Commercial Market Outlook 2021–2040*. Boeing, 2021.

[16] European Environment Agency. *Transport and environment report 2020: Train or plane?* Denmark: Publications Office of the European Union, 2020.

[17] G. Marcias, M. Casula, M. Uras, A. Falqui, E. Miozzi, E. Sogne, S. Pili, I. Pilia, D. Fabbri, F. Meloni, M. Pau, A. Sanna, J. Fostinelli, and G. Massacci. *Occupational Fine/Ultrafine Particles and Noise Exposure in Aircraft Personnel Operating in Airport Taxiway*. Environments, 2019.

[18] A. Rios, L. Benitez, and C. Lecompte. *Sources, characteristics, toxicity, and control of ultrafine particles: An overview*. Geoscience Frontiers, 2021.

[19] C. Terzano, F. Stefano, V. Conti, E. Graziani, and A. Petroianni. *Air pollution ultrafine particles: toxicity beyond the lung*. European Review for Medical and Pharmacological Sciences, 2010.

[20] K. Moller, C. Brauer, S. Mikkelsen, J. Bonde, S. Loft, K. Helweg-Larsen, and L. Thygesen. *Cardiovascular disease and long-term occupational exposure to ultrafine particles: A cohort study of airport workers*. International Journal of Hygiene and Environmental Health, 2019.

[21] E. Kahir, K. Kim, S. Jahan, and R. Brown. *A review of airborne polycyclicaromatic hydrocarbons(PAHs)and their human health effects*. Environmental International, 2013.

[22] R. Habre, H. Zhou, S. Eckel, T. Enebish, S. Fruin, T. Bastain, E. Rappaport, and F. Gilliland. *Short-term effects of airport-associated ultrafine particle exposure on lung function and inflammation in adults with asthma*. Environmental International, 2018.

[23] B. Stacey. *Measurement of ultrafine particles at airports: A review*. Atmospheric International, 2018.

[24] D. Schraufnagel. *The health effects of ultrafine particles*. Experimental and Molecular Medicine, 2020.

[25] G. Ratliff, C. Sequeira, I. Waitz, M. Ohsfeldt, T. Thrasher, M. Graham, and T. Thompson. *Aircraft Impacts on Local and Regional Air Quality in the United States*. PARTNER, 2009.

[26] N. Alexis, C. Barnes, L. Bernstein, A. Nel, D. Peden, D. Sanchez, S. TArlo, and P. Williams. *Health effects of air pollution*. Journal of Allergy and Clinical Immunology, 2004.

[27] Z. Fotourehchi. *Health effects of air pollution: An empirical analysis for developing countries*. Atmospheric Pollution Research, 2016.

[28] M. Veleminsky, J. Stejskalova, and R. Sram. *The impact of air pollution to central nervous system in children and adults*. Neuro Endocrinol Lett., 2017.

[29] Dr Christian and N. Jardine. *Calculating the Environmental Impact of Aviation Emissions*. Oxford University Centre for the Environment, 2005.

[30] D. Gu, K. Andreev, and M. Dupre. “Major Trends in Population Growth Around the World”. In: *China CCDC Weekly* 28 (2021), pp. 604–613.

[31] N. Bullerdiek, U. Neuling, and M. Kaltschmitt. *A GHG reduction obligation for sustainable aviation fuels (SAF) in the EU and in Germany*. Hamburg University of Technology: Journal of Air Transport Management, 2020.

[32] T. Hari, Z. Yaakob, and N. Binitha. “Aviation biofuel from renewable resources: Routes, opportunities and challenges”. In: *Renewable and Sustainable Energy Reviews* 42 (2015), pp. 1234–1244.

[33] T. Hari, Z. Yaakob, and N. Binitha. “Aviation biofuel from renewable resources: Routes, opportunities and challenges”. In: *Renewable and Sustainable Energy Reviews* 42 (2015), pp. 1234–1244.

[34] D. Verstraete. “Long range transport aircraft using hydrogen fuel”. In: *Int J Hydrog Energy* 38 (2013), pp. 14824–14831.

[35] A. Contreras, S. Yigit, K. Ozay, and T. Veziroglu. “Hydrogen as aviation fuel: a comparison with hydrocarbon fuels”. In: *Int J Hydrog Energy* 22 (1997), pp. 1053–1060.

[36] A. Baroutaji, T. Wilberforce, M. Ramadan, and A. Olabi. “Comprehensive investigation on hydrogen and fuel cell technology in the aviation and aerospace sectors”. In: *Renewable and Sustainable Energy Reviews* 106 (2018), pp. 31–40.

[37] International Energy Agency. *Hydrogen Production and Storage: R&D Priorities and Gaps*. 2006.

[38] H. Kuhn, C. Falter, and A. Sizmann. *Renewable Energy Perspectives for Aviation*. Munich: AIDAA, 2015.

[39] National Academies of Sciences, Engineering, and Medicine. *Commercial Aircraft Propulsion and Energy Systems Research: Reducing Global Carbon Emissions*. Washington, DC: The National Academies Press, 2016.

[40] R. Gadsbøll. *The technical application of liquefied methane as an aviation fuel*. Danish Gas Technology Centre, 2020.

[41] D.S. Lee, D.W. Fahey, A. Skowron, M.R. Allen, U. Burkhardt, Q. Chen, S.J. Doherty, S. Freeman, P.M. Forster, J. Fuglestvedt, A. Gettelman, R.R. De Leon´, L.L. Lim, M.T. Lund, R.J. Millar, B. Owen, J.E. Penner, G. Pitari, M.J. Prather, R. Sausen, and L.J. Wilcox. “The contribution of global aviation to anthropogenic climate forcing for 2000 to 2018”. In: *Atmospheric Environment* (2020).

[42] G. Balbo, L. Blom, J. Kok, C. Veiga, C. Pabsch, I. Pszczolkowski, L. Shu, A. Stokman, J. Thornton, and G. Van. *DSE Baseline Report: Ultra-Efficient Hybrid Aircraft*. Delft University of Technology, 2022.

[43] Airbus S.A.S. “Type-Certificate Data Sheet for Airbus A318-A319-A320-A321”. In: EASA.A.064 (2022).

[44] L. Jenkinson, P. Simpkin, and D. Rhodes. *Civil Jet Aircraft Design*. Elsevier LTD, 2002.

[45] E. Torenbeek. *Advanced Aircraft Design*. John Wiley And Sons Ltd, 2013.

[46] E. Torenbeek. *Synthesis of Subsonic Airplane Design*. Nijgh-Wolter Noordhoff Universitaire Uitgevers B.V., 1976.

[47] F. Oliviero. “Lecture 3: Aircraft aerodynamic analysis - Mobile surfaces of the wing”. In: *AE2111-II Aerospace Design and Systems Engineering Elements II* (2020).

[48] M. H. Sadraey. *Aircraft Design: A Systems Engineering Approach*. John Wiley And Sons Ltd, 2012.

[49] J. Guerrero, M. Sanguineti, and K. Wittkowski. “Variable cant angle winglets for improvement of aircraft flight performance”. In: *Meccanica* 55 (2020), pp. 1–31.

[50] J. Guerrero, M. Sanguineti, and K. Wittkowski. “CFD Study of the Impact of Variable Cant Angle Winglets on Total Drag Reduction”. In: *Aerospace* 5 (2018).

[51] H. Gongzhang and E. Axtelius. *Aircraft Winglet Design: Increasing the aerodynamic efficiency of a wing*. KTH Royal Institute of Technology, 2020.

[52] A. Mehta. *Different Types of Winglets and their Corresponding Vortices*. 2016.

[53] Airbus. “A320: Aircraft Characteristics Airport and Maintenance Planning”. In: (2005).

[54] J. Cousteix. *Encyclopedia of Physical Science and Technology*. 3rd ed. Toulouse, France: Academic Press, 2003.

[55] P. Spalart and J. McLean. *Drag reduction: Enticing turbulence, and then an industry*. Philosophical Transactions of The Royal Society A Mathematical Physical and Engineering Sciences, 2011.

[56] EASA. *Easy Access Rules for Additional Airworthiness Specifications (Regulation (EU) 2015/640)*. 2021.

[57] D. Scholz M. Nita. *From Preliminary Aircraft Cabin Design to Cabin Optimization*. Hamburg University of Applied Sciences, 2010.

[58] ANSYS, inc. *Granta EduPack 2021 R2*. Version 21.2.0. June 13, 2022. URL: https://www.ansys.com/products/materials/granta-edupack.

[59] G. Balbo, L. Blom, J. Kok, C. Veiga, C. Pabsch, I. Pszczolkowski, L. Shu, A. Stokman, J. Thornton, and G. Van. *DSE Midterm Report: Ultra-Efficient Hybrid Aircraft*. Delft University of Technology, 2022.

[60] Christopher Winnefeld, Thomas Kadyk, Boris Bensmann, Ulrike Krewer, and Richard Hanke-Rauschenbach. "Modelling and Designing Cryogenic Hydrogen Tanks for Future Aircraft Applications". In: *Energies* 11.1 (2018). ISSN: 1996-1073. DOI: 10.3390/en11010105. URL: https://www.mdpi.com/1996-1073/11/1/105.

[61] I. Langella. "Lecture 3: real Brayton cycle". In: *AE2230-II Propulsion and Power* (2022), pp. 16–32.

[62] I. Langella. "Lecture 4: Aero engines - Theory". In: *AE2230-II Propulsion and Power* (2022), pp. 86–101.

[63] S. L. Dixon and C. A. Hall. *Fluid Mechanics and Thermodynamics of Turbomachinery*. 7th edition. Oxford, United Kingdom: Elsevier, 2014.

[64] M. G. Zabetakis. *Flammability Characteristics of Combustible Gases and Vapors*. 1965.

[65] M. Zuhaib Akram. "Study of hydrogen impact on lean flammability limit and burning characteristics of a kerosene surrogate". In: *Energy* 231 (2021).

[66] Thierry Dubois. *Pratt, Alcoa Pioneer Use of Aluminum Fan Blades*. 2014. URL: https://www.ainonline.com/aviation-news/air-transport/2014-07-28/pratt-alcoa-pioneer-use-aluminum-fan-blades (visited on 06/15/2022).

[67] Takehiro Okura. "Materials for Aircraft Engines". In: *University of Colorado Boulder* (2015).

[68] Y. B. Zel'dovich. "The Oxidation of Nitrogen in Combustion Explosions". In: *Acta Physicochimica* (1946), pp. 577–628.

[69] R. W. Schefer, C. White, and J. Keller. "Lean Hydrogen Combustion". In: *Lean Combustion - Technology and Control* (2008), pp. 213–245.

[70] H. Nojoumi, I. Dincer, and G.F. Naterer. "Greenhouse gas emissions assessment of hydrogen and kerosene-fueled aircraft propulsion". In: *Internation Journal of Hydrogen Energy* (2008).

[71] Pratt & Whitney. *AUXILIARY POWER UNITS (APU)*. 2022. URL: https://www.pwc.ca/en/products-and-services/products/auxiliary-power-units (visited on 06/12/2022).

[72] A. Thirkell, R. Chen, and I. Harrington. *A Fuel Cell System Sizing Tool Based on Current Production Aircraft*. SAE International, 2017.

[73] Schiphol Group. *Sustainable taxiing and the Taxibot*. -.

[74] F. Oliviero. "Lecture 7: Design for Aircraft Longitudinal Stability". In: *AE3211-I Systems Engineering and Aerospace Design* (2022).

[75] T. Muneer A.Doyle. *Electric Vehicles: Prospects and Challenges*. 2020.

[76] Janardhanan R. Rani, Ranjith Thangavel, Se-I Oh, Jeong Min Woo, Nayan Chandra Das, So-Yeon Kim, Yun-Sung Lee, and Jae-Hyung Jang. "High Volumetric Energy Density Hybrid Supercapacitors Based on Reduced Graphene Oxide Scrolls". In: *ACS Applied Materials & Interfaces* 9.27 (2017). PMID: 28613816, pp. 22398–22407. DOI: 10.1021/acsami.7b03299. eprint: https://doi.org/10.1021/acsami.7b03299. URL: https://doi.org/10.1021/acsami.7b03299.

[77] T.H.G. Megson. *Aircraft Structures for Engineering Students*. 6th edition. Oxford, United Kingdom: Elsevier, 2017.

[78] E. F. Bruhn. *Analysis and design of Flight Vehicle Structures*. Jacobs, 1973.

[79] Michael Ashby, Hugh Shercliff, and David Cebon. *Materials: Engineering, Science, Processing and Design*. 1st edition. Oxford, United Kingdom: Elsevier, 2007.

[80] Gunther Moors, Christos Kassapoglou, Sergio Francisco Müller de Almeida, and Clovis Augusto Eça Ferreira. 2019.

[81] Subodh K. Das and J. Gilbert Kaufman. “Recycling aluminum aerospace alloys”. In: *Light Metals* (2007), pp. 1161–1165.

[82] European Aviation Safety Agency. *Certification Specifications for Large Aeroplanes CS-25*. 2007.

[83] Nick van Oene. *Landing Gear Design Integration for the TU Delft Initiator*. Delft University of Technology, 2019.

[84] Joris Melkert. “Lecture 7: Wing Positioning, Landing Gear and Empennage Design”. In: *AE1222-II Aerospace Design and Systems Engineering Elements* (2020), p. 41.

[85] J. Roskam. *Airplane Design*. 1st ed. Kansas: Roskam Aviation and Engineering Corporation, 1985.

[86] Clean Sky 2 JU and McKinsey Company. *Hydrogen Powered Aviation: A fact-based study of hydrogen technology, economics and climate impact by 2050*. Luxembourg: Publications Office of the European Union, 2020.

[87] B. Oreschko, M. Schultz, and H. Fricke. “Skill Analysis of Ground Handling Staff and Delay Impacts for Turnaround Modeling”. In: *Air Transport and Operations Symposium: Technische Universität Dresden* (2011).

[88] J. Mangold, D. Silberhon, N. Moebs, N. Dzikus, J. Hoelzen, T. Zill, and A. Strohmayer. “Refueling of LH2 Aircraft—Assessment of Turnaround Procedures and Aircraft Design Implication”. In: *Energies* (2022).

[89] Aerospool. *Aircraft Maintenance Manual*. 2017.

[90] National Research Council. *New Materials for Next Generation Commercial Transports*. Washington DC: National Academy Press, 1996.

[91] K. Georgiev. “Implementation of Reliability Analysis of an Aircraft System”. In: *International Conference in Military Technology* (2016).

[92] J. Fydrych and G. Consogno. “A maintenance strategy for a multi-valve cryogenic distribution system”. In: *IOP Conference Series* 278 (2017).

[93] R. Kayque dos Santos, J. Mangabeiro, and V. Grubisic. “Modeling and reliability analysis of aircraft components and systems: a case study”. In: *Universidade de Brasilia* 18 (2020).

[94] International Air Transport Association. *Aircraft Operational Availability*. 1st ed. Canada, 2018.

[95] R. Bapu. “Evaluation of Aircraft Maintainability and Aircraft Maintenance”. In: *Sathyabama University* 1 (2017).

[96] Federal Aviation Administration. *System Safety Analysis and Assessment for Part 23 Airplanes*. US Department of Transportation, 2011.

[97] Jos Sinke. *AE3211-II Reader*. Delft University of Technology, 2021.

[98] K.E. Marks J.L. Birkler J.B. Garfinkle. *Development and production cost estimating relationships for aircraft turbine engines*. United States Airforce, 1993.

[99] The Blog by Javier. *Boeing 737 vs Airbus A320 family deliveries, 1967 – 2018*. 2019. URL: `https://theblogbyjavier.com/2019/01/24/boeing-737-vs-airbus-a320-family-deliveries-1967-2018/` (visited on 06/15/2022).

[100] M. Lee, L. Li, and W. Song. “Analysis of direct operating cost of wide-body passenger aircraft: A parametric study based on Hong Kong”. In: *Chinese Journal of Aeronautics* (2018).

[101] D. Maddalon. “Estimating Airline Operating Costs”. In: *NASA* (1978).